East European Journal of Physics. 1. 211-216 (2025)
DOI:10.26565/2312-4334-2025-1-22 ISSN 2312-4334

MODELING AND THEORETICAL STUDY OF p-n HETEROJUNCTIONS BASED ON CdTe/Si: BAND ALIGNMENT, CARRIER TRANSPORT, AND TEMPERATURE-DEPENDENT ELECTROPHYSICAL PROPERTIES

Sadulla O. Sadullaev[a,b]*, Ibrokhim B. Sapaev[b,a#], Khidoyat E. Abdikarimov[c]
[a]*Institute of Fundamental and Applied Research under TIIAME NRU, Tashkent, Uzbekistan*
[b]*National Research University TIIAME, Department of Physics and Chemistry, Tashkent, Uzbekistan*
[c]*Department of interfaculty general technical sciences, Urgench State University, Urgench, Uzbekistan*
**Corresponding Author e-mail: sadullayevs@gmail.com*
Received October 7, 2024; revised January 1, 2025; accepted January 10, 2025

This paper presents a comprehensive theoretical study of p-n heterojunctions formed between cadmium telluride (CdTe) and silicon (Si) over the temperature range of 0 K to 800 K. We focus on band alignment, carrier transport mechanisms, and the temperature-dependent electrophysical properties of the heterojunctions. Through modeling approaches, we explore the energy band structure, intrinsic concentration, intrinsic electrical conductivity, and the impact of temperature variations on the heterojunction characteristics. Our findings provide insights into optimizing the performance of CdTe/Si heterojunctions for applications in photovoltaics and optoelectronics.
Keywords: *Modeling; Built-in potential; Heterojunction; Band gap; Intrinsic concentration; Intrinsic electrical conductivity*
PACS: 73.40.Lq, 73.61.Ga, 72.20.Dp, 72.80.Ey

1. INTRODUCTION

Heterojunctions have garnered significant attention in recent decades due to their extensive applications in optoelectronic and photovoltaic devices. Among these, CdTe/Si heterojunctions stand out for their potential to enhance the performance of solar cells and photodetectors, attributable to the advantageous combination of their respective material properties [1]. Cadmium Telluride (CdTe), a II-VI compound semiconductor, is renowned for its suitability in photovoltaic (PV) solar cell production, primarily owing to its exceptional absorption coefficient ($\alpha > 10^4$ cm^{-1}) and ideal band gap of 1.5 eV [2, 3]. Silicon (Si), with its established manufacturing processes, is widely utilized in the electronics industry. The integration of these two materials into p-n heterojunctions can leverage the inherent benefits of each, resulting in improved device performance and expanded functionality [4, 5].

The formation of a p-n junction between CdTe and Si introduces complexities related to band alignment and carrier transport. The band alignment of heterojunctions plays a critical role in charge separation and recombination processes, which are pivotal for device efficiency. Numerous models have been proposed to investigate the electronic properties of these heterojunctions, particularly emphasizing band offsets, energy level alignments, and carrier mobility. Despite the promising potential of CdTe/Si heterojunctions, the temperature-dependent behavior remains a significant challenge, necessitating further theoretical and experimental exploration [5-7]. Notably, doping within CdTe-based heterojunctions profoundly influences their electrical characteristics. For instance, the introduction of lead (Pb) into CdTe films has been observed to diminish hole concentration by over three orders of magnitude due to self-compensation effects, while also resulting in a decrease in charge carrier mobility with increasing temperature during annealing [8]. To achieve an efficient photoelectric heterojunction, it is imperative to investigate the electronic properties of the semiconductors involved, considering the effects of doping impurities and their optimal spatial distribution within the heterojunction [9, 10]. These insights are vital for elucidating carrier transport mechanisms and band alignment in CdTe/Si heterojunctions, particularly under varying temperature conditions.

Temperature fluctuations can significantly affect carrier transport mechanisms by altering the band gap, carrier concentration, and mobility within the materials. Specifically, the band gap of CdTe decreases with increasing temperature, which leads to variations in conduction and valence band offsets at the heterojunction interface. Such changes critically impact the overall performance of the heterojunction, especially in applications such as thermophotovoltaics and high-temperature sensors [11,12]. Furthermore, studies focusing on temperature dependence are essential for understanding the heterojunction's resilience to operational stresses, particularly in environments characterized by fluctuating thermal conditions.

Previous investigations have sought to model these effects through both analytical and numerical approaches. Workshops on mathematical modeling of semiconductor heterostructures have delved into the numerical aspects of carrier transport across various temperature regimes [13-17]. Additionally, experimental studies have assessed the structural and electrical properties of CdTe/Si heterojunctions [7,18-25]. Nevertheless, significant gaps persist in the theoretical understanding of temperature-dependent band alignment and carrier dynamics, especially when contextualized within real-world operational scenarios.

Cite as: S.O. Sadullaev, I.B. Sapaev, Kh.E. Abdikarimov, East Eur. J. Phys. 1, 211 (2025), https://doi.org/10.26565/2312-4334-2025-1-22
© S.O. Sadullaev, I.B. Sapaev, Kh.E. Abdikarimov, 2025; CC BY 4.0 license

A thorough understanding of band alignment and charge carrier transport in CdTe/Si heterojunctions is crucial for optimizing device performance. This paper endeavors to provide an in-depth theoretical exploration of the band structure, carrier dynamics, and temperature-dependent properties of CdTe/Si heterojunctions.

Additionally, various experimental methods for fabricating p-n junction structures utilizing CdTe material have been extensively researched. Emerging fabrication techniques for CdTe/Si heterojunction structures include vapor-liquid-solid (VLS) [26] growth, transient laser-induced grating (TLIG), close-spaced vapor transport (CSVT) technique [29], chemical vapor deposition (CVD) [28], transmission electron microscopy (TEM) [21] and metalorganic vapour-phase epitaxy MOVPE [17]. These methodologies have enabled researchers to successfully create innovative structures such as nanowire arrays and nanocones, which are specifically designed to enhance light absorption in CdTe/Si heterojunction structures.

This study aims to model and analyze the band alignment and carrier transport mechanisms in CdTe/Si heterojunctions, with a particular emphasis on their temperature-dependent electrophysical properties. Employing advanced simulation tools such as TCAD Sentaurus and MATLAB [4,5], we will investigate how temperature influences the key parameters that dictate the efficiency of these heterojunctions. Moreover, we will compare theoretical results with experimental data to furnish a comprehensive understanding of the factors that enhance or impede the performance of CdTe/Si-based devices.

2. MATERIALS AND METHOD

As previously mentioned, the Band Gap emerges as the most crucial parameter in semiconductor materials. Therefore, equation (1) enables the calculation of the varying temperature of the bandgap for Si, and CdTe. The formula for calculating the temperature dependence of the bandgap in semiconductor materials is typically described by the Varshni equation. It's expressed as:

$$E_g(T) = E_g(0) - \frac{\alpha \cdot T^2}{T + \beta} \tag{1}$$

Where $E_g(T)$ and $E_g(0)$ are bandgap at T and 0 K respectively, α and β are material-specific constants. This equation shows how the bandgap energy varies with temperature. The parameters α and β are experimentally determined constants for a particular semiconductor material [29]. The results of our new model and the corresponding equation (1) are depicted in Figure 3.

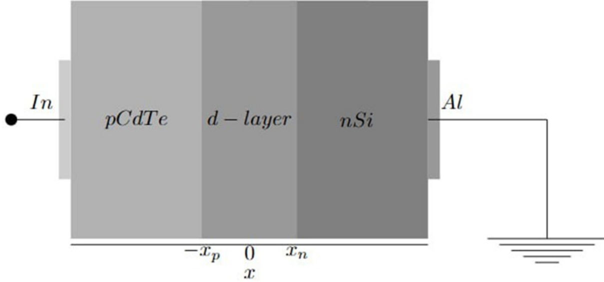

Figure 1. Schematic two-dimensional section of the p-n heterojunction structure based on pCdTe/nSi

The Figure 1 shows the 2D cross-sectional surface of the selected pCdTe/nSi sample. In this case, the p-type ohm contact is connected to In, and the n-type ohm contact is connected to Al. The band diagram corresponding to this heterojunction is shown in Figure 2.

The intrinsic concentration serves as a fundamental electrophysical parameter of semiconductor materials. The intrinsic carrier concentration n_i in a semiconductor is given by the equation:

$$n_i(T) = \sqrt{N_C(T) \cdot N_V(T)} \cdot \exp\left(-\frac{E_g(T)}{2kT}\right) \tag{2}$$

Where: $N_C(T)$ and $N_V(T)$ are the effective density of states in the conduction band and the effective density of states in the valence band. $E_g(T)$ is the energy bandgap, k is the Boltzmann constant and T is the absolute temperature.

The values of $N_C(T)$ and $N_V(T)$ depend on the material and are often expressed as functions of temperature [30,31]. The results of the corresponding equation (2) are depicted in Figure 4. Another electrophysical parameter influenced by temperature is internal conductivity. For the materials we have chosen, expression (3) corresponds to the equation for electrical conductivity as a function of temperature:

$$\sigma(T) = \sigma_0(T) \cdot \exp\left(-\frac{E_g(T)}{2kT}\right) \tag{3}$$

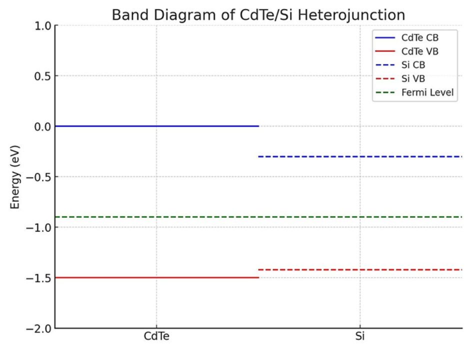

Figure 2. Band diagram of the pCdTe/nSi heterojunction

$\sigma(T)$ is the conductivity, $\sigma_0(T)$ is determined by expression (4), which indicates a linear dependence on temperature, and we have also considered that this expression is temperature-dependent. This expression (5) was analyzed in two cases: Case A, where $\sigma_0(T)$ is assumed to have a strong linear dependence on temperature, and Case B, where $\sigma_0(T)$ is considered temperature-independent. The difference between Cases A and B is presented and analyzed in Figure 5.

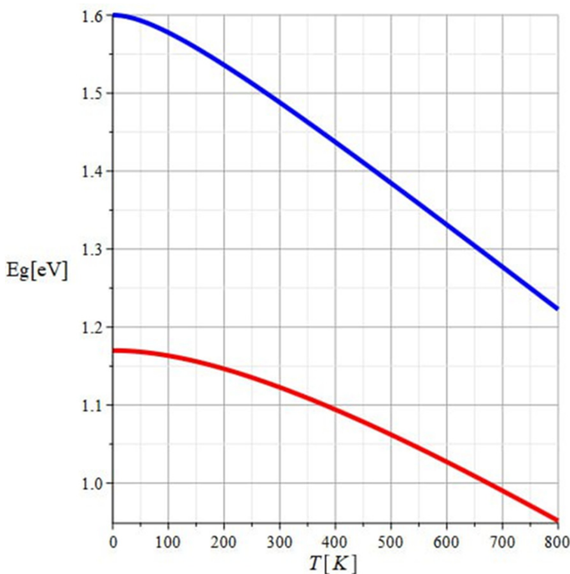

Figure 3. Band gap of a semiconductor as a function of temperature: red line for Si, blue line for CdTe

$$\sigma_0(T) = q \cdot (n(T) \cdot \mu_n(T) + p(T) \cdot \mu_p(T)) \quad (4)$$

Here, $n(T)$ and $p(T)$ are the electron and holes concentration, $\mu_n(T)$ and $\mu_p(T)$ are the electrons and hole mobility which represents the temperature dependence. If we consider equal intrinsic electrons and holes concentration $n_i(T) = p_i(T)$, expression (3) can be substituted with expression (5).

$$\sigma_i(T) = \sigma_{0i}(T) \cdot \exp\left(-\frac{E_g(T)}{2kT}\right) \quad (5)$$

The graphical representation of the result from expression (5) is depicted in Figure 5, illustrating intrinsic electrical conductivity as a function of temperature. The obtained results were derived by considering the temperature dependence of the electrophysical parameters in our model.

3 RESULTS AND DISCUSSION

This graph illustrates the well-known phenomenon of band gap narrowing with increasing temperature in semiconductor materials, which is crucial for understanding their electronic and optical properties across different operating temperatures.

Based on the analysis of Figure 3, we can conclude that both CdTe and Si exhibit significant temperature-dependent band gap narrowing from 200K to 800K. The CdTe band gap decreases more rapidly than Si, indicating a

stronger temperature dependence. This behavior has important implications for the performance of CdTe/Si heterojunction diodes across different operating temperatures.

Figure 4 shows at 300 K, $n_i(T)=1.5\cdot10^{10}[cm^{-3}]$ for Si and $n_i(T)=2\cdot10^{6}[cm^{-3}]$ for CdTe indicate the intrinsic carrier concentration. Figure 4 shows the inverse relationship of internal concentration to temperature in logarithmic form. The slopes of the lines for Si and CdTe differ, reflecting the intrinsic band gap differences between the two materials. Silicon, with a smaller band gap, shows a higher intrinsic carrier concentration at equivalent temperatures compared to CdTe, which has a larger band gap. The steeper slope of the CdTe line indicates that its intrinsic carrier concentration decreases more rapidly with decreasing temperature compared to silicon, highlighting its greater thermal stability at lower temperatures.

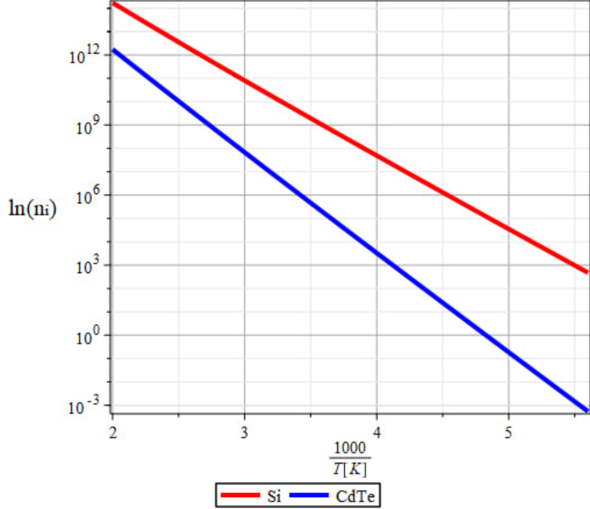

Figure 4. Internal electrical concentration as a function of temperature: red line for Si, blue line for CdTe.

At higher temperatures (left side of the graph), the intrinsic carrier concentration $n_i(T)$ of silicon is significantly higher than that of CdTe. This difference becomes more pronounced as the temperature increases due to silicon's smaller band gap, which allows for greater thermal excitation of carriers. At lower temperatures (right side of the graph), the intrinsic carrier concentration for both materials approaches lower values, but CdTe maintains a significantly lower ni compared to silicon. This makes CdTe advantageous for applications that require low carrier concentrations and minimal thermal noise at lower operating temperatures, such as infrared detectors and photovoltaics. The lower intrinsic carrier concentration in CdTe at elevated temperatures, compared to silicon, is advantageous for high-temperature applications where minimizing carrier generation is crucial, such as in high-performance photovoltaic cells. Conversely, the higher ni of silicon may benefit devices that rely on higher carrier densities for conduction, but it may also lead to increased leakage currents and thermal noise, potentially limiting its use in certain high-temperature or low-noise applications. The plot effectively illustrates the intrinsic properties of Si and CdTe and their suitability for different semiconductor applications. The analysis reveals that the choice of material for device fabrication must consider these temperature-dependent properties, especially in environments where thermal management is critical. The differences in band gap energies, as reflected in the slopes of the lines, underline the importance of material selection for optimizing the performance of semiconductor devices in varying temperature regimes.

Figure 5 shows the inverse relationship of conductivity to temperature in logarithmic form. The slope of the Si line is less steep compared to that of CdTe, indicating that silicon has a lower activation energy for conduction relative to CdTe. This suggests that at equivalent temperatures, silicon requires less energy to activate charge carriers, resulting in higher conductivity compared to CdTe. For CdTe, the steeper slope indicates a higher activation energy, which corresponds to its wider band gap. This translates to lower intrinsic conductivity at a given temperature, making CdTe more suitable for applications that require minimized leakage currents and stable performance at elevated temperatures. At higher temperatures (left side of the graph), both Si and CdTe exhibit higher conductivities, which is consistent with intrinsic conduction, where thermal energy is sufficient to excite electrons from the valence band to the conduction band. However, the higher intrinsic conductivity of Si highlights its lower band gap, enabling more electrons to be thermally excited. As the temperature decreases (right side of the graph), conductivity for both materials diminishes significantly, indicating reduced carrier availability and a shift toward extrinsic conduction dominated by impurity levels. This shift underscores the importance of doping strategies to maintain conductivity in these materials at low temperatures. CdTe's lower conductivity at higher temperatures, as evidenced by its steeper slope, suggests its advantage for applications in environments where maintaining low intrinsic carrier densities and minimal thermal noise is critical, such as in radiation detectors and high-temperature electronics. Silicon's higher intrinsic conductivity across a broad temperature range is advantageous for devices that operate efficiently at room temperature, such as microelectronics and photovoltaics. However, this characteristic may limit its effectiveness in high-temperature

environments where thermal noise must be minimized. The slopes of the linear regions for both materials can be used to extract the activation energies for conduction. This quantitative analysis provides a deeper understanding of the electronic properties of each material and helps optimize them for specific temperature-dependent applications. The Figure 5 effectively illustrates the contrasting thermal behaviors of Si and CdTe in terms of electrical conductivity. The observed differences highlight the significance of band gap energies and intrinsic material properties in determining their suitability for different semiconductor applications. The higher activation energy of CdTe suggests its preference for high-temperature environments where stability is key, while silicon's lower activation energy and higher conductivity make it ideal for room-temperature and low-temperature applications. These insights are crucial for developing efficient semiconductor devices tailored for specific operating conditions.

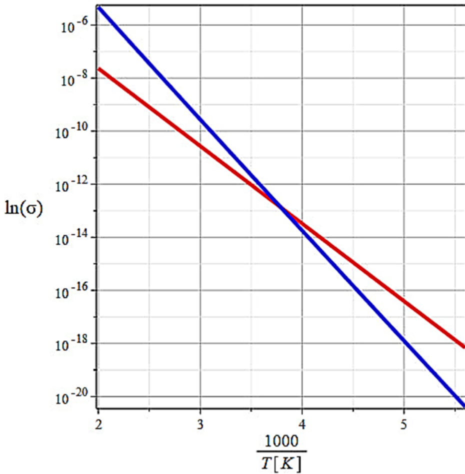

Figure 5. Internal electrical conductivity as a function of temperature: red line for Si, blue line for CdTe

CONCLUSIONS

In this study, we conducted a comprehensive modeling and theoretical analysis of p-n heterojunctions based on CdTe/Si, focusing on band alignment, carrier transport, and temperature-dependent electrophysical properties. The results indicate that the band gap and intrinsic carrier concentration of CdTe and Si are significantly affected by temperature variations. Specifically, the band gap of CdTe was found to decrease more rapidly with increasing temperature compared to Si, which highlights the strong temperature dependence of CdTe. This property is advantageous for high-temperature applications where thermal stability is critical. The intrinsic carrier concentration analysis revealed that silicon, due to its smaller band gap, maintains a higher carrier concentration at equivalent temperatures, making it suitable for applications requiring higher carrier densities.

The intrinsic conductivity analysis showed a linear relationship between conductivity and temperature. Silicon displayed a lower activation energy for conduction compared to CdTe, resulting in higher conductivity at room temperature. However, CdTe's lower intrinsic conductivity at elevated temperatures offers advantages for applications where minimizing leakage currents and maintaining stable performance are crucial.

These insights underline the importance of considering temperature-dependent properties when optimizing CdTe/Si-based devices for specific applications, such as photovoltaics, infrared detectors, and high-temperature electronics. Future work should focus on experimental validation of these theoretical findings and explore the influence of different doping strategies and material modifications on the performance of CdTe/Si heterojunctions under varying temperature conditions.

ORCID
Sadulla O. Sadullaev, https://orcid.org/0000-0003-2444-4055; **Ibrokhim B. Sapaev,** https://orcid.org/0000-0003-2365-1554
Khidoyat E. Abdikarimov, https://orcid.org/0009-0002-9994-5612

REFERENCES

[1] R.A. Ismail, K.I. Hassan, et al., Mat. Sci. Sem. Processing, **10**, 1 (2007). https://doi.org/10.1016/j.mssp.2006.12.001
[2] M.H. Ehsan, H.R. Dizaji, and M.H. Mirhaj, Digest Journal of Nanomaterials and Biostructures, 7, 629 (2012).
[3] W.A. Pinheiro, V.D. Falcão, L.R. de Oliveira Cruz, and C.L. Ferreira, Materials Research, **91**, 47 (2006). https://doi.org/10.1590/S1516-14392006000100010
[4] J.Sh. Abdullayev, and I.B. Sapaev, Eur. J. Phys. **3**(49), 21 (2024). https://doi.org/10.31489/2024No3/21-28
[5] J.Sh. Abdullayev, and I.B. Sapaev, East Eur. J. Phys. (3, (2024). https://doi.org/10.26565/2312-4334-2024-3-39
[6] A. Cao, T. Tan, *et. al*., **545**, 323 (2018). https://doi.org/10.1016/j.physb.2018.06.035
[7] T.L. Chu, S.S. Chu, and S.T. Ang, J. Appl. Phys. **64**, 1233 (1988). https://doi.org/10.1063/1.341840
[8] Sh.B. Utamuratova, *et. al*., East Eur. J. Phys. (3), 385 (2023). https://doi.org/10.26565/2312-4334-2023-3-41
[9] V.I. Chepurnov, *et. al*., Computational Nanotechnology, **8**(3), 59 (2021). https://doi.org/10.33693/2313-223X-2021-8-3-59-68

[10] F. Bouzid, E. Kayahan, M.A. Saeed, *et al*., Applied Physics A, **130**, 222 (2024). https://doi.org/10.1007/s00339-024-07377-y
[11] C.H. Su, J. Appl. Phys. **103**, 084903 (2008), https://doi.org/10.1063/1.2899087
[12] M.N. Harif, *et. al*., Crystals, **13**(5), 848 (2023). https://doi.org/10.3390/cryst13050848
[13] S.H. Zyoud, *et. al*., Crystals, **11**, 1454 (2021). https://doi.org/10.20944/preprints202110.0346.v1
[14] *Mathematics for Semiconductor Heterostructures, Modeling, Analysis, and Numerics, International Workshop,* (2012). www.wias-berlin.de/workshops/msh2012
[15] E.A.B. Cole, *Mathematical and Numerical Modelling of Heterostructure Semiconductor Devices: From Theory to Programming*, (Springer-Verlag, London, 2009). https://doi.org/10.1007/978-1-84882-937-4
[16] M.V. Dolgopolov, *et al*., Samara U., Nat. Sci. Series, **30,** 64 (2024). http://dx.doi.org/10.18287/2541-7525-2024-30-1-64-81 (in Russian)
[17] J. Chavez, X. Zhou, S. Almeida, R. Aguirre, *et al*., J. Mat. Sci. Research, **5**(3), 1(2016). https://doi.org/10.5539/jmsr.v5n3p1
[18] B.S. Chaudhari, M. Niraula, *et. al*., J. Electronic Materials, **52**, 3431–3435 (2023). https://doi.org/10.1007/s11664-023-10318-9
[19] M.A. Razooqia, *et. al*., Ad. Mat. Research, **702**, 236 (2013). https://doi.org/10.4028/www.scientific.net/AMR.702.236
[20] X. Li, J. Lu, *et. al*., Nuclear Science and Techniques, **31**, 18 (2020). https://doi.org/10.1007/s41365-020-0723-y
[21] S.R. Bera, and S. Saha, Appl. Nanosci. **6**, 1037 (2016). https://doi.org/10.1007/s13204-015-0516-5
[22] E. Napchan, "HETEROJUNCTIONS OF CdTe ON Si", Imperial College of Science and Technology, (1987)
[23] D.J. Smith, *et al*., Materials Science and Engineering B, **77**, 93 (2000). https://doi.org/10.1016/S0921-5107(00)00480-3
[24] W.F. Mohammad, Circuits and Systems, **3**, (2012). http://doi.org/10.4236/cs.2012.31007
[25] V. Mizeikis, K. Jarašiunas, *et. al*., J. Crystal Growth, **214/215**, (2000). http://doi.org/10.1016/s0022-0248(00)00075-0
[26] M.C. Putnam, *et al*., Energy & Environmental Science, **3**(8), 1037 (2010). https://doi.org/10.1039/C0EE00014K
[27] A.V. Sukach, V.V. Tetyorkin, and N.M. Krolevec, Semiconductor Physics, Quantum Electronics & Optoelectronics, **2,** 13 (2010). http://journal-spqeo.org.ua/n2_2010/v13n2-2010-p221-225.pdf
[28] S. Osono, Y. Uchiyama, *et. al*., Thin Solid Films, **430,** 165 (2003). https://doi.org/10.1016/S0040-6090(03)00100-7
[29] I.B. Sapaev, *et. al*., E3S Web of Conferences, **410**, 02057 (2023). https://doi.org/10.1051/e3sconf/202341002057
[30] I.B. Sapaev, *et. al*., E3S Web of Conferences, **413,** 04009 (2023). https://doi.org/10.1051/e3sconf/202341304009
[31] I.B. Sapaev, *et. al*., E3S Web of Conferences, **413,** 04008 (2023). https://doi.org/10.1051/e3sconf/202341304008

МОДЕЛЮВАННЯ ТА ТЕОРЕТИЧНЕ ДОСЛІДЖЕННЯ p-n ГЕТЕРОПЕРЕХОДІВ НА ОСНОВІ CdTe/Si: ВИРІВНЮВАННЯ ЗОНИ, ТРАНСПОРТ НОСІЇВ ТА ЕЛЕКТРОФІЗИЧНІ ВЛАСТИВОСТІ, ЗАЛЕЖНІ ВІД ТЕМПЕРАТУРИ

Садулла О. Садуллаєв[a,b], Іброхім Б. Сапаєв[b,a], Хідоят Е. Абдікарімов[c]
[a]Інститут фундаментальних і прикладних досліджень при TIIAME NRU, Ташкент, Узбекистан
[b]Національний дослідницький університет TIIAME, факультет фізики та хімії, Ташкент, Узбекистан
[c]Кафедра міжфакультетських загальнотехнічних наук Ургенчського державного університету, Ургенч, Узбекистан

У цій статті представлено всебічне теоретичне дослідження p-n гетеропереходів, утворених між телуридом кадмію (CdTe) і кремнієм (Si) у діапазоні температур від 0 K до 800 K. Ми зосереджуємося на вирівнюванні зон, механізмах транспорту носіїв і температурно-залежних електрофізичних властивостях гетеропереходів. За допомогою підходів моделювання ми досліджуємо енергетичну зонну структуру, власну концентрацію, власну електропровідність та вплив зміни температури на характеристики гетеропереходу. Наші результати надають нові знання для оптимізації продуктивності гетеропереходів CdTe/Si для застосувань у фотоелектричних і оптоелектронних пристроях.

Ключові слова: *моделювання; вбудований потенціал; гетероперехід; ширина забороненої зони; власна концентрація власна електропровідність*

East European Journal of Physics. **1.** 217-232 (2025)
DOI:10.26565/2312-4334-2025-1-23 ISSN 2312-4334

GRAPHENE OXIDE AND REDUCED GRAPHENE OXIDE AS HOLE TRANSPORT LAYERS FOR IMPROVED EFFICIENCY IN FULLERENE-BASED BULK HETEROJUNCTION ORGANIC SOLAR CELLS: A NUMERICAL SIMULATION STUDY

Denet Davis, K.S. Sudheer*
Optoelectronics Device Simulation Research Lab, Department of Physics, Christ College (Autonomous), Irinjalakuda, Thrissur, Kerala, India, 680125
University of Calicut, Calicut, Kerala, India, 673635
**Corresponding author: sudheersebastian@christcollegeijk.edu.in*
Received October 4, 2024; revised December 12, 2024; accepted January 13, 2025

A growing area of research in recent years has focused on improving the efficiency of [6,6]-phenyl-C61-butyric acid methyl ester (PCBM) fullerene-based bulk heterojunction organic solar cells (BHJOSC) using poly 3-hexylthiophene-2,5-diyl (P3HT) as the donor and graphene derivatives as the hole transport layer (HTL). Graphene derivatives, mainly graphene oxide (GO) and reduced graphene oxide (RGO), possess similar exceptional characteristics as that of graphene, and are good candidates as HTL in P3HT:PCBM based BHJOSC's. In this work, we use, One-Dimensional Solar Cell Capacitance Simulator (SCAPS1D) for the extensive and detailed study of two configurations, namely ITO/GO/P3HT:PCBM/Al and ITO/RGO/P3HT: PCBM/Al. Both configurations are optimized, and enhanced efficiencies are achieved by varying electrical input parameters of the device. Thereafter, design, simulation and analysis of different device combinations are done using nine distinct ETL's and three metal electrodes. ITO/GO/P3HT:PCBM/LiF/Ca and ITO/RGO/ P3HT:PCBM/LiF/Ca gave improved efficiencies of 8.00% and 12.00% respectively. Then, the influence of varying donor density of Lithium Fluoride (LiF), and effect of varying work function of Indium Tin oxide (ITO), on the device performance of these two devices is studied. A record efficiency of 16.47%, is attained for increased donor density of LiF in ITO/RGO/P3HT:PCBM/LiF/Ca configuration.
Keywords: *Bulk heterojunction organic solar cell; One Dimensional Solar Cell Capacitance Simulator; Graphene oxide; Reduced graphene oxide; Enhanced efficiency*
PACS: 85.60.-q, 84.60.Jt, 81.05.ue

1. INTRODUCTION

Bulk heterojunction (BHJ) organic photovoltaic (OPV) devices have garnered growing attention in research, driven by their promise for affordable, printable solar cells (SC) [1] that can be manufactured on flexible substrates. The typical composition of conventional BHJ photoactive material involves an interpenetrating network of electron-donor conjugated polymers [2] and electron-acceptor fullerenes, and among all the bulk heterojunction active materials, the mixture of solution-processed poly 3-hexylthiophene-2,5-diyl (P3HT) (as donor molecules) and fullerene derivative [6,6]-phenyl-C61-butyric acid methyl ester (PCBM) (as acceptor molecules) is the most researched blend [3–5]. In a simple BHJ device, both the donor and acceptor phases makes direct electrical contact with the cathode and anode, leading to recombination of carriers and current leakage [6-8]. Electron transport layers (ETL's) and hole transport layers (HTL's) are used to counteract these detrimental effects [7,8]. Identifying appropriate HTL and ETL with attention is critical for achieving improved stability and efficiency.

In the P3HT:PCBM based bulk heterojunction organic solar cell (BHJOSC), poly(3,4-ethylenedioxythiophene) polystyrene sulfonate (PEDOT:PSS) is the most extensively employed HTL [9-20]. This particular material is preferred because of its excellent conductivity and transparency, as well as its ability to improve the smoothness of the surface when applied on Indium Tin oxide (ITO). Nevertheless, the utilization of PEDOT: PSS comes with certain drawbacks, including its hygroscopicity, anisotropic charge injection, acidic nature, and batch-to-batch variations in electrical and physical properties. In order to investigate potential substitute materials for PEDOT:PSS in organic electronic devices, a great deal of research has been done [21]. In recent years graphene derivatives have emerged as a prominent alternative for PEDOT:PSS in P3HT:PCBM based bulk heterojunction organic solar cells (BHJOSC's).

Graphene oxide (GO) and reduced graphene oxide (RGO) are oxygen functionalized derivatives of graphene with a wider bandgap than graphene (0-4.66 eV) [22-27]. Since graphene is known to be the strongest and thinnest substance on Earth, with higher carrier mobility (1000–10000 $cm^2 V^{-1} s^{-1}$), [28] zero bandgap, [29] and higher electrical conductivity, [30] breaking its chemical bonds is a highly challenging task. However, GO and RGO exhibit similar remarkable properties, which have the potential to enhance the stability of devices [31-32]. Moreover, GO/RGO shows promise as a superior substitute for PEDOT: PSS as the best HTL alternative. This is due to its adjustable electrical properties, work function compatibility with P3HT:PCBM, and potential for efficient and cost-effective manufacturing methods [33-36].

Since there are multiple affordable methods for fabricating GO and RGO from graphite and, graphite is more readily available than many other materials, we choose GO and RGO as HTL for our study. One state-of-the-art process for fabricating GO is the modified Hummer's method. GO is essentially graphene that contains functional groups with

Cite as: D. Davis, K.S. Sudheer, East Eur. J. Phys. 1, 217 (2025), https://doi.org/10.26565/2312-4334-2025-1-23
© D. Davis, K.S. Sudheer, 2025; CC BY 4.0 license

oxygen, including epoxides, hydroxyls, and carboxyl's. The modified Hummer's method entails the oxidation of graphite flakes using a combination of potent acids and oxidising agents [37-39]. GO is reduced to obtain RGO. The selection of the reduction technique relies on various factors, including safety concerns, the desired characteristics of the resulting RGO, and the intended purpose. After reduction, some of the oxygen functional groups are removed, and the resulting RGO exhibits improved electrical conductivity and other properties closer to pristine graphene [40-43].

GO possesses numerous oxygen functional groups, resulting in a broader bandgap compared to RGO. Consequently, the mobility of charge carriers becomes challenging. However, the reduction of GO to RGO diminishes the bandgap, rendering RGO more appropriate for electronic applications that require semi-conductive or conductive characteristics. RGO, with improved conductivity and reduced defects, will exhibit higher charge carrier mobility, which could contribute to efficient charge transport in bulk heterojunction organic solar cells [44-46].

Researchers have successfully fabricated BHJOSC with the configurations ITO/ GO/P3HT:PCBM/Al and ITO/RGO/P3HT:PCBM/Al in which ITO acts as the anode, and Aluminium (Al) acts as the cathode. In 2010, Shao *et al.* worked on ITO/GO/P3HT:PCBM/Al, with graphene oxide (made using the modified Hummer's method) as HTL with different thickness 2nm, 4nm, and 6 nm and attained 3.5%, 2%, and 0.9%, respectively [47]. The necessity of a simulation study on the effect of varying thicknesses of HTL and active layer exists. An extensive numerical simulation study on the effect on device performance with varying thickness of 5 nm to 100 nm has not been reported elsewhere, which we have carried out successfully and found the optimum thickness of HTL and active layer for better device performance.

In 2013, Jun *et al.* worked on P3HT:PCBM BHJOSC with similar configuration with graphene oxide nanoribbon as HTL. Notably, this solar cell device does not include an electron transport layer (ETL), and impressively, the fabricated device has an efficiency of approximately 4.02% [48]. For the past few years scientists and researchers have been introducing reduced graphene oxide as hole transport layer in BHJ OSC with P3HT:PCBM as active layer, ITO as anode, and Al as cathode with device configuration ITO/RGO/ P3HT:PCBM/Al. In 2011, Nguyen *et al.* reported 3.98% efficiency with RGO as HTL, [49] and later on, in the year 2020, Fakharan *et al.* reported an improved efficiency of 4.02% for RGO produced by Nd:YAG laser production as HTL for the same configuration [50]. Modelling and extended simulation study on ITO/GO/P3HT:PCBM/Al and ITO/RGO/ P3HT:PCBM/Al have not been reported elsewhere.

Our work includes extensive and detailed numerical simulation study, of configurations ITO/GO/P3HT:PCBM/Al, and ITO/RGO/P3HT:PCBM/Al, and improving their efficiency via optimisation. We have studied the influence of thickness, electron mobility, hole mobility, and defect density of active layer on the device performance. The effect of thickness, defect density, electron mobility, hole mobility and acceptor density of HTL, interface layer defect, series resistance, shunt resistance, and operating temperature is also studied. After optimisation of ITO/GO/P3HT:PCBM/Al, we achieved an efficiency of 4.32%, which is much greater than 1.63% (standardized work)[51] and optimisation of ITO/RGO/P3HT:PCBM/Al gave an enhanced efficiency of 6.65%, which is much higher than 0.65%(standardized work) [51]. In the intention of improving device performance, we design and simulate various device combinations, by incorporating nine diverse ETL's and three cathodes. The ETL's used include, N,N'- Bis(N,N-dimethylpropan-1-amine oxide)perylene-3,4,9,10-tetracarboxylic diimide (PDINO), Poly(9,9-bis(3'-(N,N-dimethyl) -N-ethylammoinium-propyl-2,7-fluorene)-alt-2,7-(9,9-dioctylfluorene)) dibromide (PFN-Br), Zinc oxide (ZnO), Lithium Fluoride (LiF), Indium gallium zinc oxide (IGZO), C60, [6,6]-phenyl-C_{61}-butyric acid methyl ester (PCBM) and Titanium dioxide: graphene composite (TiO_2:gr) and nitrogen doped graphene(n-graphene). Whereas, Aluminium (Al), Calcium (Ca) and Silver (Ag) are the three cathodes used for the study. Enhanced efficiencies of 8.00% and 12.00% is attained for the BHJOSC's with configuration ITO/GO /P3HT:PCBM/LiF/Ca and ITO/RGO/P3HT:PCBM/LiF/Ca respectively. Thereafter, the influence of varying donor density of LiF (ETL) on the device performance of configurations ITO/GO/P3HT:PCBM/LiF/Ca and ITO/RGO/P3HT:PCBM/LiF/Ca is also studied. A record high efficiency of 16.47%, Open circuit voltage (*Voc*) of 0.7389V, short circuit current density (*Jsc*) of 26.733287mA/cm^2 and fill factor (*FF*) of 83.36% is achieved for ITO/RGO/P3HT:PCBM/LiF/Al for increased donor density of LiF. The effect of varying work function of ITO on these configurations is also examined and no significant enhancement in efficiency is attained. From our studies, it can be concluded that RGO (bandgap-1.5 eV), when used as HTL, seems to produce a higher efficiency, when compared to GO (bandgap-2.48eV). Device with Ca (2.9eV), [52] placed as cathode seem to give better device performance compared to Al (4.2eV), [53] and Ag (4.35eV) [54].

2. METHODOLOGY, MODELLING AND PARAMETER SETTING

A One-Dimensional Solar Cell Capacitance Simulator (SCAPS1D) is used for the simulation. By solving the semiconductor equations, including Poisson's equation (Eq. 1), continuity equations for electrons (Eq. 2), and equations for holes (Eq. 3), which are provided below, the software creates a working point solution in steady state [55].

$$\frac{\partial}{\partial x}\left(\varepsilon_0 \varepsilon(x) \frac{\partial \Psi}{\partial x}\right) = -q\left[-n + p - N_A^- + N_D^+ \frac{\rho_{def}(n,p)}{q}\right] \quad (1)$$

$$-\frac{\partial J_n}{\partial x} - U_n(n,p) + G = \frac{\partial n}{\partial t} \quad (2)$$

$$\frac{-\partial J_p}{\partial x} - Up(n,p) + G = \frac{\partial p}{\partial t} \quad (3)$$

where ε is the dielectric permittivity, ε_0 is the permittivity of free space, Ψ is the electrostatic potential, n is the carrier concentration of electrons, p is the carrier concentration of holes, N_D^+ is the ionized donor concentration, N_A^+ is the ionized acceptor concentration, $\rho_{def}(n,p)$ is the distribution of defects, J_n is the electron current density, and J_p is the hole current density. U_n is the recombination rate of electrons, U_p is the recombination rate of holes, and G is the generation rate. The electron and hole current densities are given by the charge transport equations. D_n and D_p are electron and hole diffusion coefficients. Electron and hole mobilities are denoted by μ_n and μ_p respectively [55].

$$J_n = D_n \frac{dn}{dx} + \mu_n n \frac{d\phi}{dx} \tag{4}$$

$$J_p = D_p \frac{dn}{dx} + \mu_p p \frac{d\phi}{dx} \tag{5}$$

The schematic diagram of simulated device structure is shown in Fig. 1 (a), and Fig. 1 (b) gives the energy band diagram of layers used in the simulation study (GO, RGO, P3HT:PCBM, PDINO, PFN-Br, LiF, ZnO, IGZO, C60, PCBM, TiO_2:gr and n-graphene). The numerical input parameters of the active layer and the hole transport layers is listed in Table 1 and the input parameters of electron transport layers is listed in Table 2 and Table 3. The input parameters are taken from previous literature.

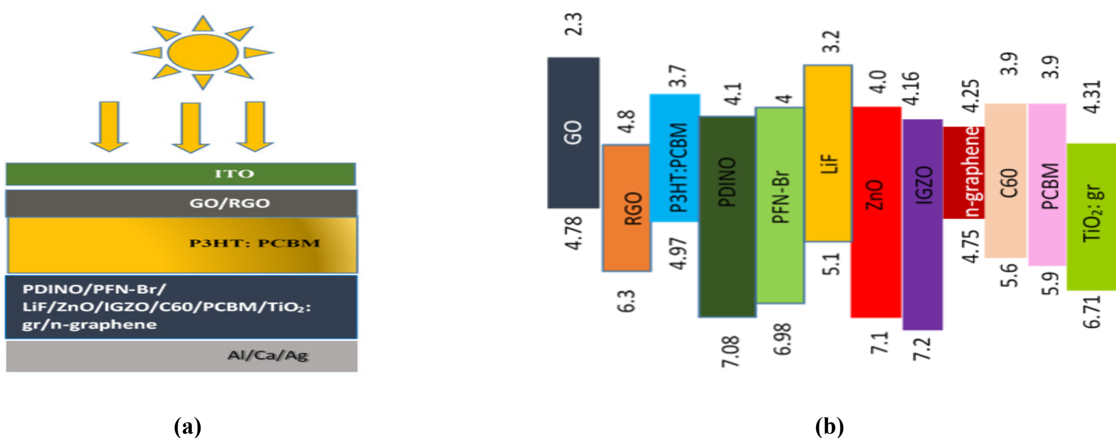

(a) **(b)**

Figure 1. Modelling of BHJOSC device: (a) schematic diagram of device structure, and (b) energy band diagram of layers GO, RGO, P3HT: PCBM, PDINO, PFN-Br, LiF, ZnO, IGZO, C60, PCBM, TiO_2:gr, and n-graphene

Capture cross section, electron and hole thermal velocity, for all layers are set to 1×10^{-15} cm^2, and 1×10^7cm/s, respectively. Furthermore, the capture cross-section for the HTL/active layer interface, and active layer/ETL interface is chosen as $1\times10^{-19}cm^2$. As in SCAPS1D, the energy level with respect to the reference (eV) is kept constant for all layers, at 0.6eV. The simulation is run at 323K operating temperature under AM1.5G light with an intensity of 1000mW/cm^2. The parameter values that are not mentioned in the table are set as given in SCAPS1D. The listed input parameters are used to standardize configurations ITO/GO/P3HT:PCBM/Al and ITO/RGO/P3HT:PCBM/Al.

Table 1. Numerical input parameters of active layer P3HT:PCBM and hole transport layer RGO

Parameters	P3HT:PCBM	Graphene oxide	Reduced graphene oxide
Thickness (nm)	100 [51]	35 [51]	35 [51]
Bandgap (E_g) (eV)	1.27 [56]	2.48 [59]	1.5 [60]
Electron affinity (χ) (eV)	3.7 [56]	2.3 [59]	4.8 [61]
Dielectric permittivity (ε_r)	3.5 [5]	10 [59]	13.3 [62]
Conduction band density CB (cm^{-3})	7.8×10^{19} [57]	1.8×10^{18} [59]	1×10^{19} [63]
Valence band density VB (cm^{-3})	7.8×10^{19} [57]	2.2×10^{18} [59]	1×10^{19} [63]
Thermal velocity of electrons V_e (cm/s)	1×10^7 [58]	1×10^7 [59]	1×10^7
Thermal velocity of holes V_h (cm/s)	1×10^7 [58]	1×10^7 [59]	1×10^7
Electron mobility μ_e (cm^2/Vs)	2×10^{-3} [58]	2.6×10^1 [59]	3.2×10^2 [64]
Hole mobility μ_h (cm^2/Vs)	2×10^{-3} [58]	1.23×10^2 [59]	3.2×10^2 [64]
Donor density N_D (cm^{-3})	0 [57]	0 [59]	0
Acceptor density N_A (cm^{-3})	0 [57]	1×10^{18} [59]	1×10^{18}
Defect density N_t (cm^{-3})	6.847×10^{15}	1×10^9 [59]	1×10^9

Table 2. Numerical input parameters of electron transport layers PDINO, PFN-Br, LiF, ZnO

Parameters	PDINO	PFN-Br	LiF	ZnO
Thickness (nm)	5 [65]	5 [66]	20 [67]	20 [71]
E_g (eV)	2.98 [65]	2.98 [66]	1.9 (varied) [68]	3.1 [72]
χ (eV)	4.1 [65]	4 [66]	3.2[68,69]	4 [73]

Parameters	**PDINO**	**PFN-Br**	**LiF**	**ZnO**
ε	5 [65]	5 [66]	9.1 [70]	9 [74]
CB (cm^{-3})	1×10^{19} [65]	1×10^{19} [66]	1×10^{20} [67,69]	2×10^{18} [74]
VB (cm^{-3})	1×10^{19} [65]	1×10^{18} [66]	1×10^{20} [67,69]	1.8×10^{19} [74]
V_e(cm/s)	1×10^{7} [65]	1×10^{7} [66]	1×10^{7} [69]	1×10^{7} [74]
V_h(cm/s)	1×10^{7} [65]	1×10^{7} [66]	1×10^{7} [69]	1×10^{7} [74]
μ_e (cm²/Vs)	2×10^{-6} [65]	2×10^{-6} [66]	1 [67,69]	1×10^{2} [74]
μ_h (cm²/Vs)	1×10^{-3} [65]	1×10^{-4} [66]	1 [67,69]	2.5×10^{2} [74]
N_D (cm^{-3})	2×10^{21} [65]	9×10^{18} [66]	1×10^{18} [67]	1×10^{18} [74]
N_A (cm^{-3})	0 [65]	0 [66]	0	0 [75]
N_t (cm^{-3})	1×10^{9}	1×10^{14} [66]	1×10^{9}	1×10^{14} [74]

Table 3. Numerical input parameters of electron transport layers IGZO, PCBM, C60, TiO_2: gr and n-graphene

Parameters	**IGZO** [75]	**PCBM** [75]	**C60** [75]	**TiO_2:graphene** [76]	**n-graphene** [77]
Thickness (nm)	5	5	5	50	0.334
E_g (eV)	3.05	2	1.7	2.4	0.5
(χ) (eV)	4.16	3.9	3.9	4.31	4.8
(ε)	10	3.9	4.2	7.8	10
CB (cm^{-3})	1×10^{19}	1×10^{19}	1×10^{19}	1×10^{19}	3×10^{19}
VB (cm^{-3})	1×10^{19}	1×10^{19}	1×10^{19}	1×10^{19}	3×10^{19}
V_e (cm/s)	1×10^{7}	1×10^{7}	1×10^{7}	1×10^{7}	1×10^{7}
V_h (cm/s)	1×10^{7}	1×10^{7}	1×10^{7}	1×10^{7}	1×10^{7}
μ_e (cm²/Vs)	15	0.02	8×10^{-2}	350	10
μ_h (cm²/Vs)	0.1	0.02	3.5×10^{-3}	350	1×10^{5}
N_D (cm^{-3})	1×10^{19}	1×10^{19}	1×10^{19}	5×10^{18}	1×10^{26}
N_A (cm^{-3})	0	0	0	0	0
N_t (cm^{-3})	1×10^{19}	1×10^{19}	1×10^{19}	1×10^{14}	1×10^{14}

3. STANDARDIZATION

A definite requirement for software validation is standardisation. The configurations, ITO/GO/P3HT:PCBM/Al and ITO/RGO/P3HT:PCBM/Al, are studied in our work, in which efficiencies of 1.63% and 0.65% are achieved [51]. Table 4 and Table 5 summarizes the validation of software via comparison of simulated and experimental outcome.

Table 4. Output parameters of ITO/GO/P3HT:PCBM/Al

	Voc (V)	*Jsc* (mA/cm²)	*FF* (%)	Efficiency (%)
Experimental	0.57±0.02	6.94±0.1	41.2±0.01	1.63±0.01
Simulation	0.5329	7.6325	40.88	1.66

Table 5. Output parameters of ITO/RGO/P3HT: PCBM/Al

	Voc (V)	Jsc (mA/cm²)	FF (%)	Efficiency (%)
Experimental	0.38±0.02	5.37±0.4	31.2±0.03	0.65±0.13
Simulation	0.3945	5.78	28.41	0.65

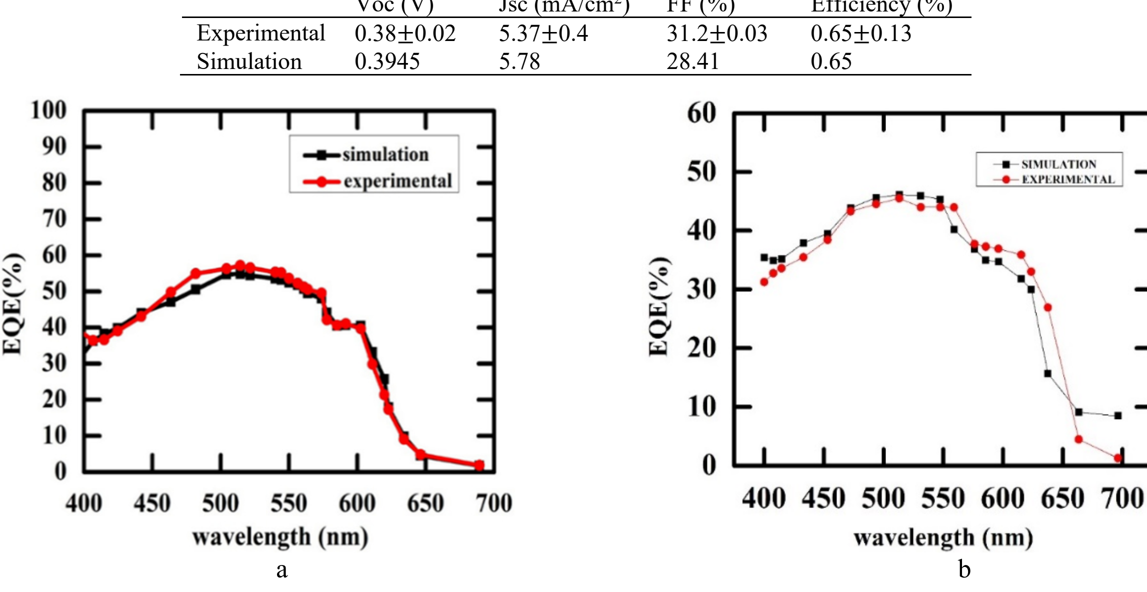

Figure 2. The matched experimental and simulation quantum efficiency graph of: (a) ITO/GO/P3HT:PCBM/Al, and (b) ITO/RGO/P3HT:PCBM/Al

Fig. 2 (a) and Fig. 2 (b) shows the matched quantum efficiency (*QE*) graph obtained from experimental results and simulation results of ITO/GO/P3HT:PCBM/Al and ITO/RGO/P3HT:PCBM/Al respectively.

4. RESULTS AND DISCUSSION

4.1. ITO/GO/P3HT: PCBM/Al

With the aim of designing a high efficiency BHJOSC with graphene oxide as HTL, an extensive numerical simulation study of ITO/GO/P3HT:PCBM/Al is done. The impact of electrical parameters, including thickness, defect density, electron mobility, and hole mobility of active layer, is studied. The effect of thickness, defect density, electron mobility, hole mobility, and acceptor density of HTL is also studied. In addition, the influence of interface (GO/P3HT:PCBM interface) defect, operating temperature, series resistance, and shunt resistance is also investigated. The device is optimised. Combination of device structures with nine distinct ETL's (PDINO, PFN-Br, LiF, ZnO, IGZO, C60, PCBM, TiO_2:gr, and n-graphene) and three metal contacts are simulated and analysed. The influence of donor density of ETL and effect of varying ITO work function on device performance of best configuration is also examined.

4.1.1. Influence of various electrical parameters of P3HT:PCBM

The input electrical parameters of the active layer play a crucial and significant role in improving the device stability and performance. The effect of input electrical parameters on device output parameters is studied and plotted in Fig. 3. The thickness of the active layer is a very important parameter for the smooth performance of BHJOSC. The thickness of the photoactive material is varied, from 20nm to 120nm, and the effect on output parameters is studied, and plotted in Fig. 3(a). As the thickness of the active material increases, efficiency rises, to a maximum value of 1.81% at 70nm and, then decreases. The reason for this is that once the thickness surpasses a specific limit (known as the optimum value), the charge carriers will need to cover a greater distance in order to reach the respective electrodes.

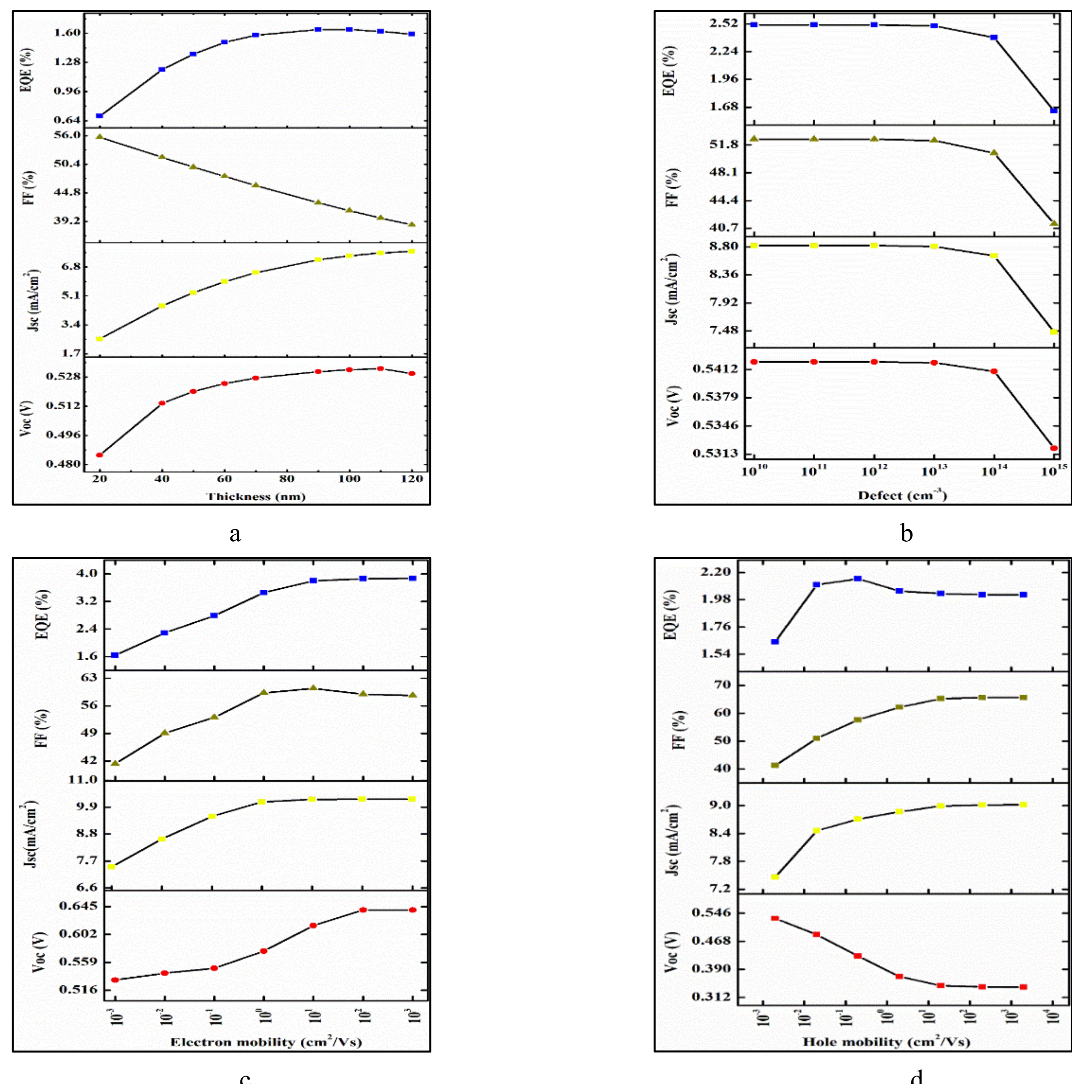

Figure 3. Variation of device output parameters of ITO/GO/P3HT:PCBM/Al with varying factors of active layer: (a) thickness, (b) defect density, (c) electron mobility, and (d) hole mobility

Consequently, as the thickness exceeds the optimum value, the efficiency declines. It is essential to increase the thickness up to a certain level to ensure optimal device performance, as this enhances light absorption and the generation of excitons.

Even though the device shows an improved efficiency at 70nm, when it comes to practical applications, 100nm is often considered as the optimum thickness for the active layer in P3HT:PCBM based BHJOSC's.

The impact of active layer defect density on device performance is depicted in Fig. 3(b). As the defect increases, from 10^{10} to 10^{15} cm^{-3}, efficiency decreases, from 2.45% to 1.66%. As defect density increases, the lifetime of carriers diminishes, resulting in an elevated recombination rate that impacts the performance of the device. A reduced defect density within the layer signifies a more polished surface, thereby contributing to a smoother device performance. Higher charge carrier mobility is necessary to reduce charge recombination as well as to promote charge collection. Fig. 3(c) and Fig. 3(d) show the effect of varying electron mobility and hole mobility of active layer on device performance. The electron mobility is varied from $2\times10^{-3}cm^2/Vs$ to $2\times10^{3}cm^2$ /Vs and a relatively enhanced efficiency of 4.11%, for $2\times10^{3}cm^2/Vs$ is attained. As the hole mobility increases, from $2\times10^{-3}cm^2/Vs$ to $2\times10^{3}cm^2/Vs$, efficiency reaches, a maximum value of 2.10% at $2\times10^{-1}cm^2/Vs$. The rise in material conductivity is affirmed by the increase in mobility. The balance of mobilities is predominantly upheld, as an imbalanced charge transport could potentially transpire if μ_e is lower.

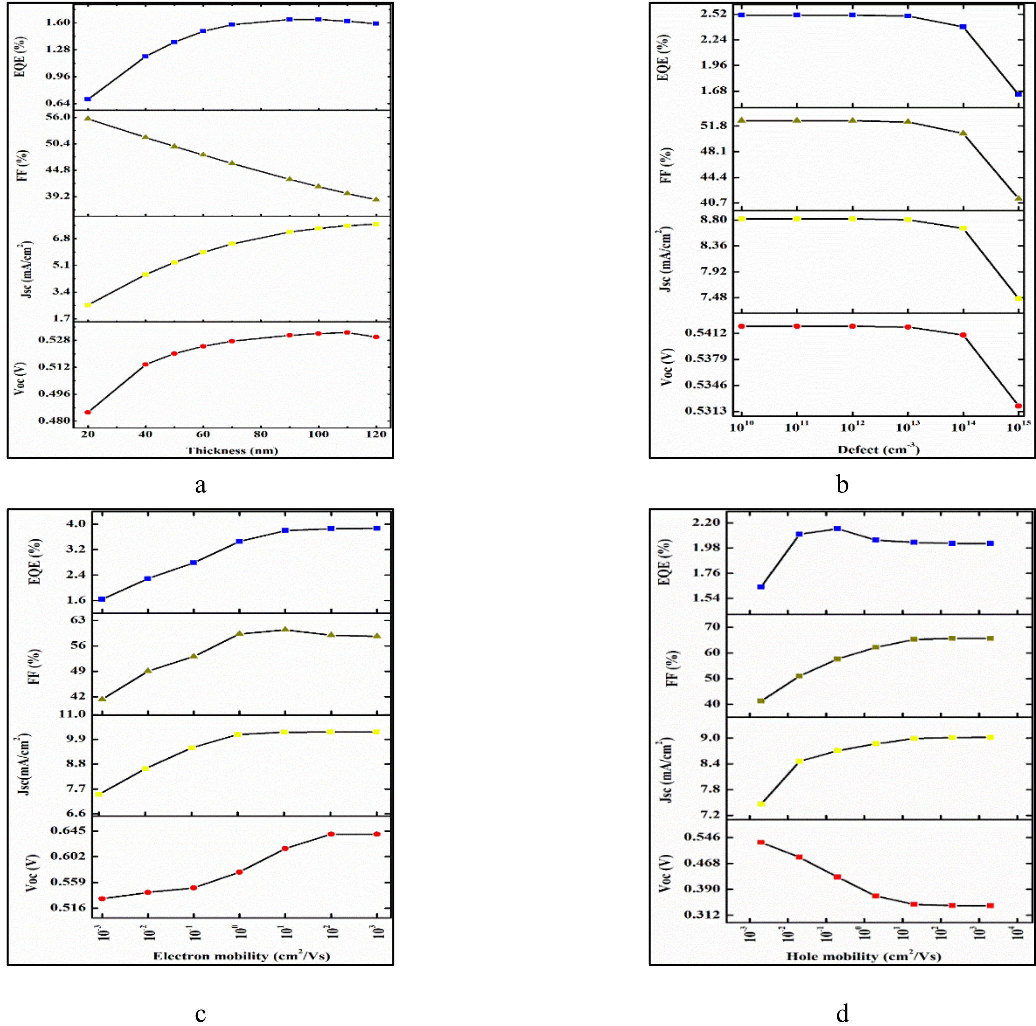

Figure 3. Variation of device output parameters of ITO/GO/P3HT:PCBM/Al with varying factors of active layer: (a) thickness, (b) defect density, (c) electron mobility, and (d) hole mobility

4.1.2. Influence of various electrical parameters of graphene oxide

The influence of the hole transport layer thickness on device performance is shown in Fig. 4(a). As the thickness for GO increases, efficiency reaches a maximum of 1.66% at 20nm, and then decreases. Researchers and device engineers often perform experiments and simulations to determine the ideal HTL thickness that maximises device efficiency. It's worth noting that the optimal thickness can vary depending on the specific materials used in the solar cell, the design of the device, and the intended application. Excessive HTL thickness can contribute to increased series resistance in the device, which can limit charge transport and reduce overall device performance. The experimental work chosen for standardisation has fabricated a BHJOSC device with 35nm thickness of GO. Our simulation study shows, 20nm thickness of GO gives good efficiency. This could be extremely helpful for the experimental fabrication of thin layered HTL in BHJOSC. Too thin or too thick HTL layers might be challenging to deposit reliably and uniformly during the manufacturing process.

As the defect of GO is varied, from 10^9 to 10^{15} cm^{-3} as shown in Fig. 4(b), efficiency remain unchanged. The device performance is not significantly affected by the defect density of graphene oxide, as indicated by this observation. However, it is preferable to have a minimal defect in the HTL layer in order to enhance its functionality.

The plot showing significance of electron and hole mobility of graphene oxide layer on device performance is given in Fig. 4(c) and Fig. 4(d). As the electron mobility of graphene oxide increases, efficiency gets improved and reaches 3.9%. The efficiency remains constant at as hole mobility changes from 2.6×10^{-3} to 2.6×10^{3} cm^2/Vs. The balance between electron and hole mobility is also maintained in the hole transport layer.

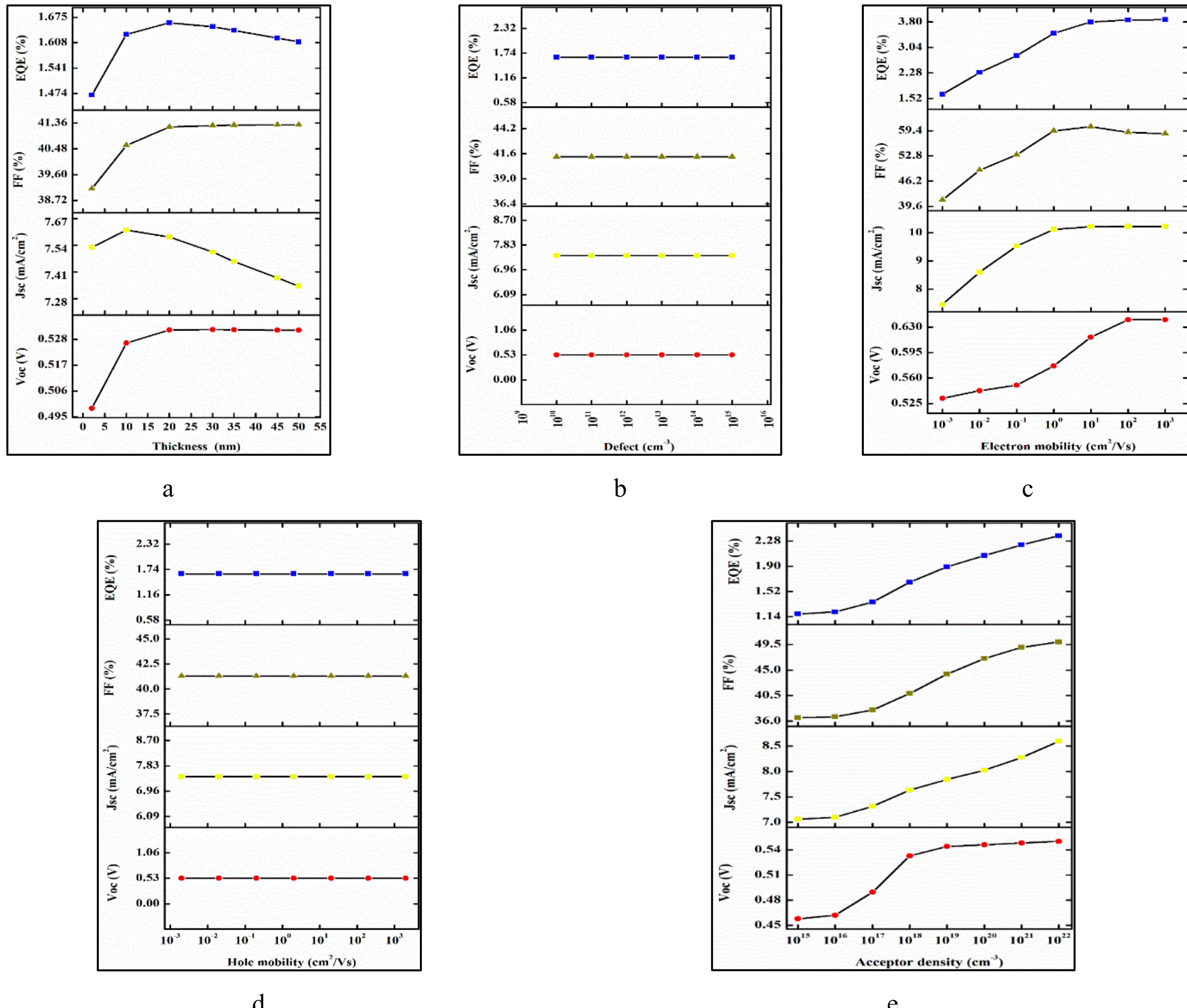

Figure 4. Variation of device output parameters of ITO/GO/P3HT:PCBM/Al with varying factors of HTL: (a) thickness, (b) defect density, (c) effect of electron mobility, (d) hole mobility, and (e) effect of acceptor density

The effect of varying acceptor density on device performance is also studied in this work. As the acceptor density is raised from $1\times10^{15}$$cm^{-3}$ to 1×10^{22} cm^{-3}, efficiency seems to increase and reaches 2.36%. Fig. 4(e) clearly shows the influence of varying acceptor density of GO on device performance. The acceptor density is varied from 1×10^{15} cm^{-3} to 1×10^{22} cm^{-3}. The efficiency seemed to increase with an increase in acceptor density. Maximum efficiency of 2.36% is achieved for 1×10^{22} cm^{-3}.

4.1.3. Influence of interface defect, temperature, series resistance and shunt resistance on the device performance

The interface defined in ITO/GO/P3HT:PCBM/Al is HTL/active layer interface (i.e grapheneoxide/P3HT:PCBM interface). Fig. 5(a) depicts the variation of device parameters with respect to change in interface defect values. The simulation is done by varying the density of interface ranging from 1×10^{10} cm^{-2} to 1×10^{15} cm^{-2}. Efficiency also decreases from 2.00% to 1.66% at 1×10^{14} cm^{-2}. It is evident from our research that achieving a low interface defect density is crucial for enhancing the performance of output devices. These findings align well with our previous results. Minimizing defects in the layers contributes to a smoother device performance. However, it is important to acknowledge that a certain level of defects is inevitable in materials and should be duly considered.

The operating temperature is varied from 250K to 500K and the device performance is studied as it appears in Fig. 5(b). The rise in temperature has a detrimental impact on the functionality of the device, resulting in a gradual decline in

performance. This decline can be attributed to the escalation in series resistance, which subsequently leads to an increase in recombination rate. It is worth noting that the influence of temperature is more pronounced in organic solar cells as opposed to inorganic solar cells. As the temperature increases from 250K to 500K, efficiency declines to 0.98%. Maintaining the device stability at very low temperature or very high temperature is a tedious task. The standardized devices are operated at a temperature of 323K, therefore, for optimization studies, the same operating temperature is utilized.

The variation of photovoltaic parameters with varying series resistance and shunt resistance is shown in Fig. 5(c) and Fig. 5(d) respectively. As the series resistance increases, from 1 to 10 Ω, efficiency decreases, from 1.59% to 1.52%. As the shunt resistance increases from 10 to 100000Ω, efficiency increases from 0.04% to 1.6%. An ideal device is commonly regarded as having no resistance. Resistances arise from leakage current, which is widely recognized as a significant concern in all device architectures.

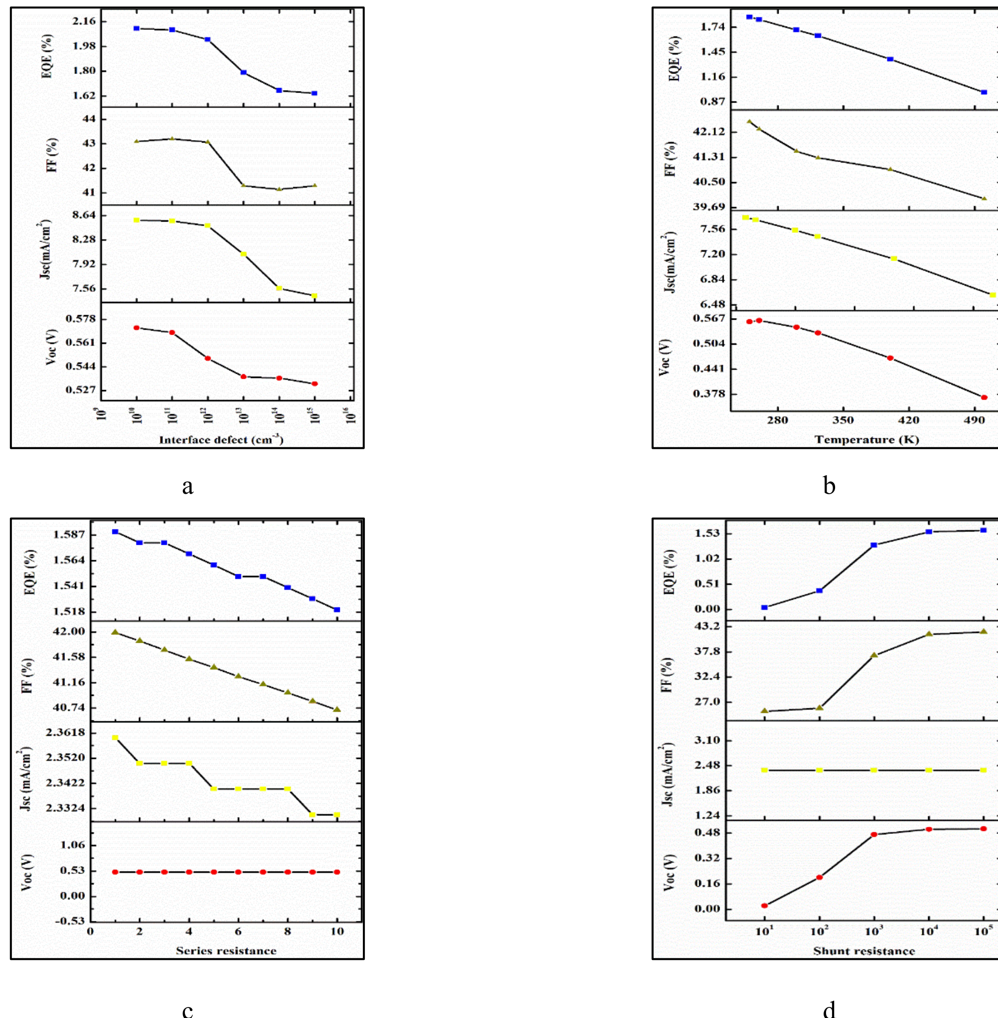

Figure 5. Variation of device output parameters of ITO/GO/P3HT:PCBM/Al with varying factors: (a) interface defect, (b) temperature, (c) series resistance, and (d) shunt resistance

After the extended numerical simulation study we optimized device configuration ITO/GO/P3HT:PCBM/Al. Table 6 summarizes the optimized output parameters after simulation. The optimized input parameters for active layer and HTL corresponds to thickness of 70nm and 20nm respectively, defect density of 6.847×10^{10} and 1.9×10^{10} cm^{-3} electron mobility of 2×10^{-3} and $2.6\times10^{3}cm^2/Vs$, hole mobility of 2×10^{-1} and $1.23\times10^{3}cm^2/Vs$.

Table 6. Optimized output values of ITO/GO/P3HT:PCBM/Al

Voc (V)	Jsc (mA/cm^2)	FF (%)	EQE (%)
0.6237	8.92765	77.6	4.32

4.1.4. Influence of diverse ETL's and different metal electrodes on device performance

The electron transport layer is crucial in boosting the efficiency of BHJOSC. The inclusion of ETL's will indeed enhance the device's performance by optimizing the transportation of charge carriers. Followed by optimisation, designing and simulation study of various combination are done with three metal electrodes (Al, Ca and Ag) and diverse ETL's (PDINO, PFN-Br, LiF, ZnO, IGZO, PCBM, C60, TiO_2:gr and n-graphene). Table 7 lists the *Voc*, *Jsc*, *FF*, and Efficiency

attained for various device configurations. Improved *Voc* of 0.9277V is attained for ITO/GO/P3HT:PCBM/PFN-Br/Al. The device ITO/GO/P3HT: PCBM/LiF/Ca gives maximum *Jsc* of 11.498525mA/cm^2 and high efficiency of 8.00%. Highest fill factor of 84.29% is achieved for the device ITO/GO/P3HT:PCBM/IGZO/Ca.

The comparison shows that device combinations with Ca as cathode showed better device performance. Our simulation study clearly shows enhanced efficiency (greater than 6.00%) for most of the configurations.

Table 7. Device output parameters of ITO/GO/P3HT: PCBM/ETL/cathode with diverse ETL's and cathodes

Back metal contact	ETL	*Voc* (V)	*Jsc* (mA/cm^2)	*FF* (%)	Efficiency (%)
Aluminium	PDINO	0.9255	10.816248	76.29	7.63
	PFN-Br	0.9277	11.4186	58.02	6.15
	LiF	0.4298	10.31244	76.88	6.01
	ZnO	0.9088	10.413318	77.43	7.33
	IGZO	0.7161	10.442410	83.63	6.25
	PCBM	0.8196	10.555798	76.74	6.64
	C60	0.8207	10.651364	76.62	6.70
	TiO_2:graphene	0.6104	10.434697	81.73	5.21
	n-graphene	0.3679	10.428822	74.44	2.86
Calcium	PDINO	0.9523	10.2493	75.85	7.40
	PFN-Br	0.8490	11.2198	81.73	7.79
	LiF	0.8517	11.498525	81.73	8.00
	ZnO	0.9186	8.868	77.58	6.32
	IGZO	0.7456	10.435529	84.29	6.56
	PCBM	0.9213	10.565869	76.55	7.45
	C60	0.9229	10.663121	76.44	7.52
	TiO_2:graphene	0.6104	10.434699	81.73	5.21
	n-graphene	0.3679	10.428695	74.44	2.86
Silver	PDINO	0.8908	9.68514	72.34	6.24
	PFN-Br	0.5766	10.05635	63.83	3.70
	LiF	0.2919	10.19363	67.48	2.01
	ZnO	0.8497	9.69244	79.38	6.54
	IGZO	0.5961	10.438554	81.26	5.06
	PCBM	0.8303	10.428956	64.99	5.65
	C60	0.8463	10.535471	73.20	6.53
	TiO_2:graphene	0.6104	10.434179	81.73	5.21
	n-graphene	0.3667	10.428614	74.41	2.85

4.1.5. Influence of donor density of ETL on the device performance of ITO/GO/P3HT:PCBM/LiF/Ca

The influence of donor density of Lithium Flouride (ETL) on the device performance of ITO/GO/P3HT:PCBM/LiF/Al is studied and plotted in Fig. 6. As the donor density is raised from 1×10^{15} to 1×10^{22}cm^{-3}, the efficiency first improves to 8.15% at 1×10^{19} cm^{-3}, remains a constant and then decreases.

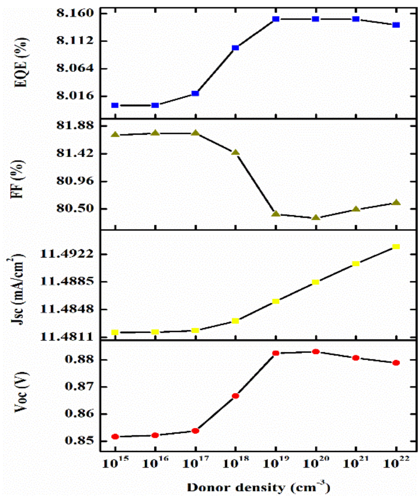

Figure 6. Influence of donor density of LiF (ETL) on device performance of ITO/RGO/P3HT:PCBM/LiF/Al

4.1.6 Influence of varying ITO work function

The impact of different work functions of ITO (anode) on the performance of, device with maximum efficiency (ITO/GO/P3HT:PCBM/LiF/Ca) is also investigated. We vary the ITO work function within the range of 4.7 to 5.00eV, and analyse the device's performance. However, only a small increase in efficiency is seen in the device's performance. Only a marginal improvement of 0.1% in efficiency is achieved when the work function is increased to 5.00eV.

4.2. ITO/RGO/P3HT: PCBM/Al

An extensive numerical simulation study of ITO/RGO/P3HT:PCBM/Al is done. The effect of thickness, defect density, electron mobility, and hole mobility of active layer, is studied. The influence of varying input parameters such as thickness, defect density, electron mobility, hole mobility, and acceptor density of HTL is also studied. Furthermore, the examination extends to the influence of interface defects (RGO/P3HT:PCBM interface), operating temperature, series resistance, and shunt resistance.

The device is optimised, and then various combination of device structures is studied. Nine ETL's (PDINO, PFN-Br, LiF, ZnO, IGZO, C60, PCBM, TiO_2:gr, and n-graphene) and three metal contacts are used to design various combinations. Study on influence of donor density of LiF (ETL) is carried out and effect of varying ITO work functions on device performance is also studied.

4.2.1. The effect of varying electrical properties of active layer on device performance

The impact of varying the active layer's thickness and defect density on the *Voc*, *Jsc*, *FF*, and efficiency is investigated and considered for device optimization. We have varied the thickness of active layer in the range of 5 to 200 nm, and the associated effect on device outcomes is analysed by maintaining all other factors constant throughout the simulations.

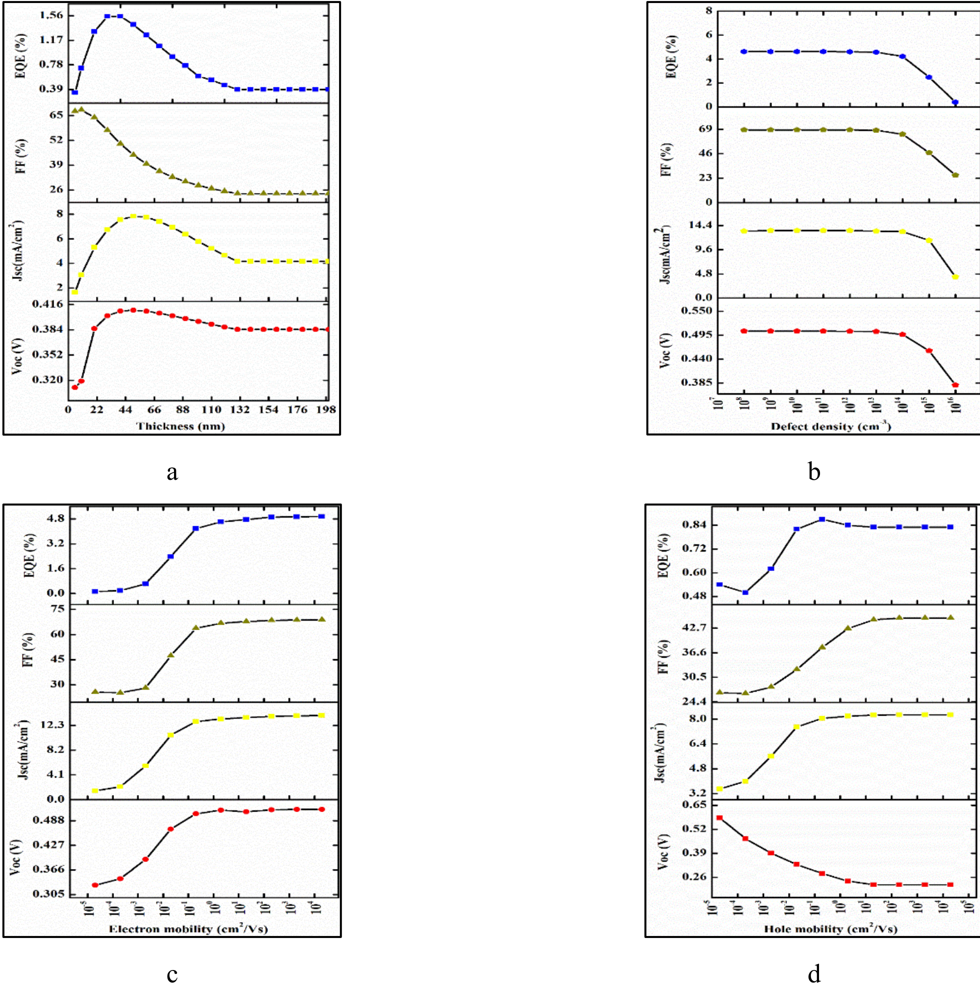

Figure 7. Variation of device output parameters of ITO/RGO/P3HT:PCBM/Al with varying factors of active layer: (a) thickness, (b) defect density, (c) electron mobility and (d) hole mobility, (a) thickness (b) defect density (c) effect of electron mobility and (d) effect of hole mobility

The effect of varying active layer thickness on device performance is shown in Fig. 7 (a), and a maximum efficiency of 1.55% is attained at 50nm. Even though we got 50nm as the optimum thickness, for P3HT:PCBM based BHJOSC 100nm is applied in experimental works.

As the thickness increases, there is a clear rise in the surface area of the active layer. Increasing the thickness up to a certain point is crucial for achieving optimal device performance, as it enhances the absorption of photons and the generation of electron-hole pairs. However, once the thickness exceeds the ideal value, the efficiency begins to decline. This can be attributed to the fact that, beyond a certain thickness limit (the optimum value), the charge carriers have to travel a greater distance to reach the corresponding electrodes.

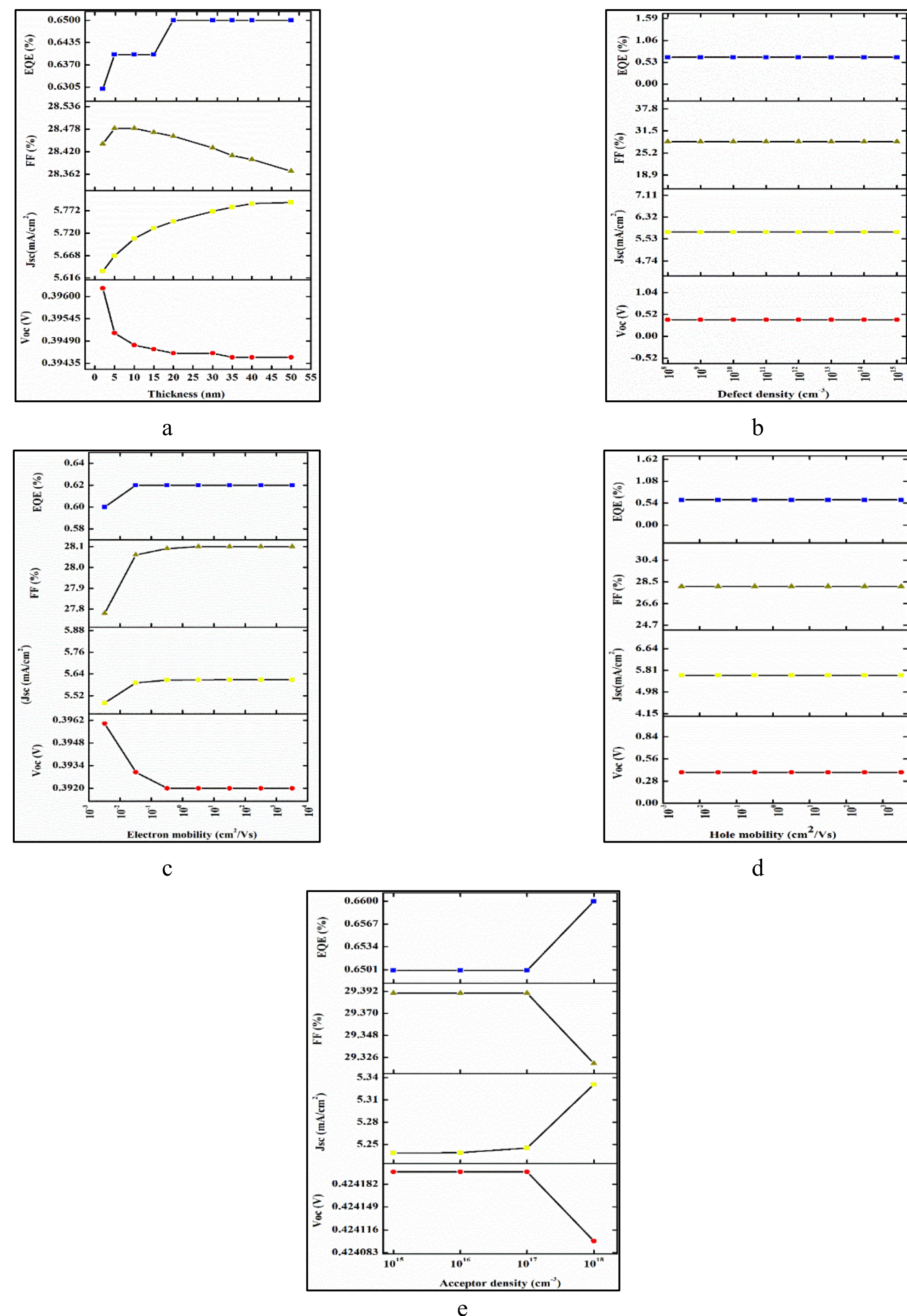

Figure 8. Variation of device output parameters of ITO/RGO/P3HT:PCBM/Al with varying factors of HTL: (a) thickness, (b) defect density, (c) electron mobility (d) hole mobility, and (e) acceptor density

Consequently, an increase in thickness beyond the optimum value significantly increases the likelihood of charge carrier recombination. Ultimately, this results in a decrease in the device's output parameters after reaching the optimum thickness value.

As the defect increases from 10^8 to 10^{16} cm^{-3}, efficiency decreases to 0.41% as shown in Fig. 7(b). The performance of the device is greatly influenced by the defect density present in the active layer. Achieving a defect-free active layer via fabrication is an extremely difficult task and is practically unattainable. Simulation study with excessive defect density in active layer is also avoided in the study, as it could significantly damage the device and impact its performance.

As the electron mobility is increased to $2\times10^4 cm^2/Vs$, efficiency increases upto 4.95%. Fig. 7(c) shows the effect of variation of electron mobility of active layer on device performance. Higher charge mobility is necessary to reduce the charge recombination as well as promote the charge collection. The effect of variation of hole mobilitiy of active layer on device performance is shown in Fig. 7(d).

As the hole mobility of the active layer is increased, efficiency of 0.86% is attained for $2\times10^4 cm^2/Vs$. The equilibrium of mobility is upheld, as the movement of electrons through the layers becomes more challenging when, μ_e is lower. An unbalanced charge transport might possibly occur if mobility range is unbalanced. The possibility of an imbalanced charge transport arises when there is an uneven distribution in the range of mobility.

4.2.2 The effect of variation of electrical properties of HTL on device performance

The effect of varying input parameters of HTL on the device performance is shown in Fig. 8. As shown in Fig. 8(a), efficiency reaches a maximum of 0.65% at 20nm thickness of RGO and then decreases. If the HTL is too thin, it might lead to incomplete hole collection, resulting in lower current and reduced efficiency. Conversely, excessive thickness of the HTL may hinder charge transport, leading to similar performance problems. The thickness of the HTL can impact the ease of hole movement within the layer and their ability to reach the anode.

As the defect of the RGO is increased from 10^8 to 10^{16} cm^{-3}, the device output parameters remain constant as shown in Fig. 8(b). This study shows that varying defect density of RGO (HTL), has no significant impact on the device performance.

The effect of varying electron and hole mobilities of RGO on device performance, is shown in Fig. 8(c) and Fig. 8(d). At an electron mobility of $3.2\times10^1 cm^2/Vs$, efficiency reaches 0.62%. As the hole mobility of RGO increases, the device performance remains unaffected.

Influence of acceptor density of HTL is shown in Fig. 8(e). As the acceptor density is raised, from 1×10^{15} to 1×10^{18} cm^{-3}, initially the efficiency remains constant at 0.65% and then improves to 0.66%.

4.2.3 Effect of interface defect, operating temperature, series resistance and shunt resistance.

The effect of interface defect on device performance is shown in Fig. 9(a). As the interface defect is increased from $10^{14} 1/cm^2$ to $10^{20} 1/cm^2$, an increase in efficiency of 0.62% at $1\times10^{17} 1/cm^2$. The interface is the reason for separation of charge carrier and reach electrodes. Introduction of HTL actually improves this, and due to the HTL/active layer interface, charge separation will occur more.

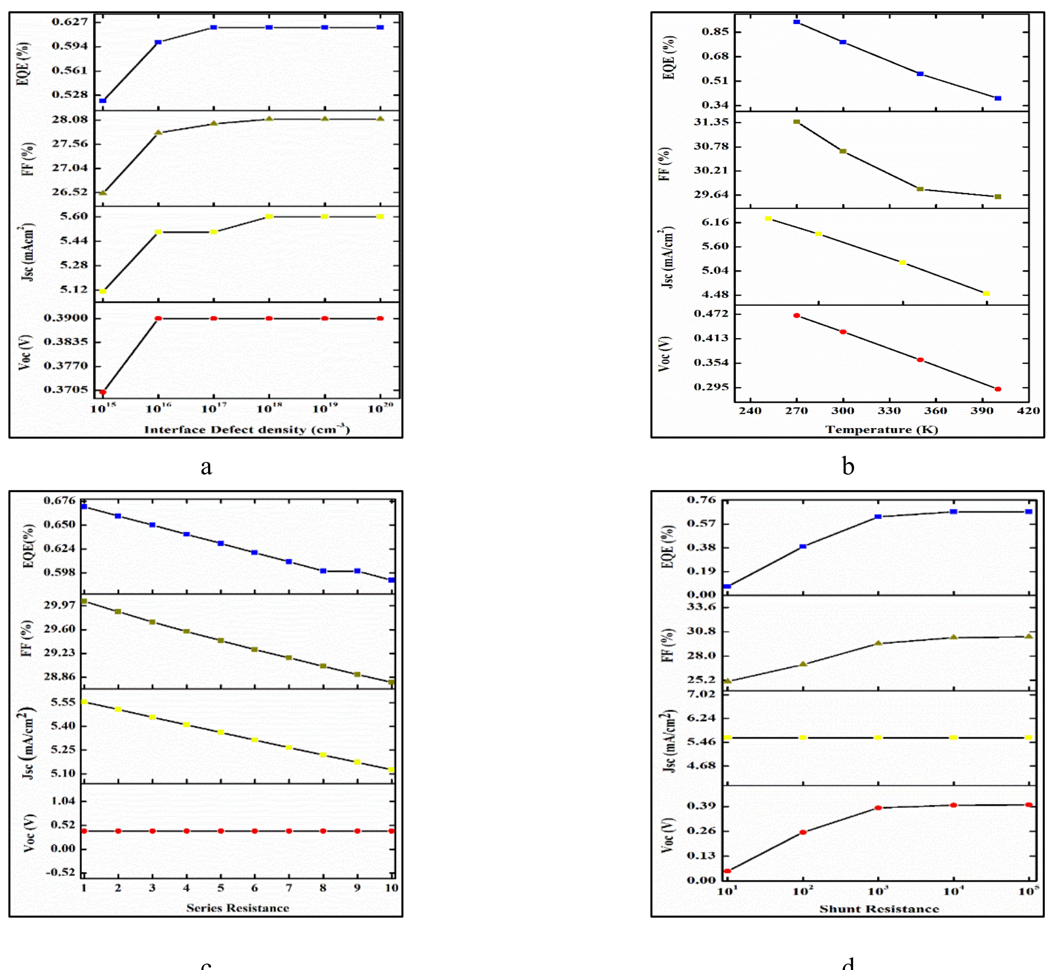

Figure 9. Variation of device output parameters of ITO/RGO/P3HT:PCBM/Al with varying factors: (a) interface defect, (b) temperature, (c) series resistance, and (d) shunt resistance

While it is generally preferred to minimize defects in the device for optimal performance, a certain level of interface defect is necessary. Neglecting the presence of this specific range of interface defect would be impractical in real-world applications.

As the temperature increases, the device output parameters are seen to be affected badly as shown in Fig. 9(b). As it reaches 600 K, efficiency reaches 0.03%. A gradual decrease in efficiency is seen. As the temperature rises, the series resistance also increases, resulting in a higher recombination rate. Organic solar cells are more significantly affected by temperature compared to inorganic solar cells. In order to conduct optimization studies, the operating temperature is established at 323K.

Fig. 9(c) and Fig. 9(d) represents the variation of photovoltaic parameters with varying series resistance and shunt resistance respectively. As the series resistance increases from 1 to 10 ohm, efficiency decreases from 0.67% to 0.59%. At open-circuit voltage, series resistance has no effect on the solar cell because there is no total current flow across the series resistance and the solar cell itself. As the shunt resistance increases from 10 to 100000 Ω, efficiency increases from 0.07% to 0.67%. The shunt resistance has no effect on the short circuit current, while the efficiency seems to increase. An ideal device is commonly regarded as having zero resistance, although the existence of such devices remains unknown. Conversely, the majority of fabricated devices possess a minimum level of resistance.

The optimization of the ITO/RGO/P3HT:PCBM/Al device has been conducted, taking into account all the aforementioned findings. The optimized thickness for active layer and HTL corresponds to 100nm and 35 nm respectively. Defect density of 5.39×10^{12} and 1.9×10^{19} cm^{-3} is chosen for active layer and HTL respectively. Electron mobility and hole mobility of active layer and HTL are chosen as 2×10^{4} and $2\times10^{-1}cm^2/Vs$, and 3.2×10^{1} and $3.2\times10^{4}cm^2/Vs$ correspondingly.

ITO/RGO/P3HT:PCBM/Al is optimized and the optimized output values are as shown in Table 8. After optimization, the efficiency of the device is significantly increased by 6.65%, surpassing the efficiency of the standardized device (0.65%).

Table 8. Device output parameters of ITO/RGO/P3HT:PCBM/Al after optimization.

Voc (V)	Jsc (mA/cm^2)	FF (%)	Efficiency (%)
0.7130	11.704530	79.73	6.65

4.2.4 ITO/RGO/P3HT:PCBM/Al with diverse electron transport layers and different cathodes

We were able to attain an efficiency of 6.65% after optimising ITO/RGO/P3HT:PCBM/ Al. Different combinations of devices are designed, simulated and analysed for improved device performance using nine ETL's and three cathodes. Introducing ETL's can actually enhance device performance via enhanced charge carrier transmission. The improvement in efficiency and device output performance with the implementation of electron transport layers is carried out. The ETL's used for this study includes PDINO, PFN-Br, ZnO, IGZO, C60, PCBM, TiO_2: gr and n-graphene. We also explore the impact of distinct cathodes, with varying work functions such as Al, Ca, and Ag. As we introduce the ETL's and cathodes band alignment of the layers is essential for the proper working of device. This is achieved by appropriately varying the electron affinity values of different layers.

Among the different configurations studied, device with configuration ITO/RGO/ P3HT:PCBM/LiF/Ca, gave a record high efficiency of 12.00%, high *Voc* of 0.7909 V and enhanced *Jsc* of 26.613796mA/cm^2. High *FF* of 81.12% was attained for the configuration ITO/RGO/P3HT:PCBM/C60/Ca. RGO has a lower bandgap compared to GO, making RGO more similar to graphene. The band alignment of RGO is also in well agreement with that of P3HT:PCBM. The electronic and optical properties of RGO is more tunable. RGO can also be doped according to the necessity of the device. Experimental studies on P3HT:PCBM based BHJOSC with RGO as HTL exists in literature, yet an extensive simulation study with diverse ETL's and different cathodes is not reported elsewhere. Table 9 lists the device output parameters of ITO/RGO/P3HT:PCBM/ETL/Cathode. Cathode has the lowest work function compared to Aluminium (4.2eV) and silver (4.35eV).

Table 9. The device output parameters of various combinations simulated using ITO/RGO/P3HT:PCBM/ETL/Cathode.

Back metal contact	ETL	*Voc* (V)	*Jsc* (mA/cm^2)	*FF* (%)	Efficiency (%)
Aluminium	PDINO	0.7309	11.84	81.07	7.02
	PFN-Br	0.7271	12.04	71.39	6.25
	LiF	0.577	12.49604	68.92	4.97
	ZnO	0.7309	11.83136	81.08	7.01
	IGZO	0.7309	11.77	81.08	6.97
	PCBM	0.731	11.74159	76.73	6.59
	C60	0.731	11.76	79.69	6.85
	TiO_2:graphene	0.7311	11.75	80.71	6.93
	n-graphene	0.5189	11.493991	70.54	4.21
Calcium	PDINO	0.731	11.8781	81.1	7.04
	PFN-Br	0.7324	12.2746	79.21	7.12
	LiF	0.7909	26.613796	56.99	12.00
	ZnO	0.731	11.87096	81.1	7.04

Back metal contact	ETL	*Voc* (V)	*Jsc* (mA/cm^2)	*FF* (%)	Efficiency (%)
	IGZO	0.7309	11.77554	81.11	6.98
	PCBM	0.7309	11.77595	81.11	6.98
	C60	0.7309	11.77854	81.12	6.98
	TiO_2:graphene	0.7311	11.74356	80.71	6.93
	n-graphene	0.5207	11.494086	70.46	4.22
Silver	PDINO	0.7308	11.81524	76.87	6.64
	PFN-Br	0.6252	11.98285	61.65	4.62
	LiF	0.4271	12.28191	64.77	3.4
	ZnO	0.7308	11.77807	81.06	6.98
	IGZO	0.7312	11.73301	80.51	6.91
	PCBM	0.7307	11.69365	59.69	5.1
	C60	0.7631	11.8055	59.89	5.4
	TiO_2:graphene	0.7311	11.74356	80.71	6.93
	n-graphene	0.4506	11.493799	72.44	3.75

4.2.5 Influence of donor density of ETL on the device performance of ITO/RGO/P3HT:PCBM/LiF/Ca

The influence of donor density of Lithium Flouride (ETL) on the device performance of ITO/RGO/P3HT:PCBM/LiF/Al is studied and plotted in Fig. 10. As the donor density is raised from 1×10^{15} to $1\times10^{22}cm^{-3}$, the efficiency first improved to 16.47% at 1×10^{20} cm^{-3} and subsequently showed a slight decrease.

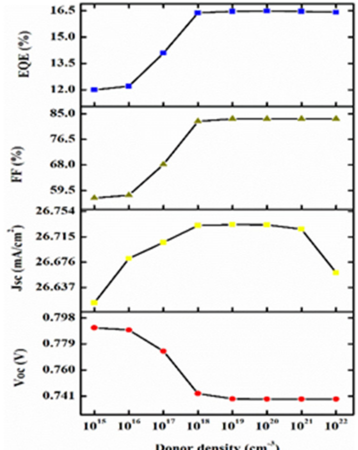

Figure 10. Influence of donor density of LiF (ETL) on device performance of ITO/RGO/P3HT:PCBM/LiF/Al

4.2.6 Influence of varying ITO work function

The impact of different work functions of ITO (anode) on the performance of, device with maximum efficiency (ITO/RGO/P3HT:PCBM/LiF/Ca) is also investigated. We vary the ITO work function within the range of 4.7 to 5.00eV, and analyse the device's performance. Nevertheless, there is no notable enhancement observed in the device's performance. Only a slight improvement of 0.09% in efficiency is attained when the work function is raised to 5.0eV.

5. CONCLUSIONS

The design and simulation of BHJOSC with the configurations ITO/GO/P3HT:PCBM/Al and ITO/RGO/P3HT:PCBM/Al have been successfully carried out in this study. The influence of input parameters of active layer and HTL, on the device performance is analysed. In addition, the influence of interface defects, series resistance, shunt resistance, and temperature is also examined.

Both the devices are optimised and an improved efficiency of 4.32% is obtained for ITO/GO/P3HT:PCBM/Al, and an increased efficiency of 6.65% is attained for ITO/RGO/P3HT:PCBM/Al. Followed by optimisation, designing and simulation study of various combinations of devices is studied using nine different ETL's and three metal contacts with different work function, (Al, Ca and Ag). The device configuration ITO/GO/ P3HT:PCBM/LiF/Ca achieved an enhanced efficiency of 8.00%. The device configuration ITO/RGO/P3HT:PCBM/LiF/Ca, exhibited a record efficiency of 12.00%. Thereafter, the influence of donor density of ETL (LiF) is also examined, and it is seen that, efficiency can be improved by increasing the donor density of ETL. The impact of changing the ITO work function on the device performance of configurations ITO/GO/P3HT:PCBM/Al and ITO/RGO/P3HT:PCBM/Ca was then investigated, which only resulted in, 0.1% and 0.09% improvement in the device efficiency respectively.

The findings of our research suggest that RGO is a more favorable choice as a hole transport layer (HTL) compared to GO. Additionally, LiF is identified as the best electron transport layer (ETL) for P3HT:PCBM based BHJOSC. Our

simulation studies have shown that Ca outperforms other cathodes in terms of achieving a high *Jsc*, increased *FF*, and enhanced efficiency. This can be attributed to the low work function property of Ca, indicating that BHJOSC performs exceptionally well with cathodes that have low work function.

Acknowledgment

The authors extend their heartfelt gratitude to Prof. Marc Burgelman from the University of Gent, Belgium for providing access to the SCAPS 1-D software.

Conflicts of interest

The authors declare that they have no relevant financial interests in the article and no other potential conflicts of interest to disclose.

ORCID

Denet Davis, https://orcid.org/0000-0001-6673-2499; **K.S. Sudheer**, https://orcid.org/0000-0002-9019-4405

REFERENCES

[1] H. Kang, et al., Adv. Mater. **28**, 7821 (2016). https://doi.org/10.1002/adma.201601197
[2] G. Yu, J. Gao, J.C. Hummelen, F. Wudl, and A.J. Heeger, Science, **270**, 1789 (1995). https://doi.org/10.1126/science.270.5243.1789
[3] T. Fukuda, *et al*., Phys. Status Solidi - Rapid Res. Lett. **5**, 229 (2011). https://doi.org/10.1002/pssr.201105232
[4] L. Lu, *et al*., Chem. Rev. **115**, 12666 (2015). https://doi.org/10.1021/acs.chemrev.5b00098
[5] B. Kadem, A. Hassan, and W.J. Cranton, J. Mater. Sci. Mater. Electron. **27**, 7038 (2016). https://doi.org/10.1007/s10854-016-4661-8
[6] S. Bichave, *et al*., Materials Today: Proceedings, (2023). https://doi.org/10.1016/j.matpr.2023.01.190
[7] H. Xu, *et al*., J. Mater. Chem. A, **8**, 11478 (2020). https://doi.org/10.1039/D0TA03511D
[8] S. Park, *et al*., Adv. Mater. **32**, 1 (2020).
[9] A.M. Mir, F. Bashir, F.A. Khanday, F. Zahoor, M. Hanif, and Z. May, IEEE Access, **12**, 10961 (2024). https://doi.org/10.1109/ACCESS.2024.3354163
[10] I. Masood, M.P. Singh, and M. Amir, "Analysis of Different Layers Thicknesses on the Performance of Organic Solar Cells," in: *2023 International Conference on Power, Instrumentation, Energy and Control* (*PIECON*), (Aligarh, 2023). pp. 1-5.
[11] M. Palewicz, A. Sikora, T. Piasecki, E. Gacka, P. Nitschke, P. Gnida, B. Jarząbek, and T. Gotszalk, Energies, **16**, 4741 (2023). https://doi.org/10.3390/en16124741
[12] D. Davis, M.S. Shamna, K.S. Nithya, and K.S. Sudheer, "Graphene as a hole transport layer for enhanced performance of P3HT:PCBM bulk heterojunction organic solar cell: a numerical simulation study," in: *IOP Conference Series: Materials Science and Engineering,* vol. 1248, (Jalandhar, Punjab, 2022), pp. 012011.
[13] G.R. Nishad, R.B. Younus, and P. Singh, "Applications of PEDOT: PSS in Solar Cells," in: *Materials for Solar Cell Technologies, II* **103**, 40 (2021), pp 40-76. https://doi.org/10.21741/9781644901410-3
[14] K.S. Ram, *et al*., Nanomater. **11**, 209 (2021). https://doi.org/10.3390/nano11010209
[15] J. Healey, *Conductive polymer films as electrodes in organic solar cells*, (Memorial University of Newfoundland, 2020).
[16] D. Ompong, *Designing thin film solar cells for optimum photovoltaic performance*, (Charles Darwin University, Australia, 2017).
[17] F. Hakim, and M.K. Alam, "Improvement of photo-current density of P3HT: PCBM bulk heterojunction organic solar cell using periodic nanostructures," in: *2017 International Conference on Electrical, Computer and Communication Engineering* (*ECCE*), (IEEE, 2017), pp. 170-174.
[18] F. Hakim, and Md.K. Alam, Sol. Energy, **191**, 300 (2019). https://doi.org/10.1016/j.solener.2019.08.073
[19] H.M. Rad, F. Zhu, and J. Singh, J. Appl. Phys. **124**, 083103 (2018). https://doi.org/10.1063/1.5031062
[20] Q. Zheng, *et al*., Sol. energy mater. sol. cells, **95**, 2200 (2011). https://doi.org/10.1016/j.solmat.2011.03.024
[21] J. Cameron, and P.J. Skabara, Mater. Horiz. **7**, 1759 (2020). https://doi.org/10.1039/C9MH01978B
[22] M.A. Velasco-Soto, *et al*., Carbon, **93**, 967 (2015). https://doi.org/10.1016/j.carbon.2015.06.013
[23] A. Iwan, and A. Chuchmała, Prog. Polym. Sci. **37**, 1805 (2012). https://doi.org/10.1016/j.progpolymsci.2012.08.001
[24] Y. Zhu, *et al*., Adv. Mater. **22**, 3906 (2010). https://doi.org/10.1002/adma.201001068
[25] R. Tarcan, *et al*., J. Mater. Chem. C, **8**, 1198 (2020). https://doi.org/10.1039/C9TC04916A
[26] N.O. Weiss, *et al*., Adv. Mater. **24**, 5782 (2012). https://doi.org/10.1002/adma.201201482
[27] K.I. Bolotin, *et al*., Solid State Commun. **146**, 351 (2008). https://doi.org/10.1016/j.ssc.2008.02.024
[28] K.I. Bolotin, "Electronic transport in graphene: Towards high mobility," in: *Graphene*, (Woodhead Publishing, 2014), pp. 199-227.
[29] X. Xu, *et al*., Chem. Soc. Rev. **47**, 3059 (2018). https://doi.org/10.1039/C7CS00836H
[30] M. Raji, N. Zari, Q.A. El Kacem, and R. Bouhfid, *Functionalized graphene nanocomposites and their derivatives*, (Elsevier, 2019).
[31] E. Singh, and H.S. Nalwa, RSC Adv. **5**, 73575 (2015). https://doi.org/10.1039/C5RA11771B
[32] B.V.R.S. Subramanyam, *et al*., J. Renew. Sustain. Energy, **12**, 054701 (2020). https://doi.org/10.1063/5.0021208
[33] J. Liu, *et al*., Adv. Mater. **26**, 786 (2014). https://dx.doi.org/10.1002/adma.201302987
[34] N.T. Ho, *et al*., Phys. Status Solidi Appl. Mater. Sci. **211**, 1873 (2014). https://doi.org/10.1002/pssa.201330611
[35] A. Van Dijken, *et al*., Organic Electronics, **4**, 131 (2003). https://doi.org/10.1016/j.orgel.2003.08.007
[36] J.M. Yun, *et al*., Adv. Mater. **23**, 4923 (2011). https://doi.org/10.1002/adma.201102207
[37] Y. Gao, *et al*., Appl. Phys. Lett. **97**, 203306 (2010). https://doi.org/10.1063/1.3507388
[38] A. Ali, *et al*., Curr. Appl. Phys. **18**, 599 (2018). https://doi.org/10.1016/j.cap.2018.02.016
[39] T.A. Amollo, G.T. Mola, and V.O. Nyamori, Sol. Energy, **171**, 83 (2018): https://doi.org/10.1016/j.solener.2018.06.068
[40] H.P. Kim, A.R.M. Yusoff, and J. Jang, Sol. Energy Mater. Sol. Cells, **110**, 87 (2013).
[41] N.M.S. Hidayah, *et al*., AIP Conf. Proc. **1892**, 150002 (2017). https://doi.org/10.1063/1.5005764
[42] Y.-J. Jeon, *et al*., Sol. Energy Mater. Sol. Cells, **105**, 96 (2012). https://doi.org/10.1016/j.solmat.2012.05.024
[43] A. Negash, A.M. Demeku, and L.H. Molloro, New J. Chem. **46**, 13001 (2022). https://doi.org/10.1039/D2NJ01974D
[44] Xu Xiang, *et al*., Carbon Letters, **32**, 557 (2022). https://doi.org/10.1007/s42823-021-00287-6

[45] T. Tene, *et al*., Front. Chem. **11**, (2023). https://doi.org/10.3389/fchem.2023.1267199
[46] Y. Wang, *et al*., Mater. Today, **21**, 186 (2018). https://doi.org/10.1016/j.mattod.2017.10.008
[47] S.S. Li, K.H. Tu, C.C. Lin, C.W. Chen, and M. Chhowalla, ACS Nano, **4,** 3169 (2010). https://doi.org/10.1021/nn100551j
[48] J. Liu, *et al*., Adv. Mater. **26**, 786 (2014). https://doi.org/10.1002/adma.201302987
[49] D.D. Nguyen, *et al*., Nanotechnology, **22**, 295606 (2011). https://doi.org/10.1088/0957-4484/22/29/295606
[50] Z. Fakharan, L. Naji, and K. Madanipour, Org. Electron. **76**, 105459 (2020). https://doi.org/10.1016/j.orgel.2019.105459
[51] J.H. Lee, *et al*., Org. Electron. **30**, 302 (2016). https://doi.org/10.1016/j.orgel.2016.01.003
[52] H. Park, P.R. Brown, V. Bulović, and J. Kong, Nano Lett. **12**, 133 (2012). https://doi.org/10.1021/nl2029859
[53] G.A. Chamberlain, Sol. Cells, **8,** 47 (1983). https://doi.org/10.1016/0379-6787(83)90039-X
[54] M. Akbi, "A method for measuring the photoelectric work function of contact materials versus temperature," in: *IEEE Transactions on Components, Packaging and Manufacturing Technology*, **4**(8), (2014), pp. 1293-1302. https://doi.org/10.1109/TCPMT.2014.2328661
[55] M. Burgelman, K. Decock, A. Niemegeers, J. Verschraegen, and S. Degrave, *SCAPS manual*, (University of Gent, 2023).
[56] S.B. Hacène, T. Benouaz, and T. Benouaz, Phys. Status Solidi (a), **211**, 862 (2014). https://doi.org/10.1002/pssa.201330320
[57] B.M. Omer, "Influence of characteristic energy of the valence band tail on performance of P3HT:PCBM bulk-heterojunction solar cell: AMPS-1D simulation study," in: *2014 IEEE 40th Photovoltaic Specialist Conference* (*PVSC)*, (IEEE, 2014), pp. 1770-1775.
[58] E.K. Chiew, M. Yahaya, and A. P. Othman, International Journal of Computational Materials Science and Engineering, **01**(01), 1250004 (2012). https://doi.org/10.1142/S2047684112500042
[59] G.A. Nowsherwan, *et al*., Nanomater. **12**, 1767 (2022). https://doi.org/10.3390/nano12101767
[60] A.S. Khune, *et al*., J. Electron. Mater. **52**, 8108 (2023). https://doi.org/10.1007/s11664-023-10711-4
[61] L. Sygellou, *et al*., J. Phys. Chem. C, **120**, 281 (2016). https://doi.org/10.1021/acs.jpcc.5b09234
[62] C. Yuwen, *et al*., Mater. Res. Express, **6**, 0950b4 (2019). https://doi.org/10.1088/2053-1591/ab149f
[63] A. Daraie, and A. Fattah, Opt. Mater. **109**, 110254 (2020). https://doi.org/10.1016/j.optmat.2020.110254
[64] W. Abdelaziz, *et al*., Sol. Energy, **211**, 375 (2020). https://doi.org/10.1016/j.solener.2020.09.068
[65] W. Abdelaziz, *et al*., Opt. Mater. **91**, 239 (2019). https://doi.org/10.1016/j.optmat.2019.03.023
[66] M.Q. Khokhar, *et al*., Mater. Sci. Semicond. Process. **134**, 105982 (2021). https://doi.org/10.1016/j.mssp.2021.105982
[67] S.-F. Wang, *et al*., J. Phys. Chem. C, **116**, 1650 (2012). https://doi.org/10.1021/jp2045146
[68] M.Q. Khokhar, *et al*., Energies, **13**, 1635 (2020). https://doi.org/10.3390/en13071635
[69] Jacob, Mohan V. Science and Technology of Advanced Materials **6** (2005): 944-949.
[70] H. Niu, *et al*., Dalton Transactions, **50**, 6477 (2021). https://doi.org/10.1039/D1DT00344E
[71] V. Srikant, and D.R. Clarke, J. Appl. Phys. **83**, 5447 (1998). https://doi.org/10.1063/1.367375
[72] B. Hussain, *et al*., Electronics, **8**(2), 238 (2019). https://doi.org/10.3390/electronics8020238
[73] A. Umar, *et al*., Micromachines, **13**(12), 2073 (2022). https://doi.org/10.3390/mi13122073
[74] K.S. Nithya, and K.S. Sudheer, Opt. Mater. **123**, 111912 (2022). https://doi.org/10.1016/j.optmat.2021.111912
[75] M. Dadashbeik, D. Fathi, and M. Eskandari, Sol. Energy, **207**, 917 (2020). https://doi.org/10.1016/j.solener.2020.06.102
[76] M.M. Shabat, G. Zoppi, "Simulation on the perovskite-based solar cell with graphene derivative," in: *The 8th International Engineering Conference on Renewable Energy & Sustainability*, (Gaza, Palestine, 2023).

ОКСИД ГРАФЕНУ ТА ВІДНОВЛЕНИЙ ОКСИД ГРАФЕНУ ЯК ДІРКОВІ ТРАНСПОРТНІ ШАРИ ДЛЯ ПІДВИЩЕННЯ ЕФЕКТИВНОСТІ ОБ'ЄМНИХ ГЕТЕРОПЕРЕХОДНИХ ОРГАНІЧНИХ СОНЯЧНИХ ЕЛЕМЕНТІВ НА ОСНОВІ ФУЛЕРЕНУ: ДОСЛІДЖЕННЯ ЧИСЛОВОГО МОДЕЛЮВАННЯ

Денет Девіс, К.С. Судхір
Дослідницька лабораторія моделювання оптоелектронних пристроїв, кафедра фізики, автономний Християнський коледж Ириджалакуда, Тріссур, Керала, Індія, 680125
Калікутський університет, Калікут, Керала, Індія, 673635

Останніми роками все більше досліджень зосереджено на покращенні ефективності об'ємних гетеропереходних органічних сонячних елементів (BHJOSC) на основі фулерену на основі метилового ефіру [6,6]-феніл-C61-масляної кислоти (PCBM) з використанням полі 3-гексилтіофен-2 ,5-діїл (P3HT) як донор і похідні графену як шар транспортування дірок (HTL). Похідні графену, головним чином оксид графену (GO) і відновлений оксид графену (RGO), мають такі ж винятковi характеристики, як і графен, і є хорошими кандидатами в якості HTL у BHJOSC на основі P3HT:PCBM. У цій роботі ми використовуємо симулятор одновимірної ємності сонячних елементів (SCAPS1D) для широкого та детального вивчення двох конфігурацій, а саме ITO/GO/P3HT:PCBM/Al та ITO/RGO/P3HT: PCBM/Al. Обидві конфігурації оптимізовані, а підвищена ефективність досягається зміною вхідних електричних параметрів пристрою. Після цього проектування, моделювання та аналіз різних комбінацій пристроїв виконуються з використанням дев'яти різних ETL і трьох металевих електродів. ITO/GO/P3HT:PCBM/LiF/Ca та ITO/RGO/P3HT:PCBM/LiF/Ca забезпечили підвищення ефективності на 8,00% і 12,00% відповідно. Потім вивчається вплив різної щільності донора фториду літію (LiF) і ефект змінної роботи виходу оксиду індію та олова (ITO) на продуктивність цих двох пристроїв. Рекордна ефективність 16,47% досягнута для підвищеної щільності донора LiF у конфігурації ITO/RGO/P3HT:PCBM/LiF/Ca.

Ключові слова: *об'ємний гетероперехідний органічний сонячний елемент; симулятор ємності одновимірної сонячної батареї; оксид графену; відновлений оксид графену; підвищена ефективність*

EAST EUROPEAN JOURNAL OF PHYSICS. 1. 233-239 (2025)
DOI:10.26565/2312-4334-2025-1-24 ISSN 2312-4334

OBTAINING AND MEASURING IMPEDANCE CHARACTERISTICS OF THE Ag_8SiSe_6 COMPOUND

R.M. Sardarly[a,b], M.B. Babanly[c], N.A. Aliyeva[a,d]*, L.F. Mashadiyeva[b], R.A. Mamadov[a], G.M. Ashirov[b], A.A. Saddinova[e], S.Z. Damirova[e]
[a]*Institute of Radiation Problems, Azerbaijan National Academy of Sciences, B. Vagabzadeh street 9, AZ 1143, Baku, Azerbaijan*
[b]*Department of Applied and General Physics, National Aviation Academy, Baku, Azerbaijan*
[c]*Named after Academician M. Naghiyev Institute of Catalysis and Inorganic Chemistry, Ministry of Science and Education Republic of Azerbaijan, H. Cavid str., 113, AZ1143, Baku, Azerbaijan*
[d]*Azerbaijan University of Architecture and Construction, Ayna Sultanova st. 5, AZ-1073, Baku, Azerbaijan*
[e]*Institute of Physics, Ministry of Science and Education Republic of Azerbaijan, H. Javid str., 131, AZ1143, Baku, Azerbaijan*
**Corresponding Author e-mail: gunel_imanova55@mail.ru*
Received July 23, 2024; revised October 13, 2024; accepted January 9, 2025

Samples of the Ag_8SiSe_6 compound were obtained by direct alloying of initial components and subsequent pressing of powders under a pressure of 0.7 GPa. Temperature dependences of conductivity (σ(T)) and permittivity (ε(T)) of the Ag_8SiSe_6 compound were studied in constant and alternating electric fields. In a constant field, the electrical conductivity is found to decrease over time (σ(t)). This phenomenon is associated with the process of charge accumulation at the interface of the ion sample and the blocking electrode. Complex impedance spectra were studied in the frequency range of 20–10^6 Hz.
Keywords: *Compound; Ionic conductivity; Complex impedance spectra*
PACS: 71.20.-b, 71.20.Nr , 71.70.Ch

1. INTRODUCTION

The development of modern materials for micro- and nanoelectronics, super capacitors, ionic conductors, mini-batteries and other devices depends on the search for new compounds that have the appropriate crystal structure, electronic and phonon spectrum, which makes it possible to implement these devices. Promising materials for these purposes include compounds of the mineral argyrodite (Ag_8GeS_6) family and phases based on them with the general formula $A^{m+}_{(12-n)/m}B^{n+}X^{2-}_6$, where *m* and *n* are the valences of *A* and *B* cations, respectively (where *A*-cations are Cu^+, Ag^+, Li^+, Cd^{2+}, Hg^{2+}; *B*-cations are Ga^{3+}, Si^{4+}, Ge^{4+}, Sn^{4+}, P^{5+}, As^{5+}; *X*-anions are S^{2-}, Se^2, Te^{2-}. These phases have a number of valuable functional properties and are being intensively studied by many research groups [1-6]. Most of these materials are of special interest due to their phase transitions, which take place close to ambient temperature [7]. High-temperature modifications, as a rule, crystallize in a cubic structure and have high ionic conductivity. Especially, copper and silver containing compounds of this family are well-known super ionic semiconductors, due to the presence of highly mobile Cu+ and Ag+ ions [8-12]. In recent years, silicon-containing argyrodites, have attracted particular interest as eco-friendly thermoelectric and ion-conducting materials [13-15].

Previously, in [16], we studied the temperature dependences of the conductivity and permittivity of the Ag_8GeSe_6 compound in direct and alternating electric fields. It was shown that this phenomenon is associated with the process of charge accumulation at the interface of the sample with ionic conductivity and the blocking electrode and the formation of a double electric layer. The observed in the studied sample dielectric relaxation is associated with the transition of the crystal to the super ionic state. It has been established that hopping conduction with a variable hopping length over localized states near the Fermi level takes place in an Ag_8GeSe_6 crystal.

The purpose of this work was to establish the features of the temperature and frequency dependence of conductivity, dielectric properties of Ag_8SiSe_6 compound in a constant and alternating field. The impedance spectra of the Ag_8SiSe_6 compound were studied in order to establish the mechanism of charge transfer and the nature of relaxation losses in the volume and at the interface between the ionic conductors and the blocking contact.

The Ag_8SiSe_6 melts congruently at 1203 K [7, 17], or 1258 K according to [18], 1268 K according to [19]. This compound has two polymorph transitions at 315 and 355 K and crystallize in 3 crystalline structures [7, 11, 13, 17]. The high-temperature (HT) modification of the Ag_8SiSe_6, like all other compounds of the argyrodite family, crystallizes in a face-centered cubic structure (Sp.gr. *F*-43*m*) with complete disordering of the cationic sublattice. HT-Ag_8SiSe_6 has the lattice periods: *a* = 1.097 nm [7, 17], or *a* = 1.09413(1) nm [13]. The intermediate modification (IT) has a simple-cubic structure (Sp.gr. $P2_13$ [11] or $P4_232$ with a lattice constant *a* = 1.087 nm [7]). The IT-Ag_8SiSe_6 modification is characterized by partial localization of silver ions [11]. According to [7, 17] LT-Ag_8SiSe_6 has a tetragonal structure (Sp.gr. *I*-4*m*2, *a* = 0.7706, *b* = 1.10141 nm).

Cite as: R.M. Sardarly, M.B. Babanly, N.A. Aliyeva, L.F. Mashadiyeva, R.A. Mamadov, G.M. Ashirov, A.A. Saddinova, S.Z. Damirova, East Eur. J. Phys. 1, 233 (2025), https://doi.org/10.26565/2312-4334-2025-1-24
© R.M. Sardarly, M.B. Babanly, N.A. Aliyeva, L.F. Mashadiyeva, R.A. Mamadov, G.M. Ashirov, A.A. Saddinova, S.Z. Damirova, 2025; CC BY 4.0 license

2. EXPERIMENTAL METHODS AND OBTAINING SAMPLES

High-purity elements (at least 99.999 wt.% purity) were used for synthesis of Ag_8SiSe_6 compound. The synthesis was carried out in ampoules evacuated to 10^{-2} Pa. To avoid a reaction between silicon and the walls of the quartz ampoule, the inner walls of the tube were graphitized by pyrolysis of toluene.

Taking into account the high vapor pressure of selenium at the melting point of Ag_8SiSe_6, this compound was synthesized in an inclined two-zone furnace. Stoichiometric amounts of elementary components were loaded into a quartz ampoule, which, after being evacuated and sealed, was placed in an inclined tube furnace. Two-thirds of the ampoule was in the oven (hot zone) and the rest of the upper part was outside the oven (cold zone). The furnace was heated to 1300 K. To prevent the ampoule from exploding due to overheating, the "cold" zone was cooled with water. After the interaction of a larger mass of components, the ampoule was completely placed in the furnace. After keeping in the oven for 4-5 hours, the ampoule was gradually cooled by in the switched off furnace mode.

The completion of the synthesis of the Ag_8SiSe_6 and the identification of this compound were controlled by differential thermal analysis (DTA) and X-ray diffraction (XRD) technique.

Figure 1 presents the DTA data for the Ag_8SiSe_6. This compound melts at 1278 K (this temperature closer to the data Piskach L.V. et al [19]). There are also two endothermic effects at 315 and 354 K on the heating DTA curve, corresponding to the polymorphic transitions.

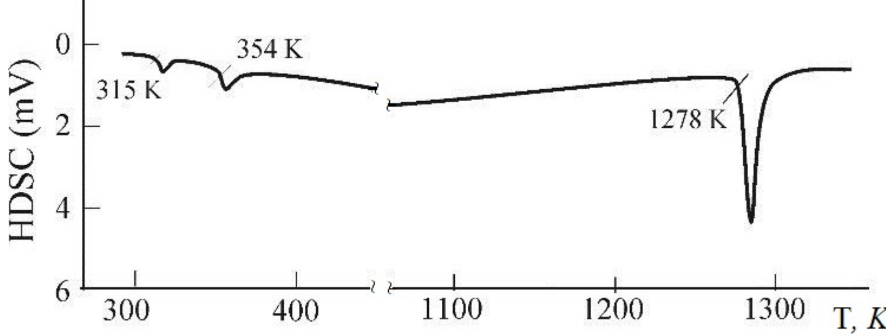

Figure 1. Heating DTA curve for the Ag_8SiSe_6

The diffraction pattern of Ag_8SiSe_6 is completely indexed in a simple-cubic lattice with Sp.gr. $P4_232$ and $a = 1.0891(3)$ nm. Obtained crystal lattice parameters almost coincided with the data of the above works [7, 11]. DTA measurements were recorded using a multichannel device based on the electronic "TC-08 thermocouple data logger" with chromel-alumel thermocuples in sealed quartz tubes. XRD was performed at room temperature using a Bruker D8 ADVANCE diffractometer (with Cu-Kα_1 radiation) within $2\theta = 10°$ to 70°. The unit cell parameters were calculated by indexing powder patterns using Topas V3.0 software.

In order to measure the temperature dependences of the permittivity and electrical conductivity of Ag_8SiSe_6 compound samples, capacitors were made, the dielectric in which was plates of the studied materials, which were compressed tablets from the powdered Ag_8SiSe_6 compound. The capacitor plates were obtained by applying silver conductive paste to the surface of the plates. The study of complex permittivity and electrical conductivity was carried out with a digital immittance meter E7-20 in the frequency range of $20÷10^6$ Hz in the temperature range of 200÷450 K. The amplitude of the measuring field was in the range of 1 – 5 V·cm^{-1}.

3. Results and discussion

3.1 Temperature dependence of electrical conductivity and permittivity

a. Electrical conductivity

The temperature dependence of the electrical conductivity of the Ag_8SiSe_6 compound in a constant field is given in Fig. 2. As can be seen from the figure, at a temperature of ~300 K, there is a leap in the dependence σ(T). The inset to the figure shows the curve ln(σ·T) on 1/T above the temperature leap as a function of σ on 1/T. According to [20-22], the temperature dependence of ionic conductivity has an activation character

$$\sigma \cdot T = \sigma_0 \exp(-\Delta E/kT)$$

where, ΔE is the activation energy of electrical conductivity. As can be seen from the inset to Fig. 1, the experimental points are well straightened, while ΔE – for Ag_8SiSe_6 turned out to be equal to 0.1 eV. It is known that this type of electrical conductivity indicates the predominant nature of ionic conductivity above the temperature leap in the σ(T) curve.

The observed sharp increase in the conductivity in Ag_8SiSe_6 compound at temperatures above 300 K is probably due to the increase in the number of ions in states where they have high mobility. From crystallographic considerations, we can assume that the structure of Ag_8SiSe_6 is most favorable to the mobility of Ag^{+1} cations, that is, the temperature increase in conductivity is due to the diffusion of Ag^{+1} ions through vacancies in the silver sublattice of the Ag_8SiSe_6 compound.

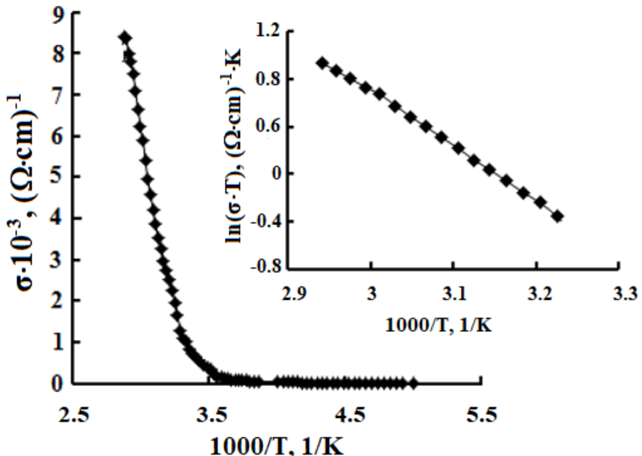

Figure 2. Temperature dependences of the electrical conductivity σ(T) of the Ag_8SiSe_6 compound in a constant field. The inset to the figure shows the dependence of ln(σ·T) on 1/T above the temperature leap as a function of σ on 1/T, that is, in the region of ionic conductivity

It is known that with the transition of the system to a state with predominantly ionic conductivity, the disorder of the cationic sublattice in the compound will increase, that is, the ions will shift from their positions at the lattice sites to the interstitial site, leaving a vacancy at the site. Collective interaction of all interstitial ions and vacancies can lead to the emergence of superionic conductivity. It is also possible that the migration of interstitial Ag^+ ion occurs by direct leap from one interstitial site to another, followed by displacement of translationally equivalent ion (Ag) in the interstitial site. In this case, the most probable type of emerging defects will be Frenkel defects, namely, mobile interstitial Ag^+ ions associated with cation vacancies. The conductivity of the Ag_8SiSe_6 compound in the superionic phase at T>300K is ~ $3·10^{-3}$ $Ohm^{-1}cm^{-1}$, the activation energy of conductivity is 0.1 eV. The structure is favourable for the free motion of Ag^+.

In this case, there will also be a charge exchange between the defects in the crystal and the resulting local polarization will lead to an increase in permittivity [23-28].

b. Permittivity

The electrical conductivity of compounds in the superionic phase is exponential in nature [29], while the temperature dependence of the permittivity is also exponential.

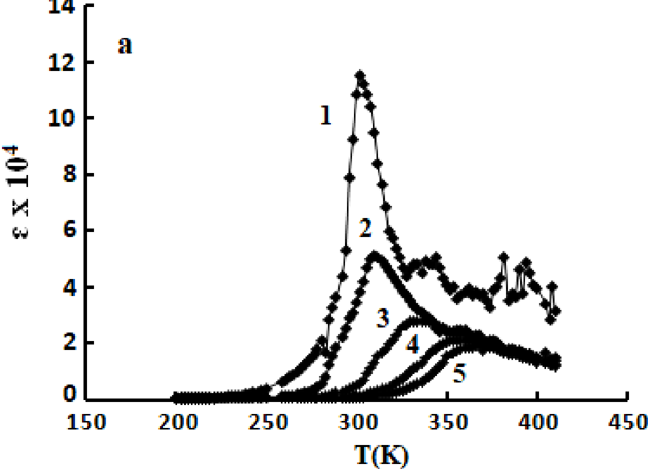

Figure 3. Temperature dependence of permittivity of Ag_8SiSe_6 compound. Measurements were performed at different frequencies of the measuring field: 1 – 10^3, 2 – 10^4, 3 – 10^5, 4 - $5·10^5$, 5 – 10^6 Hz

Fig. 3 shows temperature dependences of permittivity of Ag_8SiSe_6 compound. The measurements were performed in the temperature range of 200-400 K and frequency range of 10^2 - 10^6 Hz. The figure shows that both with increasing temperature and with increasing frequency of the measuring field, the peak value of permittivity drops and it shifts towards high temperatures. In all measured frequency and temperature ranges, the same feature is observed in dependence ε(T). Such behavior of temperature dependence of permittivity is typical for Debye-type relaxation processes in which several relaxators participate. The shift of the peak ε(T) to the high-temperature region with increasing measurement frequency may indicate that polarization processes occurring in the volume begin to play a significant role in the relaxation processes occurring at the interface.

The polarization of Ag_8SiSe_6 may be due to the diffusion of Ag^{+1} ions over vacancies, which leads to the transition of the compound to the superionic state In addition, the exponential growth of the ε(T) dependence measured in the low temperature region (i.e., at temperatures preceding the transition to the superionic state) can be explained by the influence of localized states on polarization in an alternating electric field. Polarization can be related to the hopping of charge carriers to the positions that are energetically favorable due to the creation of an electric field in the crystal, and due to lattice relaxation, there is a shift of charges, which is accompanied by the screening of the resulting polarization [23-25].

3.2. Time dependence of electrical conductivity

The feature of charge transfer of ionic conductors is a large contribution to the conductivity of ions in comparison with electron transfer. The ionic conductivity of high resistivity crystals and semiconductors, under normal conditions, is 6-7 orders of magnitude lower than the contribution of electron transfer to the overall conductivity of the sample. The Wagner polarization method was used to elucidate the relative contribution of the electronic and ionic component to the overall conductivity of Ag_8SiSe_6 samples at different temperatures. In compounds with a mixed electron-ion nature of charge transfer, a time dependence of the conductivity is observed when the conductivity is measured at direct current. The process is associated with the formation of a double electric layer in the near-surface layer of the sample. When blocking contacts are used as electrodes, mobile ions are delayed at the sample-electrode interface; as a result, a concentration gradient is created in the sample volume under the influence of the electric field, which in turn leads to the emergence of a diffusion flux of ion directed in the opposite direction to the drift flux of ion. Thus, since the drift and diffusion fluxes of ion are compensated, a current flows through the sample due to charge transfer by electrons only.

Fig. 4 shows the time dependence of the conductivity of the electrochemical cell of Ag_8SiSe_6 compound. Silver contacts blocking ionic contribution to the conductivity are used as electrodes. A constant potential difference of ~ 5V/cm is applied to the plates. The current through the sample is measured at certain time intervals.

As can be seen from the figure, in a constant field, the time dependence of electrical conductivity is nonlinear. As a result, during measurements at the initial moment of time, the total current of ions and electrons flows, while in the steady state the charge transfer is carried out only by electrons. Thus, the result of mutual compensation of the space charge region near the interface (Ag_8SiSe_6) - silver contact, which has a blocking character, is a decrease of the electric current over time in a constant field (Fig. 4)

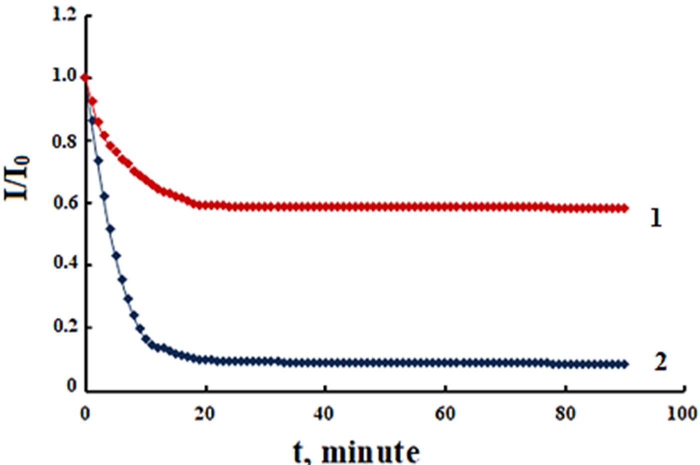

Figure 4. Time dependence of the reduced electrical conductivity $J(t)/J_0$ for Ag_8SiSe_6 compound. The measurements were performed using silver electrodes at room temperature. 1-300K, 2-350K

3.3. Impedance

The nature of electrical conductivity of samples with mixed electron-ion charge transfer is affected by relaxation processes at the interface, which lead to the blocking of charge carriers through the contact and polarization of the near-contact region. To obtain a complete picture of the conductivity of the studied sample, we have measured the complex impedance with subsequent construction of hodographs in the Cole-Cole representation.

The frequency dependence of the real Z'(ν) and imaginary Z"(ν) parts of the complex conductivity of Ag_8SiSe_6 is presented in Fig. 5. The measurements were carried out at temperatures of 200, 250, 300, 350 and 400 K. As can be seen from the figures, there is a smooth decrease in the values of the real and imaginary parts of the complex impedance with increasing operating frequency. Frequency dispersion is observed in all experimental conditions, but the nature of the dispersion is different for each measurement. A sharp decrease in Z'(ν) and Z"(ν) is observed in the low-frequency frequency range of 20-10^3 Hz, however with further increase in frequency, there is a weakening of the frequency dependence of the spectra. The observed dispersion of impedance spectra indicates the presence of electrical relaxation, which can be conveniently analyzed using impedance hodograph curves.

Impedance spectroscopy methods are widely used in measuring the dielectric parameters of solids using alternating current. This method allows to obtain the most complete information both on the relaxation processes occurring in the

thickness of the object and on the characteristics of complex conductivity at its boundaries, as well as to determine the nature of relaxation losses.

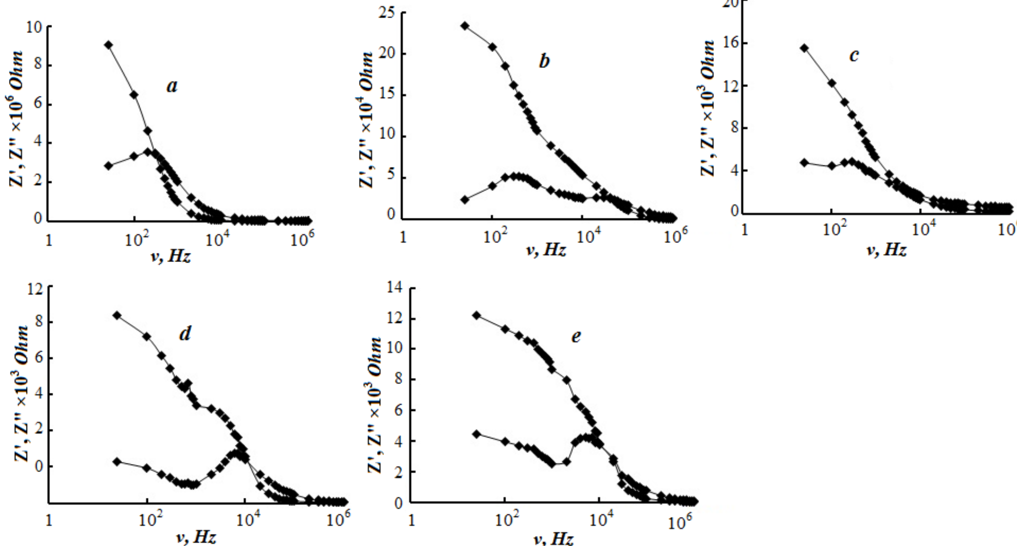

Figure 5. Frequency dependences of the real Z′(ν) and imaginary Z″(ν) parts of the complex impedance of the Ag_8SiSe_6 compound. The measurements were carried out at *a* - 200, *b* - 250, *c* - 300, *d* – 350 and *e* – 400 K

Fig. 6 shows the results of dependence of Z″(ν)/Z′(ν) at temperatures of 200, 250, 300, 350 and 400 K for Ag_8SiSe_6 compound. As can be seen from the curves in Fig. 6, the diagrams in the complex plane (Z" - Z") are semicircles (curves in Figs. *a* and *b*), while in Figs. *d* and *e*, measured at temperatures of 350 and 400 K, "rays" appear in addition to the semicircles. These rays in the low-frequency region of the hodograph obtained at 350 and 400 K are characteristic of the Warburg impedance. The idea of the Warburg impedance is based on the fact that the diffusion of carriers in the frequency range of the applied sinusoidal signal does not reach the boundary of the diffuse layer. The reason for the appearance of the diffuse Warburg impedance is the transition of the Ag_8SiSe_6 compound into the high-ionic state at 350 and 400 K. The equivalent Warburg impedance circuit is shown in Fig. 6, it has $Z_1 = R_1$ - active resistance and $Z_2 = 1/j\omega C$ - the capacitance C (j is the imaginary unit, ω is the frequency). Thus, the Warburg impedance models the process in which a sinusoidal voltage that is applied to an electrochemical cell, at one polarity causes diffusion of mobile ions from the electrode into the diffuse layer, and at the other polarity causes diffusion of mobile ions to the electrode. In this case, the process does not go beyond the diffuse layer region. [16, 23]

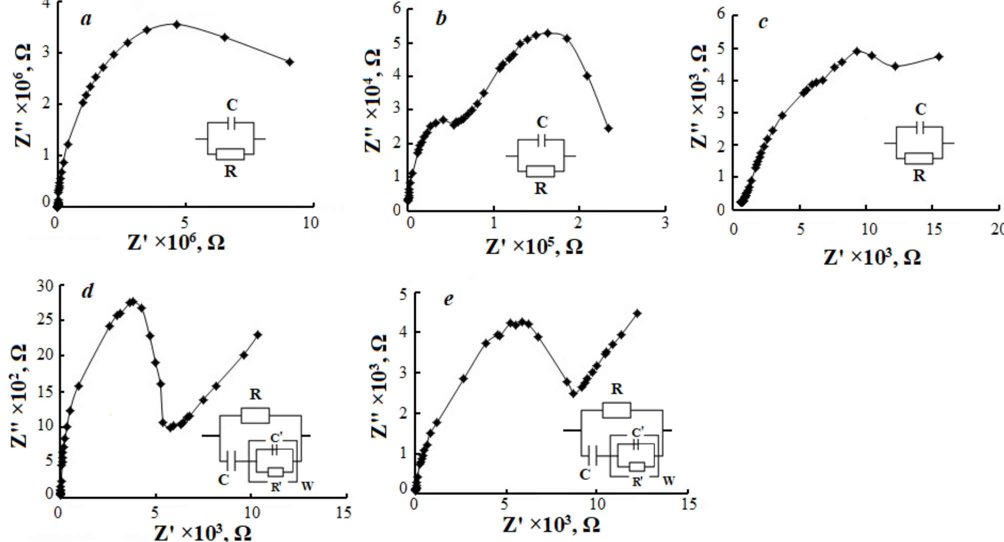

Figure 6. Hodograph of impedance Z″(Z′) of Ag_8SiSe_6. The measurements were performed at temperatures: *a* - 200, *b* - 250, *c* - 300, *d* – 350 and *e* – 400 K. An equivalent circuit is shown in the inset to the figure

3.4. Frequency dispersion ε' and ε'' for Ag_8SiSe_6 compound

The real and imaginary parts of the complex permittivity were calculated from the relations $\varepsilon' = Cd/\varepsilon_0 S$ *and* $\varepsilon'' = tg\delta\varepsilon$. Fig. 7 shows the frequency dependences of the real and imaginary parts of the complex permittivity for Ag_8SiSe_6 compound measured at temperatures of 200, 250, 300, 350 and 400K. As can be seen from the figures, the ε''(f)

dependence shows one relaxation peak at a frequency of ~10^2 Hz (Fig. 7). In the curves of ε''(f) dependence obtained at temperatures 350 and 400K, the feature is absent at 10^2 Hz, while it appears at 10^4 Hz. The above characteristics reveal dispersion, which manifests itself in in the decrease of the complex impedance values with increasing frequency of the applied electric field. From the curves in Fig. 7, it is seen that ε'(*f*) decreases by several orders of magnitude with increasing frequency from 10^1 to 10^6 Hz. At low frequencies, ε'(*f*) dependence decreases sharply; at high frequencies, the real part of the complex permittivity depends weakly on frequency, and at frequencies of ~1 MHz, it takes the value ~10. The value of high-frequency permittivity for Ag_8SiSe_6 obtained from impedance measurements is also the value of optical (high-frequency - ε_∞) permittivity of the investigated compound.

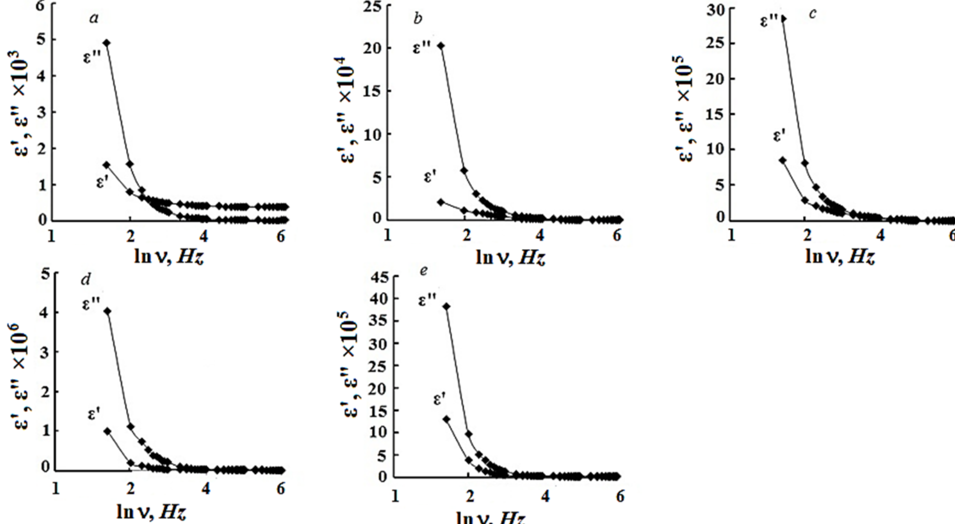

Figure 7. Frequency dispersion of the real ε' and imaginary ε'' parts of the complex permittivity of Ag_8SiSe_6 compound. The measurements were performed at temperatures of 200(a); 250(b); 300(c); 350(d) and 400(e) K

CONCLUSIONS

A decrease in electrical conductivity of Ag_8SiSe_6 compound over time has been found during measurements in a constant electric field using silver electrodes. It is shown that the conductivity has an ionic nature in a constant electric field above 300 K. By the study of complex impedance, it is established that in the considered frequency-temperature range, the electrical properties of Ag_8SiSe_6 compound are determined by the conductivity of Ag^{+1} ions in localized states, while the other is related to the accumulation of charge on blocking electrodes.

ORCID

R.M. Sardarly, https://orcid.org/0000-0003-3968-000X; **M.B. Babanly,** https://orcid.org/0000-0001-5962-3710
N.A. Aliyeva, https://orcid.org/0000-0002-8448-0552; **L.F. Mashadiyeva,** https://orcid.org/0000-0003-2357-6195
R.A. Mamadov, https://orcid.org/0000-0003-0368-1326; **G.M. Ashirov,** https://orcid.org/0000-0003-2786-5824
A.A. Saddinova, https://orcid.org/0009-0005-9967-3575; **S.Z. Damirova,** https://orcid.org/0009-0008-9536-2894

REFERENCES

[1] I. Semkiv, N. Ilchuk, and A. Kashuba, "Photoluminescence of Ag_8SnSe_6 argyrodite,' Low Temperature Physics, **48**(1), 12 (2022). https://doi.org/10.1063/10.0008957
[2] S. Lin, W. Li, and Y. Pei, "Thermally insulative thermoelectric argyrodites," Materials Today, **48**, 198–213 (2021). https://doi.org/10.1016/j.mattod.2021.01.007
[3] S. Schwarzmüller, D. Souchay, D. Günther, *et al.*, „Argyrodite-type $Cu_8GeSe_{6-x}Te_x$ ($0 \le x \le 2$): Temperature-dependent crystal structure and thermoelectric properties," Zeitschrift für anorganische und allgemeine Chemie, **644**(2), 1915–1922 (2018). http://dx.doi.org/10.1002/zaac.201800453
[4] B. Jiang, P. Qiu, E. Eikeland, *et al.*, "Cu_8GeSe_6-based thermoelectric materials with an argyrodite structure," Journal of Materials Chemistry C, **5**, 943–952 (2017). https://doi.org/10.1039/C6TC05068A
[5] Y. Fan, G. Wang, R. Wang, *et al.*, "Enhanced thermoelectric properties of p-type argyrodites Cu_8GeS_6 through Cu," Journal of Alloys and Compounds, **822**, 153665 (2020). https://doi.org/10.1016/j.jallcom.2020.153665
[6] M. Yang, G. Shao, B. Wu, *et al.*, "Irregularly shaped bimetallic chalcogenide ag_8sns_6 nanoparticles as electrocatalysts for hydrogen evolution," ACS Applied Nano Materials, **4**(7), 6745–6751 (2021). https://doi.org/10.1021/acsanm.1c00769
[7] O. Gorochov, "Les composés Ag_8MX_6 (M = Si, Ge, Sn et X = S, Se, Te)," Bulletin de la Société Chimique de France, **101**, 2263-2275 (1968).
[8] I.P. Studenyak, A.I. Pogodin, V.I. Studenyak, *et al.*, "Electrical properties of copper- and silver-containing superionic $(Cu_{1-x}Ag_x)_7SiS_5I$ mixed crystals with argyrodite structure," Solid State Ionics, **345**, 115183 (2020). https://doi.org/10.1016/j.ssi.2019.115183
[9] K.S. Weldert, W.G. Zeier, T.W. Day, *et al.*, "Thermoelectric transport in Cu_7PSe_6 with high copper ionic mobility," Journal of the American Chemical Society, **136**, 12035–12040 (2014). https://doi.org/10.1021/ja5056092

[10] G. Brammertz, B. Vermang, H. El-Anzeery, *et al.*, "Fabrication and characterization of ternary Cu_8SiS_6 and Cu_8SiSe_6 thin film layers for optoelectronic applications," Thin Solid Films, **616**, 649–654 (2016). https://doi.org/10.1016/j.tsf.2016.09.049
[11] B.K. Heep, K.S. Weldert, Y. Krysiak, *et al.*, "High electron mobility and disorder induced by silver ion migration lead to good thermoelectric performance in the argyrodite Ag_8SiSe_6," Chemistry of Materials, **29**(11), 4833–4839 (2017). https://doi.org/10.1021/acs.chemmater.7b00767
[12] T. Bernges, R. Hanus, B. Wankmiller, K. Imasato, *et al.*, "Considering the Role of Ion Transport in Diffuson-Dominated Thermal Conductivity," Advanced Energy Materials, **12**, 2200717 (2022). https://doi.org/10.1002/aenm.202200717
[13] Q. Jiang, S. Li, Y. Luo, *et al.*, "Ecofriendly highly robust Ag_8SiSe_6-based thermoelectric composites with excellent performance near room temperature," ACS Applied Materials & Interfaces, **12**(49), 54653–54661 (2020). https://doi.org/10.1021/acsami.0c15877
[14] W. Li, S. Lin, B. Ge, *et al.*, "Low sound velocity contributing to the high thermoelectric performance of Ag_8SnSe_6," Advanced Science, **3**(11), 1600196 (2016). https://doi.org/10.1002/advs.201600196
[15] A. Charoenphakdee, K. Kurosaki, H. Muta, *et al.*, "Ag_8SiTe_6: A new thermoelectric material with low thermal conductivity," Japanese Journal of Applied Physics, **48**, 011603 (2009). https://doi.org/10.1143/JJAP.48.011603
[16] R.M. Sardarly, G.M. Ashirov, L.F. Mashadiyeva, *et al.*, "Ionic conductivity of the Ag_8GeSe_6 compound," Modern Physics Letters B, **36**, 2250171 (2023). https://doi.org/10.1142/S0217984922501718
[17] A.M. Hofmann, *Silver-Selenium-Silicon, Ternary Alloys*, VCH 2, 1988. pp. 559–560.
[18] M. Venkatraman, R. Blachnik, and A. Schlieper, "The phase diagrams of M_2X-SiX_2 (M is Cu, Ag; X is S, Se)," Thermochimica Acta, **249**, 13–20 (1995). https://doi.org/10.1016/0040-6031(95)90666-5
[19] L.V. Piskach, O.V. Parasyuk, I.D. Olekseyuk, *et al.*, "Interaction of argyrodite family compounds with the chalcogenides of II-b elements," Journal of Alloys and Compounds, **421**, 98–104 (2006). https://doi.org/10.1016/j.jallcom.2005.11.056
[20] H. Iyetomi, P. Vashishta, and R.K. Kalia, "Incipient phase separation in Ag/Ge/Se glasses: clustering of Ag atoms," J. Non-Cryst. Solids, **262**, 135-142 (2000). https://doi.org/10.1016/S0022-3093(99)00692-4
[21] R.M. Sardarly, F.T.Salmanov, N.A. Aliyeva, and R. Abbasli, "Impedance Spectroscopy of $(TlGaSe_2)_{1-x}(TlInSe_2)_x$ Solid Solutions In Radio Frequency Range," Modern Physics Letters B, **34**(11), 2050113 (2020). https://doi.org/10.1142/s0217984920501134
[22] M. Jin, S. Lin, W. Li, Z. Chen, R. Li, X. Wang, and Y. Pei, Chem. Mater. **317**, 2603-2610 (2019). https://doi.org/10.1021/acs.chemmater.9b00393
[23] R.M. Sardarly, F.T.Salmanov, N.A. Aliyeva, R.N. Mehdiyeva, and S.M. Gakhramanova, "AC conductivity of superionic thallium sulfide crystals exposed to γ-irradiation," Modern Physics Letters B, **35**(33), 2150504 (2021). https://doi.org/10.1142/S0217984921505047
[24] W.L. Roth, R.E. Benenson, and C.J. Wielunski, "Particle scattering studies on foreign ions in superionic conductors," Solid State Ionics, **9-10**, 1459–1464 (1983). https://doi.org/10.1016/0167-2738(83)90195-9
[25] D.P. Almond, A.R. West, and R. Grant, "Anomalous conductivity prefactors in fast ion conductors," Solud State Ionics, **8**, 456–457, (1983). https://doi.org/10.1038/306456a0
[26] A.A. Piarristeguy, M. Ramonda, N. Frolet, M. Ribes, and A. Pradel, "High resolution electrical characterisation of Ag-conducting heterogeneous chalcogenide glasses," Solid State Ion. **181**, 1205-1208 (2010). https://doi.org/10.1016/j.ssi.2010.06.050
[27] L. Li, Y. Liu, and J. Dai, "High thermoelectric performance of superionic argyrodite compound Ag_8SnSe_6," J. Mater. Chem. C, **4**, 5806-5813 (2016). https://doi.org/10.1039/C6TC00810K
[28] A. West, *Solid State Chemistry and its Applications*, (John Wiley & Sons, 1984). http://catalysis.eprints.iitm.ac.in/3790/1/seven%20crystal%20systems-1.pdf

ОТРИМАННЯ ТА ВИМІРЮВАННЯ ІМПЕДАНСНИХ ХАРАКТЕРИСТИК СПОЛУК Ag_8SiSe_6

Р.М. Сардарли[a,b], М.Б. Бабанли[c], Н.А. Алієва[a,d], Л.Ф. Машадієва[b], Р.А. Мамадов[a], Г.М. Аширов[b], А.А. Саддінова[e], С.З. Дамірова[e]
[a]*Інститут радіаційних проблем НАН Азербайджану, вул. Б. Вагабзаде, 9, АЗ 1143, Баку, Азербайджан*
[b]*Кафедра прикладної та загальної фізики, Національна академія авіації, Баку, Азербайджан*
[c]*Інститут каталізу та неорганічної хімії імені академіка М. Нагієва Міністерства науки і освіти Азербайджанської Республіки, вул. Г. Кавіда, 113, AZ1143, Баку, Азербайджан*
[d]*Азербайджанський університет архітектури та будівництва, вул. Айна Султанова 5, AZ-1073, Баку, Азербайджан*
[e]*Інститут фізики Міністерства науки і освіти Азербайджанської Республіки, вул. Г. Джавіда, 131, AZ1143, Баку, Азербайджан*

Зразки сполуки Ag_8SiSe_6 отримано прямим легуванням вихідних компонентів і подальшим пресуванням порошків під тиском 0,7 ГПа. Досліджено температурні залежності провідності (σ(T)) і діелектричної проникності (ε(T)) сполуки Ag_8SiSe_6 у постійному та змінному електричних полях. У постійному полі електропровідність зменшується з часом (σ(t)). Це явище пов'язане з процесом накопичення заряду на межі розділу іонний зразок і блокуючий електрод. Спектри комплексного імпедансу досліджували в діапазоні частот 20–10^6 Гц.

Ключові слова: *сполука; іонна провідність; спектри комплексного імпедансу*

EAST EUROPEAN JOURNAL OF PHYSICS. 1. 240-244 (2025)
DOI:10.26565/2312-4334-2025-1-25 ISSN 2312-4334

EFFECT OF IMPURITY AND RADIATION DEFECTS ON ANISOTROPY OF Yb-DOPED GaS SINGLE CRYSTAL

R.S. Madatov[a,b], T.B. Tagiev[a], A.Sh. Khaligzadeh[a], R.M. Mamishova[a,c]*
[a]*Institute of Radiation Problems, Ministry of Science and Education Republic of Azerbaijan,*
B. Vagabzadeh street 9, AZ 1143, Baku, Azerbaijan
[b]*Department of Applied and General Physics, National Aviation Academy, Baku, Azerbaijan*
[c]*Azerbaijan University of Architecture and Construction, Ayna Sultanova st. 5, AZ-1073, Baku, Azerbaijan*
**Corresponding Author e-mail: gunel_imanova55@mail.ru*
Received July 23, 2024; revised October 7, 2024; accepted January 9, 2025

The effect of γ-quanta on the anisotropy of GaS layered single crystal, pure and alloyed with 0.1at% Yb, has been studied at a temperature range of 125-300K. Since the difference between the ionic radius of the Yb-atom and the ionic radius of the component atoms is relatively small when the studied GaS monocrystal is added with itterbium ions, the additive atom is likely to be located both inside the layers (replacing the Ga atom or between nodes) and in interlayer space. The location of impurity atoms and radiation defects in the interlayer region of the layered GaS (Yb) crystal weakens the anisotropic properties of the crystals, and the location inside the layer strengthens them. The mechanism of current flow in high electric fields follows the Frenkel model, regardless of the nature of the impurity atom.
Keywords: *Anisotropy; Defects; Impurity atom; Electrical conductivity; Activation; Thermal annealing*
PACS: 64.60.-i, 71.23.Cq

1. INTRODUCTION

Single crystals of gallium sulfide (GaS) have garnered significant attention due to their unique structural and electronic properties, which render them promising candidates for various applications in optoelectronics, photonics, and semiconducting devices [1,2]. One of the key characteristics that distinguishes GaS single crystals is their anisotropic behavior, wherein their physical and electronic properties exhibit directional dependence along different crystallographic axes [3,4].

The anisotropy of GaS single crystals arises from the anisotropic arrangement of atoms within their crystal lattice, leading to variations in properties such as electrical conductivity, optical absorption, and mechanical strength along different crystallographic directions. Understanding and characterizing this anisotropy is crucial for tailoring the material's properties to specific applications and optimizing device performance.The study of anisotropy in semiconductor materials plays a crucial role in understanding their electronic, optical, and structural properties, which are fundamental for various technological applications[5,6]. The investigation of radiation-induced defects and their impact on the anisotropic properties of semiconductor materials holds significant importance in various fields of science and technology. Yb-doped GaS single crystals, with their unique electronic and optical properties, are of particular interest for optoelectronic applications. Understanding the effect of radiation defects on the anisotropy of Yb-doped GaS is crucial for optimizing their performance in radiation-sensitive devices such as radiation detectors and sensors [1,7-10].

Radiation defects, induced by exposure to ionizing radiation, can lead to the creation of vacancies, interstitials, and dislocations within the crystal lattice of semiconductor materials [11-14]. These defects can alter the material's electronic structure, transport properties, and optical characteristics, thereby influencing its anisotropic behavior along different crystallographic directions. In the case of Yb-doped GaS, the interaction between radiation and the crystal lattice can result in complex defect configurations, impacting its conductivity, mobility, and optical absorption properties [7,9].

Despite the potential applications of Yb-doped GaS in optoelectronic devices, limited research has been conducted to investigate the specific effects of radiation defects on its anisotropic behavior. Therefore, a comprehensive understanding of the interaction between radiation-induced defects and the anisotropy of Yb-doped GaS is essential for harnessing its full potential in practical applications.

In this study, we aim to explore the effect of radiation defects on the anisotropy of Yb-doped GaS single crystals. By employing advanced characterization techniques such as X-ray diffraction, photoluminescence spectroscopy, and electrical conductivity measurements, we seek to elucidate the underlying mechanisms governing the material's response to ionizing radiation. This research contributes to the fundamental understanding of semiconductor physics and facilitates the development of radiation-resistant optoelectronic devices with enhanced performance and reliability.

2. EXPERIMENTAL TECHNIQUES

The GaS and Yb doped GaS monocrystal investigated in this study was synthesized using the Bridgman–Stockbarger method at high temperatures. To ensure purity, the crucible contained materials with high degrees of purity

Cite as: R.S. Madatov, T.B. Tagiev, A.Sh. Khaligzadeh, R.M. Mamishova, East Eur. J. Phys. 1, 240 (2025), https://doi.org/10.26565/2312-4334-2025-1-25
© R.S. Madatov, T.B. Tagiev, A.Sh. Khaligzadeh, R.M. Mamishova, 2025; CC BY 4.0 license

for Ga (99.99%), S (99.999%), and Yb (0.1%). The material in the crucible was completely melted in the hot zone at 1360 K of a two-zone Bridgman furnace and then gradually transferred to the cold zone (823 K) at a speed of 1.2 mm/h. At the outset of synthesis, the furnace temperature was slowly increased to prevent potential explosions due to high temperatures. Homogenization of the melts was achieved by stirring them at the synthesis temperature through gentle shaking of the furnace, followed by cooling within the furnace. Subsequently, the resulting polycrystalline samples were sealed in conical-bottom quartz ampoules under a vacuum of better than 10^{-2} Pa.

The crystal structure and lattice parameters were determined through X-ray analysis, revealing dimensions of a = 3.54 Å, c = 16.6 Å [15]. GaS(Yb) single crystal has p-type conductivity and is $\rho \sim 10^9$ Ohm·cm. Indium was used to make ohmic contact. The electrical properties of GaS and GaS(Yb) samples were studied in the temperature range of 125-300 K, and during the measurement, the electric voltage of the sample was measured using a B7-27A voltmeter. The current generated in the crystal was recorded using a B7-30 voltmeter-electrometer amplifier.

3. DISCUSSION OF RESULTS

Figure 1 shows the dependence of electrical conductivity anisotropy on temperature (T=125-300K) of initial (curve-1) and doped with rare earth element ytterbium (Yb) GaS monocrystal (curve-2) and after irradiation (curve-3,4). It can be seen from the 1st curve in the graph that the $\sigma_{II}/\sigma_{\perp}$ ratio does not change with the increase in temperature in the interval 125-270 K in the GaS monocrystal, it decreases sharply with the subsequent increase in temperature. The existence of an interlayer potential barrier in A_3B_6 type crystals is a fact indicating that the conductivity in the σ_{II}-direction is lower than in the $\sigma_{\perp}$ - direction (Fig. 1, curve-1). The reduction of the $\sigma_{II}/\sigma_{\perp}$- ratio in the interval of 270-300 K occurs as a result of high conductivity in the $\sigma_{\perp}$ - direction. The stability of the $\sigma_{II}/\sigma_{\perp}$-ratio in the range of 125-270 K in the low-temperature region occurs as a result of thermal ionization of shallow energetic levels.

From the temperature dependence of the anisotropy of GaS monocrystal (Yb) (Figure 1, curve-2), it can be seen that the temperature range (190-210 K) where the maximum value of anisotropy is observed shifts to the lower temperature side. In the temperature range of 125-160 K, the value of anisotropy decreases depending on the temperature.The value of anisotropy increases in the next temperature range (160-210 K) and takes the maximum value at 200K.

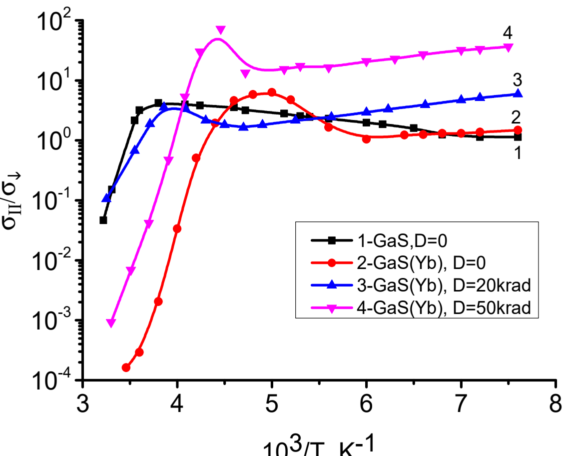

Figure 1. Temperature dependence of electrical conductivity anisotropy in GaS and GaS(Yb) monocrystals before and after irradiation

In the temperature range of 210-300 K, anisotropy sharply decreases with increasing temperature. Adding an additional Yb atom to the GaS crystal shifts the temperature corresponding to the maximum value of the $\sigma_{II}/\sigma_{\perp}$- ratio (curve-1) from 260 K to 230 K, moving it to a lower temperature region (curve-2). During the subsequent decrease in temperature, the $\sigma_{II}/\sigma_{\perp}$- ratio changes weakly. As a result of comparing perpendicular and parallel conductivity, it can be observed that during the addition, the Yb atom occupying the cation vacancy leads to a decrease in the value of the σ_{II} component directed in the parallel direction of the conductivity. Consequently, the maximum value of $\sigma_{II}/\sigma_{\perp}$ is observed at a temperature of 260 K corresponding to the V_{Yb} energy level.

The decrease in anisotropy observed in the 125-230 K temperature range in the GaS<Yb> 0.1 at % single crystal (curve-3) irradiated with a dose of D_γ = 20 krad is compared to the non-irradiated doped crystal (curve-1) and in the temperature range of 230-300 K, the anisotropy increases once again.

As can be seen from the graph, after irradiating the sample, the temperature region (190-210 K) where the maximum value of anisotropy is observed shifts to the higher temperature side. With further increase in temperature, the value of anisotropy decreases again in the temperature range of 210-300 K. When GaS(Yb) single crystal is irradiated with a dose of D_γ = 50 krad (curve-4, Fig. 1), the value of anisotropy in the temperature range of 125-200 K increases compared to (curves 1, 2 and 3). As can be seen from (Curve 4), in the temperature range of 125-220 K, the anisotropy decreases with increasing temperature, and with the subsequent increase in temperature, the anisotropy sharply increases in the temperature range of 220-230K, and it reaches its maximum value at 230 K. With further increase in temperature, the anisotropy decreases again.

A 2D (two-dimensional) [16,17] defect model was applied to clarify the results obtained from the temperature dependence of the anisotropy of the GaS single crystal doped with Yb and exposed to gamma radiation. According to the two-dimensional defect model, at the junction of the layers, the defects accumulated in the direction perpendicular to them create a potential barrier.These conditions lead to the formation of a large number of defects between the layers on the base surface of the GaS single crystal. The resulting defects form a potential barrier for charge carriers in the direction perpendicular to the layers.

The shape of the resulting potential barrier is determined by the degree of loading of defects. In relatively weak fields, the electrical conductivity in the perpendicular direction to the layers is found by the following equation:

$$\sigma_{\perp}=\sigma_{II}\frac{U}{kT^2}\exp[-\frac{U}{kT}+A\frac{U^3}{(kT^3)}], \quad (1)$$

$$A = h/24d^2um^*, \quad (2)$$

σ_{II} - the electrical conductivity of the sample in the absence of a potential barrier, U - the height of the barrier, k - Bolsman's constant, d - the width of the barrier. Let's compare the results obtained for GaS(Yb) single crystal with (curve-1).

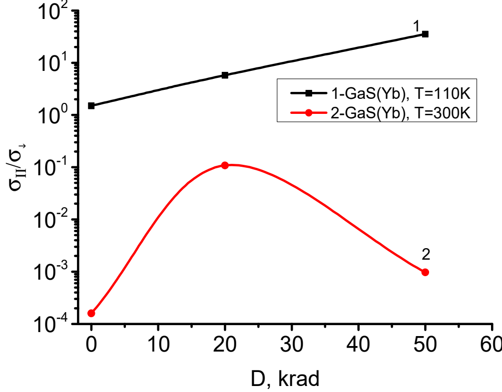

Figure 2. Dependence of the anisotropy of electrical conductivity in GaS(Yb) single crystal at different temperatures on the irradiation dose

Compared to experimental results (1), the passage of charge carriers through the potential barrier at lower temperatures (T < 200K) is tunnel-like and therefore weakly dependent on temperature.

In the temperature range of 220-300 K, the compatibility of the tunneling and activation mechanism removes the potential barrier for charge carriers, and depending on the value of A, different types of properties are revealed in the $\sigma_{II}/\sigma_{\perp} = f(T)$ curve.

Based on the obtained experimental results, the dependence of $\sigma_{II}/\sigma_{\perp} \sim f(D)$ was established at different temperatures. From the comparison of the graphs, we see that as a result of the thermal ionization of the shallow levels formed during irradiation at low temperatures, the dependence of $\sigma_{II}/\sigma_{\perp} \sim f(D)$ increases proportionally, while T = 300K has an exponential character, and as a result of the donor-acceptor interaction of deep levels, an exponential dependence is observed.

According to the obtained experimental results, it can be concluded that the high value of the anisotropy of the electrical conductivity of GaS(Yb) single crystal and their temperature activation dependence are related to the potential barrier and the accumulation of defects between the layers.

Figure 3, Figures 4 and Figure 5 show the effect of thermal annealing on the conductivity anisotropy in the GaS(Yb) crystal $[(\sigma_o-\sigma_{ot})/\sigma_o-\sigma_{krad}) \sim f(t)]$.

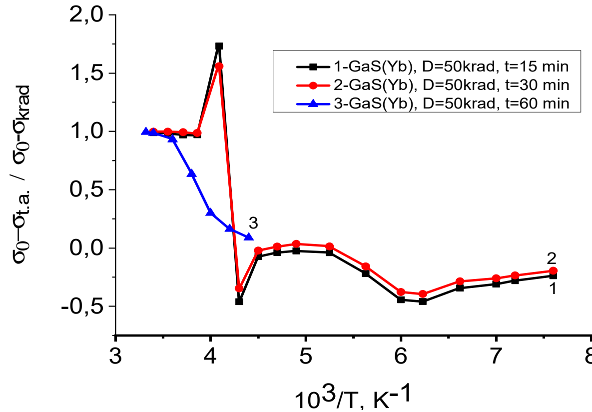

Figure 3. Temperature dependence of the $(\sigma_o/\sigma_{t.a})/(\sigma_o/\sigma_{rad})$ ratio for D = 50 rad of thermally annealed GaS(Yb) single crystal at different times (15 min, 30 min, 60 min).
σ_o – GaS(Yb) – D = 0, σ_{krad} – GaS(Yb) – D = 50 krad
$\sigma_{t.a}$ – GaS(Yb), D = 50 krad, thermal annealing at different times

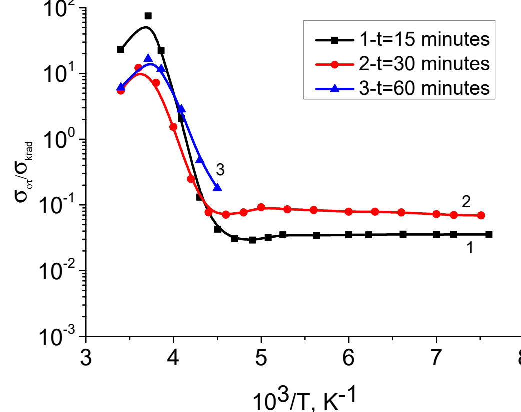

Figure 4. Temperature dependence of $(\sigma_o)/(\sigma_{krad})$ ratio of GaS(Yb) single crystal thermally annealed at different times (15 min, 30 min, 60 min) for D =50 krad:
σ_o – GaS(Yb) – D = 0; σ_{krad} – GaS(Yb) – D = 50 krad

It can be seen from Figure 3 that the ratio (σ_o-σ_{ot})/ σ_o-σ_{krad}) depends on the brewing time and consists of 4 stages. In the 1st stage, defects are settled; In the 2nd stage, the conductivity increases due to the recombination of defects, in the 3rd stage, the conductivity decreases due to the dissociation of complex defects [V_{Ga} Yb_i], and in the 4th stage, the conductivity changes weakly due to the stabilization of defects.

From the obtained results, it can be seen that the restoration of the value of electrical conductivity is complex, as the dependence varies depending on the nature and character of the defects created during exposure to ionizing rays.

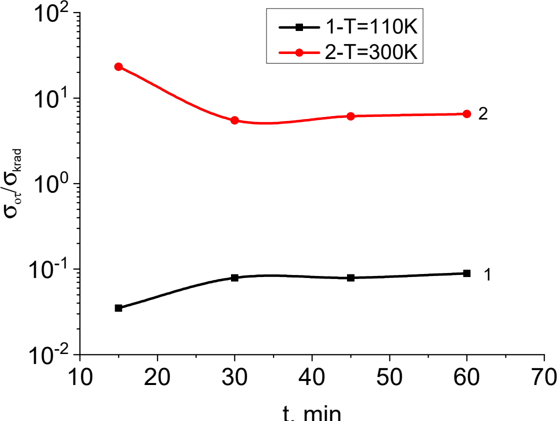

Figure 5. Dependence of the ratio (σ_o)/(σ_{krad}) of the thermally annealed GaS(Yb) single crystal at T = 110 K and 300 K for D = 50krad on the thermal annealing time. σ_o – GaS(Yb) – D = 0; σ_{krad} – GaS(Yb) – D = 50krad

CONCLUSIONS

It was found that partial filling of V_{Ga} occurs in GaS(Yb) crystal before irradiation. During irradiation, the arrangement of defects, formation of VS and complexes is observed. At high radiation doses, dissociation of complex defects occurs. During thermal annealing, the annealing process takes place in different stages depending on the rest energy of the defects. This can be explained by the fact that at the initial stage of annealing (t = 15 minutes), the amount of donor-type radiation defects is greater than the concentration of acceptor-type defects. At this stage, regrouping of defects occurs in the annealing process. During the subsequent period of brewing (15 min < t < 60min), the concentration of charge carriers increases, but the initial parameters of the sample are not restored, which is related to the formation of complex complexes in the process of reassembly of defects [V_S and V_{Ga}].

ORCID

Rahim Madatov, https://orcid.org/0000-0003-2420-2654; **Teymur Tagiev,** https://orcid.org/0009-0009-9890-8554
Aydan Khaligzade, https://orcid.org/0009-0001-6325-0440; **Rakshana Mamishova**, https://orcid.org/0000-0002-1760-8384

REFERENCES

[1] A.Z. Abasova, R.S. Madatov, and V.I. Stafeev, *Radiation-stimulated processes in chalcogenide structures*, (ELM, Baku, Azerbaijan, 2010).
[2] G. Micocci, R. Rella, P. Siciliano, and A. Tepore, "Investigation of electronic properties of gallium sulfide single crystals grown by iodine chemical transport," Journal of Applied Physics, **68**(1), 138-142 (1990). https://doi.org/10.1063/1.347105
[3] B.Q. Tagiev, A.R. Hajiev, and R.S. Madatov, "On the anisotropy of layered semiconductors GaSe and GaTe," J. Physics of the Academy of Sciences of Azerbaijan, **3**(3), 84-87 (1997). http://physics.gov.az/Dom/1997/v3article/F19970103_24.pdf (in Russian)
[4] R.H. Al-Orainy, "Growth, Characterization and Electrical Anisotropy in Layered Chalcogenide Gallium Monosulphide Single Crystals," JKAU: Sci. **22**(2), 3-12 (2010). https://www.kau.edu.sa/Files/363/Researches/64767_36125.pdf
[5] V. Augelli, V. Augelli, C. Manfredotti, and R. Murri, "Resistivity anisotropy in p-type GaSe," Nuovo Cim. **47**(1), 101-103 (1978). https://doi.org/10.1007/BF02894621
[6] P.I. Savitskii, I.V. Mintyanskii, and Z.D. Kovalyuk, "Annealing Effect on Conductivity Anisotropy in Indium Selenide Single Crystals," Physics status solidi (a), **155**(2), 451-460 (1996). https://doi.org/10.1002/pssa.2211550218
[7] R. Madatov, A. Najafov, A. Alakbarov, T. Tagiev, and A. Khaliqzadeh, "Features of electrical and photolectric properties of GaS(Yb) monocrystals," Journal of Physical Sciences, **74**(9), 1-5 (2019). https://doi.org/10.1515/zna-2018-0475
[8] R.S. Madatov, R.M. Mamishova, M.A. Mamedov, J. Ismayılov and U.V. Faradjova, "Electrophysical properties of $Pb_{1-x}Mn_xSe$ epitaxial films irradiated by γ-quanta," Turk Journal of Physics, **44**, 214–221 (2020). https://doi.org/10.3906/fiz-1906-14
[9] R.S. Madatov, T.B. Tagiev, and A.Sh. Khalygzade, "Features of the defecation mechanism in layered GaS(Yb) single crystals under irradiation with low doses of γ-quanta," Trans. Az. Nat. Acad. Sci., Physics and Astronomy, **38**(5), 90-96 (2018). http://physics.gov.az/Transactions/2018/journal2018(5).pdf (in Russian)
[10] A.S. Khaliqzadeh, "Processes Happened in the Photoelectrical Processes of GaS Monocrystal Alloyed Yb and Irradiated by γ-Rays," Works of Young Scientists, **4**(1), 37-40 (2018). https://gencalimler.az/uploads/Genc_Tedqiqatci_N2_2018.pdf (in Azerbaijan)

[11] R. Madatov, R. Mamishova, A. Abasova, and S. Alahverdiyev, "Diferential-thermal analysis and a microscopic study of the effect of γ-radiation on $CuTlSe_2$ single crystal," International Journal of Modern Physics B, **37**(30), 2350265 (2023). https://doi.org/10.1142/S021797922350265X
[12] R.S. Madatov, R.M. Mamishova, and G.B. Baylarov, "Characteristics of current injection in the narrow -band p-CuTlS single crystal," Applied Physics A, **127**, 364 (2021). https://doi.org/10.1007/s00339-021-04515-8
[13] R.S. Madatov, and R.M. Mamishova, "A study of the effect of γ-radiation on the current-carrying mechanism in the p-$CuTlS_2$ single crystal," Modern Physics Letters B, **38**(30), 2450295 (2024). https://doi.org/10.1142/S0217984924502956
[14] R.S. Madatov, T.B. Tagiev, S.A. Abushev, Sh.P. Shekili, and A.R. Mobili, "Optical and Photoelectric Properties of Gamma-Irradiated GaS:Er^{+3} Layered Crystals," Inorganic Materials, **44**(4), 333–336 (2008). https://doi.org/10.1134/S002016850804002X
[15] Y.Gutiérrez, D. Juan, S. Dicorato, G. Santos, M. Duwe, P.H. Thiesen, M.M. Giangregorio, *et al*., "Layered gallium sulfide optical properties from monolayer to CVD crystalline thin films," Optics Express, **30**(15), 27609-27622 (2022). https://doi.org/10.1364/OE.459815
[16] J. Suh, "Point Defects in Two-Dimensional Layered Semiconductors: Physics and Its Applications," PhD Thesis, University of California, Berkeley, (2015).
[17] K. Xu, L. Yin, Y. Huang, T.A. Shifa, J. Chu, F. Wang, R. Cheng, *et al*., "Synthesis, Properties and applications of 2D layered MIIIXVI (M = Ga, In; X = S, Se, Te) materials," Nanoscale, **8**, 16802-16818 (2016). https://doi.org/10.1039/C6NR05976G

ВПЛИВ ДОМІШОК ТА РАДІАЦІЙНИХ ДЕФЕКТІВ НА АНІЗОТРОПІЮ МОНОКРИСТАЛА GaS, ЛЕГОВАНОГО Yb

Р.С. Мадатов[a,b], Т.Б. Тагієв[a], А.Ш. Халігзаде[a], Р.М. Мамішова[a,c]
[a]*Інститут радіаційних проблем Міністерства науки і освіти Азербайджанської Республіки, вул. Б. Вагабзаде, 9, Баку, Азербайджан*
[b]*Кафедра прикладної та загальної фізики, Національна академія авіації, Баку, Азербайджан*
[c]*Азербайджанський університет архітектури та будівництва, вул. Айна Султанова 5, Баку, Азербайджан*

Досліджено вплив γ-квантів на анізотропію шаруватого монокристала GaS, чистого та легованого 0,1 ат.% Yb, в діапазоні температур 125-300 K. Оскільки різниця між іонним радіусом атома Yb та іонним радіусом атомів компонента відносно невелика, коли досліджуваний монокристал GaS додається з іонами ітербію, адитивний атом, ймовірно, буде розташований всередині шарів (замінюючи Ga атом або між вузлами) і в міжшаровому просторі. Розташування домішкових атомів і радіаційних дефектів у міжшаровій області шаруватого кристала GaS (Yb) послаблює анізотропні властивості кристалів, а розташування всередині шару посилює їх. Механізм протікання струму в сильних електричних полях відповідає моделі Френкеля, незалежно від природи атома домішки.

Ключові слова: *анізотропія; дефекти; домішковий атом; електропровідність; активація; термічний відпал*

East European Journal of Physics. 1. 245-249 (2025)
DOI:10.26565/2312-4334-2025-1-26 ISSN 2312-4334

INFLUENCE OF LINEAR DOPING PROFILES ON THE ELECTROPHYSICAL FEATURES OF p-n JUNCTIONS

Jo‘shqin Sh. Abdullayev
National Research University TIIAME, Department of Physics and Chemistry, Tashkent, Uzbekistan
Physical-Technical Institute of Uzbekistan Academy of Sciences, Tashkent, Uzbekistan
**Corresponding Author e-mail: j.sh.abdullayev6@gmail.com*
Received December 12, 2024; revised January 16, 2025; in final form January 21, 2025; accepted January 27, 2025

This study investigated the impact of linear graded doping concentrations on the electrophysical properties of p-n junctions based on Si and GaAs. Doping gradients ranged from $1{\cdot}10^{16}$ to $1{\cdot}10^{20}$ cm^{-4}, and the analysis was performed at temperatures between 200 K and 500 K, in 100 K increments. The Poisson equation was solved for linear doping profiles, with analytical solutions derived for both Si and GaAs materials. These solutions provided detailed insights into the electric field, potential distributions, built-in potential, and the width of the depletion region. For both materials, the built-in potential was temperature-dependent, with Si exhibiting a more significant variation due to its higher intrinsic carrier concentration. The depletion region width was influenced by both doping concentration and temperature, with GaAs showing a more pronounced variation in width, owing to its distinct material properties compared to Si. The results highlight the crucial role of doping gradients and temperature variations in shaping the performance of the linear graded p-n junctions, offering valuable implications for the design of semiconductor devices such as diodes and transistors optimized for different temperature conditions.
Keywords: *Linear graded p-n junction; Built-in potential; Electrostatic properties; Linear graded doping; Cryogenic temperatures*
PACS: 73.40. Lq, 73.61.Cw, 73.61.Ey, 72.20.Jv

INTRODUCTION

Although research on new materials for semiconductor electronic devices is expanding, silicon (Si) and gallium arsenide (GaAs) remain dominant in practical applications [1-4]. Consequently, the study of the electrostatic properties of these materials continues to be a crucial area of research [5-7]. The p-n junction, a fundamental component in semiconductor devices made from Si and GaAs, plays a pivotal role in current transfer, electrostatic characteristics, and the operation of devices across a broad range of power and temperature conditions. The performance of these devices is intricately linked to a comprehensive understanding of the operating principles of the p-n junction and the external factors that influence it [8-9]. These factors include the effects of incomplete ionization at low temperatures [10-11], the influence of geometric size [12], and other related phenomena [13].

One of the key factors affecting the behavior of p-n junctions is the doping profile, which governs the electric field and the carrier dynamics within the junction. Specifically, the impact of non-uniform doping concentration profiles on the operation of p-n junctions has been underexplored both analytically and experimentally. Traditionally, p-n junctions have been studied with uniform or step-function doping profiles; however, these idealized models do not always capture the complexities of real-world devices, particularly those operating under extreme conditions. Experimental studies [14-18] suggest that non-uniform doping profiles, such as linear grading, can significantly influence the electrostatic properties and overall performance of p-n junctions. Nevertheless, this area remains insufficiently investigated and warrants more in-depth analysis.

Linear graded p-n junctions, in which the doping concentration varies gradually and linearly across the junction, offer distinct advantages over both uniform and non-uniform doping profiles [19]. In these junctions, the gradual transition between the p-type and n-type regions results in a more uniform built-in electric field, which reduces carrier recombination and improves charge carrier collection efficiency [20-23]. This characteristic makes linear graded p-n junctions particularly beneficial for applications such as solar cells, photodetectors, light-emitting diodes (LEDs), and power devices, where efficiency and performance are closely tied to the smooth distribution of charge carriers. Moreover, the gradual change in doping concentration can lower the breakdown voltage, enhance device reliability, and improve high-speed performance.

However, the theoretical understanding of the electrostatic properties of linear graded p-n junctions, particularly regarding their temperature dependence, remains limited. To address this gap, this article focuses on the analytical investigation of the electrostatic properties of linear graded p-n junctions made from Si and GaAs, studied over a wide temperature range. By examining the effects of linear grading on the electric field, potential distribution, and depletion region, this research aims to provide a deeper understanding of how doping profiles influence device performance. Additionally, this study will explore how external factors, such as temperature and geometric size, interact with the doping profile to affect the behavior of p-n junctions in real-world applications. The insights gained from this research could lead to improved design strategies for a variety of semiconductor devices, particularly in environments where high efficiency, reduced recombination, and stable operation over temperature are crucial.

Cite as: J.Sh. Abdullayev, East Eur. J. Phys. 1, 245 (2025), https://doi.org/10.26565/2312-4334-2025-1-26
© J.Sh. Abdullayev, 2025; CC BY 4.0 license

MATERIAL AND METHODS

In fact, p-n junctions are formed by combining p-type and n-type semiconductors through processes like diffusion, ion implantation, epitaxial growth, or alloying, with precise control of doping and structure quality. The junction's unique properties arise from the depletion region created by carrier recombination, enabling applications in forward and reverse bias modes, including advanced structures like radial and heterojunctions. Uniform doping profiles are formed by evenly distributing dopants through methods like ion implantation or epitaxial growth, ensuring consistent electrical properties. Nonuniform profiles are created by varying dopant concentration using graded diffusion or selective implantation, enabling tailored device performance. As highlighted in the Introduction, this article addresses the problem of p-n junctions with non-uniform doping concentrations, which have not been extensively studied.

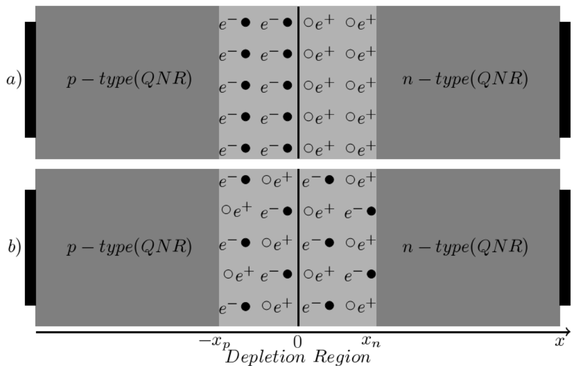

Figure 1. Schematic representation of a 2D cross-section of the modeled planar p-n junction: a) uniform doping profile, and b) non-uniform doping profile

Figure 1 illustrates a planar p-n junction with: a) a uniform doping profile, and b) a non-uniform doping profile, highlighting distinct characteristics in current transfer mechanisms and electrostatic distributions between the two cases. The depletion region extends from $-x_p$ to x_n, with its width denoted as W, linear graded p-n junction specific to the junction structure and as expressed: $\left|-x_p\right| = \left|-\frac{W}{2}\right| = x_n = \frac{W}{2}$. To identify these unique properties, it is essential to solve the Poisson equation for each specific case. To simplify finding solutions, approximations are applied, but only for the low injection case. The Poisson equation for the low injection case is written as equation (1).

$$\frac{dE(x)}{dx} = -\frac{d^2\varphi(x)}{dx^2} = \frac{q}{\varepsilon\varepsilon_0}\cdot\left(N_D(x) - N_A(x)\right). \tag{1}$$

Where $E(r)$ represents the electric field, ε denotes the permittivity of the semiconductor material, for Si ε is 11.9, for GaAs ε is 12.9, $\varepsilon_0 = 8.85\cdot10^{-12}$ F·m^{-1} vacuum permittivity. The linear doping profile can be represented as (2):

$$N_D(x) - N_A(x) = a\cdot x \tag{2}$$

If the width of the depletion region is non-uniform, as in case b), the acceptor doping concentrations $N_A(x)$ and donor doping concentrations $N_D(x)$ are expressed qualitatively as functions of distance. a is the doping gradient. These expressions are solved together under boundary conditions $E(-x_p) = 0$ and $E(x_n) = 0$, for the depletion region, the distribution of the electric field is given by equation (3a), while for other regions, the electric field distribution is described by equation (3b).

$$E(-x_p < x < x_n) = \frac{q\cdot a}{2\varepsilon\varepsilon_0}\cdot\left(x^2 - \left(x_n\right)^2\right), \tag{3a}$$

$$E(x \le -x_p,\, x_n \ge x) = 0\,. \tag{3b}$$

Along with the electric field distribution, it is also important to determine the electrostatic potential distribution. Using the following expression $\varphi(x) = -\int E(x)dx$ and $\varphi(x \le -x_p) = 0$, $\varphi(x \ge x_n) = \varphi_{bi}(T) - U_{p-n}$ initial conditions, the electrostatic potential is obtained from expression (4). The built-in potential is represented by $\varphi_{bi}(T)$, and the external source voltage is represented by U_{p-n}.

$$\varphi(-x_p < x < x_n) = \frac{q\cdot a}{6\varepsilon\varepsilon_0}\cdot\left(x^3 - 3x_n^2\cdot x\right). \tag{4}$$

Using the selected initial conditions, the width of the depletion region was determined and is expressed by equation (5). From equation (5), it can be seen that the width of the depletion region depends on temperature, built-in potential, and the doping gradient.

$$W = \sqrt[3]{\frac{24\varepsilon\varepsilon_0}{q \cdot a} \cdot \left(\varphi_{bi}(T) - U_{p-n}\right)}. \quad (5)$$

Another important parameter is the built-in potential, expressed by equation (6) for a linearly graded doping concentration in a p-n junction.

$$\varphi_{bi}(T) = \frac{2kT}{q} \cdot \ln\left(\frac{a \cdot x_n}{n_i(T)}\right). \quad (6)$$

Where k is the Boltzmann constant, T is the temperature, q is the charge of an electron, $n_i(T)$ is the intrinsic carrier concentration of the semiconductor. At 300 K (room temperature), the intrinsic carrier concentration of Si is approximately $n_i(300) = 1.5 \cdot 10^{10}\ cm^{-3}$, for GaAs approximately $n_i(300) = 1.7 \cdot 10^{6}\ cm^{-3}$. The results derived from the above analytical expressions are presented and analyzed in the “Results and Discussion” section.

RESULTS AND DISCUSSION

The results presented and analyzed in this section correspond to temperatures ranging from 200 K to 500 K in 100 K increments, with a doping gradient spanning from $1 \cdot 10^{16}\ cm^{-4}$ to $1 \cdot 10^{20}\ cm^{-4}$. In Figure 2, the width of the depletion region of a linearly graded p-n junction made of Si material depends on the doping gradient at different temperatures.

In silicon (Si), the doping gradient remains largely unchanged as temperature increases from 200K to 500K. However, the carrier concentration increases with temperature, affecting the material's conductivity and recombination rates. The depletion region width decreases linearly with increasing doping concentration, as a higher doping concentration strengthens the electric field, reducing the width of the depletion region. Gallium Arsenide (GaAs) is a high-performance semiconductor with a direct bandgap of 1.42 eV, making it ideal for optoelectronic applications like LEDs and laser diodes. It has high electron mobility, which enables fast switching in high-speed electronics, but lower thermal conductivity than silicon. GaAs is widely used in high-frequency devices, such as radar and satellite communications, but its higher cost and fabrication complexity limit its use compared to silicon. In Figure 3, the width of the depletion region of a linearly graded p-n junction made of GaAs material depends on the doping gradient at different temperatures.

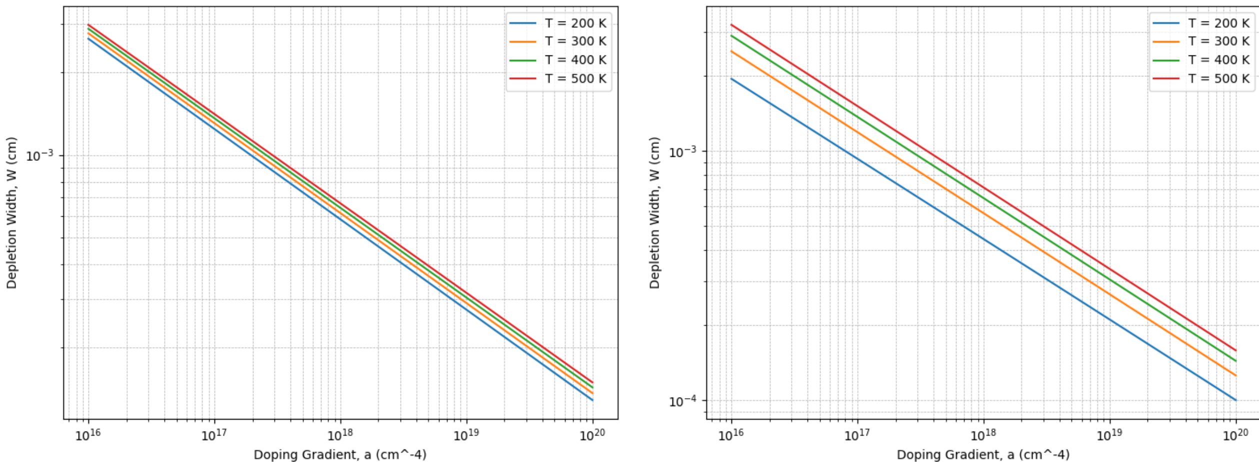

Figure 2. The width of the depletion region in a linearly graded p-n junction based on Si as a function of the doping gradient at different temperatures

Figure 3. The width of the depletion region in a linearly graded p-n junction based on GaAs as a function of the doping gradient at different temperatures

Compared to Si, GaAs undergoes more significant changes as the temperature increases from 200 K to 500 K. In both materials, the depletion region width decreases linearly with increasing doping concentration. In Si, the depletion region width changed from 22 µm to 5.8 µm, while in GaAs, it changed from 83.4 µm to 0.833 µm. At 200 K, the depletion region width changes from 22 µm for $1 \cdot 10^{16}\ cm^{-4}$ to 5.8 µm for $1 \cdot 10^{20}\ cm^{-4}$. As temperature increases, the width decreases further, with similar trends observed at 300K, 400K, and 500K, showing a more pronounced reduction with higher doping concentrations.

Figure 4 demonstrates that the built-in potential of a linearly graded p-n junction based on GaAs increases consistently with both temperature and doping concentration. At 200 K, the built-in potential ranges from 1.187 V to 1.23 V. At 300 K, it increases to a range of 1.2187 V to 1.46 V. At 400 K, the range shifts to 1.387 V to 1.653 V, and at

500K, it varies between 1.527 V and 1.86 V. This trend clearly indicates a consistent increase in the built-in potential with rising temperature and doping concentration. Similarly, the width of the depletion region in the Si-based linearly graded p-n junction decreases as the doping gradient increases from $1\cdot10^{16}\ cm^{-4}$ to $1\cdot10^{20}\ cm^{-4}$ across temperatures ranging from 200K to 500K. As temperature increases, the width decreases further, with similar trends observed at 300K, 400K, and 500K, showing a more pronounced reduction with higher doping concentrations. Figure 5 illustrates that the built-in potential of a linearly graded p-n junction based on Si increases with both temperature and doping concentration. At 200K, the built-in potential ranges from 0.78 V to 0.923 V. At 300 K, it increases to a range of 0.9321 V to 1.123 V. At 400K, the range extends from 1.038 V to 1.26 V, and at 500 K, it varies between 1.082 V and 1.41 V. This shows a consistent increase with both temperature and doping concentration. Similarly, the width of the depletion region in the GaAs-based linearly graded p-n junction decreases as the doping gradient increases from $1\cdot10^{16}\ cm^{-4}$ to $1\cdot10^{20}\ cm^{-4}$, across temperatures ranging from 200K to 500K.

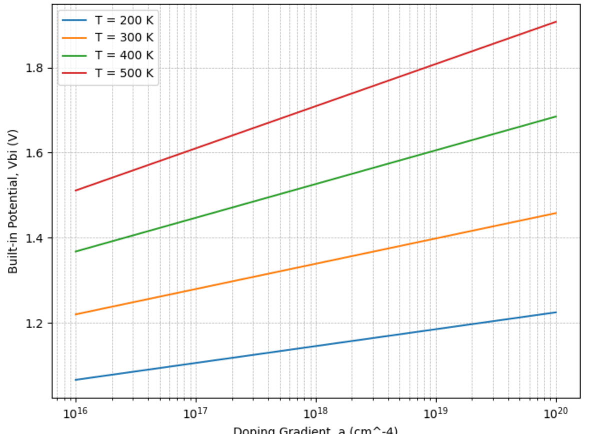

Figure 4. The built-in potential of a linearly graded p-n junction based on GaAs as a function of the doping gradient at different temperatures

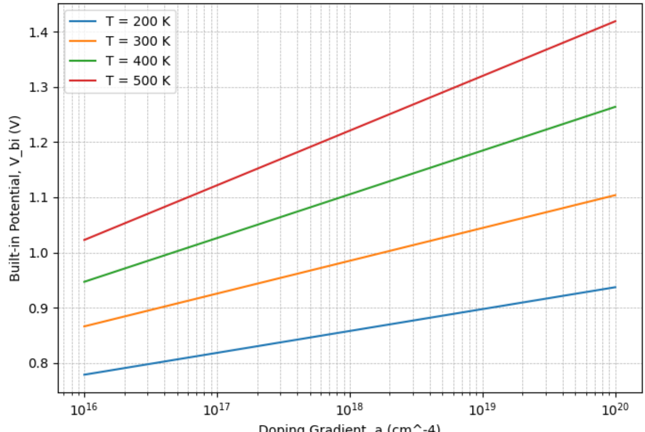

Figure 5. The built-in potential of a linearly graded p-n junction based on Si as a function of the doping gradient at different temperatures

For GaAs, the impact of the doping gradient on the depletion region width is more prominent at higher doping concentrations compared to Si. Across the temperature range of 200 K to 500 K, the depletion region width exhibits significant variation, with more substantial changes occurring at higher doping gradients. At low doping concentrations, the temperature dependence is relatively minor, whereas at high doping concentrations, the depletion width decreases sharply with increasing temperature, demonstrating a more pronounced effect than in Si. This highlights GaAs's greater sensitivity to both temperature and doping concentration, particularly at elevated doping gradients. The built-in potential of the GaAs-based junctions increases consistently with both doping concentration and temperature, ranging from 1.187 V at 200K to 1.86V at 500K for doping concentrations between $1\cdot10^{16}\ cm^{-4}$ and $1\cdot10^{20}\ cm^{-4}$. In comparison, the built-in potential for Si-based junctions ranges from 0.78V to 1.41V across the same temperature and doping concentration range. Additionally, the width of the depletion region in both materials decreases with increasing doping concentration, but this effect is much more pronounced in GaAs, with changes from 83.4 μm to 0.833 μm at temperatures ranging from 200K to 500K. In contrast, Si shows smaller variations, with the depletion width changing from 22 μm to 5.8 μm over the same temperature range.

CONCLUSIONS

In conclusion, this study provides a comprehensive analysis of the electrostatic properties of linearly graded p-n junctions based on Si and GaAs, with a focus on the effects of doping gradients and temperature variations. The results reveal distinct behaviors between GaAs and Si, with GaAs exhibiting a more pronounced dependence on temperature and doping concentration. At higher doping concentrations, GaAs shows a more significant reduction in the depletion region width with increasing temperature, highlighting its greater sensitivity compared to Si. This behavior underscores GaAs's heightened sensitivity to temperature fluctuations and doping gradients, especially at high doping levels.

The study emphasizes the pivotal role of doping gradients and temperature in shaping the electrostatic properties of p-n junctions. GaAs, with its superior electron mobility and direct bandgap, offers enhanced performance for high-frequency and optoelectronic applications. However, its increased sensitivity to temperature and doping concentration presents both challenges and opportunities for device optimization. In contrast, Si remains more stable with respect to temperature changes, making it a more predictable material, but it may not achieve the same performance levels in specialized applications. These findings are crucial for the design of semiconductor devices, particularly in applications where efficiency, reduced recombination, and stable operation across varying temperatures are critical. The insights gained can inform the optimization of p-n junctions for a range of devices, such as LEDs, photodetectors, and power devices, ensuring improved performance and reliability in diverse operating environments.

ORCID
Jo'shqin Sh. Abdullayev, https://orcid.org/0000-0001-6110-6616

REFERENCES

[1] R. Ragi, R.V.T. da Nobrega, U.R. Duarte, and M.A. Romero, IEEE Trans. Nanotechnol. **15**(4), 627 (2016). https://doi.org/10.1109/TNANO.2016.2567323
[2] E. Gnani, A. Gnudi, S. Reggiani, and G. Baccarani, IEEE Trans. Electron Devices, **58**(9), 2903 (2011). https://doi.org/10.1109/TED.2011.2159608
[3] Z. Arefinia, and A. Asgari, Solar Energy Materials and Solar Cells, **137**, 146 (2015). https://doi.org/10.1016/j.solmat.2015.01.032
[4] O.V. Pylypova, A.A. Evtukh, P.V. Parfenyuk, I.I. Ivanov, I.M. Korobchuk, O.O. Havryliuk, and O.Yu. Semchuk, Opto-Electronics Review, **27**(2), 143 (2019). https://doi.org/10.1016/j.opelre.2019.05.003
[5] J.Sh. Abdullayev, and I.B. Sapaev, East Eur. J. Phys. (4), 329 (2024). https://doi.org/10.26565/2312-4334-2024-4-37
[6] R.D. Trevisoli, R.T. Doria, M. de Souza, S. Das, I. Ferain, and M.A. Pavanello, IEEE Trans. Electron Devices, **59**(12), 3510 (2012). https://doi.org/10.1109/TED.2012.2219055
[7] J.S. Abdullayev, and I.B. Sapaev, East European Journal of Physics, (3), 344-349 (2024). https://doi.org/10.26565/2312-4334-2024-3-39R
[8] B. Pal, K.J. Sarkar, and P. Banerji, Solar Energy Materials and Solar Cells, **204**, 110217 (2020). https://doi.org/10.1016/j.solmat.2019.110217
[9] J.Sh. Abdullayev, and I.B. Sapaev, Eurasian Physical Technical Journal, **21**(3), 21 (2024). https://doi.org/10.31489/2024No3/21-28
[10] P. Dubey, B. Kaushik, and E. Simoen, IET Circuits, Devices & Systems, **13**(6), 6763 (2019). https://doi.org/10.1049/iet-cds.2018.5169
[11] M.-D. Ko, T. Rim, K. Kim, M. Meyyappan, and C.-K. Baek, Scientific Reports, **5**(1), 11646 (2015). https://doi.org/10.1038/srep11646
[12] J. Abdullayev, and I. Sapaev, Physical Sciences and Technology, **11**(3-4), 39 (2024). https://doi.org/10.26577/phst2024v11i2b05
[13] A.M. de Souza, D.R. Celino, R. Ragi, and M.A. Romero, Microelectronics J. **119**, 105324 (2021). (https://doi.org/10.1016/j.mejo.2021.105324).
[14] L.O. Olimov, Semiconductors, **46**(7), 898 (2012). https://doi.org/10.1134/S1063782612070159
[15] L. Olimov, and I. Anarboyev, Silicon, **14**, 3817 (2022). https://doi.org/10.1007/s12633-021-01596-1
[16] L.O. Olimov, Appl. Sol. Energy, **46**, 118 (2010). https://doi.org/10.3103/S0003701X1002009X
[17] J.Sh. Abdullayev, I.B. Sapaev, and Kh.N. Juraev, Low Temp. Phys. **51**, 60 (2025) https://doi.org/10.1063/10.0034646
[18] M.C. Putnam, S.W. Boettcher, M.D. Kelzenberg, D.B. Turner-Evans, J.M. Spurgeon, E.L. Warren, *et al*., Energy & Environmental Science, **3**(8), 1037 (2010). https://doi.org/10.1039/C0EE00014K
[19] R. Elbersen, R.M. Tiggelaar, A. Milbrat, G. Mul, H. Gardeniers, and J. Huskens, Advanced Energy Materials, **5**(6), 1401745 (2014). https://doi.org/10.1002/aenm.201401745
[20] I. Sapaev, B. Sapaev, D. Abdullaev, J. Abdullayev, A. Umarov, R. Siddikov, A. Mamasoliev, *et al*., E3S Web of Conferences, **383**, 04022 (2023). https://doi.org/10.1051/e3sconf/202338304022
[21] L.O. Olimov, "Adsorption of alkali metals and their effect on electronic properties of grain boundaries in bulk of polycrystalline silicon," Semiconductors, **44**, 602 (2010). https://doi.org/10.1134/S106378261005009X
[22] L.O. Olimov, Appl. Sol. Energy, **44**, 142 (2008). https://doi.org/10.3103/S0003701X08020187
[23] L. Olimov, and I. Anarboyev, AIP Conf. Proc. **3244**, 060015 (2024). https://doi.org/10.1063/5.0242092

ВПЛИВ ЛІНІЙНИХ ПРОФІЛІВ ЛЕГУВАННЯ НА ЕЛЕКТРОФІЗИЧНІ ОСОБЛИВОСТІ P-N-ПЕРЕХОДІВ

Джошкін Ш. Абдуллаєв
Національний дослідницький університет ТІІАМЕ, фізико-хімічний факультет, Ташкент, Узбекистан
Фізико-технічний інститут Академії наук Узбекистану, Ташкент, Узбекистан

У цій роботі досліджено вплив лінійного градієнта концентрації легування на електрофізичні властивості p-n переходів на основі Si і GaAs. Градієнти легування становили від $1 \cdot 10^{16}$ до $1 \cdot 10^{20}$ см$^{-4}$, а аналіз проводили при температурах від 200 K до 500 K з кроком 100 K. Рівняння Пуассона було розв'язане для лінійних профілів легування, а аналітичні рішення отримані для матеріалів Si і GaAs. Ці розв'язки дали детальне уявлення про електричне поле, розподіл потенціалів, вбудований потенціал і ширину області виснаження. Для обох матеріалів вбудований потенціал залежав від температури, причому Si демонстрував більш значну зміну через вищу концентрацію власних носіїв. На ширину області збіднення впливають як концентрація легування, так і температура, причому GaAs демонструє більш виражену варіацію ширини, що пояснюється його відмінними властивостями порівняно з Si. Отримані результати підкреслюють вирішальну роль градієнтів легування і температурних варіацій у формуванні характеристик лінійних градуйованих p-n переходів, пропонуючи цінні висновки для проектування напівпровідникових приладів, таких як діоди і транзистори, оптимізованих для різних температурних умов.

Ключові слова: *лінійний градуйований p-n перехід; вбудований потенціал; електростатичні властивості; лінійне градуйоване легування; кріогенні температури*

East European Journal of Physics. **1.** 250-255 (2025)
DOI:10.26565/2312-4334-2025-1-27 ISSN 2312-4334

OPTICAL PERFORMANCE AND CRYSTAL STRUCTURE OF TiO_2 THIN FILM ON GLASS SUBSTRATE GROWN BY ATOMIC LAYER DEPOSITION

Temur K. Turdaliev
Arifov Institute of Ion-Plasma and Laser Technologies of Uzbekistan Academy of Sciences
100125, Durmon Yuli st. 33, Tashkent, Uzbekistan
Corresponding Author e-mail: turdaliev@iplt.uz
Received September 9, 2024; January 16, 2025; accepted January 20, 2025

This study investigates the formation of the optical properties and crystal structure of TiO_2 thin films, with a thickness of approximately 1.5 micrometers, grown on a glass substrate using the atomic layer deposition method with titanium tetraisopropoxide and water as precursors. X-ray diffraction and Raman spectroscopy analyses confirmed that the TiO_2 films crystallize in the anatase polymorphic phase. The films exhibit a nanocrystalline structure with an average crystallite size of approximately 28 nanometers, as established by X-ray diffraction measurements. The X-ray diffraction pattern revealed distinct peaks at 2θ angles of 25.3°, 38.6°, 48.0°, 55.0°, and 70.4°, corresponding to the (101), (112), (020), (121), and (220) crystallographic planes, while the Raman spectra exhibited pronounced peaks at frequencies of 143, 194, 392, 514, and 637 cm^{-1}, all characteristic of the anatase phase of TiO_2. The Tauc method applied to the absorption spectra of the thin film showed that it has a direct bandgap of 3.2 eV and an indirect bandgap of 2.3 eV.
Keywords: *Titanium dioxide thin films; Atomic layer deposition; Anatase phase; X-ray diffraction; Raman spectroscopy; Bandgap energy; Optical properties; Urbach energy; Nanocrystalline structure*
PACS: 78.66.-w, 68.55.Jk, 78.30.-j, 73.61.Ng

INTRODUCTION

In recent years, there has been significant interest in TiO_2 due to its unique properties, including high chemical stability, low toxicity, and a variety of structural phases [1–3]. One of the key features of TiO_2 is its ability to actively absorb ultraviolet radiation while remaining transparent in the visible spectrum, making it an ideal material for optoelectronic applications. The optical properties of TiO_2 are determined by its crystalline phase, particle size, and the presence of defects, which can affect light transmission and absorption [4, 5]. The bandgap width of TiO_2 varies depending on the synthesis method and ranges from 2.6 to 3.3 eV [6, 7]. Due to these characteristics, the material is promising for the creation of optoelectronic devices. In particular, the optical properties of TiO_2 allow for enhanced light absorption in solar cells, which improves energy conversion efficiency [8]. Additionally, its application as a material for heterojunction solar cells opens up further possibilities for the development of highly efficient photovoltaic systems [9]. In addition to solar cells, TiO_2 thin films have found widespread applications in a range of advanced technologies. TiO_2 films are also extensively can used in self-cleaning surfaces due to their photocatalytic activity, where under ultraviolet light, they can break down organic contaminants, making them ideal for use in building materials, glass coatings, and environmental purification [10, 11]. Moreover, TiO_2 thin films serve as efficient dielectric layers in capacitors and as gate insulators in field-effect transistors due to their excellent insulating properties [12]. In gas sensor technology, the sensitivity of TiO_2 to various gases, such as hydrogen, makes it a valuable material for detecting pollutants and hazardous gases in the environment [13]. Another promising application is in photocatalytic water splitting for hydrogen production, where TiO_2 acts as a photoanode, contributing to sustainable energy solutions. Thin TiO_2 films can also be used as buffer layers, particularly for the catalytic growth of carbon nanotubes [14, 15]. The combination of optical transparency, photocatalytic activity, and chemical stability also makes TiO_2 thin films suitable for use in medical devices and antibacterial coatings, adding to their versatility across multiple industries.

There are numerous methods for obtaining thin films of TiO_2, including the sol-gel method [6], reactive magnetron sputtering [16], solvothermal synthesis [17, 18], and atomic layer deposition (ALD) [19]. These methods make it possible to form films with various morphologies, ranging from nanoparticles [20] to nanotubes [21, 22] and nanorods [23], allowing the material's properties to be adapted to specific tasks depending on the field of application.

In this work, we study the features of the formation of optical properties and the crystalline structure of a titanium dioxide thin film obtained by the ALD method using titanium tetraisopropoxide (TTIP) and water as precursors. A comprehensive structural analysis was carried out, as well as an investigation of the film's optical properties using absorption spectroscopy at room temperature.

EXPERIMENT

TiO_2 was deposited onto a pre-prepared glass substrate using the thermal ALD method on an SI PEALD system (SENTECH Instruments GmbH). During the deposition process, TTIP and water were used as the primary precursors, while nitrogen was employed as both the carrier and purging gas.

Cire as: T.K. Turdaliev, East Eur. J. Phys. 1, 250 (2025), https://doi.org/10.26565/2312-4334-2025-1-27
© T.K. Turdaliev, 2025; CC BY 4.0 license

The deposition parameters were as follows: nitrogen flow rate was 120 cm³/min, reactor pressure was approximately 60 Pa, substrate temperature was around 225°C, and each cycle duration was 8 seconds. The process consisted of 5 steps in the following sequence: an initial purge; introduction of TTIP for 0.5 seconds; nitrogen purging for 3 seconds; introduction of H_2O for 1.5 seconds; and final nitrogen purging for 3 seconds. Under these conditions, the growth rate per cycle was 0.2 nm, and the deposition process was carried out for 7500 cycles. As a result, a sample with a TiO_2 film thickness of 1500 nm was obtained. A visual representation of the titanium dioxide film deposition process by the ALD method is shown in Figure 1.

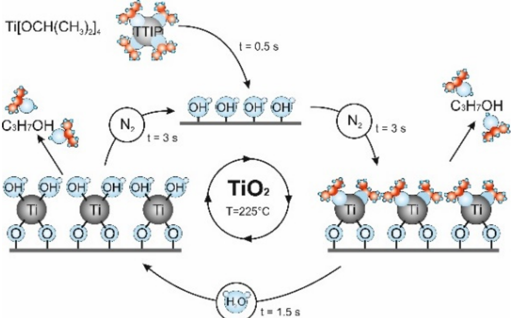

Figure 1. Schematic diagram of the ALD process of TiO_2 on a glass substrate

XRD Structural Analysis

TiO_2 can exist in three crystalline forms: the stable rutile phase and two metastable phases—anatase and brookite [3]. Both rutile and anatase have a tetragonal structure but differ in lattice parameters and space groups. Rutile is more stable at high temperatures, whereas anatase and brookite form at lower temperatures and transform into rutile upon heating. Each of these phases possesses unique optical and structural characteristics, making them suitable for various technological applications.

X-ray diffraction analysis of the samples was carried out using a PANalytical Empyrean diffractometer, confirming the formation of the TiO_2 film in the anatase polymorph after the deposition process. As shown in Figure 2, the diffraction pattern of the freshly deposited sample exhibits clear peaks characteristic of the anatase phase of TiO_2 at 2θ angles: 25.3°, 38.6°, 48.0°, 55.0°, and 70.4°, corresponding to the (101), (112), (020), (121), and (220) crystallographic planes of anatase. Additionally, no reflections characteristic of other TiO_2 polymorphs, such as rutile or brookite, were observed, confirming the purity of the anatase phase [6, 24].

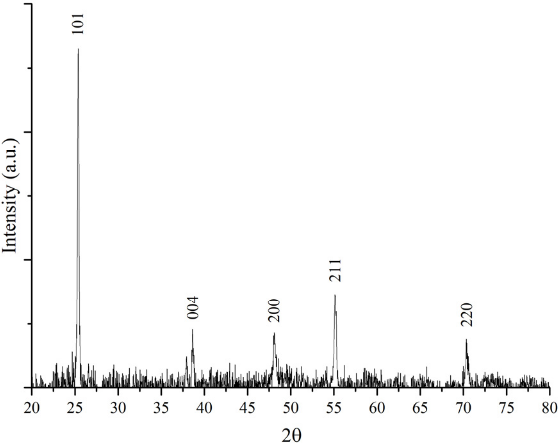

Figure 2. X-ray diffraction pattern of the TiO_2 film. Characteristic reflections for the anatase phase of titanium dioxide are observed at 2θ angles: 25.3° (101), 38.6° (004), 48.0° (200), 55.0° (211), and 70.4° (220)

The interplanar spacing of the crystal (d) was calculated based on the obtained diffraction patterns using Bragg's equation [6]:

$$d = \frac{n\lambda}{2sin\theta} \tag{1}$$

where d is the interplanar spacing between atomic planes, n = 1 is the order of diffraction, λ = 1.5406 Å represents the wavelength for CuKα radiation, and θ is the diffraction angle.

The obtained d values were subsequently used to calculate the crystal lattice parameters. For the tetragonal structure, the lattice parameters a and c were determined using the following equation:

$$\frac{1}{d^2} = \frac{h^2+k^2}{a^2} + \frac{l^2}{c^2} \tag{2}$$

h, k, and *l* are the Miller indices for the corresponding crystallographic planes, and *a* and *c* are the lattice parameters. The calculated lattice parameters were $a = 0.3785$ nm and $c = 0.9513$ nm, which are in agreement with the literature values for the anatase phase of TiO_2 [21].

The average crystallite size was calculated using the Scherrer formula [6, 25]:

$$D = \frac{K\lambda}{\beta cos\theta} \tag{3}$$

where D is the average crystallite size, K is the Debye-Scherrer constant, λ is the wavelength of CuKα radiation equal to 0.15406 nm, β is the full width at half maximum (FWHM) of the peak, and θ is the Bragg angle.

Five peaks corresponding to different crystallographic planes were selected for the calculation, and β values (FWHM) were measured for each. The crystallite sizes of TiO_2 were approximately 44.36 nm at the 2θ = 25.36° peak, 30.93 nm at 2θ = 38.63°, 18.15 nm at 2θ = 48.13°, 25.02 nm at 2θ = 55.16°, and 17.21 nm at 2θ = 70.41°. Therefore, the average crystallite size of TiO_2, calculated as the arithmetic mean, was approximately 28 nm.

Structural Analysis by Raman Scattering

The structure of the resulting film was investigated using an InVia Raman spectrometer with a resolution ≤ 0.5 cm^{-1} in the visible range. The Raman scattering spectra of the deposited TiO_2 film, presented in Figure 3, show well-defined peaks at frequencies of 143, 194, 392, 514, and 637 cm^{-1}. These bands were identified through factor group analysis. It is known that the Raman spectrum of the anatase phase of TiO_2 contains six active modes with peaks at 144, 194, 397, 517, 513, and 639 cm^{-1} [26, 27], corresponding to the symmetries 1A1g, 2B1g, and 3Eg.

The peaks at frequencies 143, 194, and 637 cm^{-1} are associated with the Eg phonon modes, while the peak at 394 cm^{-1} corresponds to the B1g mode. The Raman line at 514 cm^{-1} represents a doublet composed of vibrational modes A1g and B1g [28]. For the rutile phase, four active Raman modes with symmetries B1g, Eg, A1g, and B2g are typically observed at frequencies 144, 243, 447, and 612 cm^{-1}. Based on the data from [26-28], it can be concluded that the Raman spectrum confirms that the crystalline structure of the film is the anatase polymorph of TiO_2.

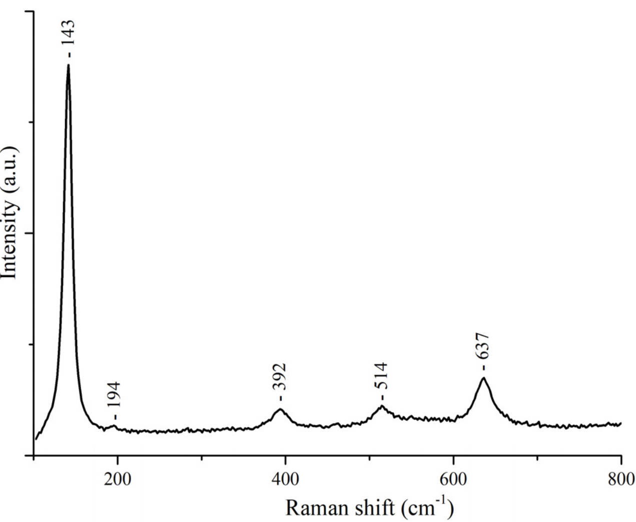

Figure 3. Raman scattering spectrum of the TiO_2 film, showing characteristic peaks of the anatase phase at frequencies of 143, 194, 392, 514, and 637 cm^{-1}

Optical Absorption Spectrum Analysis of the Film

The absorption spectra in the range of 200-1000 nm were investigated using a Shimadzu UV-3600i Plus spectrometer. The absorption coefficient was calculated for the 1500 nm thick film based on the Bouguer-Lambert-Beer law using the following formula:

$$\alpha = \frac{2.303A(\lambda)}{d} \tag{4}$$

where A(λ) is the absorption value corresponding to the wavelength, and d is the film thickness in centimeters.

Figure 4 presents the spectrum of the calculated absorption coefficient, which shows that the film absorbs in the ultraviolet range and is transparent in the visible range. A sharp decline in the absorption coefficient begins around 350-400 nm, corresponding to the material's intrinsic absorption edge. The absorption edge exhibits an exponential dependence on photon energy, indicating a high Urbach energy level. According to [29, 30], this may suggest that the film is a polycrystal with randomly oriented grains. This phenomenon can be explained by the Volmer-Weber crystallization mechanism during the film formation on the substrate, likely due to the lack of chemical bonding between the precursors and the substrate at the initial stage of the process. It could also be a result of quantum size effects caused

by the nanoscale structure. Furthermore, the increase in Urbach energy in such films is often associated with the formation of oxygen vacancies and other defects, which leads to the broadening of absorption tails and a decrease in the crystallinity of the material [31, 32].

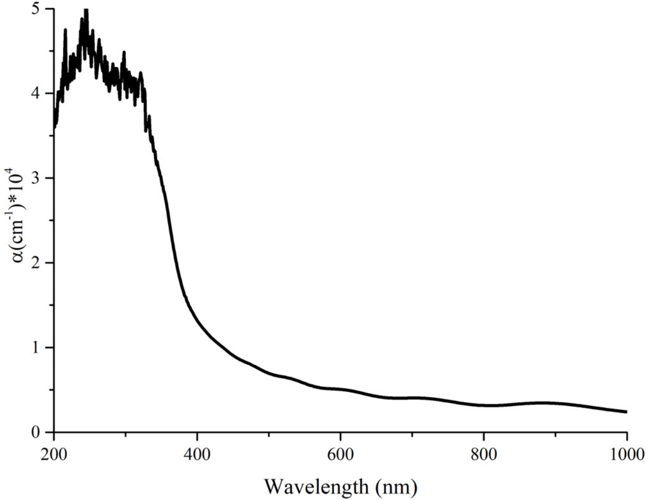

Figure 4. Absorption coefficient of the TiO_2 film in the 200–1000 nm range

The optical bandgap was determined using the Tauc function [19, 29, 30], based on the obtained absorption coefficient α using the following expression:

$$(\alpha h\nu)^n = A\,(h\nu - Eg) \qquad (5)$$

where A is a material-dependent constant, Eg is the bandgap energy of the semiconductor, hv is the photon energy, and n is a variable that can take different values depending on the type of electronic transition. Specifically, for an allowed indirect transition, n=1/2, and for an allowed direct transition n=2 [29].

For nanostructured TiO_2 films and nanoparticles, both direct and indirect transitions are possible, which can be explained by their quantum confinement effects and altered electronic structure compared to macroscopic samples. Depending on the size of the nanoparticles and their crystalline structure, an increase or decrease in the bandgap width can be observed, which may be associated, for instance, with the appearance of defects such as oxygen vacancies in the TiO_2 crystallite structure.

The extrapolation of the linear segments of the $(\alpha h\nu)^n$ curves to their intersection with the abscissa (Figure 5) allowed us to estimate the indirect bandgap as 2.3 eV and the direct bandgap as 3.2 eV. Therefore, the presence of linear segments for both transitions indicates that the absorption edge in the TiO_2 film is formed by both direct and indirect allowed interband transitions.

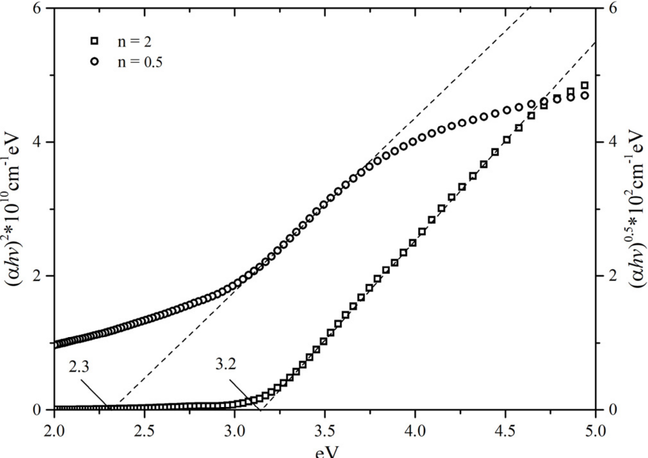

Figure 5. Determination of the bandgap width in the studied film. The square symbols represent the Tauc plot for direct interband transitions, while the circular symbols indicate the plot for indirect transitions.

CONCLUSION

The structural analysis results obtained through XRD and Raman spectroscopy confirm that titanium dioxide films crystallize in the anatase polymorphic phase under thermal ALD conditions. The films exhibit a nanocrystalline structure

with an average crystallite size of approximately 28 nm, as determined from the XRD data. Raman spectroscopy further revealed phonon modes characteristic of anatase, thereby verifying the presence of this phase within the films. The exponential shape observed at the absorption edge suggests a degree of structural disorder, leading to an increase in the Urbach energy. This behavior can be attributed to the Volmer-Weber crystallization mechanism, which is typically associated with the formation of nanocrystalline films, where nucleation occurs predominantly on the surface with limited substrate interaction. The observed bandgap width was slightly smaller than values reported in the literature, indicating the presence of oxygen vacancies within the film's structure. While the widening of the bandgap with decreasing nanoparticle size is typically linked to quantum confinement effects that constrain electron and hole movement, increasing the transition energy between the valence and conduction bands, in this case, the observed reduction in bandgap width suggests that oxygen vacancies have a substantial impact on the film's optical properties, altering the transition energy and offsetting the quantum confinement effects.

Acknowledgments

The authors gratefully acknowledge the financial and technical support provided by the Ministry of Higher Education, Science, and Innovation under project number IL-5421101842

ORCID

Temur K. Turdaliev, https://orcid.org/0000-0002-0732-9357

REFERENCES

[1] A. Garzon-Roman, C. Zúñiga-Islas, and D.H. Cuate-Gomez, Silicon, **16**, 61 (2024). https://doi.org/10.1007/s12633-023-02652-8
[2] A. Garzon-Roman, C. Zúñiga-Islas, D.H. Cuate-Gomez, and A. Heredia-Jimenez, Sens. Actuators A: Phys. **349**, 114064 (2023). https://doi.org/10.1016/j.sna.2022.114064
[3] V. Morgunov, S. Lytovchenko, V. Chyshkala, D. Riabchykov, and D. Matviienko, East Eur. J. Phys. (4), 18 (2021), https://doi.org/10.26565/2312-4334-2021-4-02
[4] D. Li, H. Song, X. Meng, T. Shen, J. Sun, W. Han, and X. Wang, Nanomaterials, **10**, 546 (2020). https://doi.org/10.3390/nano10030546
[5] A. Soussi, A. Ait Hssi, and M. Boujnah, J. Electron. Mater. **50**, 4497 (2021). https://doi.org/10.1007/s11664-021-08976-8
[6] Y. R. Park and K. J. Kim, Thin Solid Films, **484**, 34 (2005). https://doi.org/10.1016/j.tsf.2005.01.039
[7] P. Makuła, M. Pacia, and W. Macyk, J. Phys. Chem. Lett. **9**, 6814 (2018). https://doi.org/10.1021/acs.jpclett.8b02892
[8] W.A.A. Garhoom, and Z. Al Shadidi, East Eur. J. Phys. (4), 164 (2021). https://doi.org/10.26565/2312-4334-2021-4-22
[9] H. Al Dmour, East Eur. J. Phys. (3), 555 (2023). https://doi.org/10.26565/2312-4334-2023-3-65
[10] Y. Wei, Q. Wu, H. Meng, Y. Zhang, and C. Cao, RSC Advances, **13**(30), 20584-20597 (2023). https://doi.org/10.1039/D2RA07839B
[11] C. He, J. He, S. Cui, X. Fan, S. Li, Y. Yang, X. Tan, *et al*., Nanomaterials, **13**(24), 3123 (2023). https://doi.org/10.3390/nano13243123
[12] D.A. Deen, J.G. Champlain, and S.J. Koester, Appl. Phys. Lett. **103** (7), 073504 (2013). https://doi.org/10.1063/1.4818754
[13] D. Nunes, E. Fortunato, and R. Martins, Discover Materials, **2**, 2 (2022). https://doi.org/10.1007/s43939-022-00023-5
[14] H.-H. Li, G.-J. Yuan, B. Shan, X.-X. Zhang, H.-P. Ma, Y.-Z. Tian, H.-L. Lu, and J. Liu, Nanoscale Research Letters, **14**, 119 (2019). https://doi.org/10.1186/s11671-019-2947-5
[15] I.J. Abdisaidov, S.G. Gulomjanova, I.K. Khudaykulov, and K.B. Ashurov, East Eur. J. Phys. (3), 355-358 (2024). https://doi.org/10.26565/2312-4334-2024-3-41
[16] D. Rafieian, W. Ogieglo, T. Savenije, and R.G.H. Lammertink, AIP Adv. **5**, 097168 (2015). https://doi.org/10.1063/1.4931925
[17] K. Al-Attafi, H.A. Mezher, A.F. Hammadi, A. Al-Keisy, S. Hamzawy, H. Qutaish, and J.H. Kim, Nanomaterials **13**, 1940 (2023). https://doi.org/10.3390/nano13131940
[18] H.Y. He, Res. Chem. Intermed. **36,** 155 (2010). https://doi.org/10.1007/s11164-010-0125-6
[19] T.K. Turdaliev, K.B. Ashurov, and R.K. Ashurov, Journal of Applied Spectroscopy, **91**, (2024). https://doi.org/10.1007/s10812-024-01783-z
[20] M. Aravind, M. Amalanathan, and M.S.M. Mary, SN Appl. Sci. **3**, 409 (2021). https://doi.org/10.1007/s42452-021-04281-5
[21] V. Galstyan, E. Comini, G. Faglia, and G. Sberveglieri, Sensors, **13**, 14813 (2013). https://doi.org/10.3390/s131114813
[22] A.A. Rempel, A.A. Valeeva, A.S. Vokhmintsev, and I.A. Weinstein, Russ. Chem. Rev. **90**, 1397 (2021). https://doi.org/10.1070/RCR4991
[23] J. Jitputti, Y. Suzuki, and S. Yoshikawa, Catal. Commun. **9**, 1265 (2008). https://doi.org/10.1016/j.catcom.2007.11.016
[24] J. Jia, H. Yamamoto, and T. Okajima, Nanoscale Res. Lett. **11**, 324 (2016). https://doi.org/10.1186/s11671-016-1531-5
[25] J. Andújar, T. Theivasanthi, T. Thirugnanasambandan, and M. Alagar, arXiv: Chem. Phys. (2013). https://arxiv.org/pdf/1307.1091
[26] A.E. Maftei, A. Buzatu, G. Damian, N. Buzgar, H.G. Dill, and A.I. Apopei, Minerals, **10**, 988 (2020). https://doi.org/10.3390/min10110988
[27] D. Rajkumar, H. Umamahesvari, and P. Nagaraju, J. Mater. Sci.: Mater. Electron. **34**, 38 (2023). https://doi.org/10.1007/s10854-022-09106-8
[28] O. Frank, M. Zukalova, B. Laskova, J. Kürti, J. Koltai, and L. Kavan, Phys. Chem. Chem. Phys. **14**, 14567 (2012). https://doi.org/10.1039/C2CP42763J
[29] I. Y. Bouderbala, A. Guessoum, and S. Rabhi, Appl. Phys. A, **130**, 205 (2024). https://doi.org/10.1007/s00339-024-07366-1
[30] C.M. Mahajan, JOM, **75**, 448 (2023). https://doi.org/10.1007/s11837-022-05621-5
[31] V.R. Akshay, B. Arun, G. Mandal, and M. Vasundhara, Phys. Chem. Chem. Phys. **21**, 12991 (2019). https://doi.org/10.1039/C9CP01351B
[32] Y. Alaya, R. Souissi, M. Toumi, M. Madani, L. El Mir, N. Bouguila, and S. Alaya, RSC Adv. **13**, 21852 (2023). https://doi.org/10.1039/D3RA02387G

ОПТИЧНІ ХАРАКТЕРИСТИКИ ТА КРИСТАЛІЧНА СТРУКТУРА ТОНКОЇ ПЛІВКИ TiO_2 НА СКЛЯНІЙ ПІДКЛАДЦІ, ВИРОЩЕНОЇ ШЛЯХОМ ОСАДЖЕННЯ АТОМАРНОГО ШАРУ

Темур К. Турдалієв
Інститут іонно-плазмових і лазерних технологій імені Арифова Академії наук Узбекистану
100125, вул. Дурмон Юлі 33, Ташкент, Узбекистан

У цьому дослідженні досліджується формування оптичних властивостей і кристалічної структури тонких плівок TiO_2 товщиною приблизно 1,5 мікрометра, вирощених на скляній підкладці методом атомарного шарового осадження з тетраізопропоксидом титану та водою як попередниками. Рентгенівська дифракція та спектроскопія комбінаційного розсіювання підтвердили, що плівки TiO_2 кристалізуються в поліморфній фазі анатазу. Плівки демонструють нанокристалічну структуру із середнім розміром кристалітів приблизно 28 нанометрів, як встановлено рентгенівськими дифракційними вимірюваннями. Рентгенівська дифракційна картина виявила чіткі піки під кутами 2θ 25,3°, 38,6°, 48,0°, 55,0° і 70,4°, що відповідають (101), (112), (020), (121) і (220) кристалографічних площинах, тоді як спектри КРС демонструють виражені піки при частоти 143, 194, 392, 514 і 637 $см^{-1}$, усі характерні для фази анатазу TiO_2. Метод Таука, застосований до спектрів поглинання тонкої плівки, показав, що вона має пряму заборонену зону 3,2 еВ і непряму заборонену зону 2,3 еВ.

Ключові слова: *тонкі плівки діоксиду титану; атомне шарове осадження; фаза анатазу; рентгенівська дифракція; раманівська спектроскопія; енергія забороненої зони; оптичні властивості; енергія Урбаха; нанокристалічна структура*

East European Journal of Physics. **1.** 256-259 (2025)
DOI:10.26565/2312-4334-2025-1-28 ISSN 2312-4334

MORPHOLOGICAL STUDIES OF $(Ge_2)_{1-X}(ZnSe)_X$ SOLID SOLUTIONS

A.Sh. Razzokov[a], A.S. Saidov[b], M.A. Shonazarova[c], J.A. Razzakov[a], D.E. Koshchanova[a]*
[a]Urgench State University, 14 Kh. Alimdjan, Urgench, 220100, Uzbekistan
[b]Physical-Technical Institute NPO "Physics-Sun of the Academy of Sciences of the Republic of Uzbekistan, 2B, Ch. Aitmatov St., Tashkent, 100084, Uzbekistan
[c]Leipzig University, 10 Augustplatz, Leipzig 04109, Germany
**Corresponding Author e-mail: dona23042014@gmail.com*
Received September 16, 2024; revised January 20, 2025; accepted February 7, 2025

Single-crystal films of the $(Ge_2)_{1-x}(ZnSe)_x$ solid solution from a limited tin solution-melt in the temperature range from 1023 K to 803 K at a cooling rate of 1-1.5 K/min on an EPOC installation were grown on Ge substrates and GaAs. The gap between the substrates was 0.65÷1.2 mm. It was established that the lowest values of dislocation density ($N_D=2\cdot10^4\div10^5$ cm^{-2}) were recorded in epitaxial films at T_{NC} = 893 K. Technological conditions for obtaining GaAs- $(Ge_2)_{1-x}(ZnSe)_x$ heterostructure with a smooth boundary have been achieved. Film substrate and the supercooling temperature was ΔT = 7.2°C.
Keywords: *Epitaxial layer; Heterostructure; Solid solution; Dislocation; Single-crystal*
PACS: 74.78.Fk; 68.65.-k; 64.75.Nx

INTRODUCTION

The growth of crystalline perfect semiconductor solid solutions is of undoubted interest for the development of modern semiconductor instrumentation, since a solid solution synthesized from several semiconductor compound components, can combine the advantages of each of them [1,2]. Variable solid solutions belonging to the class $(C^{IV})_{1-x}(A^{II}B^{VI})_x$ make it possible to vary the basic electrophysical and photoelectric parameters of semiconductor materials within wide limits when their chemical compositions change [3,4]. We have obtained epitaxial layers $(Ge_2)_{1-x}(ZnSe)_x$, but to date, morphological studies that determine the photoelectric and electrophysical properties have not been sufficiently studied [5].

Defects and dislocations at the substrate-film interface serve as additional recombination centers, which worsens the injection properties in homo- and heterojunctions of the structure [6,7]. In addition, they significantly reduce the separation coefficient of light-generated electron-hole pairs in photoelectric converters [8]. Therefore, the selection of components and chemical compounds that form the necessary solid solutions is associated with many parameters that must be taken into account: sufficient solubility of the components in solvent at a given temperature; slight discrepancy between lattice parameters and thermal expansion coefficients of crystal-forming chemical compounds and substrates, crystal orientations, etc. [9,10].

It is known that solid solutions based on Ge ZnSe systems, depending on their chemical composition, allow the variation of basic electrophysical and optical parameters of semiconductor materials within a wide range. Considering the above, this work studied the conditions for forming solid solutions based on ZnSe and GeGe compounds and the features of their structure [11,12].

MATERIALS AND METHODS

The composition of the melt solution, consisting of Ge, ZnSe and Sn, was determined from the state diagrams of Sn–Ge–ZnSe alloys [11]. To prepare the liquid melt solution, we used the literature data described in [13,14].

Proven experimental scientific methods were used. Typically, substrates are used with certain smallest slopes during the growth of films from the liquid phase, which promote the formation of epitaxial layers on the surface of the substrate. Any surface of a solid has a certain roughness, so the surface energy is distributed unevenly and affects the growth of the solid solution on the substrate, as well as the formation of dislocations, which are associated with technological parameters, such as crystallization onset temperature (T_{OC}), growth rate (υ), gap between substrates (δ), composition of components in the melt solution with substrate orientations, etc.

The substrates were chemically pure (99.999%) Ge(111) and GaAs(100) plates with charge carrier concentration $n=(1\div5)\cdot10^{17}$cm^{-3}, $n=(4\div7)\cdot10^{17}$cm^{-3}, respectively, donor type of conductivity. The diameter and thickness of the substrate were 20 mm and 350-400 μm, respectively. To obtain a certain composition of the melt solution based on a tin solvent, germanium and zinc selenide powders were used.

To grow a graded-gap solid solution $(Ge_2)_{1-x}(ZnSe)_x$, we used a vertical-type quartz reactor with horizontally located substrates in an EPOS-type installation. The growth of the epitaxial layer was carried out from a small volume of tin solution-melt, limited to two substrates in the atmosphere, which were purified with palladium hydrogen, which

Cite as: A.Sh. Razzokov, A.S. Saidov, M.A. Shonazarova, J.A. Razzakov, D.E. Koshchanov, East Eur. J. Phys. 1, 256 (2025), https://doi.org/10.26565/2312-4334-2025-1-28
© A.Sh. Razzokov, A.S. Saidov, M.A. Shonazarova, J.A. Razzakov, D.E. Koshchanov, 2025; CC BY 4.0 license

made it possible to minimize the amount of consumed solution-melt. First, a vacuum was created in the reactor to a residual pressure of 10^{-2} Pa, then purified hydrogen was passed through the reactor for 30 minutes, and after that the heating process began. When the temperature reached the required value, the system switched to automatic mode. Homogenization of the melt solution was carried out within 40-50 minutes. Then the substrates on a graphite holder were brought into contact with the melt solution and, after filling the gaps between the substrates with the melt solution, they were raised 1 cm above the solution level. The growth of epitaxial layers $(Ge_2)_{1-x}(ZnSe)_x$ was stopped at the right moment by draining the melt solution from the substrates using a centrifuge.

The surface morphology of the grown films was studied using scanning electron microscopy (SEM EVO MA 10 (Zeiss)) and a CoreAFM setup.

Specific resistance, mobility and concentration of the main charge carriers were determined using an HMS-7000 installation (Hall effect measurement system).

EXPERIMENTAL AND DISCUSSION

Crystalline perfect epitaxial layers $(Ge_2)_{1-x}(ZnSe)_x$ were grown from a limited tin solution-melt with forced cooling (at a rate of 1-1.5 K/min) in the temperature range from 1023 K to 803 K on Ge(111) substrates, GaAs(100) [15]. A detailed description of the method used is presented in [16]. The resulting epitaxial layers were single-crystalline and had a sphalerite-type lattice, which is confirmed by XRD studies [15]. A detailed description of the method used is presented in [16]. The resulting epitaxial layers were single-crystalline and had a sphalerite-type lattice, which is confirmed by XRD studies [15]. Mutual substitution of components in the lattice did not lead to its noticeable deformation. That is, when replacing Zn and Se atoms located nearby in the lattice with germanium atoms, the energy of elastic distortions of the crystal lattice was minimal, therefore, the possibility of continuously forming a number of substitutional solid solutions, which can be designated as $(Ge_2)_{1-x}(ZnSe)_x$.

During the growth of an epitaxial film from a tin solution-melt, in the resulting varizone solid solution, the substitution process occurred by replacing atoms not separately statistically located in the lattice in Zn and Se with germanium atoms, and by replacing the Zn and Se atoms located in pairs in the lattice (the so-called dimers or “molecules" ZnSe in terminology [17]) for two germanium atoms (Ge-Ge), which contributed to the growth of epitaxial layers on the substrate. This process is schematically presented in Figure 1.

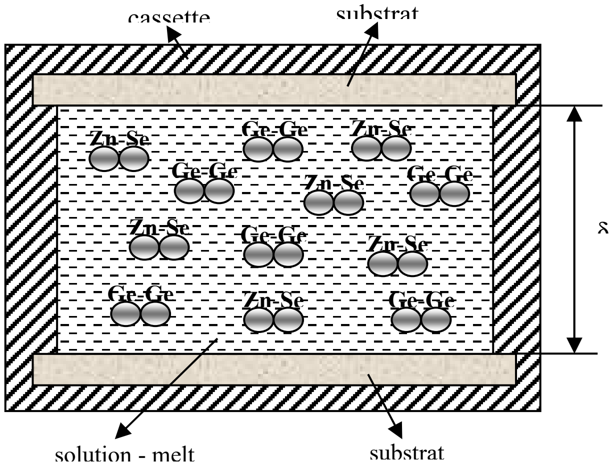

Figure 1. Scheme for the formation of a varizone solid solution from a Sn-Ge-ZnSe solution-melt (the thickness of the gap between the substrates δ= 1 mm).

In Figure -1 it is schematically shown the dissolved components Zn, Se, Ge in a tin solvent located between horizontally located substrates.

Epitaxial films $(Ge_2)_{1-x}(ZnSe)_x$ are grown from a Ge + ZnSe + Sn melt solution onto a Ge substrate without technological difficulties due to the saturation of the liquid phase relative to Ge + ZnSe; this prevents melting of the surface layer of the substrate-film interface at the front crystallization. If growth is carried out on a “foreign” GaAs substrate, then due to the unsaturation of the Ge + ZnSe + Sn system of the solution-melt relative to GaAs, it will lead to dissolution of the substrate. To prevent such a process, an equilibrium state of the system must be established between the liquid (solution-melt) and solid phase (substrate). Therefore, the liquid phase must be supercooled relative to the solid phase-substrate. For the thermodynamic equilibrium of this system, using the following formulas, you can determine the temperature or contact supercooling:

$$\Delta T = \frac{T_L}{\Delta H} \cdot \frac{EM}{1-\nu} \left(\frac{a_1 - a_2}{a_1}\right)^2 \cdot \frac{1}{f}.$$

Where, ΔH - the enthalpy of layer dissolution, T_L- the liquidus temperature, E and ν - Young’s modulus and Poisson’s ratio, M - the molar volume, a_1, a_2 - the lattice parameters of the substrate and the solid phase, f - the stabilization factor.

Based on theoretical calculations, the supercooling temperature for the solution-melt system Ge + ZnSe + Sn was predetermined and applied in the growth process. It has been established that when growing a $(Ge_2)_{1-x}(ZnSe)_x$ solid solution on a GaAs substrate from the liquid phase, the optimal supercooling temperature is ΔT = 7.2°C. Thus, the technological condition for obtaining a GaAs- $(Ge_2)_{1-x}(ZnSe)_x$ heterostructure with crystalline perfection and a smooth substrate-film boundary has been achieved.

The resulting solid solution films were mirror-smooth, and to study their surface we carried out morphological studies. Three-dimensional images of the surface of the $(Ge_2)_{1-x}(ZnSe)_x$ epitaxial film obtained using an atomic force microscope showed that a quantum dot is formed in the surface layer with a width of 110 nm and a height of 14 nm (Figure 2 (a, b)).

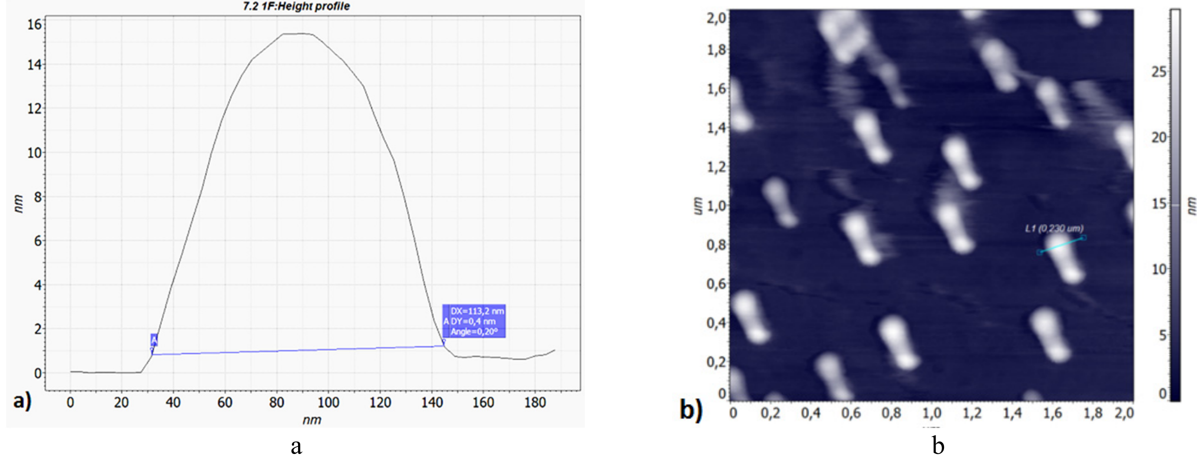

a b

Figure 2. Three-dimensional **(a)** - (image size 2×2 μm^2) and two-dimensional **(b)** - image of the surface of epitaxial films $(Ge_2)_{1-x}(ZnSe)_x$, (quantum dot size: width 110 nm, height 14 nm)

The forming quantum dots in the form of a dipole are directed strictly in one direction, with the same slope, which indicates the monocrystalline nature of the resulting epitaxial film. The forming quantum dots in the form of a dipole are directed strictly in one direction, with the same bias, which indicates the orderliness of the grown layers and the monocrystalline nature of the resulting epitaxial film. The figure also shows that the film layers formed consist of pairs of ordered nanoclusters. This is probably due to the potential field of the surface layer.

And also, to study the morphology of the films, we selected the composition of the etchant (we used mixtures of concentrated hydrofluoric (HF), nitric (HNO_3) and acetic (CH_3COOH) acids, in the ratios 1hHF+3hHNO$_3$+4hCH$_3$COOH). To identify dislocation, etch pits on the (111) plane, the samples were etched in a solution, then the etchant was diluted with deionized water and washed. After this process, using a scanning electron microscope (SEM), images of dislocations on the surface of the grown $(Ge_2)_{1-x}(ZnSe)_x$ epitaxial layers were obtained and the dislocation densities were determined. According to experimental data, the dislocation density N_D in grown semiconductor solid solutions $(Ge_2)_{1-x}(ZnSe)_x$ depended on many technological parameters: growth temperature, forced thorough cooling, orientation and cleanliness of substrates, type of solvent. Therefore, in order to reduce the dislocation density, experiments were carried out at different T_{OC} values. It was found that the lowest values of dislocation density (N_D=2·10^4÷10^{5}cm^{-2}) were recorded in epitaxial films at T_{OC} = 893 K (Figure 3).

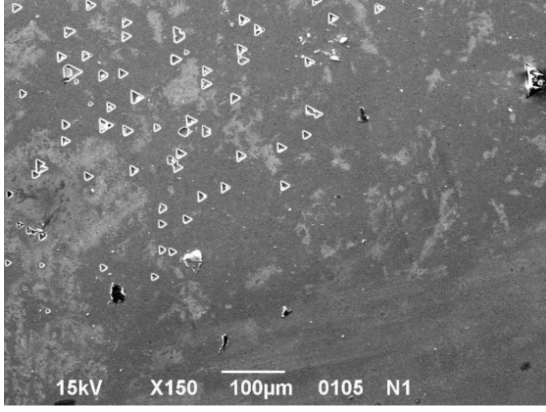

Figure 3. Photographs of dislocations on the surface of $(Ge_2)_{1-x}(ZnSe)_x$ epitaxial layers (obtained using SEM EVO MA 10 (Zeiss))

Subsequently, some electrophysical properties of the resulting films were studied: the resistivity, Hall mobility and charge carrier concentration at a temperature of 300 K were determined: ρ = 0.5÷5 Ohm·cm, μ_p = 30÷60 cm^2/V·s, n_p = (5÷7)·10^{18} cm^{-3}. The films had hole type conductivity.

CONCLUSIONS

Thus, the possibility of obtaining crystalline perfect epitaxial layers of solid growth from a limited tin solution-melt is shown. Thieves $(Ge_2)_{1-x}(ZnSe)_x$ on GaAs substrates with (100) orientation and Ge with (111) orientation. Based on theoretical calculations, the supercooling temperature for the solution-melt of the Ge + ZnSe + Sn system was predetermined, which is equal to ΔT = 7.2 °C. The technological conditions for obtaining a solution-melt of GaAs-$(Ge_2)_{1-x}(ZnSe)_x$ heterostructures from the Ge + ZnSe + Sn system without sub-dissolution of the "foreign" substrate using supercooling have been established experimentally. It was found that the lowest values of dislocation density N_D=2·10^4÷10^5 cm^{-2}) were recorded in epitaxial films at T_{OC} = 893 K. In the future, these solid solutions can be used as graded-gap semiconductor materials with controlled electrophysical and photoelectric properties in field of semiconductor instrument making.

ORCID

D.E. Koshchanova, https://orcid.org/0009-0003-0927-2475

REFERENCES

[1] Y. Wang, *et al.*, "Bandgap broadly tunable GaZnSeAs alloy nanowires," Physical Chemistry Chemical Physics, **15**(8), 2912-2916 (2013). https://doi.org/10.1039/C2CP43718J
[2] W. Huang, *et al.*, "Composition-dependent perfect band gap tuning of $ZnS_{1-x}Se_x$ solid solutions for efficient photocatalysis," Journal of Physics and Chemistry of Solids, **130**, 41-45 (2019). https://doi.org/10.1016/j.jpcs.2019.02.008
[3] S. Schorr, *et al.*, "Electronic band gap of Zn_{2x} $(CuIn)_{1-x}X_2$ solid solution series (X= S, Se, Te)," Journal of alloys and compounds, **414**(1-2), 26-30 (2006). http://dx.doi.org/10.1016/j.jallcom.2005.07.014
[4] M. Kaji, *et al.*, "Liquid-phase epitaxy of GaAs-ZnSe Ga_2Se_3 alloy crystals on a ZnSe substrate," Journal of crystal growth, **178**(3), 242-245 (1997). https://doi.org/10.1016/S0022-0248(96)01187-6
[5] M.S. Saidov, A.S. Saidov, and A.Sh. Razzakov, "Liquid Phase Epitaxy Photoluminescence and Photoelectrical Properties of Variband $(Ge_2)_{1-x}(ZnSe)_x$ Layers," in: *Tenth International Workshop on Physics of Semiconductor Devices*, (India, 1999), pp. 1424-1427.
[6] S. Fujiwara, Y. Namikawa, M. Irikura, K. Matsumoto, T. Kotani, and T. Nakamura, "Growth of dislocation-free ZnSe single crystal by CVT method," Journal of Crystal Growth, **219**(4), 353-360 (2000). https://doi.org/10.1016/S0022-0248(00)00671-0
[7] Q. Zhang, H. Li, Y. Ma, and T. Zhai, "ZnSe nanostructures: Synthesis, properties and applications," Progress in Materials Science, **83**, 472-535 (2016). https://doi.org/10.1016/j.pmatsci.2016.07.005
[8] D.W. Parent, A. Rodriguez, J.E. Ayers, and F.C. Jain. "Photoassisted MOVPE grown (n)ZnSe/(p+)GaAs heterojunction solar cells," Solid-State Electronics, **47**(4), 595-599 (2003). https://doi.org/10.1016/S0038-1101(02)00334-9
[9] Y. Li, D. Yang, W. Nan, L. Zhang, H. Yu, B. Zhou, and Z. Hu, "The crystal growth of ZnSe by the traveling heater method with the accelerated crucible rotation technique," Journal of Crystal Growth, **589**, 126684 (2022). https://doi.org/10.1016/j.jcrysgro.2022.126684
[10] G.B. Stringfellow, "Epitaxial growth of metastable semiconductor alloys," Journal of Crystal Growth, **564**, 126065 (2021). https://doi.org/10.1016/j.jcrysgro.2021.126065
[11] A. Heurtel, A. Marbeuf, H. Tews, and Y. Marfaing, "Liquid phase epitaxy of ZnSe in Sn: Calculation of the ternary phase diagram and electronic properties," Journal of Crystal Growth, **59**(1-2), 167-171 (1982). https://doi.org/10.1016/0022-0248(82)90319-0
[12] V.P. Maslov, A.V. Fedorenko, V.P. Kladko, O.Y. Gudymenko, K.M. Bozhko, and N.M. Zashchepkina, "Structure and electrical resistance of the passivating ZnSe layer on Ge," Semiconductor Physics, Quantum Electronics & Optoelectronics, **24**(4), 425-430 (2021). https://doi.org/10.15407/spqeo24.03.425
[13] M. Rubinstein, "Solubilities of gallium arsenide in metallic solvents," J. Electrochem. Soc. **113**, 752 (1966). https://doi.org/10.1149/1.2424107
[14] J.P. Fleurial, and A. Borshchevsky, "Si-Ge-metal ternary phase diagram calculations," J. Electrochem. Soc. **137**, 2928 (1990). https://doi.org/10.1149/1.2087101
[15] A.S. Saidov, *et al.*, "Liquid-phase epitaxy of solid solutions $(Ge_2)_{1-x}$ $(ZnSe)_x$," Materials chemistry and physics, **68**(1), 1-6 (2001). http://dx.doi.org/10.1016/S0254-0584(00)00230-3
[16] A.S. Saidov, and A.S. Razzokov, "Obtaining and morphological studies of epitaxial layers of the $Si_{1-x}Ge_x$ solid solution," Siberian Physical Journal, **15**(2), 84-91 (2020). https://doi.org/10.25205/2541-9447-2020-15-2-84-91
[17] A.S. Saidov, *et al.*, "Investigation of the Crystallographic Perfection and Photoluminescence Spectrum of the Epitaxial Films of $(Si_2)_{1-x}(GaP)_x$ (0≤x≤1) Solid Solution, Grown on Si and GaP Substrates with the Crystallographic Orientation (111)," Advances in Condensed Matter Physics, 1-8 (2021). http://dx.doi.org/10.1155/2021/3472487

МОРФОЛОГІЧНІ ДОСЛІДЖЕННЯ ТВЕРДИХ РОЗЧИНІВ $(Ge_2)_{1-x}(ZnSe)_x$

А.Ш. Раззоков[a], А.С. Саїдов[b], М.А. Шоназарова[c], Й.А. Раззаков[a], Д.Є. Кощанова[a]
[a]*Ургенчський державний університет, 220100, Ургенч, 14 Х. Алімджан, Узбекистан*
[b]*Фізико-технічний інститут НВО «Фізика-Сонце» Академії наук Республіки Узбекистан, 2Б, Ч. Айтматова, Ташкент, Узбекистан*
[c]*Лейпцизький університет, 10 Аугустплатц, Лейпціг, Німеччина*

Монокристалічні плівки твердого розчину $(Ge_2)_{1-x}(ZnSe)_x$ з обмеженого розчину-розплаву олова в діапазоні температур від 1023 K до 803 K при швидкості охолодження 1-1,5 К/хв на установці ЕРОС були вирощені на підкладках Ge та GaAs. Зазор між підкладками становив 0,65÷1,2 мм. Встановлено, що найменші значення густини дислокацій (ND=2·10^4÷10^5 cm^{-2}) зафіксовано в епітаксіальних плівках при TNC = 893 K. Були досягнуті технологічні умови отримання гетероструктури GaAs-$(Ge_2)_{1-x}(ZnSe)_x$ з гладкою межею. Температура плівкової підкладка і переохолодження становила ΔT = 7,2°C.
Ключові слова: *епітаксіальний шар; гетероструктура; твердий розчин; дислокація; монокристал*

EAST EUROPEAN JOURNAL OF PHYSICS. **1.** 260-264 (2025)
DOI:10.26565/2312-4334-2025-1-29 ISSN 2312-4334

INFLUENCE OF IMPLANTATION OF ACTIVE METAL IONS ON THE COMPOSITION, EMISSION AND OPTICAL PROPERTIES OF MgO FILMS

M.B. Yusupjonova*, D.A. Tashmukhamedova, B.E. Umirzakov, S.S. Pak, Z.R. Saidakhmedova, Sh.K. Salieva
Tashkent State Technical University named after Islam Karimov, Tashkent, 100095 Republic of Uzbekistan
**Corresponding Author e-mail: ftmet@mail.ru*
Received November 26, 2024; revised January 21, 2025; accepted February 3, 2025

The composition, electronic structure, emission and optical properties of MgO/Mg films implanted with Ba+ and Na+ ions before and after annealing were studied by using a combination of secondary and photoelectron spectroscopy methods. It has been shown that after ion implantation, amorphous films consisting of Mg – Ba – O, Mg – O, Ba – O compounds, as well as unbound Ba and Mg atoms, are formed in the surface layers. In this case, eφ of the surface decreases. It has been determined that the emission efficiency of ion-doped layers is higher than that of MgO layers. Post-implantation annealing at T = 900 K leads to the formation of a homogeneous $Mg_{0.4}Ba_{0.6}O$ film with a thickness of 30 – 35 Å in the case of Ba^+ ion implantation. It has been revealed that the photoelectron escape depth λ of the three-component film is 1.5 times greater than that of Mg oxide. The main mechanisms of changes in the electronic structure, emission and optical properties of MgO during ion implantation and subsequent annealing have been identified.
Keywords: *Thermal oxidation; Ion implantation; Photoelectron spectroscopy; Quantum yield; Emission efficiency; Yield depth*
PACS: 61.72.uj, 68.55.Ln

INTRODUCTION

Metal oxides are promising in various fields of electronics and electronic engineering [1–5], in particular, photoelectric devices, ultraviolet photodetectors, sensors, thermal and electrical insulators, semiconductors, fuel cell additives, antimicrobial materials, optical electronics and nanoelectronics. The unique physical properties of high-quality magnesium oxide films allow them to be used as buffer layers and substrates for superconducting coatings [6], for structures based on wide-bandgap semiconductors [7], in spintronics devices [8], protective layer of plasma display panels [9], one of the materials for pyrochemical technology of spent nuclear fuel reprocessing [10, 11] and as coatings for spacecraft [12].

Various methods have been used to create and study thin MgO films: high-frequency sputtering [13 – 15], thermal treatment [16, 17], chemical spray pyrolysis [18 – 20], laser ablation [21], arc plasma melting [22], and aerosol assisted chemical vapor deposition technique [23].

The spatial distribution of structural features of MgO film on sapphire was determined in combination with X-ray structural analysis and layer-by-layer plasma etching and the presence of a thin transition layer with signs of rhombohedral deformation has been revealed in [13]. High transparent and antireflective properties of MgO thin film with an average transmittance of about 91.48% in the visible range, as well as a high reflectivity in the IR range have been found by the authors of [19]. These results can be used as an optical window or a buffer layer, and a well-reflective surface will prevent an increase in surface temperature under the influence of solar radiation, which can be used in solar cell applications.

We have previously studied the processes of formation of nanosized phases on the Si and GaAs surface during implantation of Ba^+, Na^+ and O^+_2 ions [24 – 27]. We have also studied the effect of implantation of active metal ions on the composition, structure, emission and electrophysical properties of SiO_2 and CaF_2 films [28 – 30].

However, investigations on obtaining nanosized phases and films on the surface of MgO films using the ion implantation method have not been conducted yet. The composition, crystal and electronic structure, emission and optical properties of thin films of Mg oxides with nanosized structures have not practically been studied.

This article will present the results of experimental studies on the effect of low-energy (E_0 = 0.5 – 5 keV) implantation of Ba^+ and Na^+ ions on the composition, structure, and physical properties of MgO/Mg films.

EXPERIMENTAL TECHNIQUE

All technological impacts (Mg oxidation, temperature treatment, ion implantation) and studies of the composition, electronic structure and physical properties have been carried out in the same ultra-high vacuum device. MgO films have been obtained by thermal oxidation of Mg. MgO with a thickness of θ = 800 Å has mainly been used. Before oxidation, Mg has been outgassed at T = 1,200 K under a vacuum of 10^{-7} Pa for 5–6 hours. Then, O_2 molecules have been admitted to the device to a pressure of $5 \cdot 10^{-3}$ Pa, which fell on the Mg surface heated at T = 1,000 K. Active metal ions Ba^+ and Na^+ have been created by surface ionization.

Cite as: M.B. Yusupjonova, D.A. Tashmukhamedova, B.E.Umirzakov, S.S. Pak, Z.R. Saidakhmedova, Sh.K. Salieva, East Eur. J. Phys. 1, 260 (2025), https://doi.org/10.26565/2312-4334-2025-1-29
© M.B. Yusupjonova, D.A. Tashmukhamedova, B.E.Umirzakov, S.S. Pak, Z.R. Saidakhmedova, Sh.K. Salieva, 2025; CC BY 4.0 license

The elemental and chemical composition of the nanofilms has been determined by Auger electron spectroscopy (AES), and the electronic structure has been determined by ultraviolet photoelectron spectroscopy (UPES). The error in determining the atomic concentration was ~ 5 – 8 at.%. To determine the depth distribution profile of impurities, layer-by-layer Auger analysis has been performed by sputtering the sample surface with 1 keV Ar^+ ions at an incidence angle of ~ 80° relative to the normal; the etching rate was ~ (3 ± 1) Å/min. The quantum yield of photoelectrons Y has been measured at a photon energy of hν ≈ 10.8 eV. The energy dependence of the secondary electron emission coefficients (SEEC) σ has been measured in the primary electron energy range of E_p = 100 – 1500 eV.

EXPERIMENTAL RESULTS AND DISCUSSION

The MgO/Mg system was outgassed at T = 800 K for 2 – 3 hours before the research. Implantation of Ba^+ and Na^+ ions was performed with the energy E_0 = 1 keV at the saturation dose $D = 6\cdot10^{16}$ cm^{-2} in a vacuum of $5\cdot10^{-7}$ Pa at room temperature. The composition, structure and physical properties of the ion-implanted sample do not change significantly starting from $D = 6\cdot10^{16}$ cm^{-2}, i.e. this dose is the saturation dose $D_н$. Table 1 shows the emission parameters of MgO/Mg films with a thickness d = 800 Å, before and after ion implantation, where σ_m is the maximum value of σ, λ is the depth of the yield of true secondary and photoelectrons. It is evident that after ion implantation the values of σ_m, Y and λ increase noticeably. This can be explained by the fact that compounds of the Mg – O, Me – O, Mg – Me – O type are formed, as well as unbound Mg and Me (Ba or Na) atoms in the ion-implanted layer. In this case, excess Ba (Na) atoms with a thickness of 0.5 – 0.6 monolayers are formed on the surface, which leads to a decrease in the work function of the surface. Apparently, the emission efficiency of Ba + O and Ba + Mg + O compounds is significantly higher than the emission efficiency of MgO. All this leads to a noticeable increase in the depth of the yield of true secondary and photoelectrons, therefore, the values of σ_m and Y increase to 1.5 – 2 times (see Table 1).

Table 1. Emission parameters of MgO before and after implantation of $Ba^+$and Na^+ ions with E_0=1 keV, $D=6\cdot10^{16}$ cm^{-2}

Subject of research	σ_m	E_{pm}, eV	η at (E_p = 500 eV)	Y at hν = 10.8 eV	λ, Å
MgO	3.9	800	0.22	$3\cdot10^{-4}$	400
$Ba^+ \to$ MgO	7.2	1000	0.32	$6\cdot10^{-4}$	600
$Na^+ \to$ MgO	8.1	1000	0.25	$7\cdot10^{-4}$	600

Thus, the growth of σ_m of magnesium oxide after implantation of sodium and barium ions can be caused by a decrease in eφ, an increase in λ and the formation of an oxide film with a comparatively high emission efficiency.

Post-implantation annealing was carried out at different temperatures in order to obtain a homogeneous three-component film with good stoichiometry. The temperature of 900 K was optimal for obtaining a polycrystalline Mg + Ba + O film. Fig. 1 shows the initial part of the Auger spectra of pure Mg, an MgO/Mg film, an MgO film bombarded with Ba^+ ions with E_0 = 1 keV at $D = D_н$ and heated at T = 900 K for 40 min, and the Auger spectrum of a thick BaO film is shown for comparison.

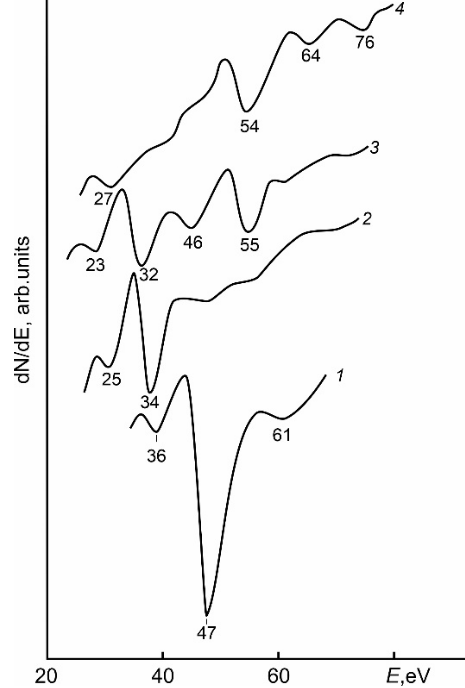

Figure 1. Auger spectra: 1 – pure Mg, 2 – Mg with MgO film, 3 – MgO implanted with Ba^+ ions with E_0 = 1 keV and heated at T = 900 K for 40 min, 4 – thick BaO/Mg film

It is evident that during the formation of the MgO film, the $L_{23}VV$ peak (47 eV) of Mg shifts sharply toward lower energies and other peaks characteristic for MgO appear. Analysis of the full spectrum of MgO showed that all peaks characteristic for Mg disappear in this case. After bombardment with Ba^+ ions and subsequent annealing, the main peak of MgO observed at E = 34 eV shifts toward lower energies by 2 eV. New peaks also appear at energies of 23, 46 and 55 eV. The positions and shapes of these peaks differ from those for a thick BaO film. It can be assumed that compounds of the Mg + Ba + O type are formed in this case. To estimate the concentration of atoms, we used high-energy Auger peaks of Mg (1189 eV), Ba (584 eV), O (503 eV) and determined the concentrations of these elements using the formula $C_x = \frac{I_x/S_x}{\sum I_i/S_i}$.

Figure 2 shows the distribution profiles of Ba, Mg and O atoms by depth h for MgO implanted with Ba^+ ions with E_0 = 1 keV at D = $6\cdot10^{16}$ cm^{-2} and heated at T = 900 K for 40 min. It is evident from Figure 2 that after heating at T = 900 K, the surface concentrations of Mg, Ba and O are ~ 18 – 20, 30 – 32 and 48 – 50 at.%, respectively. It is possible to assume that a three-component compound with the approximate composition $Mg_{0.4}Ba_{0.6}O$ is formed on the surface of MgO in this case. These concentrations do not change significantly to a depth of 35 – 40 Å, i.e. a $Mg_{0.4}Ba_{0.6}O$ film with a thickness d = 35 – 40 Å is formed. The Ba concentration decreases monotonically from ~ 20 – 25 at.% to zero, and the Mg concentration increases from 30 – 35 at.% to 50 – 52 at.% in the range of h = 40 – 80 Å. In the studied region of h, the O concentration does not change noticeably and is ~ 50 – 52 at.%.

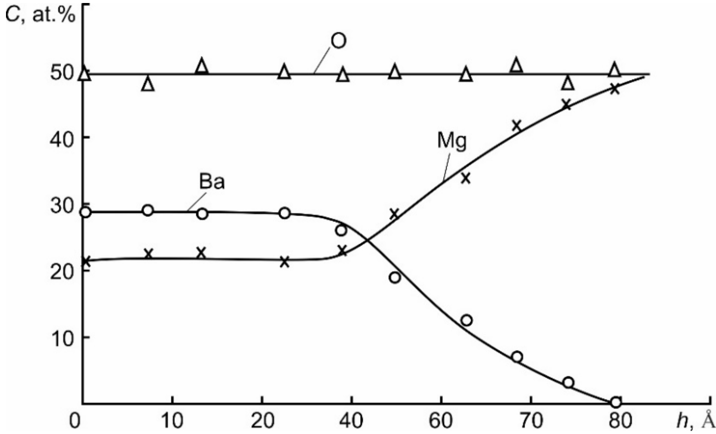

Figure 2. Profiles of the distribution of Mg, Ba and O atoms by depth h for MgO implanted with Ba^+ ions with E0 = 1 keV at D = $6\cdot10^{16}$ cm^{-2} and heated at T = 900 K.

Fig. 3 shows the photoelectron spectra for a MgO film and MgO with a $Mg_{0.4}Ba_{0.6}O$ nanofilm, recorded at hν = 15.6 eV. It is evident that the MgO spectrum has 2 maxima at E_b = – 1.5 eV and – 6.2 eV, respectively, caused by the excitation of electrons from the 3s states of Mg electrons and the 2p states of O electrons. The peculiarity in the region of E_b = – 3.8 eV can be associated with the hybridization of the 3s states of Mg with the 2p state of O. The spectrum width ΔE for MgO is ~ 7.4 eV. Using the formula hν = ΔE + Φ, we can determine Φ, which is ~ 8.2 eV. Here Φ is the photoelectron work function, the value of which is $E_{vac} – E_V$; E_B is the vacuum level, E_V is the top of the valence band.

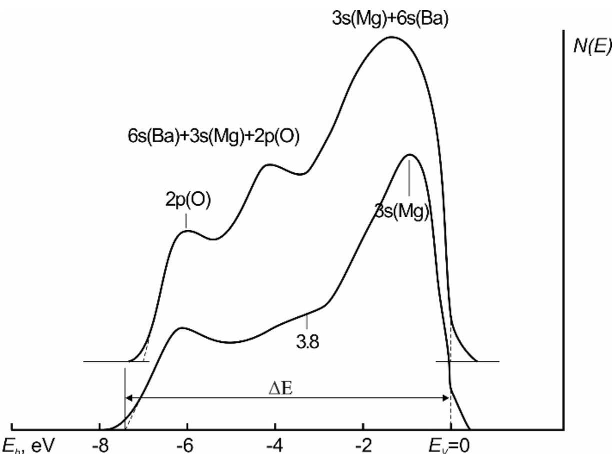

Figure 3. Photoelectron spectra: 1 – MgO/Mg; 2 – $Mg_{0.4}Ba_{0.6}O$/MgO/Mg

If we take into account that χ (electron affinity) for MgO is ~1.0 eV [31], then the band gap width $E_g = E_V - \chi$ = 7.2 eV. The spectrum contains 3 maxima in the case of the $Mg_{0.4}Ba_{0.6}O$ film. Here, the spectrum width

decreases by ~ 0.4 eV, and the area under the curve (i.e., the quantum yield of photoelectrons) increases by ~ 1.4 – 1.5 times. Possible interpretations of the formation of maxima are shown in curve 2.

Table 2 shows the band-energy parameters of MgO and $Mg_{0.4}Ba_{0.6}O$ films. It is evident that the values of E_g, σ_m and Y of the three-component film are significantly greater than those of the MgO film.

Table 2. Band-energy parameters and values of σ_m and Y

Films	Structure	Thickness, Å	Φ, eV	E_g, eV	χ, eV	σ_m	Y
MgO/Mg	polycrys.	800	8.2	7.2	1.0	3.9	$3\cdot10^{-4}$
$Mg_{0.4}Ba_{0.6}O$/MgO	polycrys.	40	8.6	7.8	0.8	5.5	$5\cdot10^{-4}$

CONCLUSIONS

1. It has been shown that low-energy implantation of Ba^+ and Na^+ ions leads to a significant increase in the maximum value of the SEE coefficients and the quantum yield of photoelectrons. The main mechanisms leading to these changes have been revealed.
2. The method of implantation of Ba^+ ions into MgO with subsequent annealing has been used to obtain and determine the optimal conditions (energy and dose of ions, temperature of post-implantation annealing) for the synthesis of $Mg_{0.4}Ba_{0.6}O$ type films for the first time.
3. It has been pointed that the density of state of valence electrons and the parameters of the energy bands of MgO and $Mg_{0.4}Ba_{0.6}O$ differ significantly from each other.

ORCID

M.B. Yusupjonova, https://orcid.org/0000-0003-1189-687X; **D.A. Tashmukhamedova,** https://orcid.org/0000-0001-5813-7518
B.E. Umirzakov, https://orcid.org/0000-0002-9815-2111; **S.S. Pak,** https://orcid.org/0009-0004-0229-3895
Z.R. Saidakhmedova, https://orcid.org/ 0009-0003-5363-7590; **Sh.K. Salieva,** https://orcid.org/0009-0004-4022-9309

REFERENCES

[1] G. Balakrishnana, R. Velavana, K.M. Batoob, and E.H. Raslan, "Microstructure, optical and photocatalytic properties of MgO nanoparticles," Results Phys. **16**, 103013 (2020). https://doi.org/10.1016/j.rinp.2020.103013
[2] D. Lu, Q. Jiang, X. Ma, K. Wang, X. Fu, Y. Huang, and B. Hou, "Characterization of Zn in a polycrystalline MgO film Mater," Charact. **173**, 110955 (2021). https://doi.org/10.1016/j.matchar.2021.110955
[3] B. Nagappa, and G.T. Chandrappa, "Mesoporous nanocrystalline magnesium oxide for environmental remediation," Microporous Mesoporous Mater. **106**, 212-218 (2007).
[4] C.H. Park, J.Y. Choi, M.S. Choi, Y.K. Kim, and H.J. Lee, "Effects of MgO thin film thickness and deposition rate on the lifetime of ac plasma display panel," J. Surf. Coat. Technol. **197**, 223-228 (2005).
[5] F.M. Tezel, U. Veli, and I.A. Kariper, "Synthesis of MgO thin films: How heat treatment affects their structural, electro-optical, and surface properties," Materialstoday Communication, **33**, 104962 (2022). https://doi.org/10.1016/j.mtcomm.2022.104962
[6] I.M. Kotelyansky, V.B. Kravchenko, V.A. Luzanov, and A.T. Sobolev, Bull. Materials Sci. **14**(2), 479 (1991). (in Russian)
[7] Y. Chen, H. Ko, S. Hong, and T. Yao, "Layer-by-layer growth of ZnO epilayer on Al_2O_3(0001) by using a MgO buffer layer," Appl. Phys. Lett. **76**(5), 559-561 (2000). https://doi.org/10.1063/1.125817
[8] W.H. Butler, X.-G. Zhang, T.C. Schulthess, and J.M. MacLaren, "Spin-dependent tunneling conductance of Fe|MgO|Fe sandwiches," Phys. Rev. **63**(5), 054416 (2001). https://doi.org/10.1103/PhysRevB.63.054416
[9] A.I. Ektessabi, H. Nomura, N. Yasui, and Y. Tsukuda, "Ion beam processing of MgO thin films," Thin Solid Films, **447–448**, 383-387 (2004). https://doi.org/10.1016/S0040-6090(03)01092-7
[10] O.A. Golosov, S.S. Khvostov, N.V. Glushkova, M.V. Evseev, S.V. Staritsy, Yu.P. Zaikov, V.A. Kovrov, *et al.*, "Corrosive and mechanical resistance of MgO ceramics under metallizing and mild chlorination of spent nuclear fuel in molten salts," Ceramics International, **47**(3), 3306-3311 (2021). https://doi.org/10.1016/j.ceramint.2020.09.171
[11] Zh. Xu, U. Eduok, and J. Szpunar, "Effect of annealing temperature on the corrosion resistance of MgO coatings on Mg alloy," Surf. Coating. Technol. **357**, 691-697 (2019). https://doi.org/10.1016/j.surfcoat.2018.10.076
[12] M.M. Mikhailov, and V.A. Goronchko, "Optical properties and radiation stability of polypropylene modified with MgO nanoparticles," Spacecrafts & Technologies, **6**(2), 102-108 (2022). https://doi.org/10.26732/j.st.2022.2.04
[13] V. A. Luzanov, "Growth Features of Thin Epitaxial Magnesium Oxide Films on Sapphire," Journal of Communications Technology and Electronics, **64**(7), 720–721 (2019). https://doi.org/10.1134/S1064226919070118
[14] B.Ç. Toprak, H.İ. Efkere, S.Ş. Aydın, *et al.*, "Structural, morphological, optical and electrical characterization of MgO thin films grown by sputtering technique on different substrates," J. Mater. Sci: Mater Electron, **35**, 1389 (2024). https://doi.org/10.1007/s10854-024-13116-z
[15] D. Cáceres, I. Colera, I. Vergara, R. González, and E. Román, "Characterization of MgO thin films grown by rf-sputtering," Vacuum, **67**(3–4), 577-581 (2002). https://doi.org/10.1016/S0042-207X(02)00251-8
[16] T.T. Magkoev, G.S. Grigorkina, V.B. Zaalishvili, O.G. Burdzieva, E.N. Kozyrev, G.E. Tuaev, and K. Fukutani, "Feature of the MgO(111) Surface As a Substrate for Deposited Nanosized Au Particles in the Adsorption and Interaction of CO, NO, and O_2 Molecules," Russian Journal of Physical Chemistry A, 94(2), 401–404 (2020). https://doi.org/10.1134/S0036024420010203
[17] G.P. Panasyuk, E.A. Semenov, I.V. Kozerozhets, Kh.E. Yorov, L.A. Azarova, and A.I. Khol'kin, "A New Method of Synthesis of Nanosized Metal Oxide Powders," Doklady Chemistry, **482**, Part 1, 201–203 (2018). https://doi.org/10.1134/S0012500818090033
[18] M.H. Al-Timimi, W.H. Albanda, and M.Z. Abdullah, "Influence of Thickness on Some Physical Characterization for Nanostructured MgO Thin Films," East Eur. J. Phys. (2), 17 (2023). https://doi.org/10.26565/2312-4334-2023-2-17

[19] M. Tlili, C. Nefzi, B. Alhalaili, C. Bouzidi, L. Ajili, N. Jebbari, R. Vidu, *et al*., "Synthesis and Characterization of MgO Thin Films Obtained by Spray Technique for Optoelectronic Applications," Nanomaterials, **11**(11), 3076 (2021). https://doi.org/10.3390/nano11113076
[20] O.V. Diachenko, A.S. Opanasuyk, D.I. Kurbatov, N.M. Opanasuyk, O.K. Kononov, D. Nam, H. Cheong // ACTA PHYSICA POLONICA A. 2016. V. 130. No. 3. P. 805 – 810. https://doi.org/10.12693/APhysPolA.130.805
[21] P. Płóciennik, D. Guichaoua, A. Zawadzka, A. Korcala, J. Strzelecki, *et al*., "Optical properties of MgO thin films grown by laser ablation technique," Optical and Quantum Electronics, **48**(5), 277 (2016). https://dx.doi.org/10.1007/s11082-016-0536-8
[22] A. Kruk, "Fabrication of MgO high transparent ceramics by arc plasma synthesis," Opt. Mater. **84**, 360 (2018). https://doi.org/10.1016/j.optmat.2018.07.001
[23] S.D. Ponja, I.P. Parkin, and C.J. Carmalt, "Magnesium Oxide Thin Films with Tunable Crystallographic Preferred Orientation via Aerosol-Assisted CVD," Chemical Vapor Deposition, **21**(4-5-6), 145-149 (2015). https://doi.org/10.1002/cvde.201507156
[24] B.E. Umirzakov, D.A. Tashmukhamedova, and K.K. Kurbanov, "Estimation of changes in parameters of a crystal lattice and energy bands upon variation in the size of nanocrystals and nanofilms of silicides prepared by ion implantation," Journal of Surface Investigation, **5**(4), 693 (2011). https://doi.org/10.1134/S1027451011070214
[25] D.A. Tashmukhamedova, "Study of composition and electronic structure of $CoSi_2$/Si interface," Bulletin of the Russian Academy of Sciences: Physics, **70**(8), 1409 (2006).
[26] Z.A. Isakhanov, Z.E. Mukhtarov, B.E. Umirzakov, and M.K. Ruzibaeva, "Optimum ion implantation and annealing conditions for stimulating secondary negative ion emission," Technical physics, **56**(4), 546-549 (2011). https://doi.org/10.1134/S1063784211040177
[27] Kh.Kh. Boltaev, Zh.Sh. Sodikjanov, D.A. Tashmukhamedova, B.E. Umirzakov, "Composition and Structure of $Ga_{1-x}Na_xAs$ Nanolayers Produced near the GaAs Surface by Na^+ Implantation," Technical Physics, **62**(12), 1882-1884 (2017). https://doi.org/10.1134/S1063784217120040
[28] M.B. Yusupjanova, D.A. Tashmukhamedova, and B.E. Umirzakov, "Composition, morphology, and electronic structure of the nanophases created on the SiO_2 Surface by Ar^+ ion bombardment," Tech. Phys. 61, 628-630 (2016). https://doi.org/10.1134/S1063784216040253
[29] B.E. Umirzakov, T.S. Pugacheva, A.K. Tashatov, and D.A. Tashmuchamedova, "Electronic structure and optical properties of CaF_2 films under low energy Ba^+ ion-implantation combined with annealing," Nuclear Instruments and Methods in Physics Research Section B: Beam Interactions with Materials and Atoms, **166-167**, 572-576 (2000). https://doi.org/10.1016/S0168-583X(99)01151-9
[30] B.E. Umirzakov, D.A. Tashmukhamedova, M.K. Ruzibaeva, F.G. Djurabekova, and S.B. Danaev, "Investigation of change of the composition and structure of the CaF_2/Si films surface at the low-energy bombardment," Nuclear Instruments and Methods in Physics Research Section B: Beam Interactions with Materials and Atoms, **326**, 322-325 (2014). https://doi.org/10.1016/j.nimb.2013.10.094
[31] D.A. Tashmukhamedova, and M.B. Yusupjanova, "Formation of Nanoscale Structures on the Surface of MgO Films Upon Bombardment with Low-Energy Ions," Journal of Surface Investigation: X-ray, Synchrotron and Neutron Techniques, **15**(5), 1054-1057 (2021). https://doi.org/10.1134/S1027451021050402

ВПЛИВ ІМПЛАНТАЦІЇ АКТИВНИХ ІОНІВ МЕТАЛІВ НА СКЛАД, ЕМІСІЮ ТА ОПТИЧНІ ВЛАСТИВОСТІ ПЛІВОК MgO

М.Б. Юсупжонова, Д.А. Ташмухамедова, Б.Є. Умірзаков, С.С. Пак, З.Р. Сайдахмедова, Ш.К. Салієва
Ташкентський державний технічний університет імені Ісдама Карімова, Ташкент, 100095 Республіка Узбекистан

За допомогою комбінації методів вторинної та фотоелектронної спектроскопії досліджено склад, електронну структуру, емісійні та оптичні властивості плівок MgO/Mg, імплантованих іонами Ba+ та Na+ до та після відпалу. Показано, що після іонної імплантації в поверхневих шарах утворюються аморфні плівки, що складаються із сполук Mg – Ba – O, Mg – O, Ba – O, а також незв'язаних атомів Ba і Mg. При цьому eφ поверхні зменшується. Визначено, що ефективність випромінювання іонно-легованих шарів вища, ніж у шарів MgO. Постімплантаційний відпал при T = 900 K призводить до утворення однорідної плівки $Mg_{0,4}Ba_{0,6}O$ товщиною 30 – 35 Å у разі імплантації іонів Ba+. Виявлено, що глибина виходу фотоелектронів трикомпонентної плівки в 1,5 рази більша, ніж у оксиду Mg. Встановлено основні механізми зміни електронної структури, емісійних та оптичних властивостей MgO під час іонної імплантації та подальшого відпалу.

Ключові слова: *термічне окислення; іонна імплантація; фотоелектронна спектроскопія; квантовий вихід; ефективність еміссії; глибина виходу*

East European Journal of Physics. **1.** 265-271 (2025)
DOI:10.26565/2312-4334-2025-1-30 ISSN 2312-4334

INFLUENCE OF SIO_2 NANOPARTICLES ON THE CHARACTERISTICS OF A POLYVINYL ALCOHOL-BASED PROTON EXCHANGE COMPOSITE MEMBRANE

U.F. Berdiev, I.Kh. Khudaykulov*, Sh.Ch. Iskandarov, A.J. Amirova, Kh.B. Ashurov
U.A. Arifov Institute of Ion-Plasma and Laser Technologies, Academy of Sciences of Uzbekistan
100125, Durmon Yuli str. 33, Tashkent, Uzbekistan
**Corresponding Author e-mail: i_khudaykulov@mail.ru*
Received September 12, 2024; revised January 23, 2025; accepted January 25, 2025

This paper presents a study of nanocomposite membranes based on cross-linked polyvinyl alcohol with silica nanoparticles, fabricated by solution casting, for application in vanadium redox batteries (VRFBs). The structure of the membranes was studied by Fourier transform infrared spectroscopy (FT-IR). It was found that the nanoparticles were successfully integrated into the matrix of the proton exchange membrane to improve its performance. The synthesis of silica nanoparticles by in situ sol-gel method in polymer solution showed better performance compared to the addition of prepared nanoparticles. The membrane properties such as mechanical properties, water absorption, ion exchange material (IEM), proton conductivity and permeability to vanadium ions were investigated. The nanocomposite membranes showed higher water absorption, IEM and lower permeability for vanadium ions compared to Nafion117 membrane. The test results of single cell VRFB with nanocomposite membranes showed higher Coulomb yield (CE) and efficiency (EE) up to 81.51% compared to Nafion117. The self-discharge rate of VRFBs with nanocomposite membranes was lower than that of Nafion117. After 50 test cycles, the nanocomposite membrane showed stable battery performance. The results indicate that nanocomposite membranes are a promising and affordable alternative material for Nafion117 in VRFBs.
Keywords: *Proton exchange membrane; Nanocomposite membranes; Polyvinyl alcohol-based separation membranes; Nafion117; Vanadium redox flow batteries; Tetroethoxysilane; Alkylbenzosulfonic acid*
PACS: 81.05.Lg; 82.45.Yz; 82.35.Lr

1. INTRODUCTION

Vanadium redox flow batteries (VRFBs) have attracted much attention in recent decades due to their outstanding advantages such as low cost, high efficiency, good cyclic stability and promising applications in large-scale energy storage. In VRFBs, the proton exchange membrane (PEM) is an important separator between the catholyte and anolyte, which prevents the mixing of electrolytes while allowing the migration of conductive H^+ and SO_4^{2-} ions to complete the electrical circuit. An ideal PEM should have high ionic conductivity, low permeability to vanadium, high mechanical strength and good chemical stability [1]. For real commercialization of VRFB, the cost of its separator is crucial. Although many high-performance PEMs can be prepared from specially designed polymers and fillers, the cost associated with the complete synthesis process can be very high. In addition, these syntheses cannot be easily scaled up. The most widely used Nafion membranes, typical perfluorinated sulfonic acid polymeric materials developed by DuPont, are recognized as a reference material for VRFBs due to their high proton conductivity and excellent chemical stability. However, problems with the high permeability to vanadium in Nafion membranes, as well as their low ion selectivity and high cost, still limit their widespread application in VRFBs [2]. Sulfinated polymers have attracted attention because of their good proton conductivity over a wide temperature range and low fabrication cost [3]. Modification or synthesis conditions due to the use of strong sulfating agents lead to partial degradation of the polymer chain and cause undesirable change in the polymer by rearrangement of intermediate functional units of sulfo groups [4]. As another disadvantage, there are reports in which the sulfonic group undergoes substitution by electrophilic aromatic proton substitution mechanicm to reduce the hydrolytic stability of the membrane [5]. To address these drawbacks, polymerization of sulfated aromatic monomers [6] is underway, but the use of expensive catalysts limits its large-scale production. Meanwhile, the preparation of commercial anion exchange membrane involves chloromethylation using chloromethyl methyl ether which is considered hazardous to the environment, followed by amination of polymers [7].

To eliminate such operations such as sulfation/amination, an alternative approach is to provide the polymer matrix with inorganic materials to obtain inorganic-organic composite ion exchange membranes that will have the properties and characteristic features of inorganic and organic compounds [8]. The inherent hydrophilicity of polyvinyl alcohol (PVA), abundant reactive hydroxyl groups and low cost are reasons for its selection as a typical host matrix [9]. Among the numerous inorganic materials, silica, including porous silicon, which has demonstrated significant potential for solar energy applications [10], is the most commonly used inorganic filler used in PVA matrix to improve the mechanical strength, thermal stability, water retention capacity and proton conductivity of the membrane [11]. Incorporation of silica nanoparticles into the PVA membrane using a solution-gel in situ (sol-gel) process is a novel approach compared to direct physical mixing [12]. Silicon dioxide nanoparticles in the composite is dominated by certain interconnected conductive channels due to the uniform distribution of nanoparticles [13]. The compatibility of organic and inorganic phases is

Cite as: U.F. Berdiev, I.Kh. Khudaykulov, Sh.Ch. Iskandarov, A.J. Amirova, Kh.B. Ashurov, East Eur. J. Phys. 1, 265 (2025), https://doi.org/10.26565/2312-4334-2025-1-30
© U.F. Berdiev, I.Kh. Khudaykulov, Sh.Ch. Iskandarov, A.J. Amirova, Kh.B. Ashurov, 2025; CC BY 4.0 license

determined by multiple covalent bonds, hydrogen bonds and electrostatic interactions [14]. Enhancement of proton conductivity in PVA/SiO_2 composite membranes is achieved by various strategies, of which the most common practices include (a) incorporation of functionalized silica, (b) functionalization of PVA, and (c) blending of PVA/SiO_2 with charged polymers/nanomaterials [15-16]. A group of scientists created based on the above methods used to fabricate a PVA/SiO_2 composite separator with high proton conductivity for energy devices [17]. Hybrid membranes have been developed by dispersing sulfated nanosilica in a cross-linked PVA matrix with sulfated tetraethoxysilane (TEOS) [18]. The PVA and chitosan membrane composite with silica gel functionalized with poly (2-acrylamido-2-methyl-1-propanesulfonic acid) showed good thermal and oxidative stability [19]. Controlling the level of functionalization and crosslinking plays a key role, as excessive functional groups can impair the mechanical stability and insufficient crosslinking negatively affects the membrane stability.

The aim of the present study is to investigate the effect of different types of silica nanoparticles on the properties of proton exchange membranes. This paper presents the synthesis of PVA/SiO_2 composite membrane by mixing silica nanoparticles with PVA. Two membranes were fabricated in which SiO_2 was filled with SiO_2 by sentinel sol gel method in polymer solution and prepared with mechanical solution blending of prepared SiO_2 nanopowder. The SiO_2 and PVA matrix functioned as a barrier for vanadium ions, formed a well-defined conductive structure to transfer charge balancing hydrated protons during vanadium flow battery operation.

2. EXPERIMENTAL

For the experiments we used standard PVA grade "h" with viscosity 18 mPa×s and degree of hydrolysis 89%, (average M=85000-146000 g/mol), tetroethoxysilane (TEOS) and similar alkylbenzosulfonic acid (ABSA), succinic acid "hh", hydrochloric acid grade "hh" and on Sigma-Aldrich. The prepared silica nanopowders were obtained from the authors [20], pre-milled with a Retsch PM-400 nanomill (Germany) to mechanically activate the powdered material. Deionized water with a resistivity of 10 MΩ was used. To compare the characteristics of the obtained membranes we used a commercial sample of Nafion117 membrane from DuPont Co.

To prepare the first membrane sample, an aqueous solution of PVA with concentrations of 2.5, 5 and 10 wt.% was prepared by dissolving PVA in deionized water at 80°C and stirring constantly for 6 hours. The solution was cooled to room temperature before adding succinic acid at a molar ratio of PVA:JA of 1:0.25. The solution was stirred at 70℃ for 4 hours. After that, a solution of H_2O, HCl and TEOS taken in the molar ratio of 5:0, 1:1 was added. Stirring was continued for another 2 hours, then the solution was poured into Plexiglas and then heated at 40℃ for 24 hours to induce cross-linking reaction. The resulting membrane was separated and then soaked in 0.5 M alkylbenzosulfonic acid solution for 1 hour. The membrane was heated at 40℃ for 2 hours to delineate the crosslinking reaction. Before molding, the mixture was ultrasonicated for 30 min to avoid aggregation. The resulting composite membranes were labelled as 1-PVA/SiO_2.

For the preparation of the second membrane sample, the synthesis sequence was carried out in the same way, only after complete dissolution of the polymer, mechanically activated silica nanopowder was added. The rest of the synthesis steps were continued accordingly. The obtained composite membranes were denoted as 2-PVA/SiO_2.

FT-IR spectra of the membranes were measured on a Nicolet 6700 spectrometer instrument in the range of 4000-600 cm^{-1}. The samples were dried at 50°C for 2 h before measurement. The mechanical properties of the blended membranes were measured using a Shimadzu AGS-X. rupture machine at room temperature. The samples were tested at an elongation rate of 5.0 mm/min.

The membranes were dried at 80℃ in vacuum for 24 h and the dry weight of the samples was weighed. The membranes were then immersed in deionized water for 24 h at room temperature. After wiping off the water adhering to the surface of the membranes, the mass and dimensions of the wet membranes were measured. The water absorption and swelling coefficient were determined using the following equations:

$$Water\ uptake = \frac{W_{Wet} - W_{dry}}{W_{dry}} \times 100\%,$$

where W_{wet} and W_{dry} are the masses of membranes in wet and dry states, respectively.

$$\text{swelling ratio} = \frac{L_{Wet} - L_{dry}}{L_{dry}} \times 100\%,$$

where L_{wet} and L_{dry} are the size of membranes in wet and dry states, respectively.

Ion exchange capacity of membranes (IEM) was determined by titration method. Dry membranes were immersed in NaCl solution with a concentration of 1 mol/L for 24 hours. This solution was titrated with 0.01 mol l-1NaOH using phenol-phthalein as an indicator. The IEM of the samples was calculated according to the following equation:

$$\text{IEM} = \frac{V(NaOH) \times C(NaOH)}{W_{dry}}.$$

Where V (NaOH) is the volume of NaOH solution consumed, C(NaOH) is the concentration of NaOH solution, and W dry is the weight of dry membrane.

The area resistance of the membranes was measured by the method described in the literature [21]. The measurement was performed using a two-chamber device consisting of two cells separated by a membrane. Both compartments were filled with 1 M H_2SO_4. The effective area of the membrane was 0.500 cm^2. The electrical resistivity was measured by electrochemical impedance spectroscopy (EIS) (CORTEST 350CS, China) in the frequency range of 100 kHz to 100 MHz. The resistance value related to membrane conductivity was determined from the high-frequency intersection of the impedance with the real axis. The area impedance R was calculated using the following expressions:

$$R=(r_1-r_2)S$$

where r_1 and r_2 are electrical resistances of the cell with and without membrane, respectively. Proton conductivity was calculated from the equation:

$$\varrho=L/R$$

where L and R are the thickness and resistance area of the membrane, respectively.

To measure the permeability of vanadium ions, the membranes were exposed to a solution of 1.5 M $VOSO_4$ and 3 M H_2SO_4 (left cell reservoir) and a solution of 1.5 M $MgSO_4$ and 3 M H_2SO_4 (right cell reservoir). $MgSO_4$ was used to equalize ionic strength and reduce the effect of osmotic pressure. The effective membrane area was 0.5 cm^2. Samples from the left cell reservoir were taken at regular intervals and analyzed for vanadium ion concentration using a UV spectrometer (UV-2550, SHIMADZU). Vanadium ion permeability was calculated from the following equation:

$$V_R=\frac{dC_R(t)}{dt}=A_\tau^P[C_L-C_R(t)]$$

where P – is the permeability to vanadium ions, C_L is the concentration of vanadium ions in the left reservoir, and $C_R(t)$ is the concentration of vanadium ions in the right cell reservoir as a function of time. A_τ^p — membrane area, V_R – volume of the cell reservoir. Usually, the change in the concentration of vanadium ions in the left cell reservoir can always be insignificant.

To test the resulting membranes, a single VRB cell was assembled by placing a membrane between two parts of graphite plate electrodes with an effective reaction area of 50 mm^2. The material of the current collector was a graphite plate. The initial negative and positive electrolytes were solutions of 1.5 M V^{3+} in 3.0 M H_2SO_4 and 1.5 and VO^{2+} in 3.0 M H_2SO_4, respectively. The volume of electrolyte on each side of the cell was 100 ml. Both positive and negative electrolytes were cycled into the respective half-cell at a rate of 0.5 L/min. A charge-discharge cycle was conducted at CORTEST 350CS, China with a constant current density of 50 mA cm^{-2} at 25°C. The charge and discharge cutoff voltages were set to 1.65 V and 0.8 V, respectively, to avoid corrosion of graphite felts and graphite plates. Coulomb efficiency (CE), voltage efficiency (VE) and energy efficiency (EE) of the cell are calculated using the following equations:

$$CE=\frac{Q_{discharge}}{Q_{charge}}\times 100\%=\frac{I_{charge}t_{discharge}}{I_{charge}t_{charge}}\times 100\%=\frac{t_{discharge}}{t_{charge}}\times 100\%$$

$$VE=\frac{V_{discharge}}{V_{charge}}\times 100\%$$

$$EE=CE\times VE$$

3. RESULTS AND DISCUSSION

Composite membranes containing silicon dioxide nanoparticles are obtained. During the manufacture of these membranes, 2.5% silica nanoparticles were added to the composition based on the weight of the polymer.

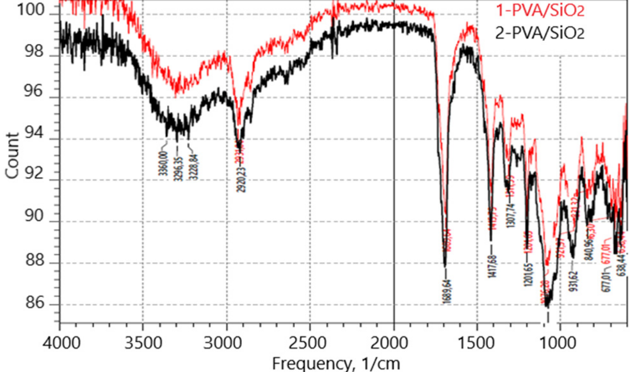

Figure 1. FTIR-ATR spectra of 1-PVA/SiO_2 and 2-PVA/SiO_2 nanocomposite membranes

PVA crosslinking is visible from FT-ATR membrane spectra (Fig. 1). Characteristic peaks of PVA and SiO_2, i.e. ~ 3360 (OH draw), ~ 1450 (OH bend) and ~ 1080 cm^{-1} (C-OH draw) [22] and symmetrical Si-O-Si stretch band at ~ 840 cm^{-1} and asymmetrical Si-O-Si stretch at 1076 – 1201 cm^{-1} were positive for both membranes [23]. On close inspection of the spectra, instead of a broad peak for OH, there is a small protrusion with a certain amount of tensile noise signal, indicating effective thermal crosslinking of the membrane. The spectra also showed characteristic C-H, C = O and C = O bands at 2920, 1049 and 1076 cm^{-1}, respectively. In addition, two characteristic peaks at 1007 and 1034 cm^{-1} were assigned to the bands containing SO_3H- groups, respectively [24].

The water absorption coefficient, the swelling coefficient of the IEM are important parameters for characterizing the proton exchange membrane. Many important properties of the membrane, such as proton conductivity and water uptake, are related to IEM and directly depend on the content of free sulfonic acid groups in the membrane. It can be seen that the IEM of the membranes decreases with an increase in nanoparticles in the polymer matrix by 10% (Table 1). High water uptake can improve proton conductivity. However, this also leads to poor dimensional stability and high permeability of vanadium. It was to regulate these membrane characteristics that silica nanoparticles were introduced into the PVA polymer matrix. In addition, the formation of a crosslinked network structure due to silica nanoparticles reduces the free volume in mixed membranes for water molecules, which leads to a decrease in water absorption. The swelling ratio reflects dimensional stability, and a lower swelling ratio is necessary to maintain the size stability of the membrane for a long time. The permeability of vanadium ions is a crucial parameter for VRFB, which is the ability to prevent mixing of positive and negative electrolytes with each other. Diffusion of vanadium ions through the membrane will lead to self-discharge of the battery. This study measured the permeability to vanadium ions of nanocomposite membranes. The vanadium ion concentration in the right tank versus time is shown in Figure 2 and the calculated vanadium permeability coefficients are shown in Table 1.

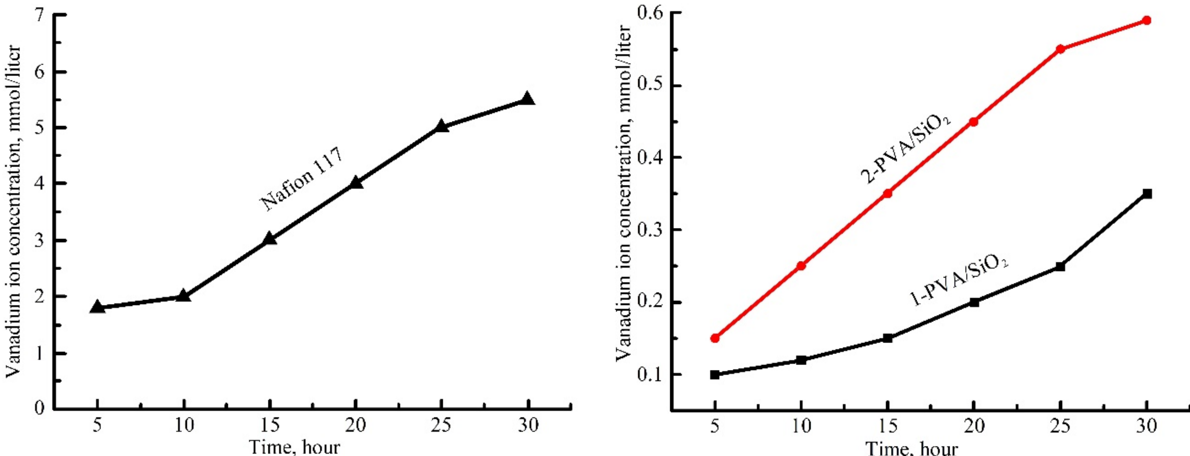

Figure 2. Concentration of vanadium ions in the right cell reservoir by membrane Nafion117 and composite membranes 1-PVA/SiO_2 and 2-PVA/SiO_2

Table 1. Basic properties of nanocomposite membranes and Nafion117 membrane

No.	Membrane type	IEM (mmol/liter)	Swelling ratio (%)	Water uptake (%)	Vanadium ion permeability coefficient (10^{-8} cm^2 s^{-1})	Tensile strength, MPa	Relative lengthening at rupture,%
1	1-PVA/SiO_2						
	2,5% SiO_2	1.47	36.7	22	6.1	2.8	78
	5% SiO_2	1.2	29.5	20	5.8	5.6	52
	10% SiO_2	0.83	21	17	4.7	8.3	43
2	2- PVA /SiO_2						
	2,5% SiO_2	1.13	29.3	21,7	3.8	1.8	50
	5% SiO_2	0.93	23.2	19	3.5	6	85
	10% SiO_2	0.86	26	18	3.4	7.5	27
3	Nafion 117	0.92	20	17	54.8	96	168

All nanocomposite membranes have a lower vanadium ion permeability than the Nafion117 membrane. The permeability of the membrane is 1-PVA/SiO_2, 5.8x10^{-8} cm^2s^{-1} compared to the membrane Nafion117 54.8×$10^{-8}cm^2s^{-1}$. It can also be seen that the permeability of the mixed membranes decreases with increasing silica in the nanocomposite. The difference in vanadium ion permeability between nanocomposite membranes and Nafion117 membrane is determined by their microstructure. The microstructure of the Nafion117 membrane consists of two parts: highly hydrophilic sulfone functional groups and highly hydrophobic fluorocarbon main chains. This will result in

hydrophobic/hydrophilic microphase separation. Because of the high flexibility of fluorocarbon, clusters of hydrophilic sulfone groups tended to form hydrophilic domains.

Not only protons, but also vanadium ions could penetrate these membrane domains when used in VRFB. Compared to the Nafion117 membrane, the backbone PVA/SiO_2 less hydrophobic, which prevents the aggregation of dispersed sulfone groups into hydrophilic domains. Thus, the water-filled channels in the membrane are PVA/SiO_2 narrow and branched compared to those in the Nafion117 membrane.

Many important properties, such as proton conductivity and swelling, are associated with IEM. IEM directly depends on the content of free sulfonic acid groups in the membrane. From Table 2. it can be seen that the IEM of the composite membranes did not change and did not depend on the content of silica nanoparticles, but they were closer to those of Nafion 117. Typical charge-discharge curves of a single VRFB with composite membranes and Nafion 117 are shown in Fig. 3. The capacity of a single VRB cell using Nafion117 and composite membranes is shown in Table 2.

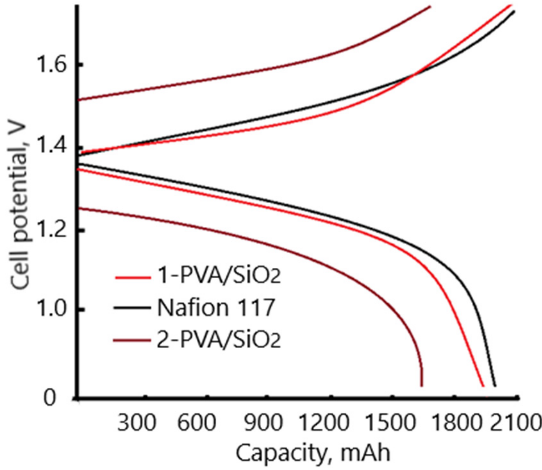

Figure 3. Charge-discharge curves for VRFB with Nafion 117 and membranes 1-PVA/SiO_2 and 2-PVA/SiO_2.

Table 2. Electrochemical properties of nanocomposite and Nafion117 membranes.

№	Membrane type	IEM (mmol g^{-1})	Proton conductivity $mS\times cm^{-1}$	CE(%)	VE(%)	EE(%)
1	1-PVA/SiO_2					
	2,5% SiO_2	0.83	10.9	97.3	70.1	70.36
	5% SiO_2	0.86	12.6	99.5	83.8	81.51
	10% SiO_2	0.82	9.6	94.6	76.3	75.3
2	2- PVA /SiO_2					
	2,5% SiO_2	0.85	10.3	92.3	70.2	70.1
	5% SiO_2	0.82	9.2	91.2	70.8	74.2
	10% SiO_2	0.84	9.8	90.7	73.2	72.8
3	Nafion 117	0.91	12	92.6	83.3	76.8

The discharge test was performed at the same current density of 50 mA cm^{-2} for all membranes. Coulomb efficiency of VRB with all composite membranes showed almost the same efficiency compared to VRB with Nafion117 membrane. In addition, n CE increased from 97.3% to 99.5% by increasing the amount of silica from 2.5% to 5% in the sol-gel 1-PVA/SiO_2 membranes and then decreased to 94.6% in the 10% silica membrane. In 2-PVA/SiO_2 membranes, CE showed values of about 90-92%. This is because the CE of VRFB is determined by the membrane permeability to vanadium ions and ion permeability. All composite membranes have significantly lower permeability than the Nafion117 membrane. In addition, with an increase in silica, the proton conductivity of vanadium ions and the conductivity of vanadium ions decrease. Thus, a balance between ion permeability and vanadium permeability can be achieved by varying the composition of the composite membranes in the VRFB system.

4. CONCLUSIONS

Nanocomposite membranes based on cross-linked polyvinyl alcohol with silicon dioxide nanoparticles were made by solution casting for use in VRFB. The membrane structure was characterized by FT-IR methods. The results showed that the nanocomposites were successfully embedded in the proton-exchange membrane matrix and showed good results. The synthesis of silica nanoparticles by sol gel method in a polymer solution has been established to give the membrane better qualities than the addition of finished nanoparticles in a polymer solution. Membrane properties such as mechanical properties, water absorption, IEM, proton conductivity and vanadium ion permeability were investigated. Compared to

Nafion117 membranes, nanocomposite membranes showed high water absorption, IEM and lower permeability to vanadium ions. In a single cell test, VRFB with nanocomposite membranes showed a higher CE than Nafion117, EE membranes up to 81.51%. The self-discharge rate of VRFB with the nanocomposite membrane was lower than that of the Nafion117 membrane. After 50 test cycles, the mixed membrane showed stable battery performance. Given these results, nanocomposite membrane membranes are expected to be ideal available membranes that can Nafion117 competitive for VRFB applications.

Funding

The authors gratefully acknowledge the financial and technical support provided by the Ministry of Higher Education, Science, and Innovation under project number IL-5421101842.

ORCID

U.F. Berdiev, https://orcid.org/0000-0003-2808-0105; **I.Kh. Khudaykulov,** https://orcid.org/0000-0002-2335-4456
Sh.Ch. Iskandarov, https://orcid.org/0000-0002-3002-9141; **Kh.B. Ashurov,** https://orcid.org/0000-0002-7604-2333

REFERENCES

[1] M.A. Hickner, H. Ghassemi, Y.S. Kim, B.R. Einsla, and J.E. McGrath, "Alternative polymer systems for proton exchange membranes (PEMs)," Chem. Rev. **104**, 4587-4611 (2004). https://doi.org/10.1021/cr020711a
[2] C.H. Lin, M.C. Yang, and H.J. Wei, "Amino-silica modified Nafion membrane for vanadium redox flow battery," Journal of Power Sources, **282**, pp.562–571 (2015). https://doi.org/10.1016/j.jpowsour.2015.02.102
[3] M.-S. Kang, Y.-J. Choi, I.-J. Choi, T.-H. Yoon, and S.-H. Moon, "Electrochemical characterization of sulfonated poly(arylene ether sulfone) (S-PES) cation-exchange membranes," J. Membr. Sci. **216**, 39–53 (2003). https://doi.org/10.1016/S0376-7388(03)00045-0
[4] X. Zhang, Q. Liu, L. Xia, D. Huang, X. Fu, R. Zhang, S. Hu, *et al.*, "Poly (2, 5-benzimidazole)/sulfonated sepiolite composite membranes with low phosphoric acid doping levels for PEMFC applications in a wide temperature range," Journal of membrane science, **574**, 282-298 (2019). https://doi.org/10.1016/j.memsci.2018.12.085
[5] R.K. Nagarale, G.S. Gohil, and V.K. Shahi, "Recent developments on ion-exchange membranes and electro-membrane processes," Adv. Colloid Interface Sci. **119**, 97–130 (2006). https://doi.org/10.1016/j.cis.2005.09.005
[6] M.K. Pagels, S. Adhikari, R.C. Walgama, A. Singh, J. Han, D. Shin, and C. Bae, "One-Pot Synthesis of Proton Exchange Membranes from Anion Exchange Membrane Precursors," ACS Macro Lett. **9**, 1489–1493 (2020). https://doi.org/10.1021/acsmacrolett.0c00550
[7] P.K. Prajapati, N.N. Reddy, R. Nimiwal, P.S. Singh, S. Adimurthy, and R.K. Nagarale, "Polyaniline@porous polypropylene for efficient separation of acid by diffusion dialysis," Sep. Purif. Technol. **233**, 115989 (2020). https://doi.org/10.1016/j.seppur.2019.115989
[8] G.M. Aparicio, R.A. Vargas, and P.R. Bueno, "Protonic conductivity and thermal properties of cross-linked PVA/TiO_2 nanocomposite polymer membranes," J. Non Cryst. Solids, **522**, 119520 (2019). https://doi.org/10.1016/j.jnoncrysol.2019.119520
[9] Y. Jin, J.C. Diniz da Costa, and G.Q. Lu, "Proton conductive composite membrane of phosphisilicate and polyvinyl alcohol," Solid State Ion. **178**, 937–942 (2007). https://doi.org/10.1016/j.ssi.2007.04.005
[10] V.M. Rotshteyn, T.K. Turdaliev, and Kh.B. Ashurov, "On the Question of the Possibility of Using Nanocrystalline Porous Silicon in Silicon-Based Solar Cells," Applied Solar Energy, **57**(6), 480–485 (2021). https://doi.org/10.3103/S0003701X21060153
[11] T. Kamjornsupamitr, T. Sangthumchai, S. Youngme, and S. Martwiset, "Proton conducting composite membranes from crosslinked poly(vinyl alcohol) and poly(styrene sulfonic acid)-functionalized silica nanoparticles," Int. J. Hydrogen Energy, **43**, 11190–11201 (2018). https://doi.org/10.1016/j.ijhydene.2018.04.198
[12] U. Berdiev, I. Khudaykulov, Sh. Iskandarov, and T. Turdaliev, "Mechanical properties of a proton exchange composite membrane synthesized on the basis of polyvinyl alcohol," Uzbek Physical Journal, **25**(4), 72-76 (2024). https://doi.org/10.52304/.v25i4.479 (in Russian)
[13] Y. Zhang, M. Guo, H. Yan, G. Pan, J. Xu, Y. Shi, and Y. Liu, "Novel organic–inorganic hybrid composite membranes for nanofiltration of acid and alkaline media," RSC Adv. **4**, 57522 (2014). https://doi.org/10.1039/C4RA09090J
[14] Y. Wang, D. Wang, J. Wang, and L. Wang, "Preparation and characterization of a sol-gel derived silica/PVA-Py hybrid anion exchange membranes for alkaline fuel cell application," J. Electroanal. Chem. **873**, 114342 (2020). https://doi.org/10.1016/j.jelechem.2020.114342
[15] J.M. Dodda, P. Belský, J. Chmelar, T. Remis, K. Cmolna, M. Tomáš, L. Kullova, *et al.*, "Comparative study of PVA/SiO2 and PVA/SiO2/glutaraldehyde (GA) nanocomposite membranes prepared by single-step solution casting method." J. Mater. Sci. **50**, 6477–6490 (2015). https://doi.org/10.1007/s10853-015-9206-7
[16] E. Sgreccia, *et al.*, "Silica containing composite anion exchange membranes by sol–gel synthesis: A short review," Polymers, **13**(11), 1874 (2021). https://doi.org/10.3390/polym13111874
[17] H. Beydaghi, M. Javanbakht, and A. Badiei, "Cross-linked poly(vinyl alcohol)/sulfonated nanoporous silica hybrid membranes for proton exchange membrane fuel cell," J. Nanostruct. Chem. **4**, 97 (2014). https://doi.org/10.1007/s40097-014-0097-y
[18] S.N. Hegde, B.B. Manuvalli, and M.Y. Kariduraganavar, "A Unique Approach for the Development of Hybrid Membranes by Incorporating Functionalized Nanosilica into Crosslinked sPVA/TEOS for Fuel Cell Applicationsm" ACS Appl. Energy Mater. **5**, 9823–9829 (2022). https://doi.org/10.1021/acsaem.2c01525
[19] C. Panawong, S. Tasari, P. Saejueng, and S. Budsombat, "Composite proton conducting membranes from crosslinked poly(vinyl alcohol)/chitosan and silica particles containing poly(2-acrylamido-2-methyl-1-propansulfonic acid)," J. Appl. Polym. Sci. **139**, 51989 (2022). https://doi.org/10.1002/app.51989
[20] M. Kurbanov, S. Tulaganov, U. Nuraliev, L. Andriyko, O. Goncharuk, N. Guzenko, Y. Nychyporuk, *et al.*, "Comparative characteristics of the structure and physicochemical properties of silica synthesized by pyrogenic and fluoride methods," Silicon, **15**(3), 1221-1233 (2023). https://doi.org/10.1007/s12633-022-02087-7

[21] G.J. Hwang, and H. Ohya, "Preparation of cation exchange membrane as a separatorfor the all-vanadium redox flow battery, J. Membrane Sci. **120**, 55(1996). https://doi.org/10.1016/0376-7388(96)00135-4
[22] V.V. Binsu, R.K. Nagarale, V.K. Shahi, and P.K. Ghosh, "Studies on N-methylene phosphonic chitosan/poly(vinyl alcohol) composite proton-exchange membrane," React. Funct. Polym. **66**, 1619–1629 (2006). https://doi.org/10.1016/j.reactfunctpolym.2006.06.003
[23] R.K. Nagarale, G.S. Gohil, V.K. Shahi, and R. Rangarajan, "Preparation of organic–inorganic composite anion-exchange membranes via aqueous dispersion polymerization and their characterization," J. Colloid Interface Sci. **287**, 198–206 (2005). https://doi.org/10.1016/j.jcis.2005.01.074
[24] D.S. Kim, H.B. Park, J.W. Rhim, and Y.M. Lee, "Preparation and characterization of crosslinked PVA/SiO_2 hybrid membranes containing sulfonic acid groups for direct methanol fuel cell applications," J. Memb. Sci. **240**, 37-48 (2004). https://doi.org/10.1016/j.memsci.2004.04.010

ВПЛИВ НАНОЧАСТИНОК SIO_2 НА ХАРАКТЕРИСТИКИ ПРОТОНООБМІННОЇ КОМПОЗИТНОЇ МЕМБРАНИ НА ОСНОВІ ПОЛІВІНІЛОВОГО СПИРТУ

У.Ф. Бердієв, І.Х. Худайкулов, Ш.Ч. Іскандаров, А.Й. Амірова, Х.Б. Ашуров
Інститут іонно-плазмових і лазерних технологій імені У.А. Арифова Академії наук Узбекистану
100125, Дурмон Юлі вул. 33, Ташкент, Узбекистан

У цій статті представлено дослідження нанокомпозитних мембран на основі зшитого полівінілового спирту з наночастинками кремнезему, виготовлених методом лиття з розчину, для застосування в ванадієвих окисно-відновних батареях (VRFB). Структуру мембран вивчали методом інфрачервоної спектроскопії з перетворенням Фур'є (FT-IR). Було виявлено, що наночастинки були успішно інтегровані в матрицю протонообмінної мембрани для підвищення її продуктивності. Синтез наночастинок кремнезему золь-гель методом in situ в розчині полімеру показав кращу продуктивність порівняно з додаванням готових наночастинок. Були досліджені такі властивості мембрани, як механічні властивості, водопоглинання, іонообмінний матеріал (IEM), протонна провідність і проникність для іонів ванадію. Нанокомпозитні мембрани продемонстрували вищі водопоглинання, IEM і нижчу проникність для іонів ванадію порівняно з мембраною Nafion117. Результати випробувань однокомпонентного VRFB з нанокомпозитними мембранами показали вищий кулонівський вихід (CE) і ефективність (EE) до 81,51% порівняно з Nafion117. Швидкість саморозряду VRFB з нанокомпозитними мембранами була нижчою, ніж у Nafion117. Після 50 циклів тестування нанокомпозитна мембрана показала стабільну роботу акумулятора. Результати показують, що нанокомпозитні мембрани є перспективним і доступним альтернативним матеріалом для Nafion117 у VRFB.
Ключові слова: *протонообмінна мембрана; нанокомпозитні мембрани; розділові мембрани на основі полівінілового спирту; Нафіон117; ванадієві окисно-відновні батареї; тетроетоксисилан; алкілбензосульфонова кислота*

EAST EUROPEAN JOURNAL OF PHYSICS. **1**. 272-275 (2025)
DOI:10.26565/2312-4334-2025-1-31 ISSN 2312-4334

ANALYSIS OF THE ION BEAM COMPOSITION OF InSb AND $(InSb)_{0.98}Bi_{0.02}$ OBTAINED BY LIQUID METAL ION SOURCE

F.E. Mammadov*, S.A. Aliev, I.I. Gurbanov, Sh.O. Eminov, A.J. Khalilov, E.M. Akberov, A.A. Badalov
Institute of Physics of the Ministry of Education and Science of the Republic of Azerbaijan
G. Javidave., 131, Az1143, Baku, Azerbaijan
**Corresponding Author e-mail: Shikhamirem@gmail.com, mammadov.f.e@gmail.com*
Received November 5, 2024; revised January 21, 2025; in final form January 26, 2025; accepted February 6, 2025

To investigate the mass composition of the ion beam obtained through field ion emission, a mass analyzer designed analogous to the Wien velocity filter was utilized. This Wien filter analyzer operates based on the principle of intersecting mutually perpendicular electric and magnetic fields (E×B) to classify charged particles according to their mass and charge. The ion beam was obtained using mInSb and $InSb_{0.98}Bi_{0.02}$ as the working materials. The mass composition of the ion group was analyzed using this method. In the experiments, it was found that the ion beam obtained using InSb as the working substance had a homogeneous composition, consisting solely of $(InSb)^+$ ions. However, in contrast, when the working substance was $(InSb)_{0.98}Bi_{0.02}$, it was determined that the ion beam had a miscellaneous composition. In addition to $(InSb)^+$ ions, the ion beam was found to contain $((InSb)_{0.98}Bi_{0.02})^+$ and $(Bi)^+$ ions.
Key words: *Liquid metal ion sources; LMIS; Sharp emitter; Ion beam; Mass analysis; InSb; InSbBi*
PACS: 29.25.Ni; 52.25.Tx; 81.16.Rf

INTRODUCTION

A highly promising method for modification various surface structures is the deposition of nanodroplets on a conductive surface. Liquid metal ion sources (LMIS) or electrohydrodynamic ion sources (EHD emitters) with sharp emitters are commonly used for this purpose [1]. Sharp emitters exhibit the highest current density and a remarkably small emission area. They are capable of generating charged droplets of the working substance with nanoscale dimensions. The ability to focus the generated beams to submicron sizes makes them suitable for applications in microtechnology. Moreover, the generation of nanoparticles with diverse compositions is of great interest for thin film deposition and nanotechnology.

Under specific operating conditions, these sources also generate charged nanoparticles [2]. The determination of the emission area size in these sources has been the subject of extensive experimental and theoretical research. Theoretical estimates for the diameter of the emission area indicate a value of around 3-4 nm [3]. Based on this size, a high initial current density on the order of $10^8 A/cm^2$ is achieved.

Liquid metal ion sources have been the subject of intensive research in recent years, particularly for applications in submicrometer lithography, ion-stimulated chemical synthesis, implantation, and microanalysis. These sources are being studied for their capability to fabricate, analyze, and process surface relief with submicrometer resolution using focused ion beams. Initially, liquid metal ion sources relied on pure metals with low melting points as the working substances. However, addressing numerous contemporary technological tasks, including localized ion implantation, ion beam mixing, direct non-resistive ion lithography, and the fabrication of micro and nanoelectromechanical systems, necessitates the application of ion beams with various masses, charge states, and chemical properties [4]. This fact has stimulated the development of liquid metal ion sources using alloys, which allow for the generation of a wide range of different ions [5].

The purpose of the work is to obtain ion beams in liquid metal ion sources based on InSb and $(InSb)_{0.98}Bi_{0.02}$ working materials and to study their composition using an (E×B) Wien velocity filter [6].

EXPERIMENT

The experiment was conducted in a vacuum chamber, specifically a Leybold-Heraeus type A700Q, and the overall schematic of the experiment is provided in Figure 1 [7,8]. A needle made of nickel-chromium (NiCr) with a diameter of 0.5 mm was used as the needle material. The needle was placed in a graphite container and heated to the melting temperature of the working substance (approximately 450°C) by the impact of thermo-electrons emitted from a heated cathode. Prior to the experiment, the needle tip was chemically treated and sharpened to ensure optimal wetting of the needle surface with the working substance.

It is known that Wien mass filters are mass and energy separators that operate by separating charged particles in crossed electric and magnetic fields perpendicular to each other. In our experiments, a mass analyzer similar to the Wien velocity filter was used for the mass analysis of ion beams, with crossed (E×B) fields. A homogeneous magnetic field in the analyzer was created by two smooth ferrite plates measuring (120×80×12) mm, positioned at a distance of 20 mm

Cite as: F.E. Mammadov, S.A. Aliev, I.I. Gurbanov, Sh.O. Eminov, A.J. Khalilov, E.M. Akberov, A.A. Badalov, 2025; East Eur. J. Phys. 1, 272 (2025), https://doi.org/10.26565/2312-4334-2025-1-31
© F.E. Mammadov, S.A. Aliev, I.I. Gurbanov, Sh.O. Eminov, A.J. Khalilov, E.M. Akberov, A.A. Badalov, 2025; CC BY 4.0 license

from each other. The magnetic field strength in the analyzer had a magnitude of 11.2×10^4 A/m. To generate the electric field, a specific controllable voltage was applied from a DC voltage source to the parallel electric plates (with a distance of 2 cm between them) resembling a capacitor configuration. The analyzer was positioned between the extractor and the collector. The collector is connected to ground through an ammeter, where the neutralization of positive ions occurs. In the experiments, the ion currents in the extractor and collector circuits were measured. Currents as low as 10^{-12}A were detected in the collector circuit using a DC current amplifier, KEITHLER 6487.

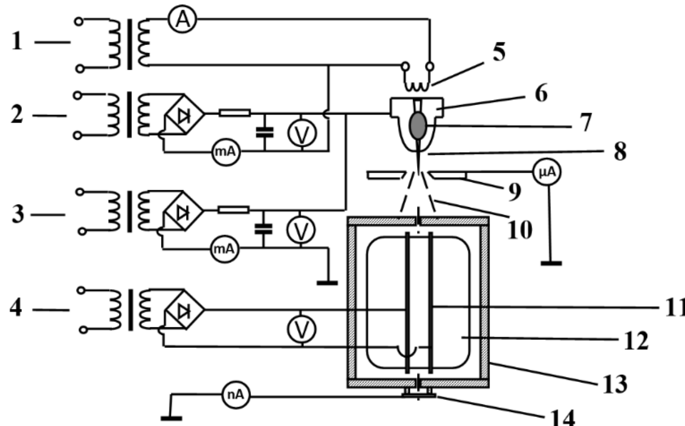

Figure 1. Experimental scheme of investigating the composition of the ion group using a Wien filter
1) electrical circuit of the heated cathode; 2) thermo-electron emission current circuit; 3) circuit of the extracting emission electric field; 4) circuit of constant voltage applied to the analyzer's electric plates; 5) filament; 6) container; 7) working substance; 8) needle; 9) extractor; 10) ion beam; 11) magnet; 12) frame; 13) plate; 14) collector.

The ion source was mounted on a Leybold-Heareus vacuum system, which provided vacuum of 6×10^{-6}mbar. The ion source was heated to the melting temperature of the working substance using therms-electrons emitted from the heated cathode [9]. To heat the working material to its melting temperature, the dependence of the container's temperature on the power supplied to the heater was used. At the same time, a high electric field is applied between the ion source and the extractor in advance. Once the source is heated and the working material melts, ion emission occurs, and the optimal power of the heater is maintained constant. In the experiments, the characteristics of the ion and nanoparticle phases were determined by gradually increasing the extraction voltage. Ion emission occurred above a threshold voltage of (5-6) kV between the source and the extractor (with a needle-extractor distance of approximately 0.5 mm) [10]. By applying a constant voltage to the plates of the analyzer, with emission currents ranging from 30-60 μA, the ion beam was separated based on the particles' mass and charge. The current in the collector circuit was measured using a picoammeter. Peaks in the current were observed in the collector circuit at specific constant voltage values on the analyzer, allowing for the determination of the mass composition of the ion beam.

RESULTS AND DISCUSSION

Theoretical values of the fixed voltage applied to the plates generating the electric field of the analyzer were calculated in order to observe the current generated by the charged particles, which are potentially present in the ion beam obtained from InSb and $(InSb)_{0.98}Bi_{0.02}$ materials, in the collector circuit. For the current generated by particles of equal mass and charge to be observed in the collector circuit, it is essential for these particles to move in a straight trajectory inside the analyzer without sensing the electric and magnetic fields. To achieve this, the forces exerted on the particles by the electric and magnetic fields inside the analyzer must balance each other.

$$F_E = F_B; \Rightarrow qE = qvB \Rightarrow v = \frac{E}{B} = \frac{U}{Bd} \Rightarrow v = \sqrt{\frac{2qU_0}{m}}$$

In this case, F_E and F_B represent the forces exerted by the electric and magnetic fields, respectively, on the charged particles passing through the analyzer. By solving the last two equations simultaneously, we obtain the following expression for the fixed voltage applied to the plates creating the electric field of the analyzer [11]:

$$U = \sqrt{\frac{qN_A}{M} \cdot 2U_0 d^2 B^2}$$

Through this principle, we can find the voltage at which particles of different masses and charges in the beam can provide maximum collector current. Here, U represents the voltage applied to the plates generating the electric field of the analyzer, q is the charge of a singly ionized particle, N_A is Avogadro's number, M is the molar mass, U_0 is the accelerating voltage applied to the extractor, d is the distance between the plates generating the electric field, and B is the

induction of the magnetic field. According to the above principle, theoretical calculations have been performed to determine the theoretical values of the fixed voltages at which different charged ions, whose presence is estimated in the composition of the ion beam entering the analyzer, can produce maximum collector current. The calculated values are given in Table 1 below.

Table 1. Voltage of the analyzer according to the value of mass and charge for different ions

Ion species	U (V, DC)
$(InSb)_4^+$	95
$(InSb)_3^+$	110
$(InSb)_2^+$	130
$(InSb)^+$	190
$(InSbBi)^+$	140
$(Bi)^+$	210

In the experiment conducted using InSb as the working material, the composition of the ion beam was investigated with an accelerating voltage of 6 kV and an emission current of 40 µA. The extractor was connected to ground through a microammeter. Only around a voltage of 190 V, a peak was observed (Figure 2). According to the table, this result corresponds to $(InSb)^+$ ions, which are singly ionized with a specific charge of q/m_0 = 4.09·10^{5}C/kg. Therefore, the emitted ion beam consists exclusively of $(InSb)^+$ions. The same observation is obtained when the beam current is varied within the range of (30-50) µA.

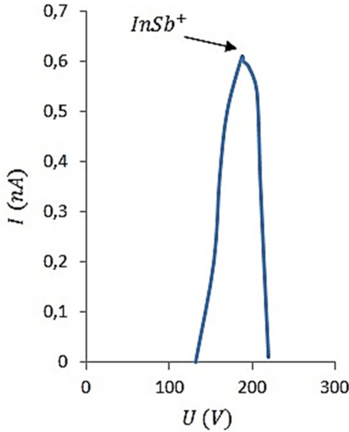

Figure 2. Composition analysis of the InSb ion beam ($U_0 = 6kV, I_b = 40\mu A$)

When the ion source based on $InSb_{0.98}Bi_{0.02}$working material was used, and the extractor voltage was 6 kV and 6.2 kV, with a beam current of 30 µA and 60 µA, the composition of the beam was investigated, and the results are presented in Figure 3. As observed in the figure, three distinct peaks are visible in both cases. These peaks correspond to ions with specific voltages: +190V for $(InSb)^+$, 142V for $((InSb)_{0.98}Bi_{0.02})^+$ and +210V for Bi^+ (Figure 3). The ion beam obtained from the combination of $InSb_{0.98}Bi_{0.02}$is not monatomic; instead, it consists of subclusters composed of ionized $(InSb)^+$, $((InSb)_{0.98}Bi_{0.02})^+$, and Bi^+ ions. The $((InSb)_{0.98}Bi_{0.02})$ ions have a specific charge of q/m_0=2.16·10^5 C/kg. It is observed that as the beam current increases, the peak corresponding to Bi+ ions decreases in height. This is because of the higher accelerating voltage, which results in a larger portion of Bi atoms in the composition of $(InSb)_{0.98}Bi_{0.02}$semiconductor being emitted.

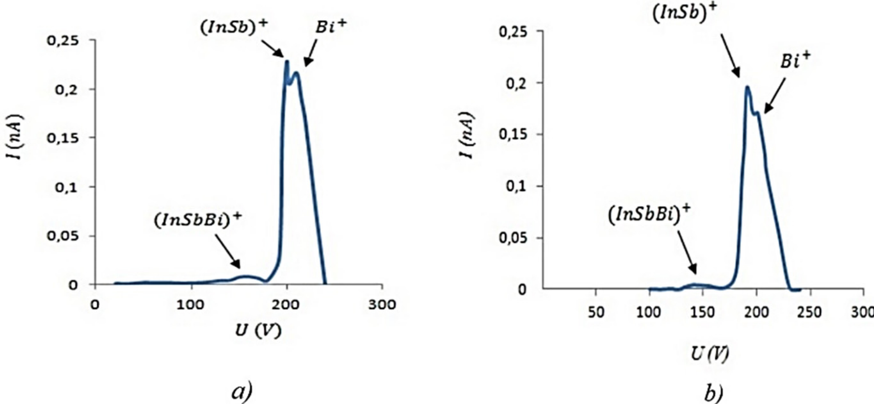

Figure 3. Composition analysis of the $(InSb)_{0.98}Bi_{0.02}$ ion beam: a) $U_0 = 6kV, I_b = 30\mu A$; b) $U_0 = 6.2kV, I_b = 60\mu A$

Thus, the results of the experiments conducted for the mass analysis of the ion groups obtained through the ion source of the considered compounds are in full agreement with the theoretically calculated values. The width of the slit at the entrance of the mass analyzer is 200 μm, and the diameter of the slit at the exit is 2 mm. These dimensions have been determined for analyzing the composition of a specific portion of the ion beam current, taking into account the resolving power of the analyzer.

CONCLUSIONS

Composition analysis of ion beams was conducted using the field ion emission method for ion sources based on InSb and $(InSb)_{0.98}Bi_{0.02}$ as working materials. The ion beam obtained from the InSb substrate was monatomic and comprised solely of singly ionized $(InSb)^+$ ions. However, the beam obtained from the $(InSb)_{0.98}Bi_{0.02}$ material consisted of three subclusters, each consisting of singly ionized ions. The experimental results align with theoretical calculations.

Data availability statement

The manuscript was performed at the laboratory "Infrared photoelectronics and plasma phenomena" of the Institute of Physics Ministry of Science and Education of Azerbaijan Republic.

ORCID

I.I. Gurbanov, https://orcid.org/0009-0002-8054-4376; **Sh.O. Eminov,** https://orcid.org/0000-0002-4589-0452
E.M. Akberov, https://orcid.org/0009-0009-7625-5724

REFERENCES

[1] P.A. Mazharov, V.G. Dudnikov, and A.B. Tolstoguzov, "Electrohydrodynamic emitters of ion beams" UFN, **190**, 1293 (2020). https://doi.org/10.3367/UFNr.2020.09.038845
[2] C. Cruz, K. Paurezzaci, and A. Wagner, "Ion cluster emission and deposition from liquid gold ion sources," J. Appl. Phys. **58**, 2724–2730 (1985). https://doi.org/10.1116/1.570316
[3] D.R. Kingham, and L.W. Swanson, "A theoretical model of a liquid metal ion source," Vacuum, **34**(10-11), 941-945 (1984). https://doi.org/10.1016/0042-207X(84)90175-1
[4] L. Bruchhaus, *et. al*., "Comparison of technologies for nano device prototyping with a special focus on ion beams," J. Appl. Phys. Rev. **4**, 011302 (2017). https://doi.org/10.1063/1.4972262
[5] L. Bischoff, P. Mazarov, L. Bruchhaus, and, J. Gierak, "Liquid metal alloy ion sources—An alternative for focussed ion beam technology," Applied Physics Reviews, **3**(2), 021101 (2016). https://doi.org/10.1063/1.4947095
[6] L. Bischoff, N. Klingner, P. Mazarov, K. Lenz, R. Narkowicz, W. Pilz, and F. Meyer, "Dysprosium liquid metal alloy ion source for magnetic nanostructures," Journal of Vacuum Science & Technology B, **40**(5), 05282 (2022). https://doi.org/10.1116/6.0001837
[7] I.S. Gasanov, I.I. Gurbanov, and E.M. Akbarov, Eur. Phys. J. D, **69**, 75 (2015). https://doi.org/10.1140/epjd/e2015-50531-0
[8] I.S. Gasanov, I.I. Gurbanov, and E.M. Akbarov, ACTA Physica Polonica A, **134**(1), 119 (2018). https://doi.org/10.12693/APhysPolA.134.119
[9] S.A. Aliyev, F.E. Mammadov, E.M. Akberov, I.I. Gurbanov, A.A. Badalov, and Sh.O. Eminov, "Main elements and characteristics of electrohydrodynamic ion sources based on InSb," Azerbaijan J. of Physics, **XXIX**(3), section En, 19-23 (2023).
[10] L. Bischoff, N. Klingner, P. Mazarov, W. Pilz, and F. Meyer, "Boron liquid metal alloy ion sources for special focused ion beam applications," Journal of Vacuum Science & Technology B, **38**(4), (2020). https://doi.org/10.1116/6.0000073
[11] I.S. Gasanov, *Plasma and beam technology,* (Science, 2007), pp. 67-68. (in Russian)

АНАЛІЗ СКЛАДУ ІОННОГО ПУЧКА InSb ТА $InSb_{0,98}Bi_{0,02}$, ОТРИМАНОГО З ВИКОРИСТАННЯМ РІДКИХ МЕТАЛІВ

Ф.Е. Мамедов, С.А. Алієв, І.І. Гурбанов, Ш.О. Емінов, А.Дж. Халілов, Е.М. Акберов, А.А. Бадалов
Інститут фізики Міністерства освіти і науки Республіки Азербайджан, пр. Г. Джавіда, 131, Az1143, Баку, Азербайджан

Для дослідження масового складу пучка іонів, отриманого за допомогою польової іонної емісії, використовувався мас-аналізатор, розроблений аналогічно фільтру швидкості Віна. Цей аналізатор фільтра Wien працює на основі принципу перетинання взаємно перпендикулярних електричного та магнітного полів (E×B) для класифікації заряджених частинок відповідно до їх маси та заряду. Іонний пучок отримано з використанням робочих матеріалів mInSb та $InSb_{0,98}Bi_{0,02}$. Цим методом аналізували масовий склад іонної групи. В експериментах було виявлено, що іонний пучок, отриманий з використанням InSb як робочої речовини, має однорідний склад, що складається виключно з іонів (InSb)+. Однак, на відміну від цього, коли робочою речовиною був $(InSb)_{0,98}Bi_{0,02}$, було визначено, що іонний пучок має різний склад. Крім іонів (InSb)+, було виявлено, що пучок іонів містить іони $((InSb)_{0,98}Bi_{0,02})+$ і (Bi)+.

Ключові слова: *рідкометалеві іонні джерела, LMIS, гострий емітер, іонний пучок, масовий аналіз, InSb, InSbBi*

EAST EUROPEAN JOURNAL OF PHYSICS. 1. 276-283 (2025)
DOI:10.26565/2312-4334-2025-1-32 ISSN 2312-4334

DOPING OF SILICON WITH GADOLINIUM ATOMS – STRUCTURAL DISTRIBUTION AND RAMAN SPECTRAL CHANGES

Sh.B. Utamuradova[a], Sh.Kh. Daliev[a], J.J. Khamdamov[a], Kh.J. Matchonov[a]*, M.K. Karimov[b], Kh.Y. Utemuratova[c]

[a]*Institute of Semiconductor Physics and Microelectronics at the National University of Uzbekistan, 20 Yangi Almazar st.,*
[b]*Urgench State University, Department of Physics, Urgench, Uzbekistan*
[c]*Karakalpak State University, Nukus, Karakalpakstan*
**Corresponding Author e-mail: husniddin94_04@bk.ru*

Received October 17, 2024; revised February 6, 2025; in final form February 10, 2025; accepted February 11, 2025

In this study, we investigated silicon samples doped with gadolinium using two different methods: incorporation during growth and diffusion treatment at elevated temperatures. Scanning electron microscopy (SEM) and energy-dispersive spectroscopy (EDS) were used to analyze the surface microstructure and impurity atom distribution, while Raman spectroscopy revealed characteristic phonon mode shifts induced by gadolinium doping. It was found that doping during growth results in a more uniform structure with fewer large defects, although localized regions enriched in carbon and oxygen remain. In contrast, diffusion doping leads to the formation of pronounced inhomogeneities, indicating significant dislocation formation and structural defects due to lattice parameter mismatches. The results demonstrate the influence of the doping method on the silicon surface state, elastic stress distribution, and the emergence of new vibrational modes, which can be utilized for the targeted modification of material properties in spintronic, optoelectronic, and sensor devices.

Keywords: *Silicon; Gadolinium; Doping; Diffusion; SEM; EDS; Raman Spectroscopy; Structural defects; Phonon Spectra; Crystal Lattice Defects; Optoelectronics; Magnetic Characteristics*
PACS: 68.37.Hk, 33.20.Fb

INTRODUCTION

Silicon is a key material in the modern semiconductor and optoelectronic industries due to its unique electrical and optical properties [1–6]. However, to expand its scope of application, its characteristics require modification. One promising approach to such modification is the introduction of rare earth elements, in particular gadolinium (Gd), which can significantly affect the magnetic and optical properties of silicon. Studies show that the integration of gadolinium atoms into the silicon crystal lattice changes its interaction with light and magnetic characteristics, which opens up new prospects for the use of such materials in optoelectronics, sensor devices, and spintronics.

Doping silicon with gadolinium atoms leads to structural changes that significantly affect its optical and magnetic properties. In particular, the introduction of Gd causes deformations of the crystal lattice and changes the optical activity of silicon. According to a number of studies, the inclusion of gadolinium can increase the photochemical (photoactive) ability of silicon to interact with radiation. This is explained by the fact that gadolinium retains localized f-electrons and, hence, magnetic moments even when embedded in a silicon lattice, which is especially important for spintronic applications [5–11].

One of the key effects of gadolinium doping in silicon is the reduction in the density of dangling bonds. It has been established that trivalent Gd^{3+} ions contribute to minimizing defects in the crystal structure, thereby improving the electronic properties of the material and reducing the number of surface imperfections. Additionally, gadolinium interacts with silicon to enhance the magnetic properties of the system, making it more suitable for applications in magnetic sensors and spintronic devices.

Despite these beneficial effects, certain limitations arise when doping silicon with gadolinium. Firstly, the distribution of Gd within the crystal volume can be uneven, making it challenging to achieve reproducible material characteristics-an issue particularly critical for high-precision devices. Secondly, localized stresses and defects introduced into the crystal lattice may restrict the efficiency of silicon in specific applications, such as photonic devices and high-frequency microelectronics.

Raman spectroscopy (RS) is an effective method for studying crystalline materials, including semiconductors such as silicon [12-15]. During the Raman scattering process, light interacts with phonons (quanta of crystal lattice vibrations), leading to changes in the energy and frequency of the scattered photons and the formation of characteristic spectral lines. Analyzing these spectral changes allows for the identification of structural defects and material properties.

Doping silicon with rare-earth elements such as gadolinium significantly influences the defect structure and deformation processes within the crystal lattice. The corresponding changes in Raman spectra reflect these structural rearrangements, providing insights into the nature of the defects that emerge. Understanding how the incorporation of Gd alters Raman scattering in silicon is of great interest for practical applications in electronics, optics, and nanotechnology. This study focuses on the analysis of one- and two-phonon Raman spectra of single-crystal silicon doped with gadolinium atoms.

Cite as: Sh.B. Utamuradova, Sh.Kh. Daliev, J.J. Khamdamov, Kh.J. Matchonov, M.K. Karimov, Kh.Y. Utemuratova, East Eur. J. Phys. 1, 276 (2025), https://doi.org/10.26565/2312-4334-2025-1-32

© Sh.B. Utamuradova, Sh.Kh. Daliev, J.J. Khamdamov, Kh.J. Matchonov, M.K. Karimov, Kh.Y. Utemuratova, 2025; CC BY 4.0 license

MATERIALS AND METHODS

For the investigation, n-Si and p-Si samples with an initial resistivity of 0.3–40 Ω·cm were prepared. Prior to doping, the samples underwent thorough acid-peroxide cleaning, followed by the removal of oxide layers using an HF solution. High-purity gadolinium films (99.999%) were deposited onto the cleaned silicon surfaces via vacuum deposition under high-vacuum conditions (10^{-7}–10^{-8} Torr). Doping was carried out through diffusion at 1473 K for 20 hours, followed by rapid cooling. The structural and elemental characteristics of the resulting materials were analyzed using energy-dispersive spectroscopy (EDS) and scanning electron microscopy (SEM).

RESULTS AND DISCUSSION

A visual analysis of the microscopic images in Fig. 1a reveals that the distribution of carbon (C) and silicon (Si) atoms on the sample surface is non-uniform. The carbon distribution map shown in Fig. 1b highlights areas of localized carbon accumulation, which may result from surface effects and the interaction of carbon with lattice defects.

The energy-dispersive spectroscopy (EDS) spectra presented in Fig. 2 confirm that silicon is the predominant element in the sample composition, as indicated by the intensity of its main peak. The presence of low-intensity oxygen (O) and carbon (C) peaks suggests the formation of oxide compounds or surface contamination, which may have occurred during sample growth or storage. The quantitative analysis summarized in Table 1 shows that the weight fraction of silicon is 86.79%, carbon 11.90%, and oxygen 1.96%. The high atomic concentration of carbon (23.81%) indicates its significant presence in the surface layer.

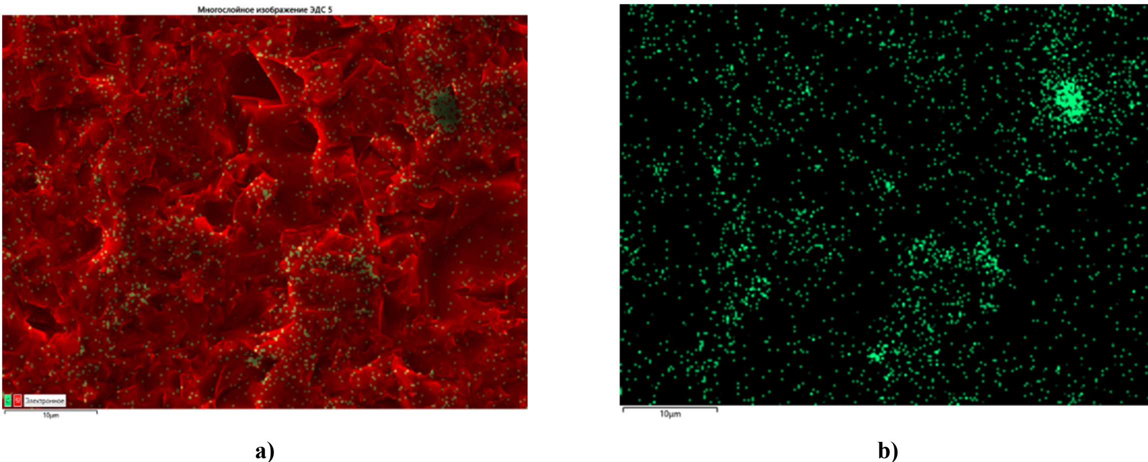

a) b)

Figure 1. SEM images of the surface of silicon doped with gadolinium during growth: (a) elemental distribution; (b) carbon distribution map.

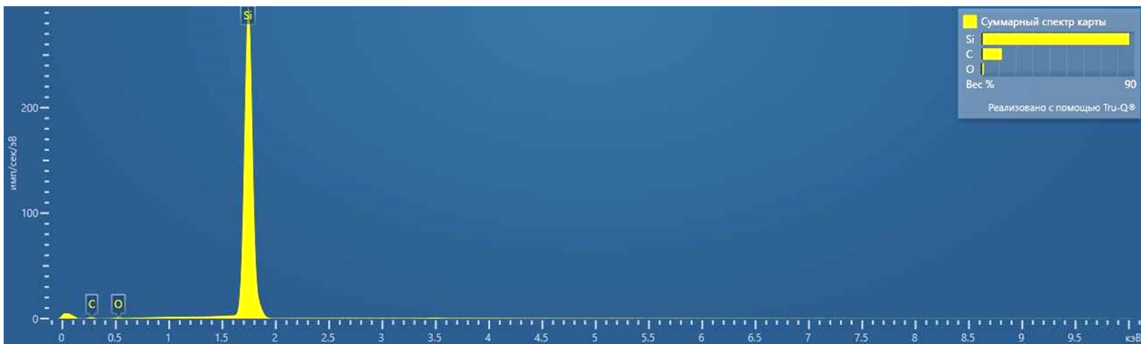

Figure 2. SEM spectrum of silicon doped with gadolinium during growth.

Table 1. Summary of elemental distribution maps for silicon doped with gadolinium during growth.

Element	Line Type	Conditional Concentration	Wt %	At. %
C (Carbon)	K-series	0.61	11.90	23.81
O (Oxygen)	K-series	0.56	1.31	1.96
Si (Silicon)	K-series	92.59	86.79	74.23
Total:			100.00	100.00

After heat treatment at 1473 K for 20 hours, the microstructure of the sample undergoes significant changes, as seen in Fig. 3. In the doped sample (Fig. 3b), compared to the original silicon (Fig. 3a), pronounced surface heterogeneity is observed. This may be attributed to the formation of defective regions, phase inclusions, and the redistribution of elements within the crystal lattice.

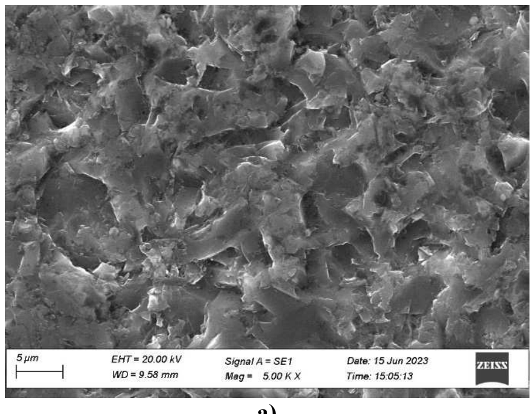

a)

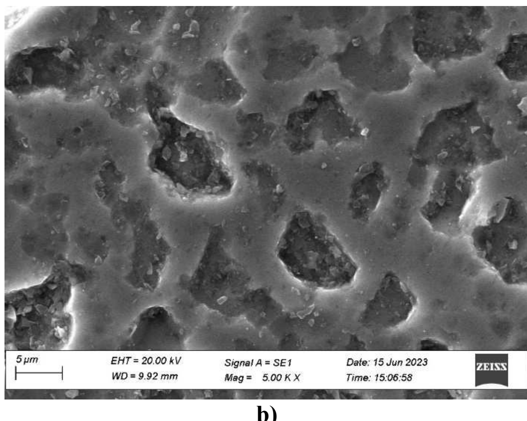

b)

Figure 3. SEM images of silicon: (a) original sample; (b) silicon doped with gadolinium via diffusion at 1473 K for 20 hours, illustrating microstructural changes in the material.

The results of energy-dispersive analysis after diffusion doping, presented in Fig. 4 and Table 2, indicate an increase in carbon content to 14.27% and a decrease in oxygen concentration to 1.20%. This change may be attributed to the selective sorption of carbon in regions with structural defects.

Figure 4. SEM spectrum of silicon doped with gadolinium via diffusion at 1473 K for 20 hours, illustrating microstructural changes in the material

Table 2. Summary of elemental distribution maps for silicon doped with gadolinium via the diffusion method at 1473 K for 20 hours.

Element	Line Type	Conditional Concentration	Wt %	At. %
C (Carbon)	K-series	0.61	11.90	23.81
O (Oxygen)	K-series	0.56	1.31	1.96
Si (Silicon)	K-series	92.59	86.79	74.23
Total:			100.00	100.00

A visual analysis of the microscopic images in Fig. 5 reveals that the diffusion of gadolinium into silicon results in large defect zones, as well as areas with pronounced porosity or a disordered structure. These structural inhomogeneities may be attributed to the following factors:

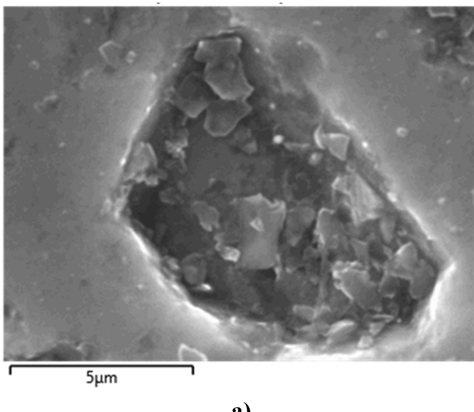

a)

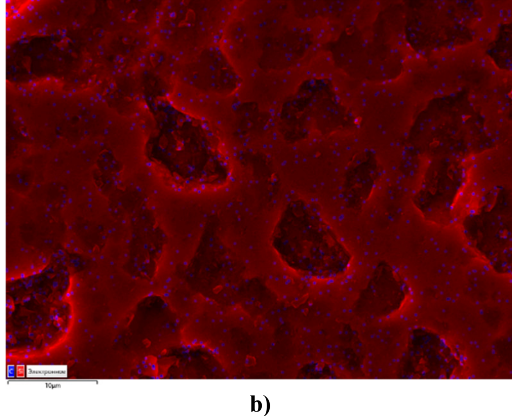

b)

Figure 5. SEM images of silicon doped with gadolinium via the diffusion method at 1473 K for 20 hours, illustrating defect formation and structural changes in the material.

Crystal lattice deformations – The incorporation of gadolinium introduces additional stress centers, leading to localized distortions in the silicon structure.

Phase transitions – The formation of new phases or solid solutions based on Gd–Si results in a non-uniform distribution of gadolinium atoms, causing localized chemical and structural changes.

Surface effects and contamination – The increased presence of carbon (C) and oxygen (O) may indicate surface oxidation or the trapping of these elements in defect regions. This effect is particularly common during high-temperature processing and subsequent cooling.

A comparison of microstructural changes and chemical composition reveals that diffusion doping with gadolinium significantly alters the surface layer of silicon. This process promotes the formation of large defects, including pores, potential cracks, and localized zones of gadolinium concentration with impurities. The energy-dispersive spectra of defect zones, presented in Fig. 6 and Table 3, confirm a decrease in oxygen content (0.73%) while maintaining an elevated carbon concentration (13.15%). This observation suggests variations in the sorption mechanisms of impurity elements within defect regions.

Figure 6. SEM spectrum of elemental distribution in defect regions of silicon doped with gadolinium via diffusion at 1473 K for 20 hours, illustrating microstructural changes in the material.

Table 3. Summary of elemental distribution maps in defect regions of silicon doped with gadolinium via the diffusion method at 1473 K for 20 hours.

Element	Line Type	Conditional Concentration	Wt %	At. %
C (Carbon)	K-series	0.65	13.15	26.02
O (Oxygen)	K-series	0.29	0.73	1.08
Si (Silicon)	K-series	87.12	86.13	72.90
Total:			100.00	100.00

Diffusion doping with gadolinium at 1473 K for 20 hours results in pronounced microstructural heterogeneity, characterized by the formation of defective regions, elemental redistribution, and localized phase transformations. In the doped samples, an increase in carbon concentration to 14.27% is observed, likely due to its selective sorption at structural defects. In defective zones, a reduced oxygen content (0.73%) is recorded, which is probably related to differences in the adsorption kinetics of oxygen and carbon.

Raman scattering (RS) analysis of gadolinium-doped silicon samples was performed using a SENTERRA II Raman spectrometer (Bruker), which offers high spectral sensitivity and a resolution of approximately 4.0 cm^{-1}. To ensure measurement accuracy (~0.2 cm^{-1}), automatic calibration was conducted using NIST standards (acetaminophen, silicon).

The spectra were excited using a 532 nm laser with a maximum power of 25 mW. Spectral data were recorded in the range of 50-4265 cm^{-1}, with an exposure time of 100 s, followed by summation of two spectra. To ensure accurate intensity comparisons between samples, the spectra were normalized to the peak at 510 cm^{-1}, which is the most intense in the analyzed range. Prior to normalization, the baseline was subtracted from each spectrum.

According to the literature [12-18], the lattice constant mismatch between Gd and Si can induce significant elastic stresses in thin layers, affecting both the electronic band structure and phonon spectra. Additionally, when there is a large discrepancy between lattice parameters in epitaxial multilayer structures, numerous defects are formed, degrading the quality of heterostructures. In the case of a Gd_xSi_{1-x} solid solution, lattice deformation is less critical compared to pure components (Gd and Si), as the actual lattice constant of the Gd_xSi_{1-x} layer lies between the values for Gd and Si. Furthermore, the layer thickness (5 μm) facilitates stress relaxation. Changes in the vibrational (phonon) spectra in this system clearly indicate the presence of Gd–Si bonds.

Doping silicon with gadolinium induces significant modifications in its vibrational spectra. These alterations stem from the incompatibility between the lattice parameters of Gd and Si, leading to the formation of structural defects and localized mechanical stresses.

Fig. 7 presents the Raman spectrum of gadolinium-doped p-type silicon with a resistivity of 0.3 Ω·cm. Spectrum analysis reveals a significant broadening of the main peak at 510 cm^{-1}, indicating an increased density of defects in the

crystal lattice. Additionally, extra vibrational modes are observed at 123, 148, 238, and 303 cm⁻¹, which may be attributed to the formation of impurity complexes and localized structural distortions.

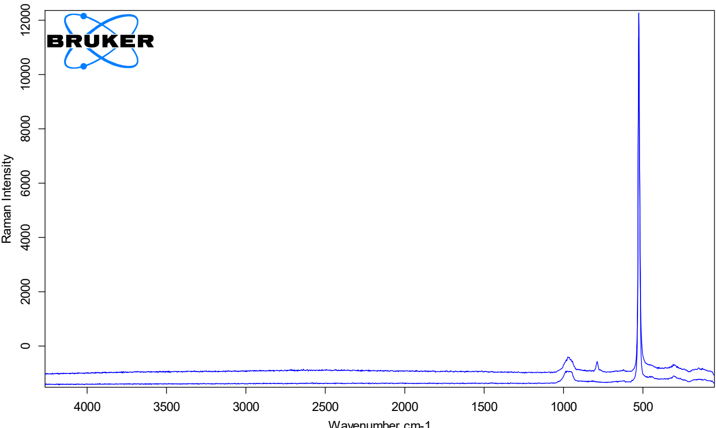

Figure 7. Raman spectrum of p-type silicon doped with gadolinium (Gd):
1 – Raman spectrum of the initial Si samples; 2 – Raman spectrum of p-Si<Gd> samples with an initial resistivity of ρ = 0.3 Ω·cm.

Fig. 8 presents the Raman spectra of n-type silicon samples with a specific resistivity of 10 Ω·cm.

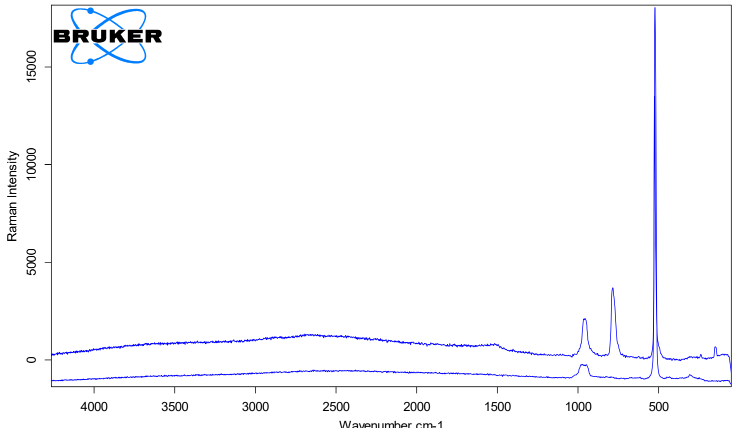

Figure 8. Raman spectrum of n-type silicon doped with gadolinium (Gd):
1 – Raman spectrum of the initial Si samples; 2 – Raman spectrum of n-Si<Gd> samples with an initial resistivity of ρ = 10 Ω·cm.

With increasing specific resistivity, an enhancement in the intensity of additional spectral lines is observed, indicating modifications in the band structure of silicon due to the incorporation of gadolinium atoms. In particular, the intensification of the bands at 456 cm⁻¹ and 954 cm⁻¹ may be associated with the formation of amorphous phases and the presence of oxide inclusions.

Fig. 9 presents the Raman spectra of n-type silicon samples with a specific resistivity of 15 Ω·cm.

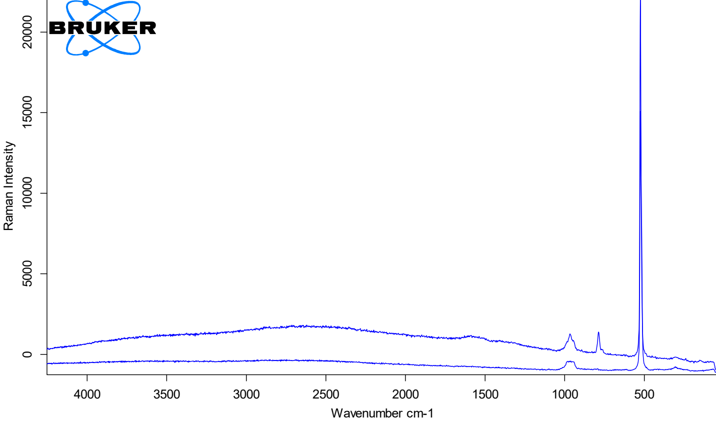

Figure 9. Raman spectrum of n-type silicon doped with gadolinium (Gd):
1 – Raman spectrum of the initial Si samples; 2 – Raman spectrum of Gd_xSi_{1-x} samples with an initial resistivity of ρ = 15 Ω·cm.

This spectrum exhibits a further enhancement of vibrational modes in the region of 68, 784, 1340, and 1610 cm^{-1}, which may be attributed to the formation of stable Gd–Si impurity complexes. Of particular interest is the intense peak at 784 cm^{-1}, which can be interpreted as evidence of a strong chemical bond between gadolinium and silicon atoms.

Solid solutions of Gd–Si with varying Gd and Si content are characterized by frequency shifts in the local vibrations of Gd–Gd, Gd–Si, and Si–Si, associated with variations in strain within the films. According to Raman spectroscopy data, three primary vibrational regions can be identified [14-20]: Gd–Gd near 238 cm^{-1}, Gd–Si around 783 cm^{-1}, Si–Si at approximately 510 cm^{-1}.

The position of these spectral lines is significantly influenced by built-in stresses resulting from the considerable lattice parameter mismatch between Gd and Si [18-25 It is well known that during epitaxial growth of a layer on a substrate with a different lattice constant, an initial pseudomorphic layer forms, adapting to the substrate. However, once a critical thickness is reached, the formation of dislocations becomes energetically favorable, after which the layer grows with its own lattice constant. Such layers are referred to as relaxed or unstressed layers [18].

The frequency shift of the optical phonon mode in the crystal can also be described by the Grüneisen parameter [12], which relates the change in unit cell volume to the shift in optical phonon frequencies. This shift is presumed to result from hydrostatic (isotropic) compression or expansion of the unit cell due to the incorporation of Gd atoms.

In the region of 521–522 cm^{-1}, an intense peak is observed, corresponding to first-order scattering of optical phonons (TO – transverse optical vibrations, LO – longitudinal optical vibrations) at the Γ point of the Brillouin zone. Additionally, a detailed analysis of the peaks near 123 and 186 cm^{-1}, using Gaussian approximation, allows them to be associated with the vibrational modes of Gd [17]. The mode at 148 cm^{-1} is related to first-order scattering of acoustic phonons (TA – transverse acoustic vibrations), which may reflect vibrational contributions from the oxide film (SiO_2). The weak-intensity LO peak at 456 cm^{-1} suggests the presence of amorphous silicon components [18].

The second-order spectrum is significantly weaker, appearing in the range of approximately 100-1100 cm^{-1}. The peak around 303 cm^{-1} is typically attributed to 2TA acoustic phonons, while the broad signal between 900 and 1000 cm^{-1} is associated with 2TO phonons [12]. Furthermore, the broadening of specific peaks (e.g., in the regions of 68, 954, 1340, and 1610 cm^{-1}) suggests a high defect density or compositional fluctuations [19].

A comparison with literature sources indicates that the modes near 954, 1340, and 1610 cm^{-1} correspond to GdO vibrations, while the peaks at 1462 and 1600 cm^{-1} may be associated with third-order Raman modes related to silicon optical phonons (TO) and interstitial oxygen (O_2) vibrations, respectively [17–26].

Fig. 10 presents the Raman spectra of samples with a specific resistivity of 40 Ω·cm.

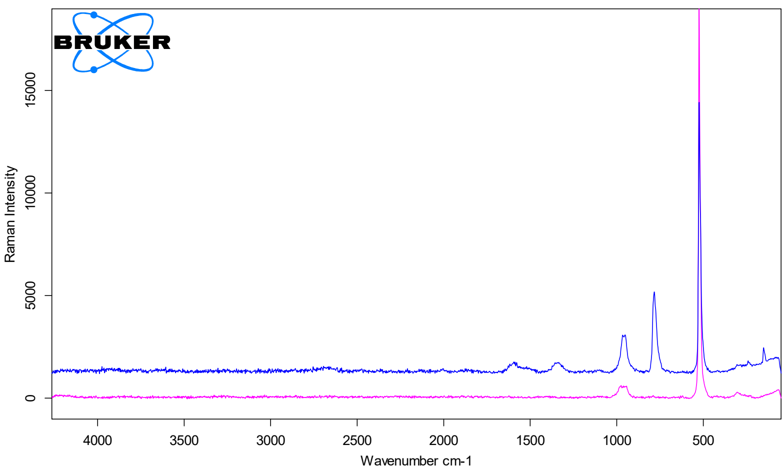

Figure 10. Raman spectrum of n-type silicon doped with gadolinium (Gd):
1 – Raman spectrum of the initial Si samples; 2 – Raman spectrum of Gd_xSi_{1-x} samples with an initial resistivity of ρ = 40 Ω·cm.

With a further increase in specific resistivity, a significant enhancement of spectral lines in the 784 - 1610 cm^{-1} range is observed, indicating a redistribution of local stresses within the crystal lattice and the formation of band engineering effects. The presence of characteristic vibrational modes Gd–Gd (~238 cm^{-1}), Gd–Si (~783 cm^{-1}), and Si–Si (~510 cm^{-1}) confirms the incorporation of gadolinium into the silicon lattice and its influence on the material's structure.

A comparative analysis of Raman spectra for samples with different initial resistivities (0.3, 13, 15, and 40 Ω·cm) reveals that with increasing resistivity - and consequently, higher Gd concentration—the intensity of peaks at ~68, 123, 148, 238, 303, 456, 784, 954, 1340, and 1610 cm^{-1} increases. The most intense peak at ~784 cm^{-1} is likely associated with Gd–Si bond vibrations.

A comparison of the results obtained from two different gadolinium doping methods—during growth and diffusion at 1473 K - demonstrates significant differences in alloying element distribution and defect formation. In the case of doping during growth, SEM images indicate a more uniform incorporation of Gd, with relatively fewer large structural defects. However, localized impurity clusters (C, O) are present, which may reflect process-specific characteristics such as incomplete surface cleaning or oxidation.

In contrast, diffusion doping at high temperatures results in more pronounced microstructural inhomogeneities and the formation of large defect zones (pores, cracks), caused by a significant lattice parameter mismatch between Gd and Si and intense dislocation formation. However, this method facilitates stress relaxation in thicker layers, as confirmed by phonon mode shifts in Raman spectra and the emergence of spectral lines associated with Gd–Si bonds.

Thus, doping during growth is preferable when thin, uniform layers with minimal large defects are required, whereas diffusion doping allows for greater control over composition and thickness but is associated with a higher density of structural defects.

The observed Raman spectral changes in gadolinium-doped silicon samples confirm the formation of Gd–Si bonds and structural modifications induced by Gd incorporation. Given that Gd doping introduces elastic stresses and localized defects, these findings provide a foundation for further optimization of processing techniques to develop functional materials with tailored electrical and optoelectronic properties.

A comparative analysis of the obtained data highlights the significant impact of doping mechanisms on the material's spectral characteristics:

Sputtering followed by crystallization ensures a uniform gadolinium distribution but is accompanied by localized oxygen and carbon accumulations, likely due to surface oxidation.

Diffusion doping at 1473 K results in intensive dislocation formation, pore generation, and point defects due to Gd-Si lattice incompatibility. However, stress relaxation occurs, as evidenced by spectral shifts in vibrational modes.

Therefore, the sputtering method with subsequent crystallization produces structurally homogeneous layers, whereas diffusion doping enables precise control over composition and thickness but is accompanied by more pronounced crystallographic rearrangements.

CONCLUSIONS

The analysis of Raman spectra in gadolinium-doped silicon confirms the significant influence of impurity atoms on the material's vibrational characteristics. New spectral modes at 68, 123, 148, 238, 303, 456, 784, 954, 1340, and 1610 cm^{-1} are observed, with their intensity increasing as the Gd concentration rises.

The formation of strong Gd–Si bonds is confirmed by the presence of a characteristic vibrational line at ~784 cm^{-1}. The results indicate that the defect structure plays a crucial role in the redistribution of impurity atoms, thereby altering the electrical, optical, and magnetic properties of doped silicon.

A comparative analysis demonstrates that gadolinium diffusion into silicon leads to the formation of complex defect-phase structures, which can either enhance material properties-such as promoting magnetic ordering-or degrade mechanical stability and electrical performance.

Optimizing diffusion parameters, including temperature, holding time, and cooling rate, is essential for achieving a balance between structural, chemical, and functional properties of gadolinium-doped silicon.

ORCID

Sharifa B. Utamuradova, https://orcid.org/0000-0002-1718-1122; **Jonibek J. Khamdamov**, https://orcid.org/0000-0003-2728-3832
Khusniddin J. Matchonov, https://orcid.org/0000-0002-8697-5591

REFERENCES

[1] S.B. Utamuradova, S.K. Daliev, A.K. Khaitbaev, J.J. Khamdamov, Kh.J. Matchonov, and X.Y. Utemuratova, "Research of the Impact of Silicon Doping with Holmium on its Structure and Properties Using Raman Scattering Spectroscopy Methods," East European Journal of Physics, (2), 274-278 (2024). https://doi.org/10.26565/2312-4334-2024-2-28

[2] J. Yang, Y. Feng, X. Xie, H. Wu, and Y. Liu, "Gadolinium-doped silicon clusters GdSin (n=2-9) and their anions: structures, thermochemistry, electron affinities, and magnetic moments", Theor Chem Acc, **135**, 204 (2016) https://doi.org/10.1007/s00214-016-1964-z

[3] M.K. Karimov, Kh.J. Matchonov, K.U. Otaboeva, and M.U. Otaboev, "Computer Simulation of Scattering Xe+ Ions from InP(001)⟨110⟩ Surface at Grazing Incidence," e-Journal of Surface Science and Nanotechnology, **17**, 179-183 (2019). https://doi.org/10.1380/ejssnt.2019.179

[4] M.S. Sercheli, amd C. Rettori, "Magnetic Properties of Gadolinium-Doped Amorphous Silicon Films," Brazilian Journal of Physics, **32**(2A), 409-411 (2002). https://doi.org/10.1590/S0103-97332002000200046

[5] M.K. Karimov, U.O. Kutliev, S.B. Bobojonova, and K.U. Otabaeva, "Investigation of Angular Spectrum of Scattered Inert Gas Ions from the InGaP (001) Surface," Physics and Chemistry of Solid State, **22**(4), 742–745 (2021). https://doi.org/10.15330/pcss.22.4.742-745

[6] Sh.B. Utamuradova, Kh.J. Matchonov, J.J. Khamdamov, and Kh.Y. Utemuratova, "X-ray diffraction study of the phase state of silicon single crystals doped with manganese". New Materials, Compounds and Applications, **7**(2), 93-99, (2023). http://jomardpublishing.com/UploadFiles/Files/journals/NMCA/v7n2/Utamuradova_et_al.pdf

[7] P.M. Fauchet, and I.H. Campbell, "Raman spectroscopy of low-dimensional semiconductors," Critical Reviews in Solid State and Materials Sciences, **14**(sup1), s79–s101 (1988). http://dx.doi.org/10.1080/10408438808244783

[8] S.B. Utamuradova, K.S. Daliev, A.I. Khaitbaev, J.J. Khamdamov, J.S. Zarifbayev, and B.S. Alikulov, "Defect Structure of Silicon Doped with Erbium," East European Journal of Physics, (2), 288-292 (2024) https://doi.org/10.26565/2312-4334-2024-2-31

[9] W. Yang, J. Chen, Y. Zhang, Y. Zhang, Jr.-H. He, and X. Fang, "Silicon-Compatible Photodetectors: Trends to Monolithically Integrate Photosensors with Chip Technology," Adv. Funct. Mater. **29**(18), 1808182 (2019). https://doi.org/10.1002/adfm.201808182

[10] M. Piels, and J.E. Bowers, "Photodetectors for silicon photonic integrated circuits," Photodetectors Materials, Devices and Applications, 3-20, (2016). https://doi.org/10.1016/B978-1-78242-445-1.00001-4

[11] K.S. Daliev, Sh.B. Utamuradova, J.J. Khamdamov, M.B. Bekmuratov, O.N. Yusupov, Sh.B. Norkulov, and Kh.J. Matchonov, "Defect Formation in MIS Structures Based on Silicon with an Impurity of Ytterbium," East Eur. J. Phys. (4), 301-304 (2024). https://doi.org/10.26565/2312-4334-2024-4-33
[12] Kh.S. Daliev, Sh.B. Utamuradova, Z.E. Bahronkulov, A.Kh. Khaitbaev, and J.J. Hamdamov, "Structure determination and defect analysis n-Si<Lu>, p-Si<Lu> by raman spectrometer methods," East Eur. J. Phys. (4), 193 (2023), https://doi.org/10.26565/2312-4334-2023-4-23
[13] R.R. Jones, D.C. Hooper, L. Zhang, D. Wolverson, and V.K. Valev, "Raman Techniques: Fundamentals and Frontiers," Nanoscale Research Letters, **14**(1), 231 (2019). https://doi.org/10.1186/s11671-019-3039-2
[14] U. Ramabadran, and B. Roughani, "Intensity analysis of polarized Raman spectra for off axis single crystal silicon," Materials Science and Engineering: B, **230**, 31–42 (2018). https://doi.org/10.1016/j.mseb.2017.12.040
[15] K.S. Daliev, Sh.B. Utamuradova, J.J. Khamdamov, Sh.B. Norkulov, and M.B. Bekmuratov, "Study of Defect Structure of Silicon Doped with Dysprosium Using X-Ray Phase Analysis and Raman Spectroscopy," East Eur. J. Phys. (4), 311-321 (2024). https://doi.org/10.26565/2312-4334-2024-4-35
[16] V.O. Vas'kovskiy, A.V. Svalov, A.V. Gorbunov, N.N. Schegoleva, and S.M. Zadvorkin, "Structure and magnetic properties of Gd/Si and Gd/Cu hybridization in lithium tetraborate," Frontiers in Physics, **2**, (2014). https://doi.org/10.3389/fphy.2014.00031
[17] K.S. Daliev, Sh.B. Utamuradova, J.J. Khamdamov, M.B. Bekmuratov, Sh.B. Norkulov, and U.M. Yuldoshev, "Changes in the Structure and Properties of Silicon During Ytterbium Doping: The Results of o Comprehensive Analysis," East Eur. J. Phys. (4), 240-249 (2024). https://doi.org/10.26565/2312-4334-2024-4-24
[18] K. Kasirajan, L.B. Chandrasekar, S. Maheswari, M. Karunakaran, and P.S. Sundaram, "A comparative study of different rare-earth (Gd, Nd, and Sm) metals doped ZnO thin films and its room temperature ammonia gas sensor activity: Synthesis, characterization, and investigation on the impact of dopant," Optical Materials, **121**, 111554 (2021). https://doi.org/10.1016/j.optmat.2021.111554
[19] T.D. Kelly, J.C. Petrosky, J.W. McClory, V.T. Adamiv, Y.V. Burak, B.V. Padlyak, I.M. Teslyuk, *et al.*, "Rare earth dopant (Nd, Gd, Dy, and Er) hybridization in lithium tetraborate," Front. Phys. **2**, (2014). https://doi.org/10.3389/fphy.2014.00031
[20] A.I. Prostomolotov, Yu.B. Vasiliev, and A.N. Petlitsky, "Mechanics of defect formation during growth and heat treatment of single-crystal silicon," **4**(4), 1716–1718 (2011). http://www.unn.ru/pages/e-library/vestnik/19931778_2011_-_4-4_unicode/147.pdf
[21] S.Z. Zainabidinov, A.Y. Boboev, N.Y. Yunusaliyev, and J.N. Usmonov, "An optimized ultrasonic spray pyrolysis device for the production of metal oxide films and their morphology," East Eur. J. Phys. (3), 293 (2024), https://doi.org/10.26565/2312-4334-2024-3-30
[22] W.-E. Hong, and J.-S. Ro, "Kinetics of solid phase crystallization of amorphous silicon analyzed by Raman spectroscopy," J. Appl. Phys. **114**, 073511 (2013). https://doi.org/10.1063/1.4818949
[23] S. Zainabidinov, Sh.Kh. Yulchiev, A.Y. Boboev, B.D. Gulomov, and N.Y. Yunusaliyev, "Structural properties of Al-doped ZnO films," East Eur. J. Phys. (3), 282 (2024). https://doi.org/10.26565/2312-4334-2024-3-28
[24] R.T.-P. Lee, K.-M. Tan, T.-Y. Liow, C.-S. Ho, S. Tripathy, G.S. Samudra, D.-Z. Chi, and Y.-C. Yeo, "Probing the $ErSi_{1.7}$ Phase Formation by Micro-Raman Spectroscopy," Journal of The Electrochemical Society, **154**(5), H361-H364 (2007). https://doi.org/10.1149/1.2710201
[25] A.S. Zakirov, Sh.U. Yuldashev, H.J. Wang, H.D. Cho, T.W. Kang, J.J. Khamdamov, and A.T. Mamadalimov, "Photoluminescence study of the surface modified and MEH-PPV coated cotton fibers," Journal of Luminescence, 131(2), 301–305 (2011). https://doi.org/10.1016/j.jlumin.2010.10.019
[26] S. Zainabidinov, A.Y. Boboev, and N.Y. Yunusaliyev, "Effect of γ-irradiation on structure and electrophysical properties of S-doped ZnO films," East European Journal of Physics, (2), 321–326 (2024) https://doi.org/10.26565/2312-4334-2024-2-37

ЛЕГУВАННЯ КРЕМНІЮ АТОМАМИ ГАДОЛІНІЮ – СТРУКТУРНИЙ РОЗПОДІЛ ТА СПЕКТРАЛЬНІ ЗМІНИ КРЕМНІЮ

Ш.Б. Утамурадова[a], Ш.Х. Далієв[a], Д.Д. Хамдамов[a], Х.Д. Матчонов[a], М.К. Карімов[b], Х.Ю. Утемуратова[c]
[a]Інститут фізики напівпровідників і мікроелектроніки Національного університету Узбекистану, вул. Янги Алмазара, 20,
[b]Ургенчський державний університет, факультет фізики, Ургенч, Узбекистан
[c]Каракалпакський державний університет, Нукус, Каракалпакстан

У цьому дослідженні ми досліджували зразки кремнію, леговані гадолінієм, використовуючи два різні методи: включення під час росту та дифузійна обробка при підвищених температурах. Скануючу електронну мікроскопію (SEM) та енергодисперсійну спектроскопію (EDS) використовували для аналізу мікроструктури поверхні та розподілу атомів домішок, тоді як раманівська спектроскопія виявила характерні зсуви фононних мод, спричинені допуванням гадолінієм. Було виявлено, що легування під час росту призводить до більш однорідної структури з меншою кількістю великих дефектів, хоча локалізовані області, збагачені вуглецем і киснем, залишаються. Навпаки, дифузійне легування призводить до утворення виражених неоднорідностей, що вказує на значне утворення дислокацій і структурних дефектів через неузгодженість параметрів решітки. Результати демонструють вплив методу легування на стан поверхні кремнію, розподіл пружних напружень і появу нових коливальних мод, які можуть бути використані для цілеспрямованої модифікації властивостей матеріалів у спінтронних, оптоелектронних і сенсорних пристроях.
Ключові слова: *кремній; гадоліній; допінг; дифузія; SEM; EDS; Раманівська спектроскопія; структурні дефекти; фононний спектр; дефекти кристалічної решітки; оптоелектроніка; магнітні характеристики*

EAST EUROPEAN JOURNAL OF PHYSICS. 1. 284-289 (2025)
DOI:10.26565/2312-4334-2025-1-33 ISSN 2312-4334

COMPARATIVE STUDY AND ANALYTICAL MODELING OF AlGaN/GaN HEMT AND MOSHEMT BASED BIOSENSORS FOR BIOMOLECULES DETECTION

Abdellah Bouguenna[a]*, Abdelhadi Feddag[b], Driss Bouguenna[c,d], Ibrahim Farouk Bouguenna[e]
[a]*Electrical Engineering Laboratory of Oran, Electronics Department, Electrical Engineering Faculty, Sciences & Technology University of Oran (MB-USTO), 31000, Oran, Algeria*
[b]*Department of Electronics. Faculty of Electrical Engineering University of Sciences and Technology of Oran, Microsystems and Embedded Systems Laboratory of Oran, Algeria*
[c]*Geomatics, Ecology and Environment Laboratory, Nature and Life Science Faculty, Mustapha Stambouli University of Mascara, 29000, Mascara, Algeria*
[d]*Common Core Science and Technology Department, Sciences and Technology Faculty, Mustapha Stambouli University of Mascara, 29000, Mascara, Algeria*
[e]*Electrical Engineering Department, Sciences and Technology Faculty, Mustapha Stambouli University of Mascara, Mascara 29000, Algeria*
**Corresponding Author e-mail: abdellah.bouguenna@univ-usto.dz*
Received December 19, 2024; revised January 22, 2025; accepted January 25, 2025

In this study, a model has been developed to analyze AlGaN/GaN high-electron-transistor (HEMT) and metal-oxide semiconductor high-electron-transistor (MOSHEMT) based biosensors. The model focuses on detecting biomolecules such as ChOx, protein, streptavidin and uricase by modulating the dielectric constant. The sensitivity parameters used for biomolecule detection include drain current, transconductance, and drain off sensitivity. The dielectric constant is adjusted based on the specific biomolecule being sensed by the biosensor. The variation in dielectric leads to changes in drain current, with an increase or decrease depending on the positive charge of the biomolecules. The HEMT device exhibits greater variations in drain current, transconductance, and drain off sensitivity compared to the MOSHEMT device when the biomolecule is present in the cavity region. The simulation results are validated by comparing them with Atlas-TCAD (atlas-technology computer aided design) and experimental data, showing excellent agreement.
Keywords: *AlGaN/GaN; HEMT; MOSHEMT; Biosensors; Biomolecules*
PACS: 87.85.fk

1. INTRODUCTION

For the detection of biochemical compounds such as enzymes, biological molecules, antibodies, etc the biosensors use chemical reactions [1]. GaN-based devices are good compared to silicon-based devices due to their large bandgap (3.4 eV), large electron saturation velocity (2.5×10^7 cm/s), and high operating temperature [2, 3]. AlGaN/GaN HEMT structures are widely utilized in biosensors due to their remarkable biocompatibility, stable material characteristics, and remarkable sensitivity to surface charge. This is primarily assigned to the close proximity of the two-dimensional electron gas (2DEG) channel to the surface, which typically reaches a density of approximately 10^{13} cm^{-2}. [4, 5]. The 2DEG are generated by spontaneous and piezoelectric polarization that are moderated by positive charges at the surface [6]. An oxide layer such as Al_2O_3 [7], is entered between barrier and gate metal which results HEMTs becomes MOSHEMTs [5, 8, 9]. The AlGaN barrier layer readily binds specific biomolecules, leading to variations in surface charges at the AlGaN/GaN interface [1]. Extensive research has been undertaken on AlGaN/GaN HEMT for the detection of various biomolecules, including proteins [10], Hg^{2+} [11], DNA [12], PSA [13], and c-erbB^{-2} [14]. This paper offers a comparative study between AlGaN/GaN HEMT and MOSHEMT based biosensors, focusing on the introduction of biomolecules into a nanogap cavity. The comparison aims to evaluate the impact of oxide material on the performance of these biosensors. To assess their suitability for biosensing applications, we simulated the I_{ds}-V_{gs}, I_{ds}-V_{ds}, transconductance, and sensitivity parameters for different biomolecules detection.

2. STRUCTURES OF AlGaN/GaN HEMT& MOSHEMT DEVICES

The diagram in Fig. 1 illustrates the structure of AlGaN/GaN HEMT and MOSHEMT devices. In the case of HEMT, the layers are grown in the following order: metal/AlGaN/GaN. In the MOSHEMT case. Additionally, a GaN buffer layer is grown on an Al_2O_3 substrate.

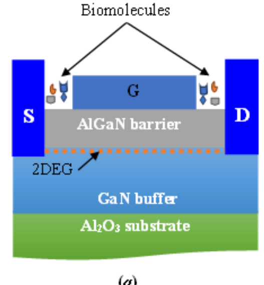

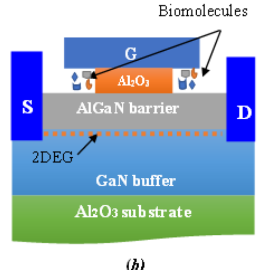

Figure 1. Model of AlGaN/GaN biosensors. *(a)* HEMT and *(b)* MOSHEMT

Cite as: A. Bouguenna, A. Feddag, D. Bouguenna, I.F. Bouguenna, East Eur. J. Phys. 1, 284 (2025), https://doi.org/10.26565/2312-4334-2025-1-33
© A. Bouguenna, A. Feddag, D. Bouguenna, I.F. Bouguenna, 2025; CC BY 4.0 license

3. ANALYTICAL MODEL OF DEVICES

In this paper, the analytical model taken from paper [15].
The analytical expression of the drain current can be formulated as

$$I_d = \frac{W_g \mu_0 C_{eff}}{L_g \delta} \left\{ \sum_{i=0}^{6} k_i \left(\psi_{gd}^i - \psi_{gs}^i \right) + k_0 ln \frac{\psi_{gd}}{\psi_{gs}} \right\} \quad (1)$$

where μ_0 is low field mobility. W_g and L_g are the width and the length of gate, respectively. $\psi_{gs} = \left(V_{gs} - V_{th} - V_s\right)^{1/3} + 2\theta$, $\psi_{gd} = \left(V_{gs} - V_{th} - V_{ds}\right)^{1/3} + 2\theta$, $\delta = V_d - V_s/E_T L_g$, $\theta = \lambda/3\,(C_{eff}/q)^{2/3}$ and E_T is the critical field.

The transconductance (g_m) is the derivation of the drain current by gate voltage at $V_{ds} = const$, it can be defined as

$$g_m = \left. \frac{\partial I_{ds}}{\partial V_{gs}} \right|_{V_{ds}=const}. \quad (2)$$

The transconductance can be extracted from Eq. (1)

$$g_m = \frac{\mu_0 W_g C_{eff}}{\rho L_g} \left[\frac{1}{3\left(\psi_{gd} - 2\theta\right)^2 - 3\left(\psi_{gs} - 2\theta\right)^2} \right] \Omega_1. \quad (3)$$

Where

$$\Omega_1 = \begin{bmatrix} \frac{288\theta^6}{(\psi_{gd} - \psi_{gs})} + 272\theta^5 + 1920\theta^4\left(\psi_{gd} - \psi_{gs}\right) + 600\theta^3\left(\psi_{gd} - \psi_{gs}\right)^2 \\ -280\theta^2\left(\psi_{gd} - \psi_{gs}\right)^3 + 195\theta\left(\psi_{gd} - \psi_{gs}\right)^4 - 18\left(\psi_{gd} - \psi_{gs}\right)^5 \end{bmatrix}. \quad (4)$$

4. RESULTS AND DISCUSSION

We will discuss the comparison of AlGaN/GaN HEMT and MOSHEMT based biosensors. The material parameters and their corresponding values employed for the simulation are outlined in Table 1 and Table 2. Furthermore, the biomolecule permittivity used in this study is listed in Table 3, and the specific values for the two different device types are delineated in Table 4.

Table 1. Constants terms. [16]

Constants	**Expressions**
k_0	$-288\theta^6$
k_1	$272\theta^5$
k_2	$-960\theta^4$
k_3	$200\theta^3$
k_4	$-70\theta^2$
k_5	$39\,\theta$
k_6	-3

Table 2. Parameters used in numerical simulations

Parameters	**Quantities**	**Values**	**Units**	**Refs.**
E_T	Critical electric field	178×10^5	V/m	[3]
φ_M	Metal work function	4.5	eV	[3]
φ_0	Natural level Potential	1.2	eV	[3]
μ_0	Low field mobility	0.06	m^2/Vs	[3]
N_D	Doping concentration	1.5×10^{16}	m^{-3}	[3]
γ_0	Experimental parameter	4.12×10^{-12}	$Vcm^{4/3}$	[17]

Table 3. Dielectric constants of biomolecules [18, 19]

Biomolecules	**Dielectric constants**
ChOx	3.3
Protein	2.5
Streptavidin	2.1
Uricase	1.54

Table 4. Device parameters used in simulation

Parameters	**Description**	**Fig. 2a [20] Sample 1**	**Fig. 2b [21] Sample 2**	**Fig. 4, 5 and 6 Our model**
x (%)	Al mole fraction	15	20	30
$\varepsilon_{ox}(F/m^2)$	Oxide permittivity	-	9.1 ε_0	9.1 ε_0

Parameters	Description	Fig. 2a [20] Sample 1	Fig. 2b [21] Sample 2	Fig. 4, 5 and 6 Our model
σ_{pol} (m^{-2})	Spontaneous polarization charge	1.15×10^{17} [22]	1.7×10^{17} [22]	1.55×10^{17} [22]
$d_{AlGaN}(nm)$	Barrier thickness	22	30	15
$L_g(\mu m)$	Gate length	1	1	0.3
$W_g(\mu m)$	Gate width	75	100	100
t_{ox} (nm)	Oxide thickness	-	16	10
h_{cavity} (nm)	Cavity width	-	-	10

The output characteristics of the AlGaN/GaN HEMT and MOSHEMT devices are compared in Fig. 2(a) and Fig. 2(b), respectively. The results from our model show a strong agreement with the experimental data [20] and [21]. Besides, the dimensions of the devices used in the experimental data were replicated exactly to validate our results. Furthermore, Matlab calculations and Atlas-TCAD were used to simulate the devices for sample 1 and sample 2, as shown in Fig. 2.

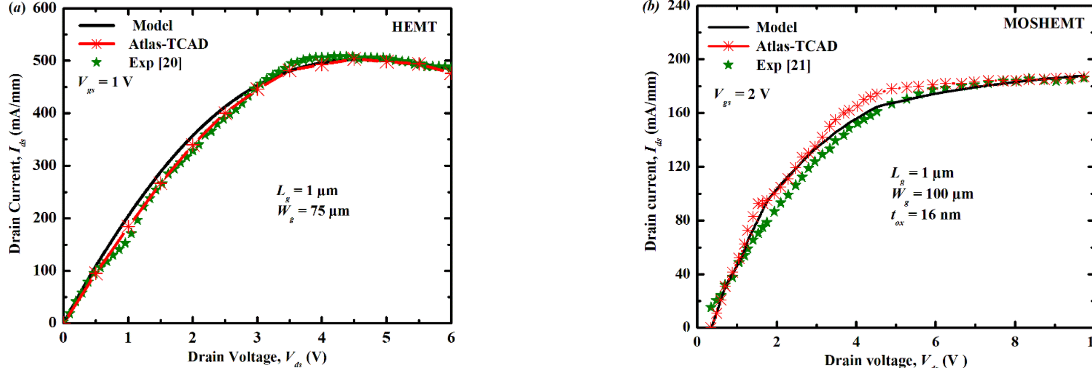

Figure 2. *I-V* output characteristics of GaN HEMT and MOSHEMT devices.
(a) HEMT and *(b)* MOSHEMT with experimental data [20] and [21], respectively

Fig. 3 illustrates the transfer characteristics of the devices with and without biomolecules. When the biomolecule is present in the cavity region, a variation in the drain current is observed. This change in drain current can be considered as a sensing parameter for biomolecule detection. Specifically, at a drain voltage of 5 V, the change in drain current is superior in HEMT device compared to MOSHEMT device. For uricase, streptavidin, protein, and ChOx, the variation in drain current is (35.69, 64.45, 81.3, and 108.36) mA in AlGaN/GaN HEMT, respectively. In contrast, the change in drain current is (7.93, 15.2, 19.88, and 28.18) mA in AlGaN/GaN MOSHEMT, respectively.

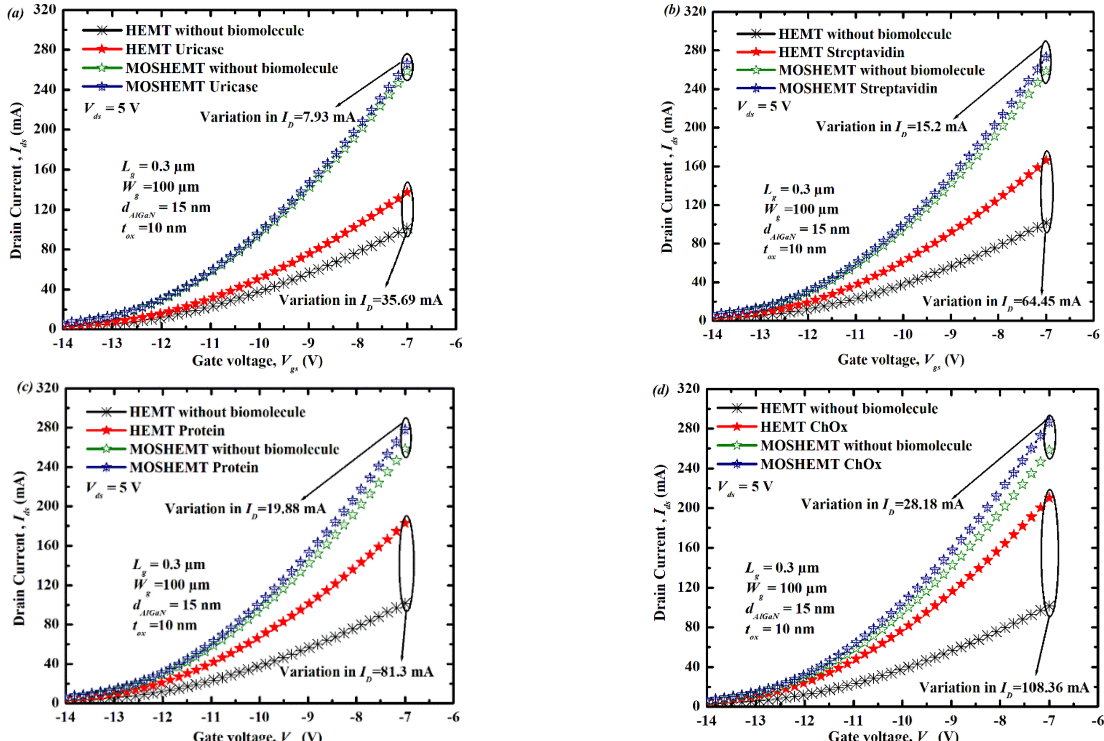

Figure 3. *I–V* transfer characteristics with different biomolecules of the both biosensors.
Change of drain current for *(a)* uricase, *(b)* streptavidin, *(c)* protein and *(d)* ChOx, respectively

Furthermore, the transconductance characteristics of HEMT and MOSHEMT devices with different biomolecules are presented in Figs. 4(a) and 4(b). The introduction of biomolecules into the cavity region leads to a change in the threshold voltage (V_{th}) and subsequently affects the transconductance (g_m). This change in transconductance can serve as a reliable sensing parameter. Notably, the HEMT devices demonstrate a greater variation in transconductance compared to the MOSHEMT devices, as shown in Figs. 4(a) and 4(b). Specifically, the variation in transconductance is (21.58, 20.05, 54.51, and 76.98) mS/mm for uricase, streptavidin, protein, and ChOx in the case of HEMT, respectively. Conversely, the variation in transconductance is (8.19, 15.86, 20.89, and 29.99) mS/mm for uricase, streptavidin, protein, and ChOx in the case of MOSHEMT, respectively.

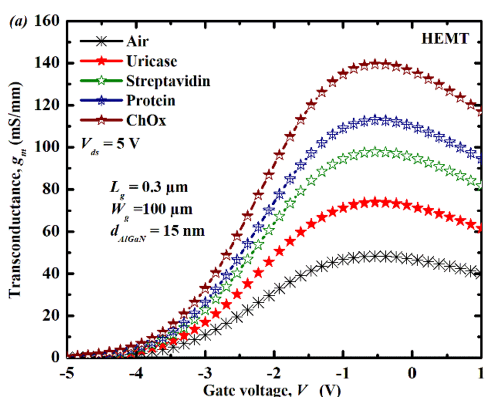

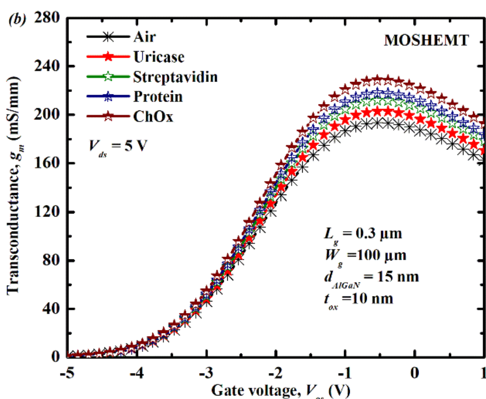

Figure 4. Comparison of the modeled transconductance characteristics with different biomolecules *(a)* HEMT and *(b)* MOSHEMT based biosensors

In Fig. 5, the sensitivity parameter of HEMT and MOSHEMT devices is compared. The results clearly indicate that the sensitivity parameter (S_{Ioff}) is significantly greater in the HEMT device compared to the MOSHEMT device. Among all the biomolecules tested, the ChOx biomolecule exhibits the highest sensitivity for the HEMT device.

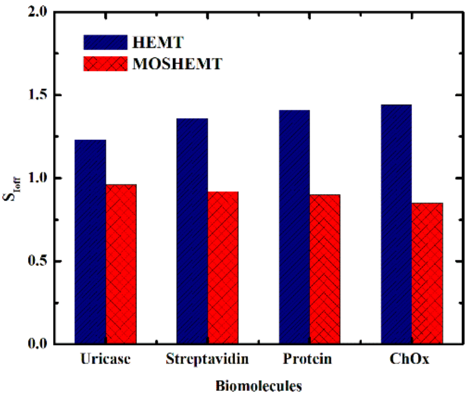

Figure 5. Sensitivity for AlGaN/GaN HEMT and MOSHEMT biosensors

Fig. 6 depicts an escalation in the relative change (sensitivity of drain current). The relative change in drain current is defined as $\Delta_{Ids} = I_{ON}^{Air} - I_{ON}^{Bio}$ [23]. The minimum and maximum relative change observed is (139.07 and 260.8) mA for uricase and ChOx for HEMT and (26.57 and 115.03) mA for uricase and ChOx for MOSHEMT, respectively.

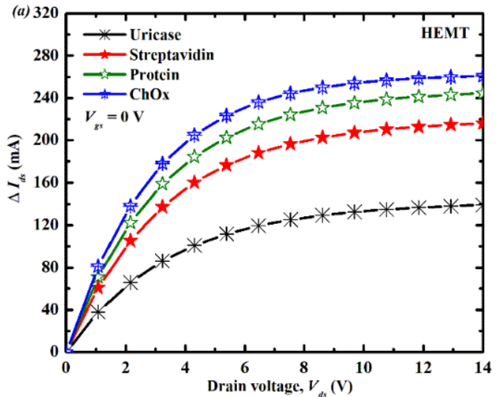

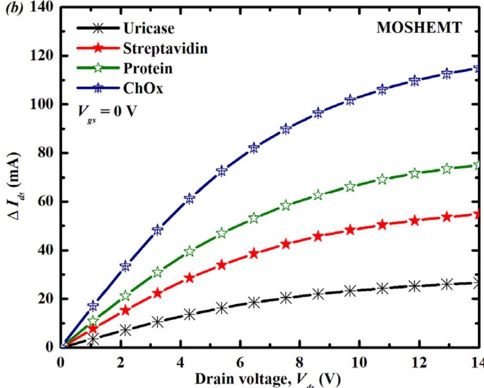

Figure 6. Relative drain ON current sensitivity for *(a)* HEMT and *(b)* MOSHEMT

Table 5. Comparative extracted values of AlGaN/GaN HEMT and MOSHEMT based biosensors.

Biomolecules	**Change in drain current ΔI_D (mA)**		**Drain-off sensitivity (S_{Ioff})**	
	AlGaN/GaN HEMT	AlGaN/GaN MOSHEMT	AlGaN/GaN HEMT	AlGaN/GaN MOSHEMT
Uricase	35.69	7.93	1.23	0.96
Streptavidin	64.45	15.2	1.36	0.92
Protein	81.3	19.88	1.41	0.9
ChOx	108.36	28.18	1.44	0.85

CONCLUSION

The analytical modeling of the both devices was proposed and compared between each other. There is a variation in drain current density and higher transconductance when the cavity region is occupied with biomolecules. This suggests that the GaN-based HEMT and MOSHEMT biosensors perform well for biosensing applications. The results obtained indicate that AlGaN/GaN HEMT based biosensors have been presented a greater change in drain current (ΔI_{on}) and sensitivity for various biomolecules. The saturation drain current and 2DEG concentration increase as the distance between the sensing area and 2DEG channel increases. However, the modulation ability of surface charge on device performance decreases with the increased sensing area-to-channel distance [24]. This implies that the sensing sensitivity decreases in AlGaN/GaN MOSHEMT based biosensors.

Conflict of interest: The authors state no conflict of interest.

ORCID

Abdellah Bouguenna, https://orcid.org/0000-0003-3492-5418; **Abdelhadi Feddag**, https://orcid.org/0009-0004-3817-0539
Driss Bouguenna, https://orcid.org/0000-0002-0660-9576; **Ibrahim Farouk Bouguenna**, https://orcid.org/0000-0001-8631-8172

REFERENCES

[1] H.M. Shaveta, A. Maali, and C. Rishu, "Rapid detection of biomolecules in a dielectric modulated GaN MOSHEMT," J. Mater. Sci: Mater Electron, **31**, 16609–16615 (2020). https://doi.org/10.1007/s10854-020-04216-7
[2] S. Verma, S.A. Loan, and A.G. Alharbi, "Polarization engineered enhancement Mode GaN HEMT: Design and Investigation," Superlattices Microstruct. **119**, 181–193 (2018). https://doi.org/10.1016/j.spmi.2018.04.041
[3] S.A. Loan, S. Verma, and A.R.M. Alamoud, "High performance charge plasma based normally-Off GaN MOSFET," IET Electron. Lett. **52**(8), 656–658 (2016). https://doi.org/10.1049/el.2015.4517
[4] Z. Gu, J. Wang, B. Miao, L. Zhao, X. Liu, D. Wu, and J. Li, "Highly sensitive AlGaN/GaN HEMT biosensors using an ethanolamine modification strategy for bioassay applications," RSC Advance, **9**, 15341–15349 (2019). https://doi.org/10.1039/C9RA02055A
[5] S.N. Mishra, R. Saha, and K. Jena, "Normally-Off AlGaN/GaN MOSHEMT as lebel free biosensor," ECS J. Solid State Sci. Technol. **9**, 1–15 (2020). https://doi.org/10.1149/2162- 8777/aba1cd
[6] S.J. Pearton, B.S. Kang, Kim S. Kim, F. Ren, B.P. Gila, C.R. Abernathy, *et al.*, "GaN-based diodes and transistors for chemical, gas, biological and pressure sensing," J. Phys: Condens. Matter, **16**, R961–R994 (2004). https://doi.org/10.1088/0953-8984/16/29/R02/meta
[7] A. Varghese, C. Periasamy, and L. Bhargava, "Fabrication and charge deduction-based sensitivity analysis of GaN MOS-HEMT device for glucose, MIG, C-erbB-2, KIM-1 and PSA detection," IEEE Trans. Nanotechnol. **18**, 747–755 (2019). https://doi.org/10.1109/TNANO.2019.2928308
[8] A. Koudymov, H. Fatima, G. Simin, J. Yang, M.A. Khan, A. Tarakji, X. Hu, *et al.*, "Maximum current in nitride-based heterostructure Field-Effect Transistors," Appl. Phys. Lett, **80**, 3216–3218 (2002). https://doi.org//10.1063/1.1476054
[9] M.A. Khan, X. Hu, G. Sumin, A. Lunev, J. Yang, R. Gaska, and M.S. Shur, "AlGaN/GaN Metal Oxide Semiconductor Heterostructure Field Effect Transistor," IEEE Elec. Dev. Letters, **21**, 63–65 (2000). https://doi.org//10.1109/55.821668
[10] C.C. Huang, G.Y. Lee, J.I. Chyi, H.T Cheng, C.P Hsu, Y.R Hsu, C.H. Hsu, *et al.*, **"**AlGaN/GaN high electron mobility transistors for protein–peptide binding affinity study," Biosens. Bioelectron. **41**, 717–722 (2012). https://doi.org/10.1016/j.bios.2012.09.066
[11] J. Cheng, J. Li, B. Miao, J. Wang, Z. Wu, D. Wu, and R. Pei, "Ultrasensitive detection of Hg^{2+} using oligo nucleotide functionalized AlGaN/GaN High Electron Mobility Transistor," Appl. Phys. Lett, **105**, 083121-1–083121-4 (2014). https://doi.org//abs/10.1063/1.4894277
[12] S.U. Schwarz, S. Linkohr, P. Lorenz, S. Krischok, T. Nakamura, V. Cimalla, C.E. Nebel, and O. Ambacher, "DNA-sensor based on AlGaN/GaN High Electron Mobility Transistor," Phys. Status Solidi A, **208**, 1626–1629 (2011). https://doi.org/10.1002/pssa.201001041
[13] B.S. Kang, H.T. Wang, T.P. Lele, Y. Tseng, F. Ren, S.J. Pearton, J.W. Johnson, *et al.*, "Prostate specific antigen detection using high electron mobility transistors," Appl. Phys. Lett. **91**, 112106 (2007). https://doi.org/10.1063/1.2772192
[14] K.H. Chen, B.S. Kang, H.T. Wang, T.P. Lele, F. Ren, Y.L. Wang, C.Y. Chang, *et al.*, "C-erbB-2 sensing using AlGaN/GaN High Electron Mobility Transistors for breast cancer detection," Appl. Phys. Lett. **92**, 192103-1–192103-3 (2008), https://doi.org/abs/10.1063/1.2926656
[15] A. Bouguenna, D. Bouguenna, A.B. Stambouli, and S.A. Loan, "Comparative Study and Modeling of AlGaN/GaN Heterostructure HEMT and MOSHEMT Biosensors," Ijneam, **16**(3), 511–522 (2023). https://doi.org/10.58915/ijneam.v16i3.1268
[16] K. Jena, R. Swain, and T.R. Lenka, "Effect of thin gate dielectrics on dc, radio frequency and linearity characteristics of lattice-matched AlInN/AlN/GaN metal–oxide–semiconductor high electron mobility transistor," IET Circuits Devices Syst. **10**, 423-432 (2016). https://doi.org/10.1049/iet-cds.2015.0332

[17] S. Baskaran, A. Mohanbabu, N. Anbuselvan, N. Mohankumar, D. Godwinraj, and C.K. Sarkar, “Modeling of 2DEG sheet carrier density and DC characteristics in spacer based AlGaN/AlN/GaN HEMT devices,” Superlattices Microstruct. **64**, 470–482 (2013). http://dx.doi.org/10.1016/j.spmi.2013.10.019
[18] P. Dwivedi, and A. Kranti, “Applicability of transconductance-to-current ratio (g_m/I_{ds}) as a sensing metric for tunnel FET biosensors,” IEEE Sensors J. **17**, 1030–1036 (2017). https://doi.org/10.1109/JSEN.2016.2640192
[19] A. Varghese, C. Periasamy, and L. Bhargava, “Analytical modeling and simulation-based investigation of AlGaN/AlN/GaN bio-HEMT sensor for C-erbB-2 detection,” IEEE Sens. J. **18**, 9595–9602 (2018). https://doi.org/10.1109/JSEN.2018.2871718
[20] Y.F. Wu, S. Keller, P. Kozodoy, B.P. Keller, P. Parikh, D. Kapolnek, S.P. Denbaars, and U.K. Mishra, “Bias dependent microwave performance of AlGaN/GaN MODFET’s up to 100 V,” IEEE Electron. Dev. Lett. **18**, 290–292 (1997). https://doi.org/10.1109/55.585362
[21] W.D. Hu, X.S. Chen, Z.J. Quan, X.M. Zhang, Y. Huang, C.S. Xia, W. Lu, and P.D. Ye, “Simulation and optimization of GaN-based metal-oxide-semiconductor high electromobility-transistor using field-dependent drift velocity model,” J. Appl. Phys. **102**, 034502 (2007). http://dx.doi.org/10.1063/1.2764206
[22] O. Ambacher, J. Smart, J.R. Shealy, N.G. Weimann, K. Chu, M. Murphy, W.J. Schaff, *et al*., “Two-dimensional electron gases induced by spontaneous and piezoelectric polarization charges in N- and Ga-face AlGaN/GaN heterostructures,” J. Appl. Phys. **85**, 3222–3233 (1999). https://doi.org/10.1063/1.369664
[23] A.M. Bhat, A. Varghese, N. Shafi, and C. Periasamy, “A Dielectrically modulated GaN/AlN/AlGaN MOSHEMT with a nanogap embedded cavity for biosensing applications,” IETE J. Res. **69**(3), 1419-1428 (2023). https://doi.org/10.1080/03772063.2020.1869593
[24] Y. Liu, X. He, Y. Dong, S. Fu, Y. Liu, and D. Chen, “The sensing mechanism of InAlN/GaN HEMT,” Cryst. **12**, 401 (2022). https://doi.org/10.3390/cryst12030401

ПОРІВНЯЛЬНЕ ДОСЛІДЖЕННЯ ТА АНАЛІТИЧНЕ МОДЕЛЮВАННЯ БІОСЕНСОРОВ НА ОСНОВІ AlGaN/GaN HEMT ТА MOSHEMT ДЛЯ ВИЯВЛЕННЯ БІОМОЛЕКУЛ

Абделла Бугенна[a], Абдельхаді Феддаг[b], Дріс Бугенна[c,d], Ібрагім Фарук Бугенна[e]
[a]*Електротехнічна лабораторія Орана, Відділ електроніки, Факультет електротехніки, Науково-технічний університет Орана (MB-USTO), 31000, Оран, Алжир*
[b]*Кафедра електроніки. Факультет електротехніки Університет наук і технологій Орана, Лабораторія мікросистем і вбудованих систем, Оран, Алжир*
[c]*Лабораторія геоматики, екології та навколишнього середовища, факультет природознавства та життя, Університет Мустафи Стамбулі, Маскара, 29000, Туш, Алжир*
[d]*Common Core Science and Technology Department, Science and Technology Faculty, Mustapha Stambouli University of Mascara, 29000, Mascara, Algeria*
[e]*Кафедра електротехніки, Факультет науки та технологій, Університет Мустафи Стамбулі в Маскара, Маскара 29000, Алжир*
У цьому дослідженні була розроблена модель для аналізу біосенсорів на основі високоелектронних транзисторів AlGaN/GaN (HEMT) і металооксидних напівпровідникових високоелектронних транзисторів (MOSHEMT). Модель фокусується на виявленні біомолекул, таких як ChOx, протеїн, стрептавідин і уриказа, шляхом модуляції діелектричної проникності. Параметри чутливості, що використовуються для виявлення біомолекул, включають струм стоку, транспровідність і чутливість стоку. Діелектрична проникність регулюється на основі конкретної біомолекули, яку відчуває біосенсор. Зміна діелектрика призводить до змін струму витоку зі збільшенням або зменшенням залежно від позитивного заряду біомолекул. Пристрій HEMT демонструє більші варіації струму стоку, транспровідності та чутливості стоку порівняно з пристроєм MOSHEMT, коли біомолекула присутня в області порожнини. Результати моделювання підтверджуються шляхом їх порівняння з Atlas-TCAD (система автоматизованого проектування атласної технології) та експериментальними даними, що демонструє чудову згоду.
Ключові слова: *AlGaN/GaN; HEMT; MOSHEMT; біосенсори; біомолекули*

EAST EUROPEAN JOURNAL OF PHYSICS. 1. 290-294 (2025)
DOI:10.26565/2312-4334-2025-1-34 ISSN 2312-4334

METHODS OF CORRECTION OF SPECTRAL CHARACTERISTICS OF SILICON PHOTODETECTORS

Mykola S. Kukurudziak[a,b]*, Vyacheslav V. Ryukhtin[a]
[a]*Rhythm Optoelectronics Shareholding Company, Holovna str. 244, 58032, Chernivtsi, Ukraine*
[b]*Yuriy Fedkovych Chernivtsi National University, Kotsyubyns'kogo str. 2, 58012, Chernivtsi, Ukraine*
**Corresponding Author e-mail: mykola.kukurudzyak@gmail.com*
Received December 21, 2024; revised February 16, 2025; accepted February 21, 2025

The paper investigates methods for shifting the spectral characteristics of silicon photodiodes toward longer wavelengths. It is established that with increasing the reverse bias voltage of the photodiode, the maximum spectral characteristic shifts towards longer wavelengths due to an increase in the collection coefficient of minority charge carriers, which determines the appearance of the spectral characteristic. With an increase in the lifetime of minor charge carriers and the resistivity of the photodiode base material, the maximum of its spectral characteristic also shifts towards longer wavelengths. Increasing the n^+-junction depth of the photodiode reduces the effect of background short-wave radiation on the useful signal of the photodiode. Silicon cut-off adsorption light filters have been proposed that eliminate the influence of background radiation with a wavelength of less than 800 nm on the photodiode signal and have a transmittance of about 75% at a wavelength of 1064 nm.
Keywords: *Silicon; Photodetector; Sensitivity; Spectral Characteristics; Optical Transmission*
PACS: 61.72. Ji, 61.72. Lk, 85.60. Dw

The main task of photodetectors is to detect monochromatic laser radiation. Therefore, photodetectors designed for such applications must demonstrate increased sensitivity at a specific wavelength (λ). The spectral sensitivity characteristic of a photodiode, *S*(λ), describes how its monochromatic sensitivity varies with wavelength. This knowledge is important not only for evaluating the operation of a photodetector with coherent radiation sources, but also for analyzing the operation with incoherent sources whose spectral composition is known [1].

Ensuring a given type of the photodetector's spectral response is usually realized by using a semiconductor material with different band gaps E_g [2], since it is the band gap that determines in which part of the spectrum the semiconductor has the greatest sensitivity to photogeneration of charge carriers (1):

$$\lambda = \frac{hc}{E_g} \tag{1}$$

where *h* is the Planck constant, *c* is the speed of light.

To shift the spectral characteristic towards longer wavelengths, materials with higher E_g are used. For example, silicon photodiodes are used for the visible and near-infrared spectrum. For the infrared spectrum, materials based on GaAs (E_g = 1.42 eV) [3, 4], Ge (E_g = 0.66 eV) [5, 6], or InP (E_g = 1.34 eV) [7] are used. The use of heterostructures (with different materials) can change the width of the bandgap in a wide range, which allows controlling the spectral sensitivity of the photodiode [8, 9]. For this purpose, multilayer structures are used, where different layers have different E_g.

When the photodiode is heated, the width of the bandgap changes, which can lead to a shift in the spectral maximum toward longer wavelengths. However, this method is less controllable and often has a negative impact on the characteristics of the photodiode [10].

An urgent task of modern photoelectronics is the development and manufacture of efficient and highly sensitive photodetectors for detecting YAG lasers (λ = 1064 nm) [11, 12]. Silicon is the main material for this task, but under normal conditions, Si-based photodiodes have a λ_{max}=800-900 nm [6, 10]. Accordingly, there is a need to develop methods for shifting the spectral maximum of silicon photodiodes (PD) towards longer wavelengths.

One of the effective methods of shifting the spectral characteristics of the PD is the use of light filters, in particular, interference bandpass filters or adsorption cutoff filters. High-quality interference bandpass filters are characterized by a high transmittance and can (T≥90%) isolate narrow spectral regions (up to 15-20 Å) [13, 14]. Striking examples of light filters for λ=1064 nm on the market are FLH051064-3 [15], or FLH1064-3 (THORLABS) with T >90% (at λ=1064 nm) and a bandwidth at λ=1041-1087 nm [16]; 20CGA1000 (NEWPORT) with a bandwidth of λ>1000 nm and T ≥90% [17]. The disadvantage of interference optical filters is the dependence of the position of the transmission bands on the angle of incidence of light, cost, complexity of manufacturing, the need for special equipment, expensive materials for creating layers, and calculation programs.

Adsorption filters are the most common class of optical filters that have spectral selectivity due to unequal absorption of light in different wavelength ranges. These are usually different semiconductor materials or types of glass [13]. Silicon adsorption filters, with or without anti-reflective coating, are a common choice for reducing the effect of short-wave

Cite as: M.S. Kukurudziak, V.V. Ryukhtin, East Eur. J. Phys. 1, 290 (2025), https://doi.org/10.26565/2312-4334-2025-1-34
© M.S. Kukurudziak, V.V. Ryukhtin, 2025; CC BY 4.0 license

radiation on the useful signal of IR photodiodes [18]. In [19], we proposed silicon adsorption light filters with an anti-reflective coating, with a bandwidth of λ>900 nm and $T \leq 60$-65% (at λ=1064 nm). The relatively low transmittance of the filters is due to the need to manufacture samples with a thickness that provides adequate mechanical strength.

A review of the sources shows that the study of the possibilities of shifting the spectral characteristics of silicon PDs towards longer wavelengths is an urgent scientific and technical task, which is the purpose of this work.

EXPERIMENTAL

The research was carried out in the manufacture of silicon 4Q *p-i-n* PDs for operation at wavelength λ = 1064 nm (Fig. 1a). PDs were made on the basis of single-crystal *p*-type FZ-Si with [111] orientation. The samples were made by diffusion-planar technology according to the technological regimes given in [20]. Silicon with different resistivity of ρ = 12-22 kΩ·cm and different lifetime of non-basic charge carriers of τ=1-2 ms was used.

The PDs with different depths of the *p-n*-junction, which was adjusted by the duration of phosphorus deposition, were studied. Samples with x_{n+-p} = 3.5-6 μm were fabricated. The spectral characteristics of sensitivity at different bias voltages were studied in the PDs made of different base materials and with different x_{n+-p}.

The possibility of increasing the transmittance of silicon light filters in combination with silicon photodiodes (PDs) is investigated. The best option for increasing the transmittance of a light filter is to reduce its thickness, but this significantly reduces its mechanical strength. We proposed to thin the filter only in the zones that are projections of responsive elements, and to leave the periphery of the light filter of sufficient thickness to ensure proper mechanical strength (Fig. 1b). This was done by etching the silicon by chemical-dynamic polishing in a solution of HNO_3:HF:CH_3COOH with a masking gold coating (Fig. 2). Gold was chosen as a masking coating because photoresists are not sufficiently chemically resistant to aggressive etching agents during prolonged etching. Since gold has poor adhesion to silicon, an adhesive sublayer of chromium was formed [21]. The metallization was applied by thermal evaporation in a vacuum. The thickness of the gold layer reached 400-500 nm, and that of chromium 30-70 nm. The etching was carried out in 3 stages of 10 min each. The thickness of the silicon base of the light filter reached 250-300 μm, and the projections of the responsive elements after chemical-dynamic polishing reached 70 μm. After CDP and metallization etching, the silicon substrates were oxidized in a dry oxygen atmosphere according to the method given in [22]. The film of SiO_2 thickness reached 180-190 nm, which corresponds to the condition of minimum reflection of radiation with λ = 1064 nm [23]. The proposed filters in combination with the PD were compared with flat silicon filters of greater thickness.

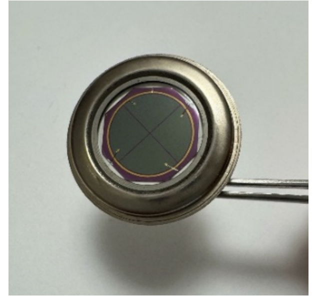
a

b

Figure 1. Images of a photodiode
(a) – without a light filter and (b) – with the proposed filter

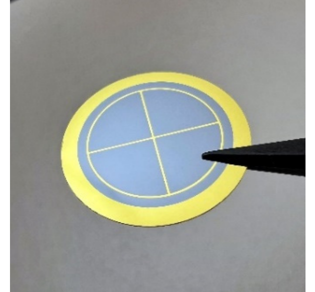
a
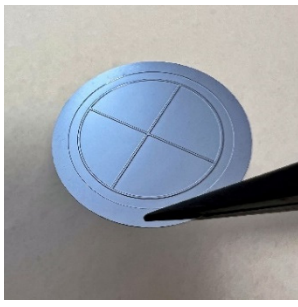
b

Figure 2. Images of a filter with a masking coating
(a) – before etching and (b) – a light filter with etched projections of responsive elements

Investigation of the transmission spectra were performed using SF-2000 spectrophotometers at room temperature. The spectral characteristics of responsivity were measured using the KSVU-23 automated spectral complex.

RESULTS OF THE RESEARCH AND THEIR DISCUSSION

A) Study of the dark currents

It was found that with an increase in the reverse bias voltage, the maximum of the spectral characteristic shifts towards longer wavelengths Fig. 3. This is due to an increase in the size of the space charge region W_i (2) [24], with an increase in which the collection coefficient of photogenerated charge carriers increases (γ) (3) [25], and the appearance and maximum spectral characteristic of the PD is primarily determined by the collection coefficient (4) [6].

$$W_i = \left(\frac{2\varepsilon\varepsilon_0\,(\phi_c - U_{bias})}{eN_A}\right)^{\frac{1}{2}}. \quad (2)$$

ε, ε_0 are dielectric constants for silicon and vacuum, respectively; φ_c is contact potential difference, e is the electron charge, N_A is concentration of acceptors, U_{bias} is bias voltage.

$$\gamma = 1 - e^{-\alpha(W_i + L_n)}, \quad (3)$$

α is absorption coefficient, L_n is diffusion length of minor charge carriers.

$$S_\lambda = (1-R)TQ\sum\gamma\frac{\lambda}{1.24} \tag{4}$$

where T is the transmission coefficient of the input window or optical filter, Q is the quantum output of the internal photoeffect, R is the reflection coefficient.

It has also been found that with an increase in the resistivity and lifetime of minority charge carriers of silicon at the same bias voltage, the maximum of the spectral characteristic also shifts towards longer wavelengths (Fig. 4). This phenomenon is also related to the charge carrier collection coefficient, since at the same bias voltage, the PD with a higher resistivity will have a larger width of the space charge region. Note that an increase in the lifetime of charge carriers also increases the collection coefficient due to an increase in the diffusion length and an increase in the collection area of photogenerated charge carriers [26].

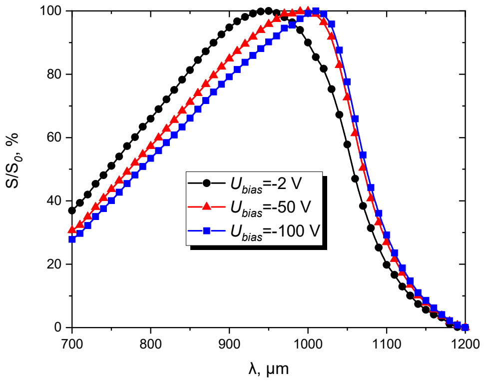

Figure 3. Relative spectral characteristic of the PD at different U_{bias}

Figure 4. Relative spectral characteristic of the PD with different ρ and τ of silicon at U_{bias}=-2 V

It should be noted that the electrophysical characteristics of silicon can degrade during technological operations, in particular thermal ones. This degradation is possible due to poor-quality chemical treatments, the introduction of uncontrolled impurities (thermodonors) from quartz tooling, the use of carrier gases or deionized water of insufficient quality. This degradation can occur to varying degrees in different batches, which will result in different maximum spectral characteristics when using the same base material [27-29].

It was found that with an increase in the depth of the n^+-p junction, the effect of short-wave background radiation on the useful signal of the photodiode decreases, i.e., the slope of the spectral response changes (Fig. 5). The decrease in the sensitivity of the photodiode to shortwave radiation with increasing x_{n+-p} is due to the fact that in *p-i-n* PDs, the photogeneration of charge carriers that reach the *p-n* junction occurs in the *i*-region, the charge carriers generated in the n^+-layer recombine before reaching the *p-n* junction. Accordingly, the generation of non-equilibrium charge carriers in the high-resistance region of the PD occurs only by those wavelengths that penetrate the *i*-region. Thus, radiation with λ = 0.95 μm is absorbed in Si at a depth of about 63 μm, and with λ = 0.7 is absorbed in Si at a depth of about 4.33 μm [30]. Accordingly, by increasing the depth of the n^+-p junction, the influence of short-wave background radiation on the photodetector signal can be excluded.

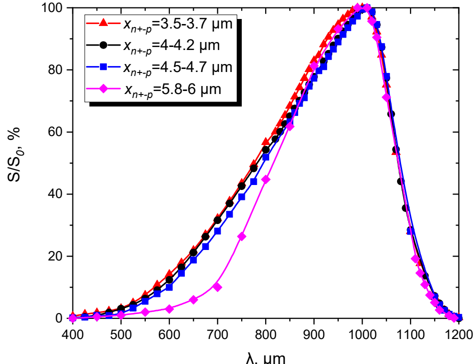

Figure 5. Relative spectral characteristic of the PD with different x_{n+-p}

An increase in the depth of the phosphorus impurity is possible with an increase in the duration of the phosphorus driving-in operation, but its significant duration is negative, since an increase in the total duration of high-temperature thermal operations provokes an increase in the degree of degradation of the electrophysical characteristics of silicon and the formation of inversion layers at the Si-SiO_2 interface, which negatively affects the final parameters of the products [28, 29, 31].

The transmission spectra of silicon light filters of different thicknesses were obtained (Fig. 6). It was found that as the thickness of the filter increases, its transmittance decreases according to the Bouguer-Lambert Beer law [32]. Thus, a

filter with a thickness of d=70 μm has a transmittance at λ=1064 nm of about T=75%, d=170 μm - T=66%, d=240 μm - T=62%, d=280 μm - T=57%. Also, from Fig. 6, it can be seen that with a decrease in the thickness of the filter, the edge of its absorption shifts towards shorter wavelengths.

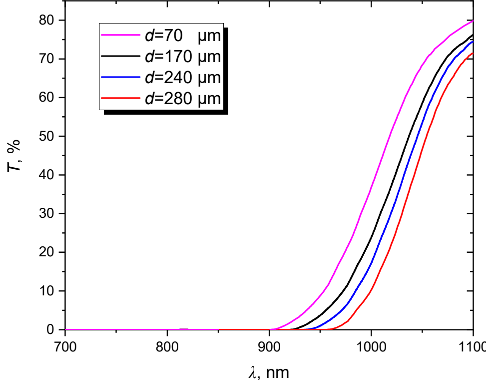

Figure 6. Transmission spectrum of light filters

We also obtained the spectral characteristics of the photodetectors with light filters (Fig. 7) and found that with an increase in the filter thickness, the maximum spectral response of the photodetector shifts towards longer wavelengths, and the short-wave edge of the photosensitivity shifts towards longer wavelengths. Thus, a photodetector with a filter with d = 430 μm becomes sensitive at λ≥ 950 μm, and has a maximum sensitivity at λ_m = 1060 nm, but has a low sensitivity value due to the high thickness of the filter. A light filter with d=70 μm becomes sensitive at λ≥800 μm, and has a maximum sensitivity at λ=1030 nm, but the absolute value of its sensitivity is almost the same as the PD without a light filter. Note that in the PD without a filter, λ_m=1020 nm, so the filter with d=70 shifts λ_m by only 10 nm.

It is worth noting that with an increase in the bias voltage, the spectral characteristic of the PD with a filter also shifts towards longer wavelengths (Fig. 8).

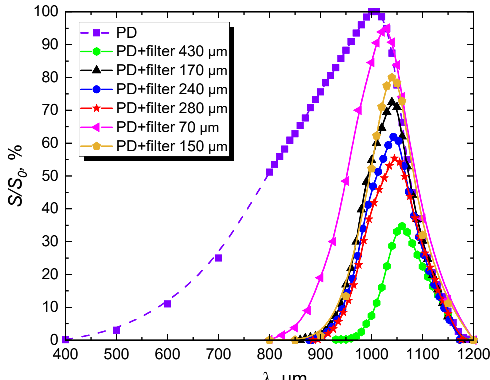

Figure 7. Relative spectral characteristic of the PD with filters of various thicknesses at U_{bais}=-120 V

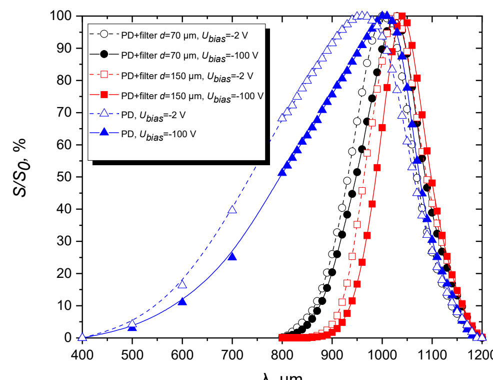

Figure 8. Relative spectral characteristic of the PD with filters of various thicknesses at U_{bais}=-2 V and U_{bais}=-100 V (characteristics are given to 100 %)

Increasing the thickness of the filter improves its selectivity. Optical concentrators can be used in the design of the PD to level the absorption of radiation by the filter thickness [33]. The proposed light filters are a cheap and no less effective analog of interference bandpass filters for the near-infrared region with a much simpler manufacturing technology.

CONCLUSIONS

The methods of correction of the spectral characteristics of silicon photodiodes, in particular, the methods of its shift towards longer wavelengths, are investigated. The following conclusions have been drawn:

1. With an increase in the reverse bias voltage of the photodiode, the maximum spectral characteristic shifts towards longer wavelengths

2. With an increase in the resistivity and diffusion length of minor charge carriers of silicon, the maximum spectral characteristic of silicon shifts towards longer wavelengths.

3. With an increase in the depth of the n^+-p junction, the effect of short-wave radiation on the useful signal of the photodiode decreases due to the absorption of short wavelengths by the n^+-layer.

4. The use of silicon cut-off adsorption light filters eliminates the influence of short-wave background radiation on the photodiode signal at λ≥800 nm. Also, the proposed filters allow to shift the maximum of the spectral characteristic

towards longer wavelengths. With the increase of the filter thickness, its optical transmittance decreases but selectivity improves.

ORCID
Mykola S. Kukurudziak, https://orcid.org/0000-0002-0059-1387

REFERENCES

[1] Z. Bielecki, et al., Bulletin of the Polish Academy of Sciences, Technical Sciences, **70**(2) (2022). https://doi.org/10.24425/bpasts.2022.140534
[2] S. Cai, et al. *Advanced Materials*, ***31***(18), 1808138 (2019). https://doi.org/10.1002/adma.201808138
[3] S.I. Krukovskyi, V. Arikov, A.O. Voronko, and V.S. Antonyuk, Journal of nano- and electronic physics, **14**(2) 02016(5pp) (2022). https://doi.org/10.21272/jnep.14(2).02016
[4] C. Jia, Journal of Materials Chemistry C, **7**(13), 3817 (2019). https://doi.org/10.1039/C8TC06398B
[5] M.K. Sharma, and J.L. Burnett, Nuclear Instruments and Methods in Physics Research Section A: Accelerators, Spectrometers, Detectors and Associated Equipment, **988**, 164943 (2021). https://doi.org/10.1016/j.nima.2020.164943
[6] A.V. Fedorenko, Technology and design in electronic equipment, **17**(3–4), 17 (2020). https://doi.org/10.15222/TKEA2020.3-4.17 (in Ukrainian)
[7] C. Li, et al., Optics & Laser Technology, **175**, 110831 (2024). https://doi.org/10.1016/j.optlastec.2024.110831
[8] I.G. Orletskyi, M.I. Ilashchuk, E.V. Maistruk, H.P. Parkhomenko, P.D. Marianchuk, I.P. Koziarskyi, and D.P. Koziarskyi, Materials Research Express, **8**(1), 015905(9pp) (2021). https://doi.org/10.1088/2053-1591/abdbf8
[9] E.V. Maistruk, M.I. Ilashchuk, I.G. Orletsky, I.P. Koziarskyi, D.P. Koziarskyi, P.D. Marianchuk, O.A. Parfenyuk, and K.S. Ulyanytskiy, Engineering Research Express, **2**(3), 035037(14pp) (2020). https://doi.org/10.1088/2631-8695/abb7e5
[10] A. Voronko, D. Novikov, and O. Shymanovskyi, Radioelectronics and Communications Systems, **66**(2), 74 (2023). https://doi.org/10.3103/S073527272302005X
[11] M. Kukurudziak, Radioelectronic and Computer Systems, **105**(1), 92-100 (2023). https://doi.org/10.32620/reks.2023.1.07
[12] Z. Wei, et al. Applied Physics B, **130**(4), 58 (2024). https://doi.org/10.1007/s00340-024-08201-4
[13] L. M. Suslikov. Scientific Bulletin of Uzhhorod University: Series: Physics, **26**, 123–143 (2009). (in Ukrainian)
[14] L. Y. Ropyak, et al. Funct. Mater, **27**(3), 638-642 (2020). https://doi.org/10.15407 / fm 27.03.638
[15] Thorlabs, Inc., Newton, NJ, USA, Passport data FLH1064-3, https://www.thorlabs.com/thorproduct.cfm?partnumber=FLH1064-3
[16] Thorlabs, Inc., Newton, NJ, USA, Passport data FLH051064-3, https://www.thorlabs.com/thorproduct.cfm?partnumber=FLH051064-3
[17] Newport Corporation, Newport Corporation 1791 Deere Avenue Irvine, California 92606, Passport data 20CGA-1000, https://www.newport.com/p/20CGA-1000?srsltid=AfmBOopEU1SnTc9rOIN1Bx2Vts3yy8XJUR76U99kNQL4QXXEtUGX3d_a
[18] V.P. Maslov, *et al*., Optoelectronics and Semiconductor Technology, **53**, 188 (2018). (in Ukrainian)
[19] M.S. Kukurudziak, in: *2023 IEEE 4rd KhPI Week on Advanced Technology* (*KhPIWeek*) (IEEE, Kharkiv, 2023), pp. 1-4. https://doi.org/10.1109/KhPIWeek61412.2023.10312979
[20] M.S. Kukurudziak, Physics and Chemistry of Solid State, **23**(4), 756 (2022). https://doi.org/10.15330/pcss.23.4.756-763
[21] M.S. Kukurudziak, and E.V. Maistruk, in: *Fifteenth International Conference on Correlation Optics*, 121261V (SPIE, Chernivtsi, 2021). https://doi.org/10.1117/12.2616170
[22] M.S. Kukurudziak, East Eur. J. Phys. (2), 289 (2023), https://doi.org/10.26565/2312-4334-2023-2-33
[23] S.B. Khan, S. Irfan, Z. Zhuanghao, and S.L. Lee, Materials, **12**(9), 1483 (2019). https://doi.org/10.3390/ma12091483
[24] N.M. Tugov, B.A. Glebov, and N.A. Charykov, *Semiconductor devices: Textbook for universities*, edited by V.A. Labuntsov, (Energoatomizdat, Moscow, 1990). (in Russian)
[25] L.K. Buzanova, and A.Y. Gliberman, *Semiconductor photodetectors* (Energia, Moscow, 1976). (in Russian)
[26] M.S. Kukurudziak, E.V. Maistruk, East Eur. J. Phys. **1**, 386 (2024), https://doi.org/10.26565/2312-4334-2024-1-39
[27] Y.V. Meteleva-Fischer, et al. Metallurgical and Materials Transactions E, **1**, 174 (2014). https://doi.org/10.1007/s40553-014-0017-6
[28] G.P. Gaidar, Journal of Physical Research, **22**(4), 4601-1 (2018). https://doi.org/10.30970/jps.22.4601 (in Ukrainian)
[29] W.S. Yoo, *et al*., Japanese journal of applied physics, **41**(7R), 4442 (2002). https://doi.org/10.1143/JJAP.41.4442
[30] M.S. Kukurudziak, Journal of Instrumentation, **19**(09), P09006 (2024). https://doi.org/10.1088/1748-0221/19/09/P09006
[31] S.M. Sze, and K.K. Ng, *Physics of semiconductor devices*, (Wiley, 2006).
[32] A.V. Igo, Opt. Spectrosc. **128**, 1125 (2020). https://doi.org/10.1134/S0030400X20080135
[33] M.-C. Wu, and C.-H. Wu, *Measurements and High-Energy Physics*, (InTech, 2011). https://doi.org/10.5772/15714

МЕТОДИ КОРЕКЦІЇ СПЕКТРАЛЬНИХ ХАРАКТЕРИСТИК КРЕМНІЄВИХ ФОТОПРИЙМАЧІВ

Микола С. Кукурудзяк[a,b], В'ячеслав В. Рюхтін[a]
[a] *АТ «Центральне конструкторське бюро Ритм», 58032, м. Чернівці, вул. Головна, 244, Україна*
[b] *Чернівецький національний університет імені Юрія Федьковича, 58002, м. Чернівці, вул. Коцюбинського, 2, Україна*

У статті досліджено методи зміщення спектральних характеристик кремнієвих фотодіодів в сторону більших довжин хвиль. Встановлено що при збільшенні напруги зворотнього зміщення фотодіода максимум його спектральної характеристики зміщується в сторону більших довжин хвиль внаслідок зростання коефіцієнта збирання неосновних носіїв заряду, який визначає вигляд спектральної характеритристики. При збільшенні часу життя неосновних носіїв заряду та питомого опору базового матеріалу фотодіода максимум його спектральної характеристики також зміщається в сторону більших довжин хвиль. Збільшення глибини гетеропереходу фотодіода зменшує вплив фонового короткохвильового випромінювання на корисний сигнал фотодіода внасліок рекомбінації фотоггенерованих носіїв заряду довжинами хиль, які поглинаються в n^+-шарі. Запропоновано кремнієві відрізаючі адсорбційні світлофільтри, які виключають вплив фонового випромінювання з довжиною хвилі менше 800 нм на сигнал фотодіода та володіють коефіцієнтом пропускання близько 75% на довжині хвилі 1064 нм.

Ключові слова: *кремній; фотоприймач; чутливість; спектральна характеристика; оптичне пропускання*

EAST EUROPEAN JOURNAL OF PHYSICS. 1. 295-300 (2025)
DOI:10.26565/2312-4334-2025-1-35 ISSN 2312-4334

POSSIBILITIES OF USING UKRAINIAN CLINOPTILOLITE (SOKYRNYTSIA DEPOSIT) IN NUCLEAR ENERGY

Oleksii Yu. Lonin[a]*, Volodymyr V. Levenets[a], Oleksandr P. Omelnyk[a], Andriy O. Shchur[a]
[a]National Science Center "Kharkiv Institute of Physics & Technology",
1, Akademichna St., Kharkiv, 61108, Ukraine
**Corresponding Author: a_lonin@kipt.kharkov.ua, a_lonin@ukr.net*
Received December 17, 2024; revised February 2, 2025; accepted February 10, 2025

The clinoptilolite from the Sokyrnytsia deposit belongs to the zeolite family and is known for its application as sorbents in nuclear energy. The sorption of cesium, strontium, cobalt, and europium ions by clinoptilolite has been studied. The research examined how the composition and structure of clinoptilolite influence sorption. Sorption properties were assessed using the sorption coefficient, which quantitatively measures clinoptilolite's interaction with radionuclides. The results revealed that clinoptilolite exhibits the highest sorption efficiency for cesium (87.0%) and strontium (80.5%). Europium showed a sorption efficiency of 73.0%, while cobalt exhibited a lower sorption efficiency of 60.0%. The study established an ion exchange sequence for these ions in the sorption process and observed a dependency on the ionic radius of the sorbed ions. The presence and concentration of competing ions significantly affected the sorption efficiency. For instance, sodium ions in the solution reduced sorption by up to 25%, depending on the radionuclide. Increased sodium ion concentration caused an additional 26% to 40% sorption reduction. Similarly, tripling the strontium concentration in the solution reduced the sorption effect. The sorption experiments were conducted under both static and dynamic conditions. Radionuclide content was determined using the characteristic X-ray emission (XRE) method. This technique analyzes the characteristic X-ray radiation of radionuclides excited by a proton beam. The experiments were carried out at the analytical nuclear-physical complex "Sokil." Samples were irradiated in the XRE channel, where targets were placed in a cassette within an irradiation chamber under a vacuum of 10^{-4} Pa. The proton beam, with a current of 200 nA and an energy of 1600 keV, was used to excite the X-ray radiation of cesium, strontium, and cobalt atoms. The characteristic X-ray radiation of the K-series of strontium atoms was detected using two detectors: the XR-100CR Si-PIN X-ray detector and the Ge(HP) detector. Considering its established radionuclide selectivity sequence, the clinoptilolite from the Sokyrnytsia deposit can be utilized in Ukraine's nuclear energy industry.
Keywords: *Zeolite; Cesium; Strontium; Cobalt; Europium*
PACS: 82.75.Jn, 68.43.-h, 28.41.Kw

INTRODUCTION

Zeolites were first discovered by F. Cronstedt in 1756. He observed that stilbite swelled and released water when heated. This phenomenon led him to coin the term "zeolite," derived from the Greek words for "boiling stone." To date, 47 minerals have been classified as zeolites. Zeolites belong to the group of framework aluminosilicates [1]. They are found on every continent, but natural zeolites do not fully meet the demands of industry and energy sectors. Thanks to advances in modern chemistry, scientists have significantly expanded the range of zeolites, enhancing their properties to suit industrial and practical applications. Currently, more than 120 synthetic zeolites are known [1].

One of the natural zeolites is clinoptilolite. It is a component of sedimentary rocks of volcanic origin. Its name originates from the Greek words "klino" (κλίνω; inclined), "ptilo" (φτερών; feather), and "lithos" (λίθος; stone). Clinoptilolite has an aluminosilicate framework formed by the connection of AlO_4 and SiO_4 tetrahedra at their vertices. An example of the atomic arrangement in the structure of clinoptilolite, typical for zeolites, is shown in Fig. 1 [2].

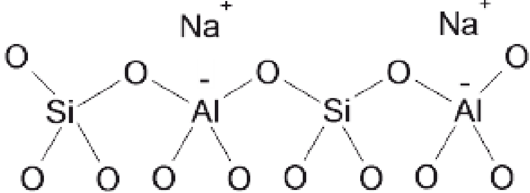

Figure 1. The fundamental structural unit of zeolites [2]

The framework features a system of cavities interconnected by channels, where cations and water molecules are located [3–6]. The cations in the channels can be exchanged for other cations. Exchangeable cations in clinoptilolite include Na^+, K^+, Ca^{2+}, Mg^{2+}, Fe^{3+}, and others (Fig. 2).

The composition and content of exchangeable ions in clinoptilolite vary depending on the deposit. For instance, the clinoptilolite content in the rock from the Neombarian region of Armenia is 85–87% [7], while in the Sokyrnytsia deposit in the Zakarpattia region of Ukraine, it ranges from 75% to 96% [8]. Such significant compositional variations highlight the need for additional quality control when using clinoptilolite as a sorbent in energy and industrial applications.

Cite as: O.Yu. Lonin, V.V. Levenets, O.P. Omelnyk, A.O. Shchur, East Eur. J. Phys. 1, 295 (2025), https://doi.org/10.26565/2312-4334-2025-1-35
© O.Yu. Lonin, V.V. Levenets, O.P. Omelnyk, A.O. Shchur, 2025; CC BY 4.0 license

Clinoptilolite has been utilized as a sorbent in nuclear energy. It was first employed during the cleanup of the Three Mile Island Nuclear Power Plant accident (USA) in March 1979, where it was used to absorb cesium [9]. The positive results of this application laid the groundwork for recommendations by the International Atomic Energy Agency (IAEA) [10].

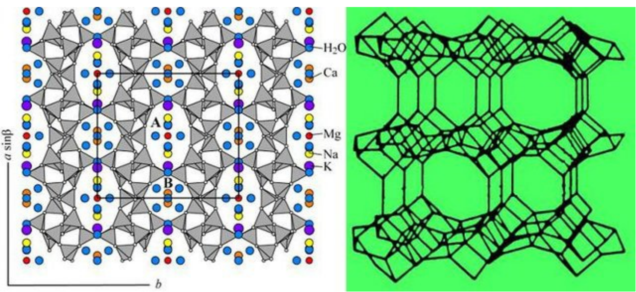

Figure 2. Crystalline structure of clinoptilolite [4]

During the cleanup of the Chornobyl Nuclear Power Plant accident (Ukraine) in April 1986, clinoptilolite was used as a radionuclide sorbent based on IAEA recommendations. Approximately 150,000 tons of zeolite sand were employed. However, clinoptilolite did not yield the expected results, unlike the Three Mile Island accident. The main reason for its limited effectiveness was the complex and diverse radionuclide contamination caused by the Chornobyl accident, which included high activity levels and a broader range of radionuclides.

This study aimed to summarize the research on the sorption of radionuclides by clinoptilolite from the Sokyrnytsia deposit, which may be present in liquid waste generated by nuclear energy facilities. Based on the results, an ion exchange series for clinoptilolite was developed to facilitate its use in mitigating radionuclide contamination.

METHODS AND OBJECTS OF THE STUDY

Objects of the Study

The object of the study was clinoptilolite from the Sokyrnytsia deposit in the Zakarpattia region of Ukraine. Two fractions of clinoptilolite were examined: 0.1 mm and 3–5 mm. The fractions were selected depending on the sorption method (static or dynamic).

Nitrates of cesium, strontium, and cobalt were used as radionuclide sources. Europium was also studied, with its source being an oxide dissolved in acid.

Methods For Studying Sorption Properties

Sorption Under Static Conditions

A 100 ml solution of nitrates was prepared using distilled water as the solvent. A 0.1 g sample of clinoptilolite (0.1 mm fraction) was used as the sorbent. Ten milliliters of the prepared solution were added to the sorbent. The mixture was periodically stirred, and the sorption process was monitored for 24 hours. Samples of 0.5 ml were taken at intervals of 1, 6, and 24 hours. For europium, a separate solution was prepared with the addition of 0.1 N hydrochloric acid.

Sorption Under Dynamic Conditions

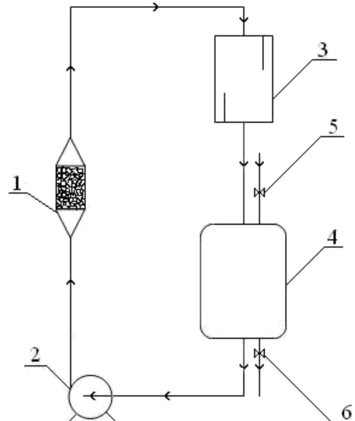

Figure 3. Diagram of the sorption setup:
1 - Sorption column; 2 – Pump; 3 - Measuring device; 4 - Collection reservoir; 5, 6 - Inflow and outflow valves respectively

A 500 ml solution of nitrates was prepared using distilled water as the solvent. A 2.0 g sample of clinoptilolite (3-5 mm fraction) was used as the sorbent. Dynamic sorption conditions were modeled using a setup (Fig. 3) [11]. The setup included a pump, a sorption column with a cartridge, a reservoir, and a measuring unit. The cartridge had a diameter of 8 mm and a height of 25 mm.

To evaluate the completeness of the sorption processes, 40–80 sorption cycles were performed, with periodic sampling. Dynamic sorption of europium was not conducted due to the use of acid as the solvent.

Preparation of Targets

Targets were prepared using carbon substrates made from carbon rods. The carbon substrates were rectangular, measuring 10 mm in length, 5 mm in width, and 2 mm in thickness. A solution (0.05 ml) containing a mixture of cesium, strontium, and cobalt isotopes was applied to the substrate and dried at 35°C. The solution was applied using an automatic pipette with adjustable volume.

Determination of Radionuclide Content Using the XRF Method

The radionuclide content was determined using the X-ray fluorescence (XRF) method. This method analyzes a proton beam's characteristic X-ray emission of radionuclides excited. This part of the work used the "Sokil" analytical nuclear physics complex [12].

Samples were irradiated with a proton beam in the XRF channel. Targets were placed in a cassette located in the irradiation chamber. A vacuum with a 10^{-4} Pa pressure was created in the chamber before measurements.

For the excitation of X-rays from cesium, strontium, and cobalt atoms, a proton beam with a current of 200 nA and an energy of 1600 keV was used. At this energy, the L-series X-ray emission of cesium atoms and K-series X-ray emission of strontium and cobalt atoms were effectively excited. The X-ray emission was measured using the XR-100CR Si-PIN X-ray detector with an energy resolution of 155 eV for the 5.89 keV line and the Ge(HP) detector. The Ge(HP) detector, made of ultrapure germanium with a crystal thickness of 8.5 mm and a sensitive surface area of 25 mm², provided higher detection efficiency for K-series X-rays of strontium (14.164 keV) compared to the Si-PIN detector. To optimize the spectral measurement conditions, collimators with diameters of 1.5 mm and 2.0 mm, as well as polyethylene filters with thicknesses of 56 µm, 100 µm, and 150 µm, and aluminum foil with a thickness of 10 µm, were tested. Based on the experimental data, a collimator with a 1.5 mm opening and a 56 µm thick polyethylene filter was selected for optimal detection of the analytical peaks while reducing background radiation interference.

The X-ray emission from strontium atoms was detected by both XR-100CR Si-PIN and Ge(HP) detectors. The external detector was placed 7 cm from the target at an angle of 135° to the proton beam direction. The X-ray emission exited the chamber through a 25 µm thick beryllium foil window.

RESULTS AND DISCUSSION

Typical spectra of cesium, strontium, cobalt, and europium confirm the feasibility of detecting these radionuclides using the X-ray fluorescence (XRF) method and the suitability of the results for assessing sorption properties. The typical spectra are presented in Figures 4-7.

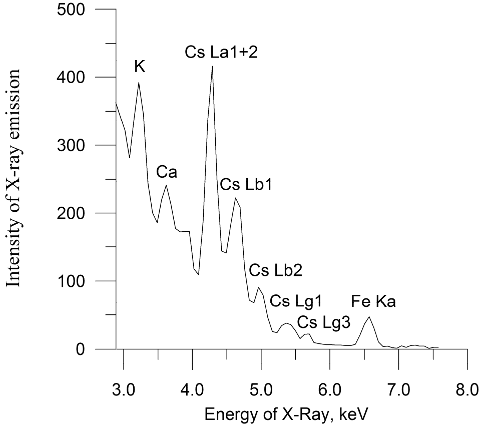

Figure 4. X-ray spectrum of the carbon target which contains 0.002 mg of cesium

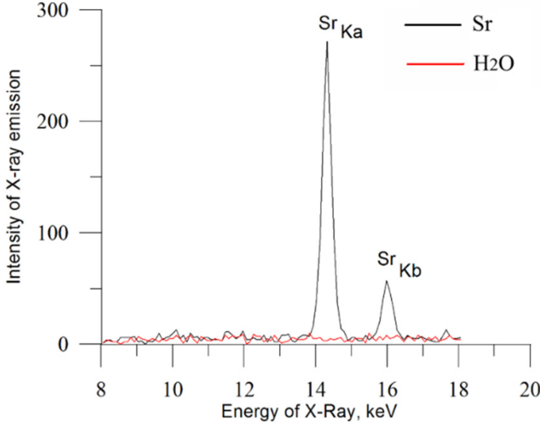

Figure 5. X-ray spectrum of the carbon target with dry water solids (H_2O), and the carbon target containing 0.0012 mg strontium (Sr)

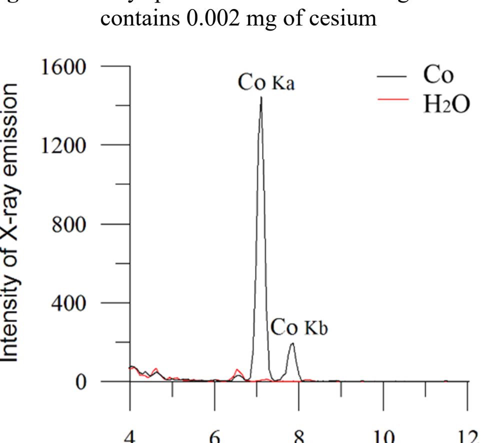

Figure. 6. X-ray spectra of the carbon target with dry water solids (H_2O) and the carbon target containing 0.0017 mg of cobalt (Co)

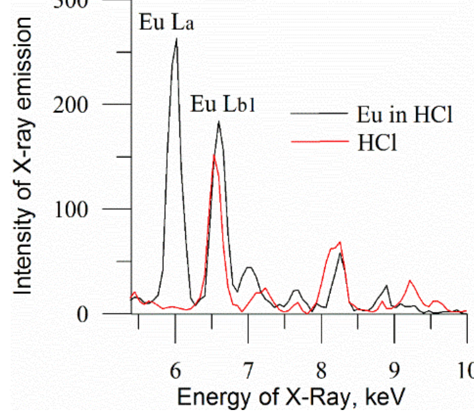

Figure.7. X-ray spectra of the carbon target with hydrochloric acid (HCl) dry residue and the carbon target containing 0.05375 mg of europium (Eu in HCl)

The sorption coefficient was used to evaluate the sorption properties quantitatively, providing insights into the interaction between clinoptilolite and radionuclides. The sorption coefficient was calculated using the formula:

$$K_s = \frac{\left(C_0 - C_p\right)\cdot 100\%}{C_0}$$

where C_o and C_p are the initial and equilibrium concentrations of the solution (mg/mL).

The sorption processes were studied under static and dynamic conditions, with adjustments made to the amount of sorbent and solution volume based on the method.

The data obtained are presented in Table 1. It was found that clinoptilolite exhibited the highest sorption efficiency for cesium (87.0%) and strontium (80.5%), followed by europium (73.0%). Cobalt displayed the lowest sorption efficiency at 60.0%.

Table 1. Sorption of radionuclides by clinoptilolite

№	Radionuclide	Sorption coefficient, %
1.	Cesium	87.0 %
2.	Strontium	80.5 %
3.	Cobalt	60.0 %
4	Europe	73.0 %

Experiments were conducted to assess the impact of competing ions and increased radionuclide concentration on sorption. These conditions were designed to simulate real-world scenarios, such as the presence of competing ions in liquid radioactive waste. Increased radionuclide concentration allowed for analyzing the performance of the sorbent under higher activity levels. The presence of competing ions, particularly sodium, significantly reduced the sorption efficiency of clinoptilolite (Table 2). For example, when sodium was present in the solution at a concentration of 0.0002 g/mL (equal to the cesium concentration in the solution), cesium sorption decreased to 46.0%. Similarly, sodium concentrations of 0.0004 g/mL reduced the sorption efficiency for cobalt and europium to 33.6% and 34.6%, respectively.

The effect of increased radionuclide concentration on sorption was analyzed using strontium as an example. A threefold increase in strontium concentration resulted in a 25% reduction in sorption efficiency (Table 2).

Table 2. Effect of competing ions and increased radionuclide concentrations on sorption

no.	Radionuclide	Radionuclide concentration, g/ml	Competing ion		Sorption coefficient, %
			Ion name	Concentration, g/ml	
1	Cesium	0.0002	sodium	- //-	87.0 %
2	Cesium	0.0002	sodium	0.0001	63.0 %
3	Cesium	0.0002	sodium	0.0002	46.0 %
4	Strontium	0.0002	- //-	- //-	80.5 %
5	Strontium	0.0006	- //-	- //-	60.6 %
6	Cobalt	0.0004	sodium	- //-	60.0 %
7	Cobalt	0.0004	sodium	0.0002	38.8 %
8	Cobalt	0.0004	sodium	0.0004	33.6 %
9	Europe	0.0005	sodium	- //-	73.0 %
10	Europe	0.0005	sodium	0.0002	47.5 %
11	Europe	0.0005	sodium	0.0004	34.6 %

The results indicate that the presence of competing ions substantially affects sorption efficiency. Sodium ions, as competitors, caused up to a 25% reduction in sorption depending on the radionuclide. Increasing the sodium concentration led to an additional 26%-40% decrease in sorption efficiency. The more pronounced effect of sodium on cesium sorption is attributed to their shared group in the periodic table (alkali metals), similar oxidation states, and competition for the same sorption sites in the clinoptilolite structure.

The effect of increased radionuclide concentration was studied using strontium sorption as an example. A threefold increase in strontium concentration reduced sorption efficiency by 20%.

Clinoptilolite demonstrates a complex sorption mechanism, involving both ion exchange and adsorption. Ion exchange occurs as a result of the need to compensate for the negative charge generated by aluminum ions interacting with the fourth oxygen ion. This charge is usually compensated by alkali metal ions, which then act as exchangeable ions. Adsorption, on the other hand, is associated with interactions between ions and the structural cavities of clinoptilolite, which are characteristic of its crystalline structure.

Based on the obtained results and the characteristics of the radionuclide ions (Table 3), it is possible to conclude the relative selectivity of clinoptilolite for these radionuclides.

Table 3. Oxidation states and ionic radii of sorbed elements

Element	Oxidation degree	Ion radius, pm
Cesium	+1	167
Strontium	+2	112
Cobalt	+2	72
Europium	+3	109

Regardless of the oxidation state of the radionuclides, the primary factor influencing sorption is the ionic radius, which allows for additional sorption, taking into account the crystalline structure of clinoptilolite. The selectivity series of radionuclides for clinoptilolite is as follows:

$$Cs^{+1} > Sr^{+2} > Eu^{+3} > Co^{+2}$$

This order corresponds to the observed sorption efficiency values and correlates with the ionic radius of the radionuclides.

The obtained data can be utilized by nuclear energy enterprises in Ukraine to optimize the use of clinoptilolite as a sorbent, both independently and as part of composite sorbents.

CONCLUSIONS

Clinoptilolite is a mineral of the zeolite group. It has been established that clinoptilolite has high sorption properties for cesium (87.0 %), strontium (80.5 %), and europium (73.0 %). The sorption properties of clinoptilolite for cobalt (60.0 %) require additional purification agents or the use of composite sorbents. Such sorption values are related to the radius of the ions to be sorbed. The large radius of the ion (cesium - 167 pm) makes it possible to perform additional sorption, taking into account the crystal structure of clinoptilolite. It was determined that the presence of competing ions (sodium) reduces sorption by 25 %. In the example of strontium sorption, it was found that an increase in the concentration of radionuclides in solution leads to a decrease in sorption by 20 %. Based on the sorption results, a range of radionuclide selectivity for Ukrainian clinoptilolite was determined. The clinoptilolite can be used in nuclear power enterprises of Ukraine, taking into account the determined range of radionuclide selectivity.

ORCID

Oleksii Yu. Lonin, https://orcid.org/0000-0002-5386-3825; **Volodymyr V. Levenets,** https://orcid.org/0000-0002-6439-0576
Oleksandr P. Omelnyk, https://orcid.org/0000-0003-2467-3632; **Andriy O. Shchur**, https://orcid.org/0000-0002-6619-4069

REFERENCES

[1] D. Breck, *Zeolite molecular sieves*, (Wiley, New York, 1974).
[2] N. Sobuś, I. Czekaj, V. Diichuk, and I.M. Kobasa, "Characteristics of the structure of natural zeolites and their potential application in catalysis and adsorption processes," Technical Transactions, **117**(1), 43 (2020). https://doi.org/10.37705/TechTrans/e2020043
[3] I. Marantos, G.E. Christidis, and M. Ulmanu, "Zeolite Formation and Deposits," in: *Natural Zeolites Handbook*, **1**, (2021). pp. 28-51. https://doi.org/10.2174/978160805261511201010028
[4] E. Chmielewská, "Natural Zeolites as Sustainable and Environmental Inorganic Resources over the History to Present," General Chemistry, **5**, 190001 (2019). https://doi.org/10.21127/yaoyigc20190001
[5] P. Miądlicki, A. Wroblewska, K. Kiełbasa, Z.C. Koren, and B. Michalkiewicz, "Sulfuric acid modified clinoptilolite as a solid green catalyst for solvent-free α-pinene isomerization process," Microporous and Mesoporous Materials, **324**, 111266 (2021). https://doi.org/10.1016/j.micromeso.2021.111266
[6] A. Mastinu, A. Kumar, G. Maccarinelli, S.A. Bonini, M. Premoli, F. Aria, A. Gianoncelli, and M. Memo, "Zeolite Clinoptilolite: Therapeutic Virtues of an Ancient Mineral," Molecules, **24**(8), 1517 (2019). https://doi.org/10.3390/molecules24081517
[7] L. Akhalbedashvili, G. Todradze, N. Kekelidze, Y. Keheyan, G. Yeritsyan, and R. Gevorkyan, Ion exchange properties of irradiated and chemically modified clinoptilolite regarding to Cs^{+} and Sr^{2+}, Chemistry, Physics and Technology of Surface, **3**(1), 281 (2010). https://cpts.com.ua/index.php/cpts/article/view/38/35
[8] O.I. Ivanenko, Yu.V. Nosachova, and T.V. Krysenko, Bulletin of National Technical University of Ukraine "Igor Sikorsky Kyiv Polytechnic Institute" Series "Chemical engineering, ecology and resource saving", **4**(19), 66 (2020). https://doi.org/10.20535/2617-9741.4.2020.219786
[9] Yu. Bondar, and S. Kuzenko, Geochemistry of Technogenesis, **5**(33), 86 (2021). https://doi.org/10.15407/10.15407/geotech2021.33.086
[10] S.G. Baxter, and D.C. Berghauser, *The selection and performance of the natural zeolite clinoptilolite in British Nuclear Fuels' site ion exchange effluent plant*, SIXEP, United States: University of Arizona, Waste management. IAEA, **86**(2), 347 (1986).
[11] A.Yu. Lonin, V.V. Levenets, I.M. Neklyudov, A. O. Shchur, "The usage of zeolites for dynamic sorption of cesium from waste waters of nuclear power plants," JRNC, **303**, 831 (2015). https://doi.org/10.1007/s10967-014-3597-9
[12] S.G. Karpus, V.V. Kuzmenko, V.V. Levenets, O.Yu. Lonin, A.P. Omelnik, A.O. Shchur, and V.I. Sukhostavets, "Modernization of the analytical nuclear-physical complex SOKIL," PAST, **2**(144), 134 (2023). https://vant.kipt.kharkov.ua/ARTICLE/VANT_2023_2/article_2023_2_134.pdf
[13] V.V. Levenets, A.Yu. Lonin, O.P. Omelnik, and A.O. Shchur, "Comparison the sorption properties of clinoptilolite and synthetic zeolite during sorption strontium from the water solutions in static conditions: Sorption and quantitative determination of strontium by the method PIXE," JECE, **4**(4), 3961 (2016). https://doi.org/10.1016/j.jece.2016.09.011
[14] A.Yu. Lonin, V.V. Levenets, O.P. Omelnik, and A.O. Shchur, "Comparison of the sorption properties of natural and synthetic zeolites for the purification of aqueous solutions from cobalt: sorption of the cobalt from aqueous solutions in dynamic conditions and the quantitative determination of cobalt by the PIXE method," JRNC, **315**, 163 (2018). https://doi.org/10.1007/s10967-017-5676-1
[15] V.V. Levenets, A.Yu. Lonin, O.P. Omelnik, A.O. Shchur, "Studies of the features of the sorption of an europium by natural and synthetic zeolites for using it in the nuclear energy," PAST, 1(125), 121 (2020). https://vant.kipt.kharkov.ua/ARTICLE/VANT_2020_1/article_2020_1_121.pdf

МОЖЛИВОСТІ ВИКОРИСТАННЯ УКРАЇНСЬКОГО КЛІНОПТИЛОЛІТУ (СОКИРНИЦЬКОГО РОДОВИЩА) В ЯДЕРНІЙ ЕНЕРГЕТИЦІ

О.Ю. Лонін, В.В. Левенець, О.П. Омельник, А.О. Щур
Національний науковий центр «Харківський фізико-технічний інститут»,
1, вул. Академічна, 61108, Харків, Україна

Кліноптилоліт Сокирницького родовища відноситься до цеолітів. Цеоліти мають застосування в ядерній енергетиці в якості сорбентів. Досліджено сорбцію кліноптилолітом іонів цезію, стронцію, кобальту та європію. Визначено, як особливості складу та структури кліноптилоліту впливають на сорбційні процеси. Для визначення сорбційних властивостей використовувався коефіцієнт сорбції, який давав можливість отримати кількісну оцінку взаємодії кліноптилоліту з радіонуклідами. Встановлено, що найвищі значення сорбції кліноптилоліт проявляє до цезію 87.0 % та стронцію 80.5 %. Сорбція європію складає 73.0 %. Сорбція кобальту знижується та складає 60.0 %. Дослідження встановило послідовність іонного обміну для цих іонів у процесі сорбції та виявило залежність від іонного радіусу сорбованих іонів. Встановлено залежність сорбції від присутності та кількості конкуруючих іонів. Присутність іону натрію (конкуруючого іону) в розчині веде до зниження сорбції на 25% в залежності від радіонукліду. Збільшення концентрації іонів натрію призвело до додаткового зниження сорбції на 26-40%. Встановлено, що збільшення концентрації стронцію в 3 рази веде до зменшення сорбції на 20 %. Дослідження сорбції проводилися в статичних та динамічних умовах. Визначення вмісту радіонуклідів проводилось за допомогою метода ХРВ (характеристичне рентгенівське випромінювання). Метод засновано на аналізі характеристичного рентгенівського випромінювання радіонуклідів, після збудження пучком протонів. Данну частину роботи виконували на аналітичному ядерно-фізичному комплексі «Сокіл». Опромінювання зразків пучком протонів проводили у каналі ХРВ. Мішені встановлювали у касету, яка була розташована у камері опромінення. До проведення вимірювань у камері створювали вакуум з тиском 10^{-4} Па. Для збудження характеристичного рентгенівського випромінювання атомів цезію, стронцію та кобальту використовували пучок протонів зі струмом 200 нА та енергією 1600 кеВ. Реєстрація характеристичного рентгенівського випромінювання K-серії атомів стронцію проводилася двома детекторами: XR-100CR Si-PIN X-Ray і Ge(HP). З огляду на встановлену послідовність радіонуклідної селективності кліноптилоліт Сокирницького родовища може бути використаний в атомній енергетиці України.

Ключові слова: *цеоліт; цезій; стронцій; кобальт; європій*

East European Journal of Physics. 1. 301-308 (2025)

DOI:10.26565/2312-4334-2025-1-36 ISSN 2312-4334

DETERMINATION OF SETUP MARGIN FOR NASOPHARYNGEAL CARCINOMA BY USING ELECTRONIC PORTAL IMAGING DEVICE

Safa Elfaramawy[a,b]*, Ehab Attalla[c], Fathi Elhussiny[a], Mohamed Alm El-Din[d], Ahmed Elmekawy[a]

[a]*Faculty of Science, Physics Department, Tanta University, Tanta, Egypt*

[b]*Alhammadi Hospital, Riyadh, Saudi Arabia*

[c]*National Cancer Institute, Cairo University, Egypt*

[d]*Faculty of Medicine, Oncology Department, Tanta University, Tanta, Egypt*

**Corresponding Author e-mail: Safaelfaramawy@yahoo.com*

Received October 12, 2024; revised November 13, 2024; accepted December 15, 2024

Introduction: This study aimed to assess three-dimensional (3D) setup mistakes and provide optimal margins for planned target volume (PTV) coverage in head and neck radiation. Methods: Ten patients participated in the trial, receiving IMRT in conjunction with weekly electronic portal imaging (EPI). A total of 170 portal pictures were analyzed. The systematic (S) and random (s) errors in the population of patients with head and neck cancer were assessed using portal images in the caudocranial longitudinal (CC) and left-right lateral (LR) orientations, measured within the anterior-posterior (AP) field. The clinical-to-planning target volume (CTV-PTV) margins were determined in accordance with ICRU Report 62 guidelines and van Herk's formulae. **Results:** The group systematic errors and random errors were 0.19 and 0.26 cm , respectively in the anteroposterior direction; the group systematic errors and random errors were 0.15 cm and 0.24 cm in SI direction, respectively; the group systematic errors and random errors were 0.13 cm and 0.25 cm in LR direction, respectively; According to the classical van-Herk formula MPTV $=2.5\Sigma +0.7\sigma$, we figured out the ideal PTV margins (MPTV) based on the setup errors and 0.65 cm, 0.55 cm, and 0.5 cm were required in the AP, SI, and RL directions. **Discussion and conclusions:** we can conclude that a 6-mm extension of CTV to PTV margin, as the optimal margin and can be reduced with increasing frequency of online verification (daily imaging) or for patients where the prescribed does not exceed tolerance doses for organs at risk.

Keywords: *Nasopharyngeal Radiotherapy; Intensity-modulated radiotherapy (IMRT); Set-up uncertainty*

PACS: 87.53.Bn, 87.55.Qr, 87.57.uq, 87.55.D

INTRODUCTION

With the extensive use of intensity-modulated conformal radiation and the strengthening of the principle of comprehensive treatment, the curative effect of nasopharyngeal cancer and patients' quality of life have been greatly improved [1–4].The success of radiotherapy largely depends on precise patient positioning and the accuracy of immobilization strategies for patients with head and neck tumors during each treatment session, particularly in the head and neck area where critical organs such as the salivary glands, spinal cord, and brain stem are in close proximity, allowing for minimal error and consequently minimise risk of toxicity and long-term morbidity [5,6]. Optimized intensity-modulated radiation therapy (IMRT) plans typically generate sharp dose gradients between the tumor and adjacent healthy tissues. Any misalignment in patient positioning can lead to insufficient tumor irradiation, heightening the risk of local recurrence, and unnecessary radiation exposure to surrounding tissues. Previous studies analyzed the influence of setup uncertainties on target volume coverage and doses to organs at risk (OAR) in HNC patients treated with image-guided radiation (IGRT) [7–9]. Geometric uncertainties present a greater challenge in IMRT planning compared to conventional methods, emphasizing the need to identify and reduce setup errors throughout the treatment process. The main difficulty lies in consistently replicating the patient's position in every treatment session, as determined by the planning CT scan. Positioning errors during treatment arise when the patient's anatomy does not align with the planned CT. These errors might be systematic (reproducible consistent errors in the same direction and amount) or random errors (variations in direction and magnitude). Systematic errors can cause changes in the cumulative dosage distribution [10–15]. Portal imaging (PI) allows for consistent imaging, quick identification of setup errors, and automated verification of treatment fields. Numerous studies have reported the use of PI-guided setup corrections for both conformal and IMRT techniques [16–29]. However, since PI is a two-dimensional imaging method, it cannot detect errors resulting from out-of-plane rotations [30–34]. That said, the dosimetric impact of rotational setup errors should be carefully considered from case to case when organs at risk are in close proximity to the target [35]. This study focused on measuring random and systematic inter-fractional setup errors using electronic portal imaging (EPI) for 10 patients diagnosed with locally advanced nasopharyngeal carcinoma undergoing IMRT, with the goal of determining the optimal clinical target volume (CTV) to planning target volume (PTV) margins necessary to ensure complete target coverage.

MATERIAL AND METHOD

Patient selection

This retrospective study was approved by the appropriate institutional review. The research focused on 10 patients diagnosed with locally advanced nasopharyngeal carcinoma, who were treated using IMRT with the simultaneous integrated boost (SIB) technique and concurrent chemotherapy [36].

Cite as: S. Elfaramawy, E. Attalla, F. Elhussiny, M.A. El-Din, A. Elmekawy, East Eur. J. Phys. 1, 301 (2025), https://doi.org/10.26565/2312-4334-2025-1-36

© S. Elfaramawy, E. Attalla, F. Elhussiny, M.A. El-Din, A. Elmekawy, 2025; CC BY 4.0 license

Definition of volumes of interest and IMRT treatment

Patients were immobilized in a supine position using standard thermoplastic head-neck-shoulder casts with five fixation points and the base plate was not fixed to the table couch of the linac. High-resolution computed tomography (CT) scans were taken in helical mode with a 3 mm slice thickness, covering the area from the skull vertex to mid-chest.

The dose to the PTV70, which includes the primary and nodal gross tumor volumes and positive lymph nodes, had been set at 70 Gy. The dose for PTV60, which encompassed the high-risk clinical target volume (CTV) and nodal CTV, was established at 60 Gy. The dose to PTV54 contained the low risk CTV was set at 54 Gy. All patients were optimized using dynamic technique (Eclipse software (Version 13.7, Varian Medical Systems, USA). Dosimetric calculations were performed using the Anisotropic Analytical Algorithm (AAA) on a 2.5 mm calculation grid, optimized with a dose volume optimizer. All patients were treated by a Clinac 600C linear accelerator equipped with 6 MV photons and an 80-leaf multileaf collimator.

Generation of DRR and portal imaging

Two orthogonal DRRs obtained from the treatment planning software, with a field size of 10×10 cm^2, gantry angle of 0° (anterior) and 90° (lateral), were transferred to the treatment unit as reference images. Portal images were acquired with the same gantry by using the EPID system attached to Varian linear accelerators

Anatomic reference landmarks included at least two well visible bony structures: external mandible profile, nasal septum, maxillary sinus and the spinous process of one of lower cervical vertebrae were generally used for the anterior images, while internal and external mandible profiles, skull base and cervical vertebral bodies, i.e. C2 and C4, were usually outlined on the lateral images (Figure 1a and b). The images were analyzed by two radiation oncologists adequately trained to reduce interobserver variability.

Measurement of set-up errors was performed at least three times during the first week of treatment and on a weekly basis thereafter. Images were matched on-line during the first week, off-line thereafter. In case of displacement exceeding 2 mm along one direction, the linac couch was adjusted to match the treatment isocenter and new EPIs were acquired.

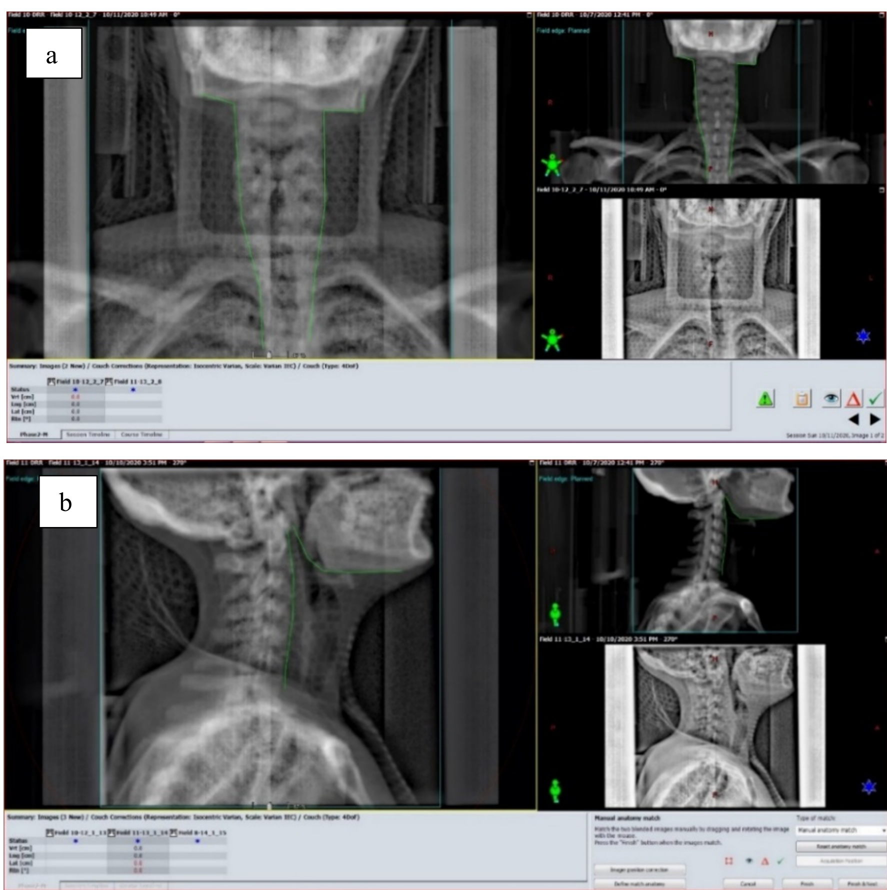

Figure 1. Matching between digitally reconstructed image (DRR) and image taken prior to treatment
(a) AP images; (b) Lateral images

Statistical methods

We followed the definition and notations of setup errors described elsewhere [37]. If we denote patients as $p \epsilon \{_p1;\ _p2;._pM\}$, and image sections for each patient as $f \epsilon \{1;\ 2;.;N\}$, then the setup error $E_{pf} = \{E_{pf}^{AP}\ ;\ E_{pf}^{SI};\ E_{pf}^{RL}\}$ can be written as $E_{pf} = S_p + R_{pf}$, where S_p is the systematic error for each patient, whereas R_{pf} is the random error introduced in

each image section. The patient (p)-specific random error σ_p is the standard deviation (SD) of R_{pf} over f. The population systematic and random variations are then calculated by the following equations [37],

$$S_p = \sum_{f=1}^{N} \frac{E_{pf}}{N}$$

$$\mu = \sum_{p=p1}^{pM} \frac{S_p}{M}$$

$$\Sigma = \left(\frac{1}{M}\sum_{p=p1}^{pM}(S_p - \mu)^2\right)^{1/2}$$

$$\sigma_p = \left(\frac{1}{N}\sum_{f=1}^{N}(R_{pf} - \overline{R_{pf}})^2\right)^{1/2}$$

$$\sigma = \left(\frac{1}{M}\sum_{p=p1}^{pM}\sigma_p{}^2\right)^{1/2}$$

where μ is the population mean of systematic variations, Σ is the standard deviation of the systematic variations, and σ is the average root-mean-square of individual random variations.

Margins resulting from setup uncertainty alone could then be estimated from the systematic and random variations. Van Herk has provided a review of margin formulae [38], and the commonly used form is $M = 2.5\Sigma + 0.7\sigma$ Margins determined by this equation assume that the minimum dose to CTV is 95% for 90% of the patients [39]. The 90% confidence range, which is lower bounded by the 5th percentile and upper bounded by the 95th percentile, could also indicate the setup margin [37].

RESULTS

A total of 170 position verification scans were acquired and analyzed (0° anterior, 90° lateral) were obtained for 10 patients, with a mean of 19 images for each patient range (18-23).

The quantification of patient set-up errors was given by the determination of the displacement frequency (μ), and it was plotted in different directions: Figure 2a anteroposterior (AP), Figure 2b craniocaudal (CC) and Figure 2c left–right (L-R), directions. It demonstrates that the largest displacement was in the A-P direction 8 mm in the posterior direction. As regards A-P direction, frequency for displacement 0.4 cm reaches to 9.83%. The frequencies of setup errors ≤ 0.3 cm in AP, SI, and RL, directions were (68.81%), (77%), and (83.5%), respectively (Figure 2).

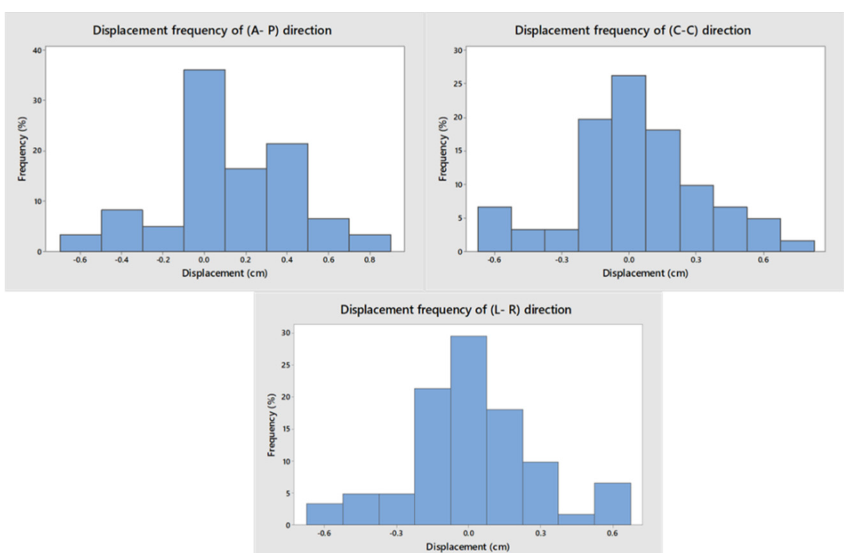

Figure 2. The distribution of the interfractional patient set-up errors for the nasopharynx: the displacements (m) of the coordinate of the nasopharynx between the digitally reconstructed radiograph and imaging portals plotted for the (a), anteroposterior (A-P) (b) craniocaudal (CC) (c) left–right (L-R) directions.

The distribution of all setup errors in three directions is shown in (Figure 3). Regardless of the duration of the fractionated radiotherapy course. The population mean and standard deviation were 0.0831±0.307, 0.0508±0.293 and 0.0051±0.26 in AP, SI and LR directions, respectively. The deviation of bony reference points in the range of (-0.6-0.8) cm, (-0.6–0.7)cm and (-0.6–0.6) cm in AP, SI and LR directions; The group systematic errors and random errors were 0.19 and 0.26 cm , respectively in the anteroposterior direction; the group systematic errors and random errors were 0.15 cm and 0.24 cm in SI direction, respectively; the group systematic errors and random errors were 0.13 cm and 0.25 cm in LR direction, respectively; According to the classical van-Herk formula MPTV =2.5Σ +0.7σ, we figured out the ideal PTV margins (MPTV) based on the setup errors. Considering the setup errors and the accuracy of deliver

radiation doses to the targets and their surrounding normal structures, margins of 0.65 cm, 0.55 cm, and 0.5 cm were required in the AP, SI, and RL directions, respectively, Table 1.

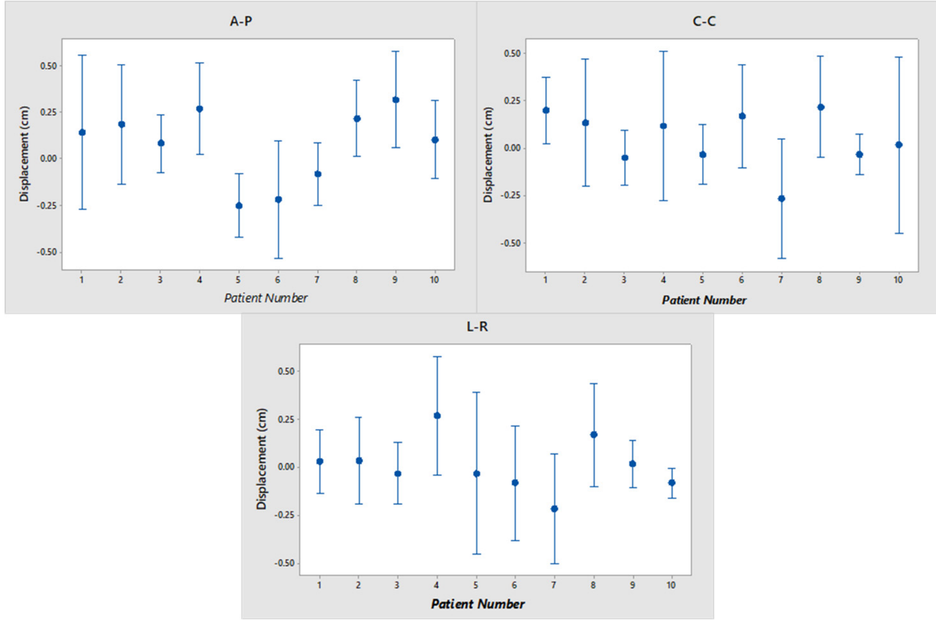

Figure 3. The distribution of all setup errors in three directions obtained EPID

Table 1. Summary of interfraction translational error (mm) in each dimension

	AP	SI	RL
M	0.0831	0.0508	0.0051
SD	0.307	0.293	0.26
Minimum	-0.6	-0.6	-0.6
Maximum	0.8	0.7	0.6
Σ	0.19	0.15	0.13
σ	0.26	0.24	0.25
MPTV	0.65	0.55	0.5

Abbreviations: M, mean of all patients' mean; SD, standard deviation; Σ, systematic setup uncertainty; σ, random setup uncertainty; RL, right–left; SI, superior–inferior; AP, anterior–posterior; MPTV, PTV margins.

DISCUSSION

The dose distribution in IMRT for head and neck cancer patients relies solely on volume data from the pretreatment CT scan, which reflects the patient's anatomical structure at that particular moment. However, this method does not consider daily changes in target volumes, organs at risk (OARs), or anatomical positioning [40]. The impact of patient setup errors is especially significant in IMRT planning because of the steep dose gradients aimed at protecting nearby OARs from excessive radiation exposure. Studies have shown that a 3 mm error in couch positioning can greatly affect the minimum dose delivered to target areas and the maximum dose to the spinal cord and brainstem in the anterior-posterior (AP) direction [41–43]. Therefore, it is essential to accurately measure and reduce patient setup errors during radiation treatment. Several studies have investigated setup accuracy in head and neck cancer patients, with results varying widely depending on factors such as tumor location, treatment techniques, fixation devices, imaging and registration methods, and the types of setup errors analyze [44–53].

This study investigated the set-up accuracy of head and neck cancer patients undergoing IMRT using EPIs to define appropriate planning margins that satisfy a target dose criterion.

In our study, we investigated set-up variations in a homogeneous patient group treated with standard thermoplastic mask immobilization with five fixation points, no base plate attachment to the linac couch, 2D-alignment procedures, and EPID-based imaging. According to Bentel [54], fixing the base plate to the treatment couch may reduce set-up mistakes by improving repeatability and preventing patient misalignment on the table, which causes out-of-plane rotations. This is most likely the reason for the decreased set-up errors observed by Humphreys et al [55]. The enhanced and reproducible setup precision in the head and neck region was likely attributable to superior immobilization for accurate treatment delivery, as even small changes from the reference anatomy of the patient's planning CT scan (pCT) have the potential to compromise the PTV coverage or sparing of healthy tissues. The use of patient immobilisation devices, such as customized headrests rather than the standard headrest provides a more reliable level of immobilization and hence minimizing the radiation dose to normal tissue structures and consequently minimize risk of toxicity and long-term morbidity [56–60].

We evaluated the accuracy of patient setup by examining systematic and random mistakes. The systematic component of an error is characterized by a consistent deviation in the same direction and of comparable magnitude across all treatment fractions (treatment preparation errors), while the random component is defined by deviations that fluctuate in both direction and magnitude for each administered treatment fraction (treatment execution errors).

There are a limitations in our study concerning the frequency of online verifications of the patient set-up, we performed EPID first 3 PIs in first week then weekly PI and the setup errors values may be affected as reported in [61-64], their results showed that the overall standard deviations of the displacements increase significantly between daily and weekly measurements so they decided to perform daily images for certain directions as like Pehlivan [61] recommended that a PI in the AP and ML orientations be conducted weekly, while in the CC orientation, it should occur every two days to effectively mitigate set-up problems. A previous study by Strabac et al. [64] has shown that the overall standard deviations of the displacements increase significantly between daily and weekly measurements in the dorsoventral and caudocranial directions, measured in the lateral PIs. The PIs measured in the AP fields in the caudocranial and left-right lateral directions, have shown no significant increase in the overall SD of the displacement due to the frequency of measurements. Marnouche et al. [65] evaluated three-dimensional 3D set-up errors using EPID and also investigated if other imaging frequency protocols were as effective as the daily imaging protocol and compered it with No Action Level 5, extended No Action Level, weekly, protocols. The study reported that a 5-mm extension of CTV to PTV margin was the optimal margin and The Daily online verification protocol was the advised verification protocol for patients treated with IMRT. The results of Youssoufi et al. [66] which obtained by weekly EPID setup verifications, almost likely aligned with our results and reported that the Setup margins 4·27, 4·2 and 4·7 mm in X, Y and Z directions, respectively.

According to our findings, the population systematic errors and random errors were 0.19 and 0.26 cm, respectively in the anteroposterior direction; the group systematic errors and random errors were 0.15 cm and 0.24 cm in SI direction, respectively; the group systematic errors and random errors were 0.13 cm and 0.25 cm in LR direction, respectively. The largest displacement was in the A-P direction 8 mm in the posterior direction and the frequency for displacement 0.4 cm reaches to 9.83% followed by SI and RL directions.

The results align with Durim et al. [67], whose investigation indicated that the overall incidence of set-up displacements above 3 mm was 3.9% in the medial-lateral (ML) direction, 8% in the superior-inferior (SI) direction, and 15.5% in the anterior-posterior (AP) direction.

Mongioj et al. [68] reported that as the therapy progressed, the displacement > 3 mm were observed more commonly at instances of significant weight loss or tumor nodal reduction and confirmed the need for a strict monitoring of patient set-up in case of isocenter change due to sequential PTVs definition and in the presence of significant weight loss and/or tumor shrinkage.

The greater displacement A-P directions is attributed due to weight loss and the size of the neck is more likely to become smaller because there is more subcutaneous adipose tissue in the neck, patients may slide along the head-holder, therefore Ove et al. [69] and SU et al and Zhang et al. [37,70] proposed registration of multiple ROIs and took an analysis of 3D setup uncertainties for multiple ROIs in head and neck region and there was a statistically significant difference in setup error between the head and neck during radiation. However, the setup error of the neck was bigger than the head and They came to the conclusion that the setup errors among head, upper neck, and lower neck in SI directions were with homogeneity ($P>0.05$); hence, the setup errors with head, upper neck, and lower neck in RL and AP directions were not with homogeneity.

In order to prevent underestimation or overestimation of actual margin, the discrepancy of geometrical set-up errors must be considered in three directions. Based on our results we can conclude that a 6-mm extension of CTV to PTV margin, as the optimal margin. Our results are similar as Strabac [64] which reported that 6.1, 5.1, 4.8 mm CTV-PTV in LR, CC and 4.8 mm CTV-PTV DV direction, respectively.

In general, performing regular position corrections and improving patient positioning would lead to a small PTV margin and lower chance of normal tissue complications.

CONCLUSIONS

This study is a report on the set-up accuracy of patients treating for HNC with IMRT. CTV-PTV margins calculated according van Herk formula and we can conclude that a 6-mm extension of CTV to PTV margin, as the optimal margin and can be reduced with increasing frequency of online verification (daily imaging) or for patients where the prescribed doesn't exceed tolerance doses for organs at risk.

Conflict of interests: The authors declare that they have no known competing financial interests or personal relationships that could have appeared to influence the work reported in this paper.

Data availability: The datasets generated during and/or analyzed during the current study are available from the corresponding author on reasonable request.

Declaration: The information in this article is correct, ethical considerations have been assessed per hospital policy, Ethical Approval is 36265MD265/8/24

ORCID
Ehab Attalla, https://orcid.org/0000-0003-4779-4445; **Fathi Elhussiny,** https://orcid.org/0000-0003-3175-4772

REFERENCES

[1] R. Wang, and M. Kang, "Guidelines for radiotherapy of nasopharyngeal carcinoma," Precis. Radiat. Oncol. **5**(3), 122–159 (2021). https://doi.org/10.1002/pro6.1123
[2] W.T. Ng, J.C.H. Chow, J.J. Beitler, J. Corry, W. Mendenhall, A.W.M. Lee, K.T. Robbins, S. Nuyts, N.F. Saba, R. Smee, W.A. Stokes, P. Strojan, and A. Ferlito, "Current Radiotherapy Considerations for Nasopharyngeal Carcinoma †," Cancers (Basel). **14**(23), 5773 (2022). https://doi.org/10.3390/cancers14235773
[3] P. Blanchard, J. Biau, F. Huguet, S. Racadot, C. Berthold, S. Wong-Hee-Kam, M.-C. Biston, and P. Maingon, "Radiotherapy for nasopharyngeal cancer," Cancer/Radiothérapie **26**(1–2), 168–173 (2022). https://doi.org/10.1016/j.canrad.2021.08.009
[4] P.L. Yip, R. You, M.-Y. Chen, and M.L.K. Chua, "Embracing Personalized Strategies in Radiotherapy for Nasopharyngeal Carcinoma: Beyond the Conventional Bounds of Fields and Borders," Cancers (Basel). **16**(2), 383 (2024). https://doi.org/10.3390/cancers16020383
[5] A. Sharma, and A. Bahl, "Intensity-modulated radiation therapy in head-and-neck carcinomas: potential beyond sparing the parotid glands," J. Cancer Res. Ther. **16**(3), 425–433 (2020). https://doi.org/10.4103/jcrt.JCRT_880_18
[6] E. Anderson, K. Pilling, S. Iqbal, and R.L. Pearson, "A retrospective analysis comparing set up errors from standard versus customised headrests for head and neck radiotherapy," Radiography **28**(3), 746–750 (2022). https://doi.org/10.1016/j.radi.2022.03.008
[7] I. Kaur, S. Rawat, P. Ahlawat, A. Kakria, G. Gupta, U. Saxena, and M.B. Mishra, "Dosimetric impact of setup errors in head and neck cancer patients treated by image-guided radiotherapy," J. Med. Phys. **41**(2), 144–148 (2016). https://doi.org/10.4103/0971-6203.181640
[8] Y. Chang, F. Xiao, H. Quan, and Z. Yang, "Evaluation of OAR dose sparing and plan robustness of beam-specific PTV in lung cancer IMRT treatment," Radiat. Oncol. **15**, 1–12 (2020). https://doi.org/10.1186/s13014-020-01686-1
[9] K. Bell, N. Licht, C. Rübe, and Y. Dzierma, "Image guidance and positioning accuracy in clinical practice: influence of positioning errors and imaging dose on the real dose distribution for head and neck cancer treatment," Radiat. Oncol. **13**, 1–13 (2018). https://doi.org/10.1186/s13014-018-1141-8
[10] J. Willner, U. Hädinger, M. Neumann, F.J. Schwab, K. Bratengeier, and M. Flentje, "Three dimensional variability in patient positioning using bite block immobilization in 3D-conformal radiation treatment for ENT-tumors," Radiother. Oncol. **43**(3), 315–321 (1997). https://doi.org/10.1016/S0167-8140(97)00055-8
[11] L. Gilbeau, M. Octave-Prignot, T. Loncol, L. Renard, P. Scalliet, and V. Grégoire, "Comparison of setup accuracy of three different thermoplastic masks for the treatment of brain and head and neck tumors," Radiother. Oncol. **58**(2), 155–162 (2001). https://doi.org/10.1016/S0167-8140(00)00280-2
[12] I. Rabinowitz, J. Broomberg, M. Goitein, K. McCarthy, and J. Leong, "Accuracy of radiation field alignment in clinical practice," Int. J. Radiat. Oncol. Biol. Phys. **11**(10), 1857–1867 (1985). https://doi.org/10.1016/0360-3016(85)90046-X
[13] R.-D. Kortmann, C.F. Hess, R. Jany, C. Meisner, and M. Bamberg, "Reproducibility of field alignment in difficult patient positioning," Int. J. Radiat. Oncol. Biol. Phys. **29**(4), 869–872 (1994). https://doi.org/10.1016/0360-3016(94)90578-9
[14] S. Kumar, K. Burke, C. Nalder, P. Jarrett, C. Mubata, R. A'hern, M. Humphreys, M. Bidmead, and M. Brada, "Treatment accuracy of fractionated stereotactic radiotherapy," Radiother. Oncol. **74**(1), 53–59 (2005). https://doi.org/10.1016/j.radonc.2004.06.008
[15] C.F. Hess, R.-D. Kortmann, R. Jany, A. Hamberger, and M. Bamberg, "Accuracy of field alignment in radiotherapy of head and neck cancer utilizing individualized face mask immobilization: a retrospective analysis of clinical practice," Radiother. Oncol. **34**(1), 69–72 (1995). https://doi.org/10.1016/0167-8140(94)01497-Q
[16] A. Bel, R. Keus, R.E. Vijlbrief, and J. V Lebesque, "Setup deviations in wedged pair irradiation of parotid gland and tonsillar tumors, measured with an electronic portal imaging device," Radiother. Oncol. **37**(2), 153–159 (1995). https://doi.org/10.1016/0167-8140(95)01627-S
[17] A. Bel, M. Van Herk, H. Bartelink, and J. V Lebesque, "A verification procedure to improve patient set-up accuracy using portal images," Radiother. Oncol. **29**(2), 253–260 (1993). https://doi.org/10.1016/0167-8140(93)90255-7
[18] S. Molana, F. Arbabi, M. Sanei, E. Hashemi, M. Tajvidi, A. Rostami, A. Tavakol, P. Kiani, Z. Fazli, and H. Ghaffari, "Evaluation of patient setup accuracy and determination of optimal setup margin for external beam radiation therapy using electronic portal imaging device," Cancer Ther. Oncol. Int. J. **11**(2), 48–55 (2018). http://dx.doi.org/10.19080/CTOIJ.2018.11.555808
[19] I.-C. Costin, and L.G. Marcu, "Factors impacting on patient setup analysis and error management during breast cancer radiotherapy," Crit. Rev. Oncol. Hematol. **178**, 103798 (2022). https://doi.org/10.1016/j.critrevonc.2022.103798
[20] T. Gupta, S. Chopra, A. Kadam, J.P. Agarwal, P.R. Devi, S. Ghosh-Laskar, and K.A. Dinshaw, "Assessment of three-dimensional set-up errors in conventional head and neck radiotherapy using electronic portal imaging device," Radiat. Oncol. **2**, 1–8 (2007). https://doi.org/10.1186/1748-717X-2-44
[21] A. Farajollahi, N. Mohammadzadeh, M. Momennezhad, S. Naseri, S. Mohebbi, F. Shahedi, and S. Mohebbi, "Evaluation of Patient Set Up Errors in Head and Neck Three-Dimensional (3D) Conformal and Intensity-Modulated Radiotherapy Using Electronic Portal Imaging Device," Iran. J. Med. Phys. **19**(5), 270–274 (2022). https://doi.org/10.22038/ijmp.2022.58298.1977
[22] J. Bijhold, J.V. Lebesque, A.A.M. Hart, and R.E. Vijlbrief, "Maximizing setup accuracy using portal images as applied to a conformal boost technique for prostatic cancer," Radiother. Oncol. **24**(4), 261–271 (1992). https://doi.org/10.1016/0167-8140(92)90233-K
[23] C.L. Creutzberg, V.G.M. Althof, H. Huizenga, A.G. Visser, and P.C. Levendag, "Quality assurance using portal imaging: the accuracy of patient positioning in irradiation of breast cancer," Int. J. Radiat. Oncol. Biol. Phys. **25**(3), 529–539 (1993). https://doi.org/10.1016/0360-3016(93)90077-9
[24] L. Dong, and A.L. Boyer, "An image correlation procedure for digitally reconstructed radiographs and electronic portal images.," Int. J. Radiat. Oncol. Biol. Phys. **33**(5), 1053–1060 (1995). https://doi.org/10.1016/0360-3016(95)02082-9
[25] T.S. Hong, W.A. Tomé, R.J. Chappell, P. Chinnaiyan, M.P. Mehta, and P.M. Harari, "The impact of daily setup variations on head-and-neck intensity-modulated radiation therapy," Int. J. Radiat. Oncol. Biol. Phys. **61**(3), 779–788 (2005). https://doi.org/10.1016/j.ijrobp.2004.07.696
[26] B. van Asselen, H. Dehnad, C.P.J. Raaijmakers, J.J.W. Lagendijk, and C.H.J. Terhaard, "Implanted gold markers for position verification during irradiation of head-and-neck cancers: a feasibility study," Int. J. Radiat. Oncol. Biol. Phys. **59**(4), 1011–1017 (2004). https://doi.org/10.1016/j.ijrobp.2004.01.022
[27] J. Gildersleve, D.P. Dearnaley, P.M. Evans, and W. Swindell, "Reproducibility of patient positioning during routine radiotherapy, as assessed by an integrated megavoltage imaging system," Radiother. Oncol. **35**(2), 151–160 (1995). https://doi.org/10.1016/0167-8140(95)01536-P

[28] D. Yan, J. Wong, F. Vicini, J. Michalski, C. Pan, A. Frazier, E. Horwitz, and A. Martinez, "Adaptive modification of treatment planning to minimize the deleterious effects of treatment setup errors," Int. J. Radiat. Oncol. Biol. Phys. **38**(1), 197–206 (1997). https://doi.org/10.1016/s0360-3016(97)00229-0
[29] Q.-S. Chen, Y.-H. Zhao, X. Chen, J.-K. Xu, Q. Gao, and J.-Y. Zhu, "Setup error of electronic portal image device in IMRT for thoracic tumors and its influence," Eur. Rev. Med. Pharmacol. Sci. **27**(24), (2023). https://doi.org/10.26355/eurrev_202312_34799
[30] P.A. Asvestas, K.K. Delibasis, N.A. Mouravliansky, and G.K. Matsopoulos, "ESTERR-PRO: A Setup Verification Software System Using Electronic Portal Imaging," Int. J. Biomed. Imaging **2007**(1), 61523 (2007). https://doi.org/10.1155/2007/61523
[31] P. Shinde, A. Jadhav, V. Shankar, and S.J. Dhoble, "Assessment of dosimetric impact of interfractional 6D setup error in tongue cancer treated with IMRT and VMAT using daily kV-CBCT," Reports Pract. Oncol. Radiother. **28**(2), 224–240 (2023). https://doi.org/10.5603/RPOR.a2023.0020
[32] K. Tsujii, Y. Ueda, M. Isono, M. Miyazaki, T. Teshima, and M. Koizumi, "Dosimetric impact of rotational setup errors in volumetric modulated arc therapy for postoperative cervical cancer," J. Radiat. Res. **62**(4), 688–698 (2021). https://doi.org/10.1093/jrr/rrab044
[33] C. Beltran, A. Pegram, and T.E. Merchant, "Dosimetric consequences of rotational errors in radiation therapy of pediatric brain tumor patients," Radiother. Oncol. **102**(2), 206–209 (2012). https://doi.org/10.1016/j.radonc.2011.06.013
[34] A. Heikkilä, E. Boman, M. Rossi, A. Vanhanen, M. Mankinen, M. Postema, and T. Koivumäki, "Dosimetric effect of rotational setup errors in volumetric modulated arc therapy and field-in-field treatment of left-sided breast cancer," Phys. Medica, **117**, 103203 (2024). https://doi.org/10.1016/j.ejmp.2023.103203
[35] W. Fu, Y. Yang, N.J. Yue, D.E. Heron, and M.S. Huq, "Dosimetric influences of rotational setup errors on head and neck carcinoma intensity-modulated radiation therapy treatments," Med. Dosim. **38**(2), 125–132 (2013). https://doi.org/10.1016/j.meddos.2012.09.003
[36] I. Ahmed, S. Krishnamurthy, R. Bhise, K. Vinchurkar, and M. Kalloli, "Concurrent Weekly Cisplatin and Simultaneous Integrated Boost-IMRT in Locally Advanced Head and Neck Squamous Cell Carcinoma—An Institutional Experience," South Asian J. Cancer **11**(03), 235–242 (2022). https://doi.org/10.1055/s-0042-1743578
[37] L. Zhang, A.S. Garden, J. Lo, K.K. Ang, A. Ahamad, W.H. Morrison, D.I. Rosenthal, M.S. Chambers, X.R. Zhu, and R. Mohan, "Multiple regions-of-interest analysis of setup uncertainties for head-and-neck cancer radiotherapy," Int. J. Radiat. Oncol. Biol. Phys. **64**(5), 1559–1569 (2006). https://doi.org/10.1016/j.ijrobp.2005.12.023
[38] M. Van Herk, "Errors and margins in radiotherapy," in *Semin. Radiat. Oncol.*, (Elsevier, 2004), pp. 52–64. https://doi.org/10.1053/j.semradonc.2003.10.003
[39] M. Van Herk, P. Remeijer, C. Rasch, and J. V Lebesque, "The probability of correct target dosage: dose-population histograms for deriving treatment margins in radiotherapy," Int. J. Radiat. Oncol. Biol. Phys. **47**(4), 1121–1135 (2000). https://doi.org/10.1016/S0360-3016(00)00518-6
[40] W. Tan, Y. Li, G. Han, J. Xu, X. Wang, Y. Li, and D. Hu, "Target volume and position variations during intensity-modulated radiotherapy for patients with nasopharyngeal carcinoma," Onco. Targets. Ther. 1719–1728 (2013). http://dx.doi.org/10.2147/OTT.S53639
[41] L. Xing, Z.-X. Lin, S.S. Donaldson, Q.T. Le, D. Tate, D.R. Goffinet, S. Wolden, L. Ma, and A.L. Boyer, "Dosimetric effects of patient displacement and collimator and gantry angle misalignment on intensity modulated radiation therapy," Radiother. Oncol. **56**(1), 97–108 (2000). https://doi.org/10.1016/S0167-8140(00)00192-4
[42] G. Liu, S. Zhang, Y. Ma, Q. Wang, X. Chen, L. Zhang, and F. Ma, "Effects of error on dose of target region and organs at risk in treating nasopharynx cancer with intensity modulated radiation therapy," Pakistan J. Med. Sci. **32**(1), 95 (2016). https://doi.org/10.12669/pjms.321.9218
[43] R. Prabhakar, M.A. Laviraj, K.P. Haresh, P.K. Julka, and G.K. Rath, "Impact of patient setup error in the treatment of head and neck cancer with intensity modulated radiation therapy," Phys. Medica **26**(1), 26–33 (2010). https://doi.org/10.1016/j.ejmp.2009.05.001
[44] E.N.J.T. van Lin, L. van der Vight, H. Huizenga, J.H.A.M. Kaanders, and A.G. Visser, "Set-up improvement in head and neck radiotherapy using a 3D off-line EPID-based correction protocol and a customised head and neck support," Radiother. Oncol. **68**(2), 137–148 (2003). https://doi.org/10.1016/S0167-8140(03)00134-8
[45] J.L. Barker Jr, A.S. Garden, K.K. Ang, J.C. O'Daniel, H. Wang, L.E. Court, W.H. Morrison, D.I. Rosenthal, K.S.C. Chao, and S.L. Tucker, "Quantification of volumetric and geometric changes occurring during fractionated radiotherapy for head-and-neck cancer using an integrated CT/linear accelerator system," Int. J. Radiat. Oncol. Biol. Phys. **59**(4), 960–970 (2004). https://doi.org/10.1016/j.ijrobp.2003.12.024
[46] E.K. Hansen, M.K. Bucci, J.M. Quivey, V. Weinberg, and P. Xia, "Repeat CT imaging and replanning during the course of IMRT for head-and-neck cancer," Int. J. Radiat. Oncol. Biol. Phys. **64**(2), 355–362 (2006). https://doi.org/10.1016/j.ijrobp.2005.07.957
[47] L.N. McDermott, M. Wendling, J.-J. Sonke, M. van Herk, and B.J. Mijnheer, "Anatomy changes in radiotherapy detected using portal imaging," Radiother. Oncol. **79**(2), 211–217 (2006). https://doi.org/10.1016/j.radonc.2006.04.003
[48] H. Alabedi, "Assessing setup errors and shifting margins for planning target volume in head, neck, and breast cancer," J. Med. Life, **16**(3), 394 (2023). https://doi.org/10.25122/jml-2022-0241
[49] S.H. Kim, S.A. Oh, J.W. Yea, and J.W. Park, "Prospective assessment of inter-or intra-fractional variation according to body weight or volume change in patients with head and neck cancer undergoing radiotherapy," PLoS One, **14**(5), e0216655 (2019). https://doi.org/10.1371/journal.pone.0216655
[50] M. Coffey, T. Greener, C. Hall, M. Van Herk, B. Mijnheer, and A. Harrison, "Geometric uncertainties in radiotherapy: technical overview of geometric uncertainties in radiotherapy," BIR Work. Party, (2003).
[51] A. Navran, W. Heemsbergen, T. Janssen, O. Hamming-Vrieze, M. Jonker, C. Zuur, M. Verheij, *et al*., "The impact of margin reduction on outcome and toxicity in head and neck cancer patients treated with image-guided volumetric modulated arc therapy (VMAT)," Radiother. Oncol. **130**, 25–31 (2019). https://doi.org/10.1016/j.radonc.2018.06.032
[52] J. Unkelbach, M. Alber, M. Bangert, R. Bokrantz, T.C.Y. Chan, J.O. Deasy, A. Fredriksson, *et al*., "Robust radiotherapy planning," Phys. Med. Biol. **63**(22), 22TR02 (2018). https://doi.org/10.1088/1361-6560/aae659
[53] W. Fangzheng, S. Quanquan, J. Chuner, Y. Zhimin, Y. Shuangyan, Y. Huanhuan, S. Jianfang, M. Sakamoto, Q. Weifeng, and F. Zhenfu, "Optimization of the margin expanded from the clinical to the planned target volume during intensity-modulated radiotherapy for nasopharyngeal carcinoma," Oncotarget, **8**(66), 110201 (2017). https://doi.org/10.18632/oncotarget.22518
[54] G.C. Bentel, L.B. Marks, K. Hendren, and D.M. Brizel, "Comparison of two head and neck immobilization systems.," Int. J. Radiat. Oncol. Biol. Phys. **38**(4), 867–873 (1997). https://doi.org/10.1016/s0360-3016(97)00075-8

[55] M. Humphreys, M.T.G. Urbano, C. Mubata, E. Miles, K.J. Harrington, M. Bidmead, and C.M. Nutting, “Assessment of a customised immobilisation system for head and neck IMRT using electronic portal imaging,” Radiother. Oncol. **77**(1), 39–44 (2005). https://doi.org/10.1016/j.radonc.2005.06.039
[56] M. Leech, M. Coffey, M. Mast, F. Moura, A. Osztavics, D. Pasini, and A. Vaandering, “ESTRO ACROP guidelines for positioning, immobilisation and position verification of head and neck patients for radiation therapists,” Tech. Innov. Patient Support Radiat. Oncol. **1**, 1–7 (2017). https://doi.org/10.1016/j.tipsro.2016.12.001
[57] S. Androjna, V.Z. Marcius, P. Peterlin, and P. Strojan, “Assessment of set-up errors in the radiotherapy of patients with head and neck cancer: standard vs. individual head support,” Radiol. Oncol. **54**(3), 364–370 (2020). https://doi.org/10.2478/raon-2020-0036
[58] M. Verma, A.A. Sait, S.K.S. Kumar, K.J.M. Das, P. Lal, and S. Kumar, “An audit of setup reproducibility in radiotherapy of head and neck cancers,” J. Radiat. Cancer Res. **7**(3), 85–89 (2016). https://doi.org/10.4103/0973-0168.197975
[59] L. Belshaw, C.E. Agnew, D.M. Irvine, K.P. Rooney, and C.K. McGarry, “Adaptive radiotherapy for head and neck cancer reduces the requirement for rescans during treatment due to spinal cord dose,” Radiat. Oncol. **14**, 1–7 (2019). https://doi.org/10.1186/s13014-019-1400-3
[60] Z. Mulla, R.K. Alwassia, E.M. Senan, S. Soaida, A.A. Mohamed, H. Almerdhemah, H.A. Iqbal, and H.M. Muamenah, “A comparative study between open-face and closed-face masks for head and neck cancer (HNC) in radiation therapy,” Reports Pract. Oncol. Radiother. **25**(3), 382–388 (2020). https://doi.org/10.1016/j.rpor.2020.03.009
[61] B. Pehlivan, C. Pichenot, M. Castaing, A. Auperin, D. Lefkopoulos, R. Arriagada, and J. Bourhis, “Interfractional set-up errors evaluation by daily electronic portal imaging of IMRT in head and neck cancer patients,” Acta Oncol. (Madr). **48**(3), 440–445 (2009). https://doi.org/10.1080/02841860802400610
[62] V. Rudat, M. Hammoud, Y. Pillay, A.A. Alaradi, A. Mohamed, and S. Altuwaijri, “Impact of the frequency of online verifications on the patient set-up accuracy and set-up margins,” Radiat. Oncol. **6**, 101 (2011). http://www.ro-journal.com/content/6/1/101
[63] M.L. Johnston, P. Vial, K.L. Wiltshire, L.J. Bell, S. Blome, Z. Kerestes, G.W. Morgan, D. O’Driscoll, T.P. Shakespeare, and T.N. Eade, “Daily online bony correction is required for prostate patients without fiducial markers or soft-tissue imaging,” Clin. Oncol. **23**(7), 454–459 (2011). https://doi.org/10.1016/j.clon.2011.02.013
[64] B. Strbac, and V.S. Jokic, “Evaluation of set-up errors in head and neck radiotherapy using electronic portal imaging,” Phys. Medica, **29**(5), 531–536 (2013). https://doi.org/10.1016/j.ejmp.2012.12.001
[65] E.A. Marnouche, M. Abdelhak, I. Lalya, N. Zaghba, A. Bazine, K. Andaloussi, M. Elmarjany, *et al.*, “Set-up errors and imaging verification protocols for head and neck cancers radiotherapy in Morocco,” J. Oncol. Res. Treat **4**(131), 2 (2019).
[66] M.A. Youssoufi, M. Bougtib, S. Douama, M.A. Erraisse, F.Z. Abboud, K. Hassouni, and F. Bentayeb, “Evaluation of PTV margins in IMRT for head and neck cancer and prostate cancer,” J. Radiother. Pract. **20**(1), 114–119 (2021). https://doi.org/10.1017/S1460396919000931
[67] D. Delishaj, S. Ursino, F. Pasqualetti, F. Matteucci, A. Cristaudo, C. Pietro Soatti, A. Barcellini, and F. Paiar, “Set-up errors in head and neck cancer treated with IMRT technique assessed by cone-beam computed tomography: a feasible protocol,” Radiat. Oncol. J. **36**(1), 54 (2018). https://doi.org/10.3857/roj.2017.00493
[68] V. Mongioj, E. Orlandi, M. Palazzi, E. Deponti, F. Marzia, C. Stucchi, C. Sangalli, C. Fallai, G. Zonca, and P. Olmi, “Set-up errors analyses in IMRT treatments for nasopharyngeal carcinoma to evaluate time trends, PTV and PRV margins,” Acta Oncol. (Madr). **50**(1), 61–71 (2011). https://doi.org/10.3109/0284186X.2010.509108
[69] R. Ove, R. Cavalieri, D. Noble, and S.M. Russo, “Variation of neck position with image-guided radiotherapy for head and neck cancer,” Am. J. Clin. Oncol. **35**(1), 1–5 (2012). https://doi.org/10.1097/COC.0b013e3181fe46bb
[70] J. Su, W. Chen, H. Yang, J. Hong, Z. Zhang, G. Yang, L. Li, and R. Wei, “Different setup errors assessed by weekly cone-beam computed tomography on different registration in nasopharyngeal carcinoma treated with intensity-modulated radiation therapy,” Onco. Targets. Ther. **2015**(8), 2545–2553 (2015). http://dx.doi.org/10.2147/OTT.S87159

ВИЗНАЧЕННЯ МЕЖІ НАЛАШТУВАННЯ ДЛЯ НОСОФАРИНГІАЛЬНОЇ КАРЦИНОМИ ЗА ДОПОМОГОЮ ЕЛЕКТРОННОГО ПОРТАЛЬНОГО ПРИСТРОЮ ВІДОБРАЖЕННЯ

Сафа Ельфарамаві[a,b], Ехаб Атталла[c], Фатхі Ельхусіні[a], Мохамед Альм Ель-Дін[d], Ахмед Ельмекаві[a]
[a]*Факультет природничих наук, факультет фізики, Університет Танта, Танта, Єгипет*
[b]*Лікарня Альхаммаді, Ер-Ріяд, Саудівська Аравія*
[c]*Національний інститут раку, Каїрський університет, Єгипет*
[d]*Факультет медицини, відділення онкології, Університет Танта, Танта, Єгипет*

Вступ. Це дослідження мало на меті оцінити помилки тривимірного (3D) налаштування та забезпечити оптимальні межі для охоплення запланованого цільового об’єму (PTV) при випромінюванні голови та шиї. **Методи:** десять пацієнтів брали участь у дослідженні, отримували IMRT у поєднанні з щотижневою електронною портальною візуалізацією (EPI). Всього було проаналізовано 170 знімків порталу. Систематичні (S) та випадкові (s) помилки в популяції пацієнтів із раком голови та шиї оцінювали за допомогою портальних зображень у каудокраніальному поздовжньому (CC) та ліво-правому латеральному (LR) напрямках, виміряних у межах передньо-заднього (AP) поля. Межі цільового об’єму від клініки до планування (CTV-PTV) були визначені згідно з рекомендаціями ICRU Report 62 та формулами ван Герка. **Результати:** групові систематичні та випадкові помилки становили 0,19 і 0,26 см відповідно в передньо-задньому напрямку; групові систематичні похибки та випадкові похибки становили 0,15 см та 0,24 см у напрямку CI відповідно; групові систематичні похибки та випадкові похибки становили 0,13 см та 0,25 см у напрямку LR відповідно; Відповідно до класичної формули Ван-Херка MPTV =$2{,}5\Sigma + 0{,}7\sigma$, ми розрахували ідеальні межі PTV (MPTV) на основі похибок налаштування та 0,65 см, 0,55 см і 0,5 см, необхідні для напрямків AP, SI та RL. **Обговорення та висновки:** ми можемо зробити висновок, що 6 мм розширення CTV до PTV межі є оптимальною межею і може бути зменшено зі збільшенням частоти онлайн-перевірки (щоденна візуалізація) або для пацієнтів, де призначені дози не перевищують допустимі дози для органів під загрозою.

Ключові слова: *променева терапія носоглотки; променева терапія з модуляцією інтенсивності (IMRT); невизначеність налаштування*

East European Journal of Physics. **1.** 309-317 (2025)
DOI:10.26565/2312-4334-2025-1-37 ISSN 2312-4334

CASSON FLOW OF BLOOD CONTAINING Au AND Ta NANOPARTICLES OVER A STENOTIC ARTERY

Suneetha Sangapatnam
Department of Applied Mathematics, Yogi Vemana University, Kadapa-516005, Andhra Pradesh, India
Corresponding Author e-mail: suneethayvu@gmail.com
Received October 22, 2024, revised December 29, 2024; accepted January 15, 2025

Computational fluid dynamics focuses a premium on investigations of blood flow via narrowed arteries due to the relevance of these issues to biological investigations. The main goal of this study is to find out how nanoparticles affect blood flow via a constricted artery. As part of our investigation into the theoretical flow scenario, we examine the significance of Casson nanofluid movement via a cardiac artery. By using the suitable delf similarity variables the PDEs transformed into ODEs. Following that, the dimensionless equations are handled employing the MATLAB computer program in the Bvp5c method. The magnetic properties of the blood flow cells were investigated by increasing the magnetic field parameter, which resulted in a reduction in blood flow as predicted. The movement trend reduced when the Casson liquid parameter increased. To improve the transmission of heat efficiency, the concentration of gold particles in the constricted artery should be increased. One may argue that iron nanoparticles are useful for delivering medications. Presently available methods may be useful for distributing drugs throughout the circulatory system. The theoretical consequences of this medication delivery method are presented in a manner that is made easier by the utilization of an illustration representation.
Keywords: *Au and Ta nanoparticles; Bvp5c method; Stenotic artery; MHD; Casson fluid*
PACS: 44.05.+e, 44.30.+v, 44.40.+a, 47.10.ad., 52.75.Fk.

1. INTRODUCTION

The arteries are becoming more blocked as a result of contemporary lifestyle behaviours such as smoking, raised cholesterol levels, and, maybe, inherited problems. The strengthening and constriction of the artery walls is a particularly prevalent ailment in the circulatory system. This condition is called coronary artery stenosis in healthcare research. Arteries with stenosis have narrowed or constricted on the inside, reducing the amount of blood along with other fluids that may reach other parts of the body. The way blood moves through arterial stenosis is an extremely significant subject to talk about when trying learn about circulation illnesses, since numerous of individuals are caused by problems with the way blood vessels are built and how blood moves through them [1]. The human heart serves as the foundational organ of a creature's circulatory system, which distributes oxygen-enriched blood via capillaries to various body regions. Therefore, a healthy life cycle depends on the heart's normal and active operation. Arterial and circulatory issues, however, have emerged as a single of the harmful illnesses causing a growing number of fatalities globally in the past few decades. The majority of these illnesses are related to the unique and aberrant flow of blood via arteries. Many medical professionals and creative thinkers have proposed theories as to why blood circulation via arteries is restricted. The most common reason for abnormal circulatory function among such methods is the formation of atheromatous plaque within vessels. Numerous doctors and imaginative individuals have developed hypotheses to explain the reason blood flow through veins is limited. The most prevalent cause of diminished cardiovascular performance across these techniques is the creation of atheromatous stones inside arteries. From a health perspective, doctors have indicated that this condition may be healed in its initial phases, yet as plaque growth gathers, it inhibits blood flow to various vascular/cardiovascular parts of the human body, potentially resulting in an exacerbated cardiac event [2]. Overall, the presence of stenotic arterial walls that contain such tiny particles might boost the appearance of limited or obstructed blood flow, aiding in assessment and therapy planning, as well as the relevance of particles in atherosclerosis as shown in Figure 1.

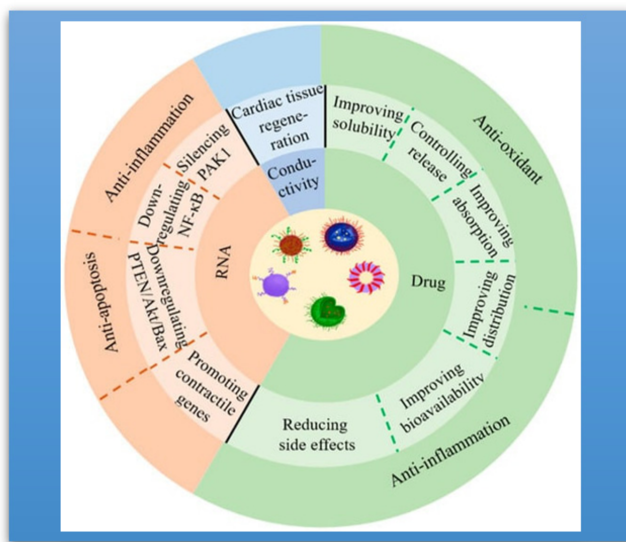

Figure 1. The use of particles in the therapy of cardiovascular diseases

Cite as: S. Sangapatnam, East Eur. J. Phys. 1, 309 (2025), https://doi.org/10.26565/2312-4334-2025-1-37
© S. Sangapatnam, 2025; CC BY 4.0 license

The improvement of the occurrence of heat transportation represents a significant contribution to the procedures that are used in technological and manufacturing applications. It is well noticed that advancements in renewable energy sources have been made using various base fluids. However, since these fundamental elements have a smaller thermal effect, the heating process takes longer. Thus, a revolutionary strategy for enhancing heat transmission in fluids is to include particles within the fundamental fluid, resulting in a nanofluid together Choi and Eastman [3]. Nanofluids offer much higher heat conductivity compared standard fluids. As a consequence, nanoparticles have been considered for a range of uses, such cooling nuclear power plants, reducing cars and equipment, freezing electrical appliances, and biomedical [4][5]. Many individuals have investigated the behavior of tiny fluids and the qualities that they possess in a variety of various manners as a result of approach. The relevance of tiny material volume proportion in relation to nanofluid dispersion was first brought to light by Tiwari and Das [6], who added to the discussion. The nanoparticles have great potential for improving disease detection and therapy precision. Nanotechnology, via cell-specific focusing on, transport of molecules to particular organelle components, and additional techniques, could assist to circumvent the constraints of traditional delivery, ranging from massive amounts challenges like biological distribution to smaller-scale obstacles like intracellular movement. To help with understand and clinical implementation of such potential nano-enabled innovations, the US National Sciences and Technology Council (NSTC) established the National Nanotechnology Initiative (NNI) in 2000, which detailed clear priorities and major obstacles for the area. These programs have endorsed contemporary attempts to examine and develop nanotechnology, with nanoparticles (NPs) accounting for a large amount of published investigation and improvement [7][8]. Several initial NP versions failed to conquer biological transport hurdles, while current NP models have used advances in regulated manufacturing procedures to add complex topologies, bio-responsive components, and targeting substances to improve delivery [9][10][11][12][13][14].

The nano-drug delivery improves the stenosis throat's clotting formation; further, this computational simulation can also predict the effects of post-treatment processes. It is witnessed from the literature that several studies [21], [22], [23], [24], explore the blood flow in different types of stenosis arteries with numerous physical aspects.

The current study was motivated by the actual usefulness of nano-drug transport techniques. The procedure regarding selecting the best therapy for coronary artery blockage constitutes a big part of this computer exercise. Computational blood flow modeling has a lot of potential to help people make decisions about how to treat circulatory illnesses. Usually, narrowing is addressed through placing tubes or devices within the stenotic artery. However, nano-drugs are being delivered more and more specifically to particular areas. Additionally, this method starts the creation of blood blockages at the blocked region within the arterial system, and computer models can be used to guess what effect these reactions will have after treatment. Various shaped, sized, along with additional features of stenosis vessels have been studied in numerous additional investigations, as demonstrated by the example mentioned above. According to the best of the author knowledge there is no research has been done on heat transfer analysis on Casson nanofluid over a stenotic artery in the presence of magnetohydrodynamics. Additional uses utilizing gold-tantalum tiny particles contain the administration of medications, tumor diagnostics, heart disease medication, and immunotherapy. Based on the above the mathematical flow equations are in terms of PDEs. With the help of similarity variables to convert the PDEs to ODEs, after that we used Bvp5c technique in MATLAB solver. Higher values of the magnetic field parameter increased velocity profile.

Heart disease-related health issues and fatalities impact a large proportion of the worldwide community. Additionally, there is no unanimity concerning how to fix these medical problems, including among medical professionals and researchers. One prevalent cardiovascular condition which may result in stenosis a narrowing of the arteries and reduced blood circulation is coronary artery disease or the accumulation of cholesterol in the artery walls. This research intends to discover the number of factors that influence the manner in which something particular moves via a blood vessel, which is a smaller segment of human body. Issues that excite interest among individuals in fluids include how they move around, the biological activities that take place inside them, and how fast the liquid moves.

2. MATHEMATICAL FORMULATION OF THE PROBLEM

- In this particular research framework, we made the assumption that the stable two-dimensional Casson fluid flow model across a stenosed artery is incompressible. Additionally, we investigated magnetohydrodynamics.
- During this area of study, we considered the fact that arterial blood moves incompressible throughout artery stenosis dimensions is $L_0/2$.
- it is preferable to work with the cylindrical coordinates (r, θ, x), where the x -axis is considered along the direction of the horizontal artery and θ and r the circumferential and radial directions, correspondingly. In the present model the flow is taken along the axial direction x and r is perpendicular to the flow. The temperature T is set to the arterial wall temperature T_w, suggesting that the wall is maintained at a constant temperature.
- In the physical model we considered blood flow along $x-axis$ and $r-axis$ is taken perpendicular to the blood flow and which is presented in Figure 2.
- A representation depicts blood moving through a cosine-shaped blood artery constricting an area $2R_0$, $R(x)$ is radius of the artery and χ is the maximum height of stenosis.

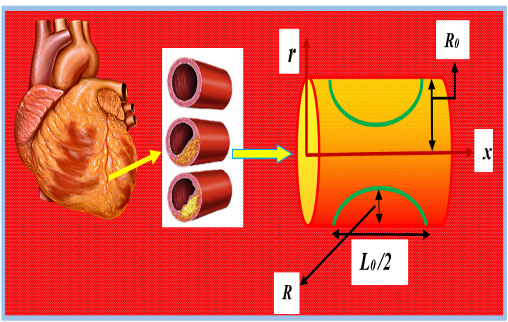

Figure 2. The artery's physical structure.

It has been decided that a profile be created should cover the stenosed area.

$$\frac{R(x)}{R_0}=\begin{cases}1-\frac{\chi}{2}\left(1+\mathrm{Cos}\left(\frac{4\pi x}{L_0}\right)\right), & -\frac{L_0}{4}<x<\frac{L_0}{4}=R_0 \\ 1 & ,otherwise\end{cases}. \tag{1}$$

The mathematical flow equations are as follows [15][16][17][18]:

$$\frac{\partial(ru)}{\partial x}+\frac{\partial(rv)}{\partial r}=0, \tag{2}$$

$$u\left(\frac{\partial}{\partial x}+v\frac{\partial}{\partial r}\right)u=\frac{\mu_{nf}}{\rho_{nf}}\left(1+\frac{1}{\beta}\right)\frac{\partial}{r\partial r}\left(r\frac{\partial u}{\partial r}\right)-\frac{\sigma_{nf}B^2}{\rho_{nf}}u, \tag{3}$$

$$\left(u\frac{\partial}{\partial x}+v\frac{\partial}{\partial r}\right)T=\frac{k_{nf}}{(\rho C_p)_{nf}}\frac{\partial}{r\partial r}\left(r\frac{\partial T}{\partial r}\right)+\frac{\sigma_{nf}B^2u^2}{(\rho C_p)_{nf}}. \tag{4}$$

The boundary conditions are [16][17]

$$\left.\begin{matrix}u=u_0,\ v=0 \text{ and } T=T_w & at\ \ r=R(x), \\ u\to 0, \text{ and } T\to T_\infty & as\ r\to\infty.\end{matrix}\right\}. \tag{5}$$

The thermo physical nature are

$$\Phi_1=\frac{\mu_{nf}}{\mu_f},\ \Phi_2=\frac{\rho_{nf}}{\rho_f},\ \Phi_3=\frac{\sigma_{nf}}{\sigma_f},\ \Phi_4=\frac{(\rho c_p)_{nf}}{(\rho c_p)_f},\ \Phi_5=\frac{k_{nf}}{k_f}. \tag{6}$$

The continuity eq. (1) can be satisfied by introducing stream function ψ for u and v such that.

$$u=\frac{1}{r}\frac{\partial\psi}{\partial r},\ v=-\frac{1}{r}\frac{\partial\psi}{\partial x}. \tag{7}$$

Then Eqs. $(3-4)$ converted as

$$\frac{1}{r}\frac{\partial\psi}{\partial r}\frac{\partial}{\partial x}\left(\frac{1}{r}\frac{\partial\psi}{\partial r}\right)-\frac{1}{r}\frac{\partial\psi}{\partial x}\frac{\partial}{\partial r}\left(\frac{1}{r}\frac{\partial\psi}{\partial x}\right)=\frac{\mu_{nf}}{\rho_{nf}}\left(1+\frac{1}{\beta}\right)\frac{\partial}{r\partial r}\left(\frac{\partial^2\psi}{\partial r^2}-\frac{1}{r}\frac{\partial\psi}{\partial r}\right)-\frac{\sigma_{nf}B^2}{\rho_{nf}}\frac{1}{r}\frac{\partial\psi}{\partial r}, \tag{8}$$

$$\left(\frac{1}{r}\frac{\partial\psi}{\partial r}\right)\frac{\partial T}{\partial x}-\left(\frac{1}{r}\frac{\partial\psi}{\partial x}\right)\frac{\partial T}{\partial r}=\frac{k_{nf}}{(\rho C_p)_{nf}}\frac{\partial}{r\partial r}\left(r\frac{\partial T}{\partial r}\right)+\frac{\sigma_{nf}B^2\psi_r{}^2}{(\rho C_p)_{nf}}. \tag{9}$$

The suitable self-similarity transformations are:

$$\left.\begin{matrix}u=\frac{u_0x}{L_0}f'(\eta),\ \ v=-\frac{R}{r}\sqrt{\frac{u_0\upsilon_f}{L_0}}f(\eta),\ \ \theta(\eta)=\frac{T-T_\infty}{T_w-T_\infty} \\ \eta=\frac{r^2-R^2}{2R}\sqrt{\frac{u_0}{\upsilon_fL_0}}.\end{matrix}\right\}. \tag{10}$$

By substituting Eq. 10 in the Eqs. (8 – 9) modified dimensionless equations are:
Modified Eq. (1) is

$$f = 1 - \frac{\chi}{2}\left(1 + \mathrm{Cos}\left(4\pi x\right)\right), \quad -\frac{1}{4} < x < \frac{1}{4} \\ = 1 \tag{11}$$

Where $f = \frac{R(x)}{R_0}$ *and* $\chi = \frac{\lambda}{R_0}$ is the dimensionless measure of stenosis in reference artery.

$$\frac{1}{\Phi_1\Phi_2}\left[\left(1+2\gamma\eta\right)\left(1+\frac{1}{\beta}\right)f''' + 2\gamma f''\right] + ff'' - f'^2 - \frac{\Phi_3}{\Phi_2}Mf' = 0 \tag{12}$$

$$\frac{\Phi_5}{\Phi_4}\frac{1}{Pr}\left[\left(1+2\gamma\eta\right)\theta'' + 2\gamma\theta'\right] + f\theta' - f'\theta + \frac{\Phi_3}{\Phi_4}MEcf'^2 = 0 \tag{13}$$

The non-dimensional boundary conditions are:

$$\left.\begin{aligned} &f\left(\eta\right) = 0,\ f'\left(\eta\right) = 1,\ \theta\left(\eta\right) = 1,\ \eta = 0 \\ &f'\left(\eta\right) \to 0,\ \theta\left(\eta\right) \to 0,\ \eta \to \infty. \end{aligned}\right\} \tag{14}$$

Here $\gamma = \sqrt{\frac{\upsilon_f L_0}{u_0 R^2}}$ curvature parameter, $M = \frac{\sigma_f B^2 L_0}{u_0 \rho_f}$ Magnetic field parameter and $Pr = \frac{k_f}{\left(\mu C_p\right)_f}$ Prandtl number and $Ec = \frac{U_w^2}{c_p\left(T_w - T_\infty\right)}$ Eckert number.

The physical quantities of C_f and Nu are

$$C_f = \frac{2\tau_w}{\rho_f U_w^2} \tag{15}$$

Here τ_w is $\tau_w = \mu_{nf} \left.\frac{\partial u}{\partial r}\right|_{r=R}$

$$Nu = \frac{xq_w}{k_f\left(T_w - T_\infty\right)} \tag{16}$$

Where q_w is $q_w = -k_{nf} \left.\frac{\partial T}{\partial r}\right|_{r=R}$

The dimensionless form of eq. (15–16) converts

$$Re_r^{1/2} C_f = \Phi_1 f''\left(0\right), \tag{17}$$

$$Re_r^{-1/2} Nu_r = -\frac{k_{nf}}{k_f}\theta'\left(0\right). \tag{18}$$

Table 1. Thermo-physical characteristics Density, Specific heat, Heat conductivity, Electrical conductivity [19]

Property	**Blood**	**Au**	**Ta**
$\rho\ (kgm^{-3})$	1050	10500	16650
$C_p\ (Jkg^{-1}K^{-1})$	3617	235	686.2
$k_f\ (Wm^{-1}K^{-1})$	0.52	429	0.52
$\sigma\ (\Omega m)^{-1}$	1.33	4.5×10^7	7.7×10^6
Pr	21		

3. NUMERICAL METHODOLOGY

The ODE equations are (12–13) with BCs (14) highly nonlinear nature. These equations are implementing a mathematical procedure called the Bvp5c technique by utilizing MATLAB software. The stages of the shooting strategy are listed below:

$$f = N_1, f' = N_2, f'' = N_3, f''' = N_3', \theta = N_4, \theta' = N_5, \theta'' = N_5'$$

Employing the substitution technique to create first-order nonlinear ODEs. Construction of a comparable mathematical setup follow the below procedure.

$$N_1' = N_2$$

$$N_2' = N_3$$

$$N_3' = -\left[\frac{1}{(1+2\gamma\eta)\left(1+\dfrac{1}{\beta}\right)\dfrac{1}{\Phi_1\Phi_2}}\left[\frac{1}{\Phi_1\Phi_2}2\gamma N_3 + N_1N_3 - (N_2)^2 - \frac{\Phi_3}{\Phi_2}MN_2\right]\right]$$

$$N_4' = N_5$$

$$N_5' = -\left[\frac{1}{(1+2\gamma\eta)\dfrac{\Phi_5}{\Phi_4}\dfrac{1}{Pr}}\left[\frac{\Phi_5}{\Phi_4}\frac{1}{Pr}2\gamma N_5 + N_1N_5 - N_2N_4 + \frac{\Phi_3}{\Phi_4}MEc(N_2)^2\right]\right]$$

As well as the boundary conditions are

$$\left.\begin{array}{l} N_1(\eta) = 0,\ N_2(\eta) = 1,\ N_4(\eta) = 1,\ at\ \eta = 0 \\ N_2(\eta) \to 0,\ N_4(\eta) \to 0\ \ as\ \eta \to \infty. \end{array}\right\}$$

4. RESULTS AND DISCUSSION

The current study examines the movement of Casson nanofluid flow across a stenotic artery. The bvp5c approach was used to provide the required solution for the updated complex coupled equations. The findings of graphs that show the effect of several critical elements between this range of values, $0.2 < M < 0.8, 0.1 < \gamma < 0.4, 0.4 < \beta < 1.6, 1.5 < Pr < 4.5,\ \ 2.0 < Ec < 2.6$. Furthermore, we take into account the Prandtl number for blood, which is 21, in addition to taking into account two distinct instances of nanofluids. We analyze each of the parameter numbers. The bvp5c procedure in MATLAB problem solver was employed throughout this investigation's initial stage, which culminated by the present study, which was preceded by a number of key variables.

Fig. 3 demonstrations that the comparison between tiny fluid and mixed nanofluid for velocity graph, for different nanoparticle volume fractions ϕ1=ϕ2 = 0.1, 0.2, 0.3. over the velocity of nanofluid. In this case hybrid nanofluid dominating to the nanofluid case. Fig. 4 effect that the influence of M on velocity graph. The diminishing trend on the velocity graph is shown at higher magnetic field parameter values. Physically speaking, a Lorentz force is created when the M grows, slowing the liquid's movement. Since the Lorentz force prevents fluid from traveling, the speed of the flow decreases due to the extra opposition, which lowers the field of motion. Additionally, the magnetic force can be utilized to control the flow speed in a stenotic artery. Because the magnetic force reduces momentum, it may help to reduce shear stress and the chance of additional harm to the arterial wall.

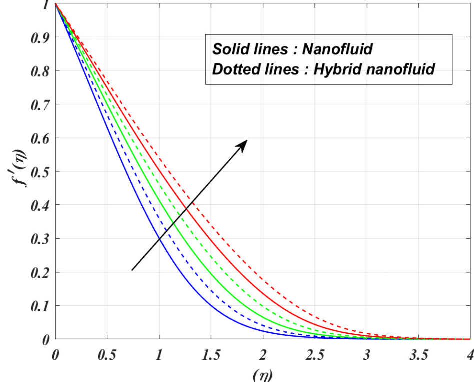

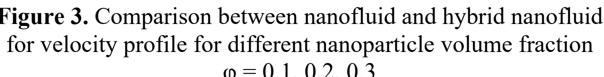

Figure 3. Comparison between nanofluid and hybrid nanofluid for velocity profile for different nanoparticle volume fraction φ = 0.1, 0.2, 0.3

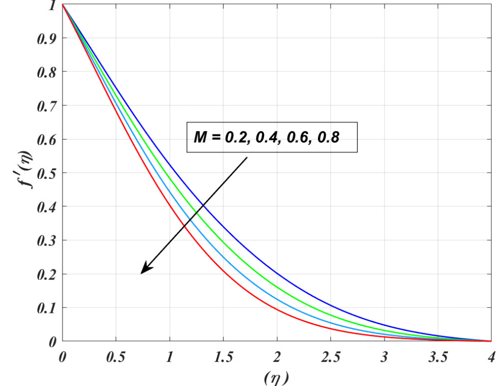

Figure 4. Influence of M on $f'(\eta)$

Fig 5. Shows that influence of γ on velocity graph. The velocity graph is enhanced as γ values are enhances. Actually, stenosis occurs in a decrease in the blood vessel membranes' dimension, therefore alters the blood flow

channel's flexibility. This might lead to changes in blood flow and related trends, which could have serious health repercussions. Additionally, the pattern researchers have seen in energy graph could potentially result from this matter, which is shown in Fig 7. The impact of β on velocity graph which is shown in Fig. 6. For the larger values of the β values the velocity graph increased. physically, Raising the Casson fluid parameter, particularly implies more non-Newtonian activities, results in a slower velocity slope over stenotic sidewall veins due to increased stress induced by yield and stronger shear-thin effects. It may have significant implications for blood flow efficiency, stress transmission, and overall heart function, particularly in instances of stenotic veins when flow has become constrained.

Fig. 8 demonstrates the impact of the Pr number. A rise in Pr causes a reduction in the energy curve. physically, the amount of the Pr factor has an inverse connection with heat diffusion. Whenever the Prandtl number exceeds expectations, heat diffusion decreases, resulting in more severe thermal dispersion. Whenever the Prandtl number increases, the heat diffusion decreases. This implies that warmth spreads slower, and heat is drawn below.

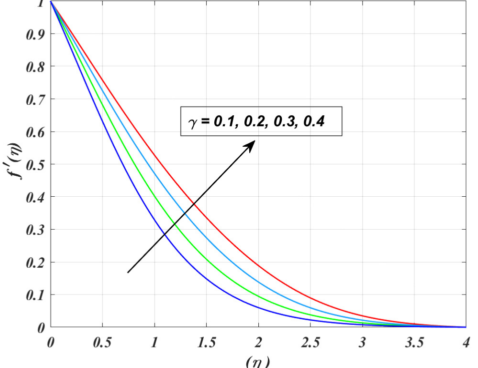

Figure 5. Influence of γ on $f'(\eta)$

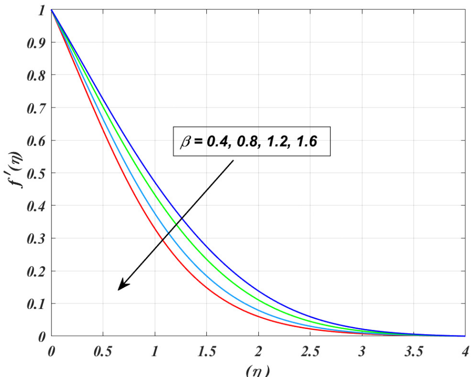

Figure 6. Influence of β on $f'(\eta)$

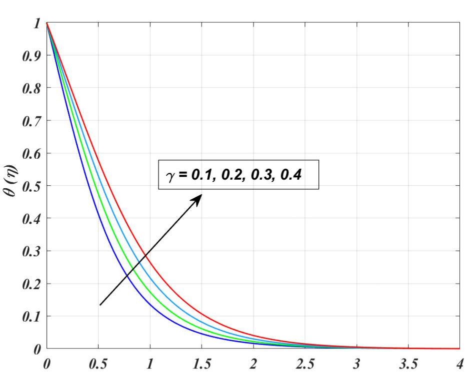

Figure 7. Influence of γ on $\theta(\eta)$

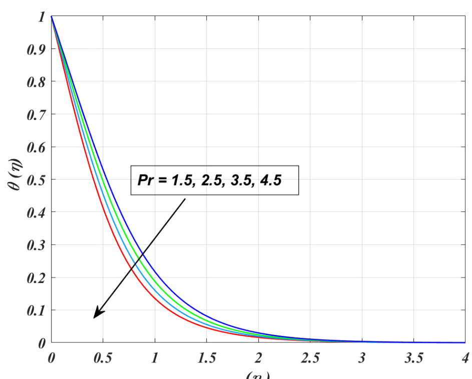

Figure 8. Influence of Pr on $\theta(\eta)$

The impact of Ec on energy graph is shown in Fig 9. Physically, the Ec impact enhances the energy and heat boundary layer thickness enhanced. Dispersion implicitly increases thermal convection, causing the thermal layer to become thicker.

Contour plots are an excellent graphical tool for learning about the complex dynamics of blood flow via constricted arteries. These factors are important for validating mathematical models, designing medical devices, diagnosing patients, and arranging medicines. If we wish to enhance the outcomes for cardiac patients, we must first understand circulatory actions, which contour charts enable when dealing with stenotic arteries. The impact of γ and M on skin friction graph is shown in Fig 10. For larger values of the M on the skin friction graph declined, a decrease in circulation of heat occurs as a result of the physical phenomena of as a result, which causes thermal dispersion to become more severe. Consequently, this results in the generation of a bigger quantity of power via activities that include motion. Despite the fact that we saw a reverse tendency on $Nu_x Re_x^{-1/2}$ graph is shown in Fig 11.

Streamlines, the exploration of liquid actions, and the representation of circulation, in specific, deliver a variety of properties that, once put into consideration combined, make them great instruments for performing research and analysis on the motions of liquids. Streamlines are particularly useful for this purpose. Especially, this holds accurate when applied to the study of the flow of fluids.

There are a variety of magnetic parameter values that have an effect on streamlines graphs, as seen in Figures 12, 13, and 14. In the direction of the primary flow, the intensity of the magnetic characteristic attracts molecules with a higher electrical conductivity. There is a correlation between the arterial network's arcs, particularly

are positioned near to the location of a narrowing of and the significant increase in velocity that occurs within the blood vessels.

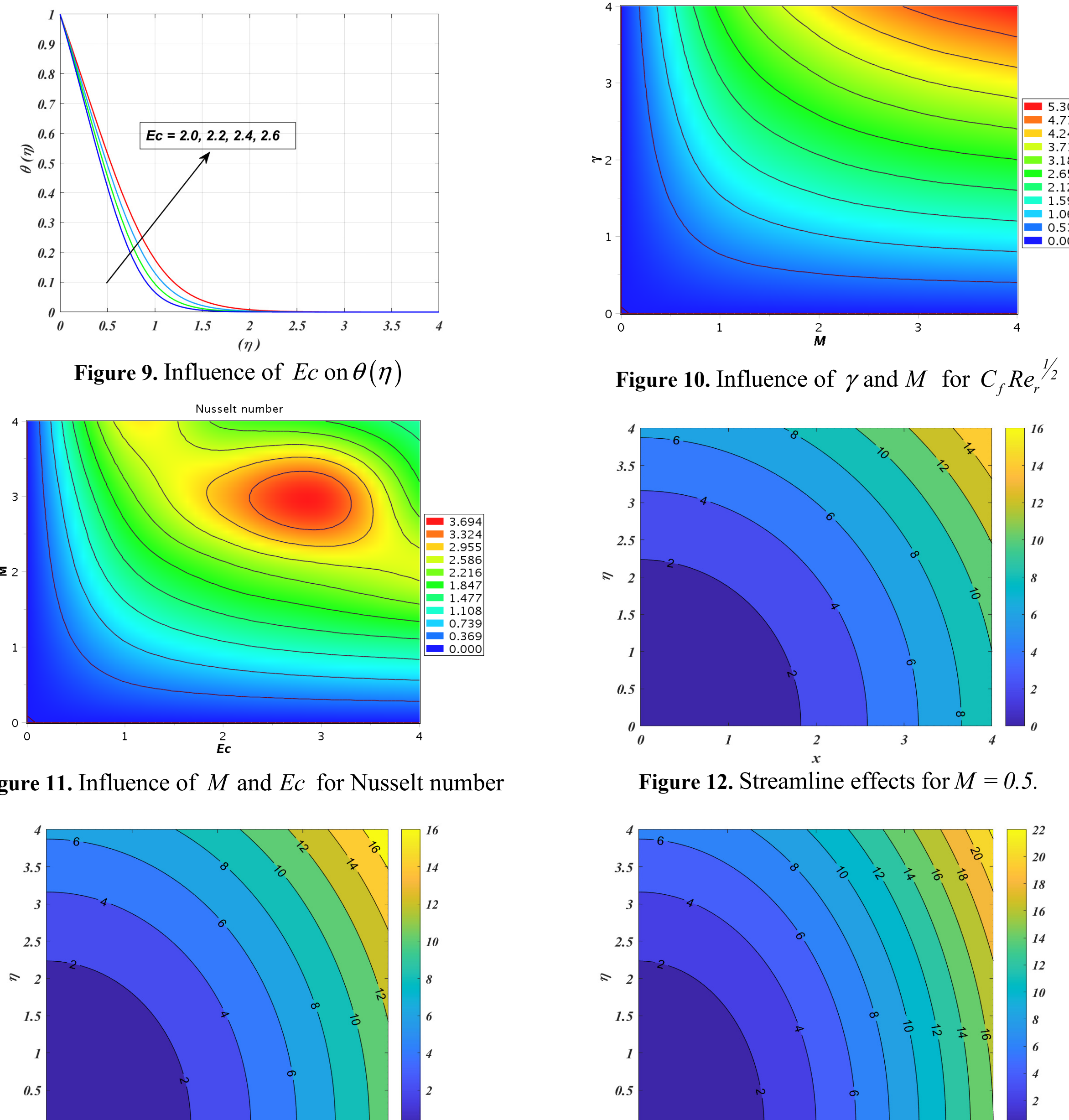

Figure 9. Influence of Ec on $\theta(\eta)$

Figure 10. Influence of γ and M for $C_f Re_r^{1/2}$

Figure 11. Influence of M and Ec for Nusselt number

Figure 12. Streamline effects for $M = 0.5$.

Figure 13. Streamline effects for $M = 1.0$.

Figure 14. Streamline effects for $M = 1.5$

Table 2. Comparision results for $C_f Re_r^{1/2}$ for various values of γ *and* ϕ_1 [20].

Waqas et al.[20]		Present outcomes (bvp5c)
γ, ϕ_1	$C_f Re_r^{1/2}$	$C_f Re_r^{1/2}$
0.1, 0.01	0.939968	0.939930
0.12, 0.01	0.924794	0.924702
0.14, 0.01	0.911311	0.911346
0.1, 0.05	1.329552	1.329553
0.1, 0.1	1.175985	1.175957

5. CONCLUSIONS

The most important results are as follows:

- The circulation architecture that is already functioning has the ability to significantly enhance the transportation of medical human resources.
- Au and Ta nanoparticles are extremely well-organized for medical transportation.

- Rising the M values, results in decreasing behavior of the velocity graph.
- Enhancing the γ values, results in enhancing behavior of the velocity graph.
- The impact of γ parameter inputs as result in enhanced energy graph.
- decreasing graph in fluid temperature is instigated by a rise in *Pr* values.
- In the present model, the *Cf* and *Nu* there is no tendency at an increasing values of the *M*.

A few recommendations for possible future study that may be included in the scope of the present investigation are provided in the following paragraphs.

- The effect of magnetic field can be estimated with the various non-Newtonian fluids like Maxwell model, Casson fluid and Sisko fluid.
- The mathematical findings obtained from the feature study may be confirmed via the execution of experimental studies.
- Finding a computational method to a multi-phase issue may be proficient through the procedure of execution an investigation.
- It is possible to deal with the theoretical framework by using a method that is known as neural network technology.
- When it comes to enhancing heat transfer as well as biochemical linkages, it is feasible to identify the components which have the greatest ability for performing so.
- Personalized therapy that takes into account the unique characteristics of every single client will undoubtedly have a prominent position in the next developments. The research that is now being conducted is significant in a number of fields that fall under the general heading of healthcare.

Acknowledgements

I am grateful for the open access funding provided by Rashtriya Uchchatar Shiksha Abhiyan (RUSA 2.0), Ministry of Human Resource Development, Department of Higher Education, Government of India, India. The funding bodies had no role in the design of the study, collection, analysis, interpretation of data, or in writing the manuscript.

Disclosure statement

No potential conflict of interest was reported by the author(s).

ORCID

Suneetha Sangapatnam, https://orcid.org/0000-0001-6627-6446

REFERENCES

[1] L. Sarwar, A. Hussain, U. Fernandez-Gamiz, S. Akbar, A. Rehman, and E.S.M. Sherif, “Thermal enhancement and numerical solution of blood nanofluid flow through stenotic artery,” Sci. Rep. **12**(1), 1–11 (2022). https://doi.org/10.1038/s41598-022-20267-8

[2] I. Shahzadi, and S. Bilal, “A significant role of permeability on blood flow for hybrid nanofluid through bifurcated stenosed artery: Drug delivery application,” Comput. Methods Programs Biomed. **187**, 105248 (2020). https://doi.org/10.1016/j.cmpb.2019.105248

[3] S.U.S. Choi, and J.A. Eastman, "Enhancing Thermal Conductivity of Fluid with Nanoparticles," in: *1995 International mechanical engineering congress and exhibition*, (San Francisco, CA, USA, 1995), **231**, 99-105 (1995).

[4] S.R.R. Reddy, G. Ramasekhar, S. Suneetha, and S. Jakeer, “Entropy Generation Analysis on MHD Ag+Cu/Blood Tangent Hyperbolic Hybrid Nanofluid Flow Over a Porous Plate,” J. Comput. Biophys. Chem. **22**(7), 881–895 (2023). https://doi.org/10.1142/S2737416523500473

[5] M. Alhadri, et al., “Response surface methodology (RSM) and artificial neural network (ANN) simulations for thermal flow hybrid nanofluid flow with Darcy-Forchheimer effects,” J. Indian Chem. Soc. **99**(8), 100607 (2022). https://doi.org/10.1016/j.jics.2022.100607

[6] R. Tiwari, and M.K. Das, “Heat transfer augmentation in a two-sided lid-driven differentially heated square cavity utilizing nanofluids,” International Journal of Heat and Mass Transfer, **50**(9-10), 2002-2018 (2007). https://doi.org/10.1016/j.ijheatmasstransfer.2006.09.034

[7] G. Ramasekhar, “Scrutinization of BVP Midrich Method for Heat Transfer Analysis on Various Geometries in the,” **13**(1), 100–107 (2024). https://doi.org/10.1166/jon.2024.2130

[8] G. Ramasekhar, and P.B.A. Reddy, “Entropy generation on Darcy–Forchheimer flow of Copper-Aluminium oxide/Water hybrid nanofluid over a rotating disk: Semi-analytical and numerical approaches,” Sci. Iran. **30**(6), 2245–2259 (2023). https://doi.org/10.24200/sci.2023.60134.6617

[9] M.J. Mitchell, M.M. Billingsley, R.M. Haley, M.E. Wechsler, N.A. Peppas, and R. Langer, “Engineering precision nanoparticles for drug delivery,” Nat. Rev. Drug Discov. **20**(2), 101–124 (2021). https://doi.org/10.1038/s41573-020-0090-8

[10] A.M. Wagner, M.P. Gran, and N.A. Peppas, “Designing the new generation of intelligent biocompatible carriers for protein and peptide delivery,” Acta Pharm. Sin. B, **8**(2), 147-164 (2018). https://doi.org/10.1016/j.apsb.2018.01.013

[11] G. Ramasekhar, and M. Jawad, “Characteristics of MWCNT, SWCNT, Cu and water based on magnetized flow of nanofluid with Soret and Dufour effects induced by moving wedge: Consequence of Falkner–Skan power law," Numerical Heat Transfer, Part A: Applications, 1–15 (2024). https://doi.org/10.1080/10407782.2024.2341270

[12] E. Blanco, H. Shen, and M Ferrari, “Principles of nanoparticle design for overcoming biological barriers to drug delivery,” Nature Biotechnol. **33**, 941–951 (2015). https://doi.org/10.1038/nbt.3330

[13] L. Kou, Y.D. Bhutia, Q. Yao, Z. He, J. Sun, and V. Ganapathy, "Transporter-guided delivery of nanoparticles to improve drug permeation across cellular barriers and drug exposure to selective cell types," Front. Pharmacol. **9**, (2018). https://doi.org/10.3389/FPHAR.2018.00027/FULL
[14] G. Ramasekhar, J. Shaik, S.R.R. Reddy, A. Divya, M. Jawad, and B.A.A. Yousif, "Numerical investigation of Casson fluid flow performance of blood containing gold and Fe3O4 nanofluid injected into a stenotic artery," Numer. Heat Transf. Part A Appl. 1–17 (2024). https://doi.org/10.1080/10407782.2024.2372465
[15] H. Waqas, U. Farooq, D. Liu, M. Alghamdi, S. Noreen, and T. Muhammad, "Numerical investigation of nanofluid flow with gold and silver nanoparticles injected inside a stenotic artery," Materials & Design, **223**, 111130 (2022). https://doi.org/10.1016/j.matdes.2022.111130
[16] T. Sajid, et al., "Magnetized Cross tetra hybrid nanofluid passed a stenosed artery with nonuniform heat source (sink) and thermal radiation: Novel tetra hybrid Tiwari and Das nanofluid model," J. Magn. Magn. Mater. **569**, (2023). https://doi.org/10.1016/j.jmmm.2023.170443
[17] S.Z.H. Shah, A. Ayub, U. Khan, A. Darvesh, E.-S.M. Sherif, and I. Pop, "Thermal transport exploration of ternary hybrid nanofluid flow in a non-Newtonian model with homogeneous-heterogeneous chemical reactions induced by vertical cylinder," Adv. Mech. Eng. **16**(5), 1–14 (2024). https://doi.org/10.1177/16878132241252229
[18] G. Ramasekhar, S. Jakeer, S. Reddy, R. Reddy, and S. Alkarni, "Biomedical importance of Casson nanofluid flow with silver and Fe 2 O 3 nanoparticles delivered into a stenotic artery : Numerical study," **9**, 23142–23157 (2024). https://doi.org/10.3934/math.20241125
[19] E.A. Algehyne, et al., "Entropy optimization and response surface methodology of blood hybrid nanofluid flow through composite stenosis artery with magnetized nanoparticles (Au-Ta) for drug delivery application," Sci. Rep. **13**(1), 1–21 (2023). https://doi.org/10.1038/s41598-023-36931-6
[20] H. Waqas, U. Farooq, D. Liu, M. Alghamdi, S. Noreen, and T. Muhammad, "Numerical investigation of nanofluid flow with gold and silver nanoparticles injected inside a stenotic artery," Materials & Design, **223**, 111130 (2022). https://doi.org/10.1016/j.matdes.2022.111130
[21] L. Sarwar, and A. Hussain, "Flow characteristics of Au-blood nanofluid in stenotic artery," International Communications in Heat and Mass Transfer, **127**, 105486 (2021). https://doi.org/10.1016/j.icheatmasstransfer.2021.105486
[22] S. Basma, et al. "Heat transfer attributes of gold–silver–blood hybrid nanomaterial flow in an EMHD peristaltic channel with activation energy," Nanomaterials, **12**(10), 1615 (2022). https://doi.org/10.3390/nano12101615
[23] H.T.Basha, K. Rajagopal, N.A. Ahammad, S. Sathish, and S.R. Gunakala, "Finite Difference Computation of Au-Cu/Magneto-Bio-Hybrid Nanofluid Flow in an Inclined Uneven Stenosis Artery," Complexity, **2022**(1), 2078372 (2022). https://doi.org/10.1155/2022/2078372
[24] H. Waqas, U. Farooq, A. Hassan, D. Liu, S. Noreen, R. Makki, M.Imran, and M.R. Ali, "Numerical and Computational simulation of blood flow on hybrid nanofluid with heat transfer through a stenotic artery: Silver and gold nanoparticles," Results in Physics, **44**, 106152 (2023). https://doi.org/10.1016/j.rinp.2022.106152
[25] I. Shahzadi, and S. Bilal, "A significant role of permeability on blood flow for hybrid nanofluid through bifurcated stenosed artery: Drug delivery application," Computer Methods and Programs in Biomedicine, **187**, 105248 (2020). https://doi.org/10.1016/j.cmpb.2019.105248

ПОТОК КЕССОНОВОЇ КРОВІ, ЩО МІСТИТЬ НАНОЧАСТИНКИ AU I TA, ПО СТЕНОТИЧНІЙ АРТЕРІЇ

Суніта Сангаратнам
Факультет прикладної математики, Університет Йогі Вемана, Кадапа-516005, Андхра-Прадеш, Індія

Обчислювальна динаміка рідини зосереджує увагу на дослідженнях кровотоку через звужені артерії через актуальність цих питань для біологічних досліджень. Основна мета цього дослідження – з'ясувати, як наночастинки впливають на кровотік через звужену артерію. У рамках нашого дослідження теоретичного сценарію потоку ми досліджуємо значення руху нанорідини Кассона через серцеву артерію. Використовуючи відповідні змінні подібності delf, PDE перетворюються на ODE. Після цього безрозмірні рівняння обробляються за допомогою комп'ютерної програми MATLAB за допомогою Bvp5c. Магнітні властивості клітин кровотоку досліджували шляхом збільшення параметра магнітного поля, що призвело до зменшення кровотоку, як було передбачено. Тренд руху зменшувався, коли параметр Кассона рідини зростав. Для підвищення ефективності передачі тепла слід збільшити концентрацію частинок золота в звуженій артерії. Можна стверджувати, що наночастинки заліза корисні для доставки ліків. Наявні на даний момент методи можуть бути корисними для розподілу ліків по системі кровообігу. Теоретичні наслідки цього методу доставки ліків представлені у спосіб, які стають зрозумілішими завдяки використанню ілюстрації.

Ключові слова: *наночастинки Au і Ta; метод Bvp5c; стеноз артерії; МГД; рідина Кассона*